

NASCTN Report 7

NIST Technical Note 2069

Characterizing LTE User Equipment Emissions: Factor Screening

Jason Coder, Adam Wunderlich, Michael Frey, Paul Blanchard,
Daniel Kuester, Azizollah Kord, Max Lees, Aric Sanders, Jolene Splett,
Lucas Koepke, Robert Horansky, Duncan McGillivray, John Ladbury,
Jeffrey Correia, Venkatesh Ramaswamy, Jerediah Fevold, Shawn Lefebre,
Jacob Johnson, John Carpenter, Mark Lofquist, Keith Hartley

This publication is available free of charge from:
<https://doi.org/10.6028/NIST.TN.2069>

NIST
National Institute of
Standards and Technology
U.S. Department of Commerce

NASCTN Report 7

NIST Technical Note 2069

Characterizing LTE User Equipment Emissions: Factor Screening

Jason Coder, Adam Wunderlich, Michael Frey, Paul Blanchard,
Daniel Kuester, Azizollah Kord, Max Lees, Aric Sanders, Jolene Splett,
Lucas Koepke, Robert Horansky, Duncan McGillivray, John Ladbury,
Jeffrey Correia, Venkatesh Ramaswamy, Jerediah Fevold, Shawn Lefebre,
Jacob Johnson, John Carpenter, Mark Lofquist, Keith Hartley
Communications Technology Laboratory
NIST

This publication is available free of charge from:
<https://doi.org/10.6028/NIST.TN.2069>

September 2019



U.S. Department of Commerce
Wilbur L. Ross, Jr., Secretary

National Institute of Standards and Technology
Walter Copan, NIST Director and Undersecretary of Commerce for Standards and Technology

Characterizing LTE User Equipment Emissions: Factor Screening

Jason Coder, Adam Wunderlich, Michael Frey, Paul Blanchard,
Daniel Kuester, Azizollah Kord, Max Lees, Aric Sanders, Jolene Splett,
Lucas Koepke, Robert Horansky, Duncan McGillivray, John Ladbury,
Jeffrey Correia, Venkatesh Ramaswamy, Jerediah Fevold, Shawn Lefebre,
Jacob Johnson, John Carpenter, Mark Lofquist, Keith Hartley

NASCTN Program Manager: Melissa Midzor

September 27, 2019



NASCTN

National Advanced Spectrum and
Communications Test Network

DISCLAIMER

Any commercial equipment, instruments, or materials explicitly or implicitly identified in this report are included in order to specify the experimental procedure adequately. Such identification does not imply any recommendation or endorsement by National Institute of Standards and Technology (NIST) or National Advanced Spectrum and Communications Test Network (NASCTN), nor is it intended to imply that the materials or equipment identified are necessarily the best available for the purpose.

National Institute of Standards and Technology Technical Note 2069
Natl. Inst. Stand. Technol. Tech. Note 2069, 192 pages (September 2019)
CODEN: NTNOEF

This publication is available free of charge from: <https://doi.org/10.6028/NIST.TN.2069>

National Advanced Spectrum and Communications Test Network (NASCTN)

The mission of the National Advanced Spectrum and Communications Test Network (NASCTN) is to provide, through its members, robust test processes and validated measurement data necessary to develop, evaluate and deploy spectrum sharing technologies that can increase access to the spectrum by both federal agencies and non-federal spectrum users.

NASCTN was formed to provide a single focal point for engaging industry, academia, and other government agencies on advanced spectrum technologies, including testing, measurement, validation, and conformity assessment. The National Institute of Standards and Technology (NIST) hosts the NASCTN capability at the Department of Commerce Boulder Laboratories in Boulder, Colorado.

NASCTN is a membership organization under a charter agreement. Members

- Make available, in accordance with their organization's rules policies and regulations, engineering capabilities and test facilities, with typical consideration for cost.
- Coordinate their efforts to identify, develop and test spectrum sharing ideas, concepts and technology to support the goal of advancing more efficient and effective spectrum sharing.
- Make available information related to spectrum sharing, considering requirements for the protection of intellectual property, national security, and other organizational controls, and, to the maximum extent possible, allow the publication of NASCTN test results.
- Ensure all spectrum sharing efforts are identified to other interested members.

Current charter members are:

- Department of Defense Chief Information Officer (DoD CIO)
- National Aeronautics and Space Administration (NASA)
- National Institute of Standards and Technology (NIST)
- National Oceanic and Atmospheric Administration (NOAA)
- National Science Foundation (NSF)
- National Telecommunications and Information Administration (NTIA)

Acknowledgments

The successful execution of this project required a diverse range of technical skills and coordination across a large number of contributors. Specifically, this work pulled together expertise in long-term evolution (LTE) communication systems, radio frequency (RF) engineering, software development, statistics, and metrology. The primary technical tasks, which are detailed in the main body of this report, included test design, test automation, data processing, and data analysis. Furthermore, several supporting technical investigations were undertaken, as described in the appendices.

The co-technical leads for the project were Jason Coder, who headed up testbed development and test execution, and Dr. Adam Wunderlich, who led experimental design, data processing, and data analysis. Within the testbed team, Dr. Daniel Kuester led development of data acquisition and testbed automation; Azizollah Kord provided LTE engineering support; Dr. Duncan McGillivray led RF testbed construction and calibration; Dr. Robert Horansky measured user equipment (UE) antenna patterns; John Ladbury carried out RF uncertainty analysis and provided metrology expertise; and Dr. Shane Allman supported test automation and execution. Within the data processing and analysis team, Paul Blanchard led the development of software for data parsing and time-alignment; Max Lees developed software for data processing and data plotting; Dr. Aric Sanders aided data processing and carried out exploratory data analysis; Dr. Michael Frey led the inferential statistical analysis; Jolene Splett performed statistical analyses; and Lucas Koepke analyzed testbed stability and assisted the statistical analysis.

MITRE Corporation personnel provided key project support in several areas. Namely, LTE expertise and assistance was provided by Jeffrey Correia, Dr. Venkatesh Ramaswamy, Jerediah Fevold, and Shawn Lefebre. Estimation of path loss distributions from cell-tower location databases was undertaken by Jacob Johnson, John Carpenter, and Mark Lofquist. Last, Dr. Keith Hartley deserves special recognition for acting as project manager and overseeing the compilation and editing of the report.

Finally, we would like to thank the many additional individuals that made valuable contributions over the course of this project. Namely, we would like to acknowledge the efforts of the test plan development team and thank those who participated in the public comment period for the test plan. Also, the technical team thanks the National Advanced Spectrum and Communications Test Network (NASCTN) program manager, Dr. Melissa Midzor, former NASCTN program managers, Dr. Michael Janezic and Dr. Sheryl Genco, the NASCTN administrative officer, Linda Derr, and Irena Stevens, NASCTN associate, for their efforts, which made project success possible.

Executive Summary

In 2014, the Federal Communications Commission (FCC) (Order FCC 14-31) established the advanced wireless services 3 (AWS-3) Band: 1695 MHz to 1710 MHz, 1755 MHz to 1780 MHz, and 2155 MHz to 2180 MHz. The FCC auctioned the AWS-3 band for commercial mobile broadband usage in the United States, which raised \$41B and required federal agencies in the AWS-3 band to look for other ways to accomplish their missions outside of the AWS-3 band. In 1755 MHz to 1780 MHz, the Department of Defense (DoD) is using a combination of sharing, consolidation, and relocation to other bands. Requests from auction winners to enter the band before the DoD has transitioned out are evaluated through the DoD early entry portal analysis capability (EEPAC), managed by the Defense Information Systems Agency (DISA) Defense Spectrum Organization (DSO). Coordination for early entry into this band depends on an interference model that was developed and agreed to by the FCC, National Telecommunications and Information Administration (NTIA), DoD, and commercial interests.

The DISA DSO through the spectrum sharing test and demonstration (SSTD) program proposed to the National Advanced Spectrum and Communications Test Network (NASCTN) a measurement campaign to quantitatively characterize long-term evolution (LTE) uplink band (UL) waveforms generated by user equipment (UE) in the 1755 MHz to 1780 MHz band with the intent to make realistic measurements of UE emissions. These measurements will be used for assessing interference to DoD systems that, for a time, will remain in the 1755 MHz to 1780 MHz band. A secondary goal of this characterization, with a documented methodology and uncertainty, is to give AWS-3 stakeholders more confidence in the coordination request evaluation (CRE) process.

In the process of conducting this characterization, NASCTN developed a suitable measurement methodology, uncertainty analysis, and a statistical analysis approach capable of investigating the cumulative and complex interactions of UE emissions and network response. Though the methods and results discussed here specifically relate to a particular frequency band of interest, the methods can be repeated in other frequency bands and for other types of equipment (e.g., narrow-band Internet of Things (IoT) type devices).

Key products of this study include:

- Distributions of effective isotropic radiated power (EIRP) from a UE in an active resource block for a variety of test configurations (e.g., path loss, UE settings, and LTE network settings).
 - Includes distributions for physical uplink shared channel (PUSCH), physical uplink control channel (PUCCH), and sounding reference signal (SRS).
- A comparison between the UEs self-reported transmit power and measured power distributions.
- 3-D Radiation pattern measurements of several common LTE UEs.
- Uncertainty analysis that includes an uncertainty budget and calculation of overall measurement uncertainty.
- Summary statistics for the test data, publicly available at <https://doi.org/10.18434/M32130>.

The objective of this test is to design, demonstrate, and validate a test methodology to measure LTE UE emissions for use in aggregate interference calculations. Specifically, this involves developing a better understanding of what factors (e.g., evolved node B (eNB) power control variables and scheduling algorithms, propagation channel, traffic type, and in-cell and adjacent-cell loading) impact the emissions of a typical commercial off-the-shelf (COTS) LTE UE.

The primary aim of the work presented here is to determine which factors have a significant impact on the distribution of PUSCH power per physical resource block (PRB). This type of experiment is called *factor screening* in the experimental design literature. This experiment, which involved 28 factors, was designed to screen a large number of factors with a practical number of tests, taking into account commercial and laboratory equipment limitations and stability.

Key Challenges:

- One of the largest factor screening experiments ever undertaken at the National Institute of Standards and Technology (NIST): 28 factors, with a complex split-plot design repeated over four rounds of testing.
- Wide range of test configurations (1056 unique configurations).
- Statistical Analysis - The response variable is a distribution, not a scalar or vector. Also, PUSCH power per PRB distributions are frequently multimodal. Not a textbook problem.
- Commercial equipment - Limited technical documentation, not intended for automated laboratory testing (e.g., frequent setting changes, time-alignment).
- Automation - Makes testing a large number of equipment configurations practical, providing sufficient data for rigorous uncertainty assessment and statistical analysis.
- Data verification - 28 different automated checks during parsing and time alignment. Each 80 min test block auto-generated 294 pages of data verification plots for manual inspection.

Key Findings:

Open-Loop vs Closed-Loop power control (see subsection 6.3.2 and subsection 6.3.3):

- PUSCH power per PRB distributions with open-loop power control spanned a much larger range than the distributions with closed-loop power control.
- PUCCH power per PRB distributions with open-loop power control spanned a much larger range than the distributions with closed-loop power control.
- Note: A follow-on experiment is planned to characterize PUSCH power variations in closed-loop mode over a range of realistic conditions. If closed-loop power control is predominantly used, this experiment would clarify the variability that can be expected under realistic conditions. Closed-loop power control could enable better prediction of UE behavior.

Measured and UE-Reported PUSCH Power per PRB (see subsection 6.3.5):

- Substantial body of work predicated on the UE's self-reported power. However, its accuracy has never been assessed before this study.
- In some scenarios, the UE reported power was a poor metric of the actual radiated power.
- However, the testing found that the UE-reported power per PRB was always more than measured power (i.e., the UE never transmitted more power than it reported.)

Comparison of Open-Loop Power Control Prediction and UE-Reported Power (see subsection 6.3.6):

- LTE PUSCH power control can be rather complicated. A simplified model of LTE power control can be used to predict PUSCH emissions. To investigate this question, the test team evaluated the predictive power of the open-loop component of the LTE power control equation.
- In both the open-loop and closed-loop power control cases, the open-loop component of the power control equation was found to have little predictive utility. In the open-loop case, the UE-reported power generally exceeded the prediction.

3-D Radiation pattern measurements of several common LTE UEs:

- Radiation pattern measurements were conducted on five different types of UEs, with different cost, physical size, operating system, and generation/age attributes.
- The UE radiation patterns were not isotropic.

- The findings can be directly incorporated into revised interference models.

Statistical Analysis

- The primary aim was to identify factors that had a statistically-significant effect on the observed PUSCH power per PRB distribution.
- A key challenge was that the response variable was an empirical distribution, not a scalar or a vector. Designed experiments typically have a univariate response and model a central tendency. This experiment was uncommon in that the power observed for each factor combination was a distribution of values, often multimodal, and not well described by mean and standard deviation. To address the distributional nature of PUSCH power, the statistical analysis utilized analysis of variance (ANOVA) and multivariate analysis of variance (MANOVA) methods to assess differences in median, spread, and skew measures derived from the percentiles of each distribution.
- A principal component analysis (PCA) of the empirical percentiles confirmed the results from the analyses based on median, spread, and skew.
- Constrained eNB factors were combined into a single sixteen-level factor. Assessing statistically-significant differences between levels of this factor required the development of a new statistical procedure: a permutation-based multivariate Tukey test.
- This screening experiment involved a large number of factors with levels that may have sometimes pushed the performance of the LTE system under study outside its normal operating conditions. The unusual features of this experiment highlight statistics lessons and approaches that can be used for future similar experiments.

Complementary Results – MITRE

- To complement the NASCTN measurements, MITRE used an independent testbed to test configurations similar to some of those used in the screening experiment.
- The MITRE testbed differed from the NASCTN set-up in several key respects, including the eNB, the power measurement method, and the methodology for simulating network loading.
- The power distributions observed in the MITRE tests were consistent with the NASCTN laboratory measurements.
- Differences between the MITRE and NASCTN testbed implementations illustrate potential alternatives that are available when constructing a similar test set-up.

The experiment design, testbed, data processing, and statistical analysis worked together successfully to produce very high resolution results – sufficient to support engineering and programmatic decisions about experimental factors. The data can be used to improve DoD/DSO interference risk assessment, inform modeling LTE UE emissions, a component of the DoD aggregate interference model, and increase DoD/DSO’s confidence in allowing commercial LTE systems to deploy.

Contents

Acknowledgments	v
Executive Summary	vi
List of Acronyms	xiv
List of Figures	xix
List of Tables	xxii
1 Introduction	1
1.1 Objective	1
1.2 Scope	2
1.3 Background	2
1.4 Overview	2
2 Experimental Factors	7
2.1 Factor Descriptions	7
2.1.1 Factor A - Path Loss	9
2.1.2 Factor B - Spatial Size of Cells	9
2.1.3 Factors C & D - Number of Loading UE	10
2.1.4 Factor E - Spatial Distribution of Loading UEs	10
2.1.5 Factors F, G, & H - UE Traffic	12
2.1.6 Factors I, J, Y, & b - eNB Scheduling	14
2.1.7 Factor K - Power Control	15
2.1.8 Factors L & M - SRS	16
2.1.9 Factors N, O, & P - P_0 and Fractional Power Control	16
2.1.10 Factor Q - Receive Diversity	17
2.1.11 Factor R - RSRP Filter Coefficients	17
2.1.12 Factor S - Maximum UL Transmit Power	17
2.1.13 Factor T & V - Resource Allocation	17
2.1.14 Factor U - Latency Reaction Timer	18
2.1.15 Factors W and X - Link Adaptation	18
2.1.16 Factor Z - SRB Uplink Scheduling Weight	18
2.1.17 Factor a - Blanked PUCCH Resources	19
2.2 Collateral eNB Factors	19
3 Test Implementation and Execution	21
3.1 Testbed Design	21
3.1.1 Test Circuit	21
3.1.2 Data and Control Connections	25
3.1.3 Test Automation	25
3.2 Equipment	26

3.2.1	LTE Infrastructure	26
3.2.2	LTE eNB	26
3.2.3	LTE UE Traffic Generator	26
3.2.4	Vector Signal Analyzer	27
3.2.5	DUT UEs - Devices and Traffic	28
3.2.5.1	USRD Monitoring Software	28
3.3	Shielded Enclosure	29
3.4	Data Acquisition	29
3.4.1	Test Sequence	29
3.4.2	Device Checks Prior to Data Collection	34
3.5	Reference Measurements	34
4	Data Processing	36
4.1	LTE UE Data Acquisition	36
4.1.1	DUT Data Output	37
4.1.2	Data Output by the Traffic Generator	37
4.2	Parsing and Spectrogram Analysis	37
4.2.1	DUT Diagnostic Monitoring Data Parsing	38
4.2.2	Traffic Generator Data Parsing and Time Alignment	40
4.2.3	Spectrogram Re-binning to LTE Resource Block and Subframe	41
4.2.3.1	Re-binning in Time	41
4.2.3.2	Re-binning in Frequency	42
4.2.3.3	Limitations	43
4.2.4	Spectrogram Timestamp Alignment	43
4.2.5	Time Alignment Consistency Checks	50
4.3	Data Aggregation and Cleaning	50
5	Experimental Design	52
5.1	Statistical Design	52
5.1.1	Overview	52
5.1.2	Technical Details	53
5.2	Test Execution	59
5.3	Factor Settings	61
6	Exploratory Data Analysis	64
6.1	Data Verification Plots	64
6.2	Notable Examples	71
6.2.1	Power-Constrained and Resource-Constrained UEs	71
6.2.2	Negative Power Headroom	78
6.2.3	Interference Aware Scheduling	84
6.2.4	Large Variation in MCS Index	90
6.3	Global Summary Plots	96
6.3.1	RSRP stability	96
6.3.2	Empirical CDFs for measured PUSCH EIRP per PRB	100
6.3.3	Empirical CDFs for measured PUCCH power per PRB	102
6.3.4	Empirical CDFs for reported SRS power per PRB	104
6.3.5	Comparison of Measured EIRP and UE-Reported PUSCH Power per PRB	104
6.3.6	Comparison of Open-Loop Power Control Prediction and UE-Reported Power	109

7	Inferential Data Analysis	111
7.1	Methods	111
7.1.1	Analysis of Variance	111
7.1.2	Hypothesis Testing	113
7.1.3	Response Variables	113
7.1.4	Multiple Comparisons	114
7.1.5	Significance Level	116
7.2	Results	116
7.2.1	Sample Size	117
7.2.2	Measured PUSCH Power	121
7.2.3	Principal Components Analysis	124
7.2.4	Reported PUSCH Power	126
7.2.5	Measured PUCCH Power	131
7.2.6	Testbed Stability	133
7.2.7	Statistical Best Practices for Wireless RF Communications Experiments	138
8	Discussion & Topics for Further Research	140
8.1	Discussion	140
8.2	Potential Topics for Further Investigation	141
A	Additional Factors Considered	145
A.1	Maximum Number of UEs transmit per TTI	145
A.2	Downlink Scheduling Algorithm Type	145
A.3	TTI Bundling	145
A.4	Time Interval for Power Command Decisions	146
B	Parameters Collected	147
C	Calibration and Verification Measurements	149
C.1	Radiated Environment	149
C.1.1	Shielding Effectiveness	149
C.1.2	Horn Antenna - Gain	151
C.1.3	Horn Antenna - UE interaction	153
C.1.4	UE placement	155
C.2	Test System	158
C.2.1	RF Circuitry	158
C.2.2	Integrated system	161
C.2.3	eNB isolation	165
C.2.4	Spectrogram power level	165
C.3	Uncertainty	166
C.3.1	Spectrum Analyzer Power Measurement Uncertainty Components	169
C.3.2	Coupled Output Power Calibration Uncertainty Components	169
C.3.3	Programmable Attenuators	169
C.4	Offset Calibration to DUT EIRP	169
D	User Equipment Antenna Pattern Measurements	170
E	Estimation of Cell-Site Path Loss Distributions	175
E.1	Data Set: LTE Network Service Provider	175

E.2	Morphology	175
E.3	Cell Radius	176
E.4	Path Loss by Morphology	176
E.5	Producing P_{UE} Distributions Using Open-Loop Power Control Equation	177
F	MITRE Lab Results In Support of NASCTN Test	180
F.1	MITRE's Multi-UE System Description	180
F.1.1	Software Control	183
F.1.2	Test Design	186
F.1.2.1	Traffic Generation	186
F.1.2.2	eNB Configuration	186
F.2	Data Acquisition	186
F.2.1	System Calibration	187
F.3	Data Processing	187
F.3.1	Downlink Synchronization and Master Information Block Extraction	187
F.3.2	Epoch Subframe Alignment	187
F.3.3	Uplink Power Computation and Spectrogram Analysis	187
F.3.4	Results	188
	Bibliography	191

Acronyms

3GPP	3rd-generation partnership project	FTP	file transfer protocol
AC	alternating current	FULA	fast uplink link adaption
ANOVA	analysis of variance	GBR	guaranteed bit rate
APN	access point name	GPS	Global Positioning System
AWS-3	advanced wireless services 3	GUI	graphical user interface
BLER	block error rate	HARQ	hybrid automatic repeat request
BSR	buffer status report	HSS	home subscriber server
CDF	cumulative distribution function	Hz	Hertz
CFI	control format indicator	I/O	input and output
CLI	command line interface	ICIC	inter-cell interference coordination
COTS	commercial off-the-shelf	IoT	Internet of Things
CQI	channel quality indicator	IP	internet protocol
CRE	coordination request evaluation	IQ	in-phase and quadrature
CSI	channel status information	IQR	interquartile range
CSV	comma separated value	kbit/s	kilo bits per second
dB	decibel	km	kilometer
dB_i	gain of an antenna relative to an isotropic antenna	KPI	key performance indicator
dB_m	dB relative to 1 mW	LAN	local area network
DCI	downlink control information	LO	local oscillator
DISA	Defense Information Systems Agency	LTE	long-term evolution
DL	downlink band	MAC	medium access control
DLL	dynamic link library	MANOVA	multivariate analysis of variance
DoD	Department of Defense	Mbit/s	mega bits per second
DSO	Defense Spectrum Organization	MCS	modulation coding scheme
DTX	discontinuous transmission	MIB	master information block
DUT	device under test	MIMO	multiple-input multiple-output
EEPAC	early entry portal analysis capability	MME	mobility management entity
EICIC	Enhanced Inter-cell Interference Coordination	MMSE	minimum mean-squared error
EIRP	effective isotropic radiated power	MP	MITRE Product
eNB	evolved node B	ms	milli second
EPC	evolved packet core	MUSE	multi UE system emulator
FCC	Federal Communications Commission	NAS	non-access stratum
FD	frequency domain	NASCTN	National Advanced Spectrum and Communications Test Network
FDD	frequency-division duplex	NBIT	NIST Broadband Interoperability Testbed
FFT	fast fourier transform	NIST	National Institute of Standards and Technology

NLCD	national land coverage database	SC-FDMA	single-carrier frequency division multiple access
NTIA	National Telecommunications and Information Administration	SDU	service data unit
NVRAM	nonvolatile random-access memory	SGW	serving gateway
OFDM	orthogonal-frequency division multiplexing	SINR	signal to interference plus noise ratio
OS	operating system	SNR	signal to noise ratio
PC	personal computer	SRB	signalling radio bearer
PCA	principal component analysis	SRF	spectrum relocation fund
PDCCH	physical downlink control channel	SRS	sounding reference signal
PDF	probability density function	SSS	secondary synchronization signal
PDU	protocol data unit	SSTD	spectrum sharing test and demonstration
PGW	packet gateway	TBS	transport block size
PHR	power headroom report	TCP	transmission control protocol
PRACH	physical random access channel	TD	time domain
PRB	physical resource block	TPC	transmission power control
PSS	primary synchronization signal	TTI	transmission time interval
PUCCH	physical uplink control channel	UDP	user datagram protocol
PUSCH	physical uplink shared channel	UE	user equipment
QAM	quadrature amplitude modulation	UL	uplink band
QCI	QoS class identifier	ULA	uplink link adaption
QoS	quality of service	US	United States
RACH	random access channel	USB	universal serial bus
RAN	radio access network	USRD	UE self-reported diagnostics
RE	resource element	UTG	UE traffic generator
RF	radio frequency	UTRAN	universal terrestrial access network
RMS	root mean square	VNA	vector network analyzer
RRC	radio resource control	VoLTE	voice over LTE
RSRP	reference signal received power	VSA	vector signal analyzer
RSRQ	reference signal received quality	WNO	wireless network operator
RSSI	received signal strength indicator	XML	extensible markup language
SA	signal analyzer		

List of Figures

1.1	Conceptual illustration of the laboratory tests showing the DUT UE at various virtual locations within Cell <i>A</i> . An adjacent cell, Cell <i>B</i> , can have some influence on the behavior of Cell <i>A</i> .	4
1.2	Conceptual view of the LTE signal flow in the factor-screening measurements.	5
2.1	Two sectors with two groups of UEs in RF near condition are closer to eNBs with less path loss, and therefore with higher RSRP.	11
2.2	Two sectors with four groups of UEs at eNB's cell edge with higher path loss, and therefore with low RSRP.	12
3.1	NASCTN Laboratory Testbed	22
3.2	A photo of the realized test circuit used in the factor screening measurements.	24
3.3	Data and control connections between the PC and the rest of the testbed.	25
3.4	Photo showing a DUT UE in a machined foam holder inside the small shielded enclosure	30
3.5	High-level test sequence specification for the experiment design specified in chapter 5.	32
3.6	Test sequence specifications to arm, acquire, and fetch within a single eNB configuration. Threads that control different devices synchronize at the dotted lines.	33
4.1	A simplified flow chart depicting the data files generated for each capture during acquisition of a dataset.	36
4.2	High-level flow chart of post-acquisition data file parsing and time alignment process.	38
4.3	Flow chart of USRD log file parsing procedure.	39
4.4	Flow chart of UTG log file parsing procedure.	40
4.5	Grid of the acquired (dashed lines) and LTE-aligned (solid lines) spectrograms. The postprocessing procedure produces power averages in each LTE-aligned block of the spectrogram, consisting of all acquired data except the excluded orange dashed lines.	41
4.6	Example of spectrogram re-binned to the LTE time and frequency grid. The frequency domain bleeding between PRB is visible between active and inactive blocks.	43
4.7	(Top) A portion of a simulated spectrogram constructed from DUT UE self-reported PRB allocations (via USRD); (bottom) a portion of the measured VSA spectrogram (on a mW power scale) from the same capture, prior to time alignment with the USRD data.	45
4.8	(Top) Portion of a simulated spectrogram constructed from DUT UE self-reported PRB allocations (via USRD); (Bottom) Portion of the measured VSA spectrogram (on a mW power scale) from the same capture, after time alignment with the USRD data.	46
4.9	DUT UE self-reported transmission power (via USRD) versus total power in corresponding PRBs in the measured VSA spectrogram, without alignment in time between the VSA and USRD. The largest spread in measured VSA power at a given USRD power is nearly 60 dB (at a reported USRD power of -21 dBm).	47
4.10	DUT UE self-reported transmission power (via USRD) versus total power in corresponding PRBs in the measured VSA spectrogram, after alignment in time between the VSA and USRD. The largest spread in measured VSA power at a given USRD power is less than 2 dB (at a reported USRD power of -21 dBm).	48
4.11	Flow chart of VSA spectrogram time alignment procedure.	49
4.12	Flow chart of VSA spectrogram starting time consistency check procedure.	51
6.1	Example VSA spectrogram captures. Grayscale range: [-58, 23] dBm.	65
6.2	Example loading UE activity time-series (Top) and PUSCH PRB allocation distributions (Bottom) for the two captures. Note: The PUSCH PRB usage values are reported by the UTG as 500 ms averages.	66
6.3	Example PUSCH Power histograms.	67
6.4	Example PUCCH Power histograms.	68
6.5	Example time-series plots. Top: Mean measured PUSCH EIRP per PRB. Middle: Number of active PRBs for PUSCH (blue) and PUCCH (red). Bottom: DUT-reported power per PRB.	69
6.6	Example time-series plots. Top: MCS Index. Upper-Middle: Number of attached loading UEs. Lower-Middle: BSR. Bottom: Measured EIRP per TTI.	70

6.7	Power-constrained versus Resource-constrained UE Example: VSA spectrogram captures. Grayscale range: [-58, 23] dBm.	73
6.7a	Power Constrained	73
6.7b	Resource Constrained	73
6.8	Power-constrained versus Resource-constrained UE Example. Top: Loading UE activity time-series. Bottom: PRB allocation distributions.	74
6.8a	Power Constrained	74
6.8b	Resource Constrained	74
6.9	Power-constrained versus Resource-constrained UE Example: PUSCH Power Histograms	75
6.9a	Power Constrained	75
6.9b	Resource Constrained	75
6.10	Power-constrained versus Resource-constrained UE Example: PUSCH Time Series.	76
6.10a	Power Constrained	76
6.10b	Resource Constrained	76
6.11	Power-constrained versus Resource-constrained UE Example: Additional KPI Time Series.	77
6.11a	Power Constrained	77
6.11b	Resource Constrained	77
6.12	Negative Power Headroom UE Example: VSA spectrogram captures. Grayscale range: [-58, 23] dBm.	79
6.13	Negative Power Headroom UE Example: loading UE activity time-series (Top) and PRB allocation distributions (Bottom).	80
6.14	Negative Power Headroom UE Example: PUSCH Power histograms.	81
6.15	Negative Power Headroom UE Example: time-series PUSCH power per PRB and allocation size.	82
6.16	Negative Power Headroom UE Example: time-series for additional KPIs.	83
6.17	Interference Aware scheduling Example: vector signal analyzer (VSA) spectrogram captures. Grayscale range: [-58, 23] dBm.	85
6.18	Interference Aware scheduling Example: loading UE activity time-series (Top) and PRB allocation distributions (Bottom).	86
6.19	Interference Aware scheduling Example: PUSCH Power histograms.	87
6.20	Interference Aware scheduling Example: time-series PUSCH power per PRB and allocation size.	88
6.21	Interference Aware scheduling Example: time-series for additional KPIs.	89
6.22	MCS variation example: VSA spectrogram captures. Grayscale range: [-58, 23] dBm.	91
6.23	MCS variation example: loading UE activity time-series (Top) and PRB allocation distributions (Bottom).	92
6.24	MCS variation example: PUSCH Power histograms.	93
6.25	MCS variation example: time-series PUSCH power per PRB and allocation size.	94
6.26	MCS variation example: time-series for additional KPIs.	95
6.27	RSRP stability plot - both UEs.	97
6.28	Difference in median RSRP between attenuator settings.	98
6.29	RSRP stability plots by UE.	99
6.30	Summary of empirical CDFs for measured PUSCH power per PRB for all test configurations in the screening experiments. This plot contains approximately 4000 unique CDFs.	100
6.31	Summary of empirical CDFs for measured PUSCH power per PRB for all test configurations organized by power control type and testbed attenuation setting.	101
6.32	Summary of empirical CDFs for measured PUCCH power per PRB for all test configurations in the screening experiments. This plot contains approximately 4000 unique CDFs.	102
6.33	Summary of empirical CDFs for measured PUCCH power per PRB for all test configurations organized by power control type and testbed attenuation setting.	103
6.34	Summary of empirical CDFs for UE-reported SRS power per PRB for all test configurations in the screening experiments. This plot contains approximately 2000 unique CDFs.	104
6.35	Overall comparisons of median UE-reported and measured PUSCH EIRP per PRB. The approximate conversion factor between measured EIRP and reported power at the DUT UE is 7.5 dB±2.3 dB.	106
6.35a	Histogram of difference.	106
6.35b	Scatter plot.	106
6.36	Scatterplots with best-fit lines through Region I and Region II.	107
6.36a	Scatterplots for Region I only	107
6.36b	Scatterplots for Region I together with Region II	107

6.37	Aggregate results for all tests of eNB configuration #10. Scatterplot of median reported power per PRB versus median measured EIRP per PRB.	108
6.38	Breakdown of tests falling in Regions I, II, or III for each eNB configuration.	108
6.39	Comparison of reported PUSCH power per PRB to prediction from the open-loop component of the LTE power control equation.	110
6.39a	Open-loop power control tests.	110
6.39b	Closed-loop power control tests.	110
7.1	Simulated studentized range (R_{max}) densities for (a) univariate, (b) bivariate, and (c) trivariate cases. The verticle red lines indicate critical values associated with $\alpha = 0.05$. The black triangles represent all possible pairs of observed differences (d_{ij}) between factor levels. Since Ω has 16 factor levels, there are 120 computed differences. Critical values are 5.26, 0.39, and 0.44 for the univariate, bivariate, and trivariate cases, respectively.	115
7.2	Approximate distribution of the number of type I errors in an experiment with 23 factor effect tests, each with $\alpha = 0.05$ significance level, in which ten of the 23 factors are assumed to have zero effect. Under these conditions the probability of no more than one type I error is 92%.	117
7.3	Heat map of measured PUSCH response distribution sample sizes obtained for each eNB and non-eNB factor combination for each round of measurements. Data is missing (grey boxes) for 118 factor combinations. Response distribution sample sizes range from 18 to 227 633.	118
7.4	Heat map of reported PUSCH response distribution sample sizes obtained for each eNB and non-eNB factor combination for each round of measurements. Data is missing (grey boxes) for 123 factor combinations. Response distribution sample sizes range from 6 to 18 802.	119
7.5	Heat map of measured PUCCH response distribution sample sizes obtained for each eNB and non-eNB factor combination for each round of measurements. Data is missing (grey boxes) for 348 factor combinations. Response distribution sample sizes range from 1 to 2084	120
7.6	Factor effect p-values for 23 experiment factors from three increasingly comprehensive analyses based on C_{50} , (C_{50}, C_S), and (C_{50}, C_S, C_Q).	122
7.7	Mean factor effects on C_{50} (PUSCH power median). Factor Ω has 16 levels; its C_{50} level means are shown in Table 7.3. Effects marked in red are not statistically C_{50} -significant.	123
7.8	Mean factor effects on C_S (PUSCH power spread). Factor Ω has 16 levels; its C_S level means are shown in Table 7.3. Effects marked in red are not statistically (C_{50}, C_S)-significant.	123
7.9	Mean factor effects on C_Q (PUSCH power skew). Factor Ω has 16 levels; its C_Q level means are shown in Table 7.3. Effects marked in red are not statistically (C_{50}, C_S, C_Q)-significant.	124
7.10	Comparison of factor effect p-values from two univariate ANOVAs, one ANOVA based on the median C_{50} and the other based on the first principal component of the power distribution. The first principal component of the power distribution should line up with the center of the distribution, in which case the results of the two analyses should be consistent with one another.	127
7.11	Comparison of factor effect p-values from two bivariate MANOVAs, one based on the pair of centile statistics (C_{50}, C_S) and the other based on the first two principal components (PC_1, PC_2).	128
7.12	Comparison of factor effect p-values from two trivariate MANOVAs, one based on the trio of centile statistics (C_{50}, C_S, C_Q) and the other based on the first three principal components (PC_1, PC_2, PC_3).	128
7.13	Relative weights of the 99 power centiles in the first three principal components of the measured PUSCH power. The first principal component is functioning as a measure of center, the second as a measure of spread, and the third as a measure of skew. The percentages are the amount of the total variability in the measured PUSCH power data explained by each principal component. Together PC_1, PC_2 , and PC_3 explain 99.72% of the variability in the data.	129
7.14	Factor effect p-values for 23 experiment factors from three increasingly comprehensive analyses based on C_{50} , (C_{50}, C_S), and (C_{50}, C_S, C_Q). Compare these p-values for reported PUSCH power with those in Figure 7.6 based on measured PUSCH power.	129
7.15	Mean factor effects on C_{50} (PUCCH power median). Factor Ω has 16 levels; its C_{50} level means are shown in Table 7.7. Effects marked in red are not statistically C_{50} -significant.	132
7.16	Median PUSCH power C_{50} at each of 45 times in 106 days of testbed operation, for each of 32 default configurations. Each configuration has a systematic downward trend, modeled by linear regression. The blue- and red-colored configuration numbers correspond to $A = -1$ and $A = +1$ attenuation levels, respectively.	134
7.17	Testbed droop, grouped by configuration attenuation level, $A = -1$ and $A = +1$. The mean testbed droops in the two groups are 2.8 dB and 4.2 dB, respectively.	135

7.18	Droop residuals from the regressions in Figure 7.16. The variation in the default testbed monitoring data after accounting for its systematic droop appears random and homoscedastic over time, and heteroscedastic over configuration. The blue- and red-colored configuration numbers correspond to $A = -1$ and $A = +1$ attenuation levels, respectively.	136
7.19	Random component of variation in measured C_{50} PUSCH power data for 32 default configurations, estimated by regression standard error. These errors are grouped by attenuation level, $A = -1$ and $A = +1$. The mean regression errors in the two groups are 1.8 dB and 3.7 dB, respectively.	137
7.20	Cross-correlation in C_{50} measured PUSCH power over time in the testbed default data. The cross-correlations are those for droop residuals for the 32 default configurations.	137
C.1	Drawing of the measurement setup with the shielded chamber's door in the open position left, and closed position right.	150
C.2	Measurement results of the horn to horn transmission with the chamber shielded door open (black line), closed (blue line), and noise floor (orange dash) of the VNA. The figure also shows the frequency spans of interest for LTE Band 3 UL (light green), and LTE Band 3 DL (dark green).	150
C.3	Calculated shielding effectiveness (purple line) from measurement results in Figure C.2. The shielding effectiveness of the chamber is better than 105 dB in the frequency span of interest for LTE Band 3 UL (light green), and LTE Band 3 DL (dark green).	150
C.4	Experiment setup for measuring the gain of the DUT antenna's and platform's effect on the antenna radiation pattern. Experiment setup in the test and small chamber (left). Experiment setup in NBIT (right). Both test setups incorporate measurements at several distances of r	151
C.5	Measured Transmission (S21) in blue and calculated gain in cyan with the aperture to aperture distance at 78 cm. The frequency span of interest for LTE Band 3 UL (light green), and LTE Band 3 DL (dark green) is also indicated.	152
C.6	Calculated gain from S-parameter measurements for the measurement setups in Table C.1. The scatter graph represents the Band 3 frequency band of interest from 1710 MHz to 1880 MHz. The median and 95 % confidence region represents the estimated gain, and respective confidence in the median gain over the frequency band and test campaign measurement separation distance of approximately 78 cm horn aperture to the top of the UE.	153
C.7	Experiment setup for ascertaining the UE's and platform's effect on the antenna radiation pattern	153
C.8	S_{11} measurement of a 50 Ohm reference load. Over the LTE Band 3 of interest the load matches well, verifying the S-parameter calibration	154
C.9	S_{11} measurement of the measurement horn pointed into free space (green) as compared to the antenna response when placed into the small chamber (blue). The frequency span of interest for LTE Band 3 UL (light green), and LTE Band 3 DL (dark green) is also indicated.	154
C.10	The S_{11} response of the measurement antenna in the presence of a UE (blue), and a 15 cm by 15 cm large metal plate (magenta). The metal plate shows significant deviations from the reference measurement, whereas the UE doesn't.	155
C.11	The S_{11} response of the measurement antenna when the UE is placed progressively closer to the measurement antenna. At the shortest separation distance there is a significant effect on the measurement antenna response, where as the initial and intermediate placements show very little change.	155
C.12	Screen-shot of the communication tester's parameter space and measurements. The reported data is for the UE positioned along the center line of the test chamber, and its top edge is geometrically aligned with the polarization of the test antenna.	156
C.13	Experiment setup for ascertaining the UE transmit power as a function of placement along the platform.	156
C.14	Diagonal placement of the UE and reference orientations. Positions will be referred to as position 1 (bottom left) through 4 (center) to 7 (top right). The phone orientation was facing "east" for all positions and cross checked with facing "west" at positions 1, 4, and 7.	157
C.15	Experiment setup for ascertaining the impact of UE rotational positioning.	158
C.16	The drawing outlines the block diagram of the RF leveling and combining circuitry used for the measurement campaign. The overall circuitry shows primary connection points ($\square\square$ connections) and denotes diagnostic test ports ($\bullet - \triangleright$ TP#) that were built into the system. A series of 4-port measurements were performed on the RF leveling and combination circuitry to verify path loss and isolation.	159
C.17	The S-parameter measurements showing a very well balanced test circuit, where cell A and B uplink and downlink pathloss are equivalent. A well balanced UL and DL path are imperative to the stability of the LTE physical layer performance.	162
C.18	The S-parameter measurement here highlights the realizable cross talk in the test architecture with attenuators AT1 and AT2 set to 0 dB attenuation.	162

C.19	The S-parameter measurements here show the conducted path loss between the eNB cell a, b ports and the chamber test port.	162
C.20	The test case for the end-to-end measurements of path loss between the major components in the test bed. The calibration planes are shown in the graphic, as close as possible to the actual input of the radiated units. r is the test height, configured at 78 cm.	163
C.21	S-parameter measurement of the transmission between the eNB cell $A_{Tx/Rx}$ port and the reference horn at the bottom of the test chamber, here AT4 was varied. The test values for AT4 were varied to evaluate whether the programmable attenuator tracks the specified attenuation.	163
C.22	S-parameter measurement with the gain of the reference horn at the bottom of the base plate subtracted out. The median within the band of interest (highlighted in green) for the AT4 = 0 curve represents the calibration value for the testbed for the path loss between the UE and the RF input to the eNB cell $A_{Tx/Rx}$	164
C.23	The S-parameter measurement with the gain of the reference horn at the bottom of the base plate subtracted out. The median transmission value in the band of interest (highlighted in green) is the calibration value for the path loss between the DUT UE and the input to the VSA.	164
C.24	Coupling between Cell <i>A</i> and Cell <i>B</i> on the eNB with both cells disabled.	165
C.25	Measurements taken to calibrate (a) spectrogram data from the signal analyzer against (b) the calibrated power sensor reference.	167
D.1	(A.) Sketch of UE in a motorized fixture with θ and ϕ . (B.) The fixture built to correspond to the schematic in A. The corresponding rotating elements are shown with red arrows.	171
D.2	Comparison of three-dimensional radiation patterns from all UE's tested with vertically polarized measurement antenna.	172
D.3	Comparison of three-dimensional radiation patterns from all UE's tested with horizontally polarized measurement antenna.	173
D.4	Distribution of EIRP measured from all UE's.	174
E.1	NLCD based Hata-Okumura Model path loss distributions.	177
E.2	Cumulative density function for rural.	178
E.3	Cumulative density function for suburban.	178
E.4	Cumulative density function for urban.	179
F.1	RF Hardware Functional Concept of MITRE Multi-UE System.	181
F.2	Software Functional Concept of MITRE Multi-UE System.	182
F.3	Test Automation Framework Architecture.	183
F.4	Reported Tx Power per PRB CDF.	184
F.5	PRB Occupancy.	185
F.6	Resource Grant from Merged Data Highlighted in Spectrogram.	188
F.7	Measured vs Reported Power Comparison	190
F.7a	Test 1	190
F.7b	Test 2	190
F.7c	Test 3	190
F.7d	Test 4	190

List of Tables

2.1	Factor List	8
2.2	RSRP Linkage to Cell Radius.	11
2.3	LTE Network Common QCI values.	12
3.1	Summary of test circuit components.	23
3.2	Validation Checks During Testing to Confirm Steady State Operation	34
5.1	Factor List	53
5.2	Experimental design for the non-eNB factors.	54
5.3	Experimental design for the eNB factors.	56
5.4	Mapping between levels for Ω and I, J, L, M, and X.	57
5.5	Expanded experimental design for the eNB factors including constrained factors.	58
5.6	Test matrix for factor screening experiment.	60
5.7	Design Factor Settings	62
5.8	Controlled Nuisance Factor Settings	63
6.1	Settings for the example plots in section 6.1 (default eNB configuration, non-eNB configuration #19).	68
6.2	Settings for the power-constrained and resource-constrained examples. Both examples were collected with a default eNB configuration.	72
6.3	Settings for the negative power headroom example (eNB configuration #8, non-eNB configuration #28).	78
6.4	Settings for the Interference Aware scheduling example (eNB configuration #5, non-eNB configuration #14).	84
6.5	Settings for the MCS variation example (eNB configuration #26, non-eNB configuration #2).	90
7.1	Experiment design factors. All factors have two levels except Ω	112
7.2	ANOVA and MANOVA p-values for the measured PUSCH data set.	121
7.3	Tukey groupings based on PUSCH C_{50} , (C_{50}, C_S) , and (C_{50}, C_S, C_Q) power responses for the sixteen levels of factor Ω . Two levels in the same Tukey group are not significantly different in their responses. The C_{50} means for Ω 's levels are reported relative to -100 dB. The levels of factor M labelled "na" indicate cases where factor M did not logically apply ("not applicable").	125
7.4	ANOVA p-values for the reported PUSCH data set.	127
7.5	Differences $(\delta_j(C_{50}), \delta_j(C_S), \delta_j(C_Q))$ in estimated PUSCH power distribution effect sizes based on reported power versus measured power for 22 two-level screening factors.	130
7.6	ANOVA p-values for the measured PUCCH data set.	131
7.7	Tukey groupings based on PUCCH C_{50} power responses for the sixteen levels of factor Ω . Two levels in the same Tukey group are not significantly different in their responses. The C_{50} means for Ω 's levels are reported relative to -100 dB. The levels of factor M labelled "na" indicate cases where factor M did not logically apply ("not applicable").	132
B.1	Summary of Data Sources.	148
C.1	Horn aperture to horn aperture separation distances measured with in the small chamber and in NBIT.	152
C.2	UE transmit power as a function of placement along the diagonal path of the platform. Graphical representation is in Figure C.14	157
C.3	VNA S-parameter measurement checks of the conducted portions of the RF test bed.	160
C.4	Sources of uncertainty and uncertainty budget for VSA captures of UE emissions.	168

E.1 Mean cell radii calculated using the ball tree algorithm after grouping eNBs into their respective morphologies. . . 176
E.2 Median modified Hata path loss for each morphology by cell tower data set. 176
F.1 Test Description. 189

Chapter 1

Introduction

The Defense Information Systems Agency (DISA) Defense Spectrum Organization (DSO) through the spectrum sharing test and demonstration (SSTD) program proposed to the National Advanced Spectrum and Communications Test Network (NASCTN) a measurement campaign to quantitatively characterize long-term evolution (LTE) uplink band (UL) waveforms generated by user equipment (UE) in the 1755 MHz to 1780 MHz band with the intent to develop realistic measurements of UE emissions. These measurements will be used for assessing interference to Department of Defense (DoD) systems that, for a time, will remain in the 1755 MHz to 1780 MHz band. This proposal was reviewed, and NASCTN developed a test plan to support this request [1]. This report describes the execution of that test plan and the results produced.

Though the methods and results discussed here specifically relate to a particular frequency band of interest, the methods shown can be repeated in other frequency bands and for other types of equipment (e.g., narrow-band Internet of Things (IoT) type devices). The results shown here are meant to inform future analyses of emissions and are not intended to define thresholds for interference or best practices for managing LTE network deployments.

1.1 Objective

The objective of this test is to design, demonstrate, and validate a test methodology to measure LTE UE emissions for use in aggregate interference calculations. Specifically, this involves developing a better understanding of what factors (e.g., evolved node B (eNB) power control variables and scheduling algorithms, propagation channel, traffic type, and in-cell and adjacent-cell loading) impact the emissions of a typical commercial off-the-shelf (COTS) LTE UE.

The assessment of these factors will be done in a laboratory environment where control over the LTE eNB, UE, network infrastructure, and environmental conditions (e.g., channel path loss values) can be exercised. The use of laboratory testing also enables the testing of a wider range of configurations, beyond what may be found in typical deployments. Testing with settings beyond what is typically found in deployments allows for the examination of specific configurations that may cause UE emissions to increase or *decrease*. Testing atypical cases also effectively increases the chance a difference between two settings levels will be detected.

In particular, these measurements yield distributions of effective isotropic radiated power (EIRP) from a UE in an active resource block for a variety of test configurations. The measurement methods used here also enable a comparison between the UE's self-reported transmit power and measured power. In addition, this work includes radiation pattern measurements of several common LTE UEs. The detailed radiation pattern results are discussed in this report and in Appendix D, but the full results can be found in a recent technical report [2].

Accompanying these measurements is a rigorous uncertainty analysis that includes an uncertainty budget and calculation of overall measurement uncertainty. A secondary goal of this characterization, with a documented methodology and uncertainty, is to give advanced wireless services 3 (AWS-3) stakeholders more confidence in the coordination request evaluation (CRE) process.

1.2 Scope

This study specifically addresses the characterization of LTE frequency-division duplex (FDD) signals emitted from COTS UEs in the 1755 MHz to 1780 MHz band. In the process of conducting this characterization, NASCTN developed a suitable measurement methodology and uncertainty analysis.

This study was limited to estimates of the variables, based on laboratory measurements, for analyzing the effects of key variables that can affect the UE behavior. In-field measurements were not considered as a part of this process. Future studies could extend this plan to include field tests.

In addition to characterizing emissions, the test also explores the relationship between self-reported transmit power of a UE and actual radiated power. Self-reported power is commonly used during in-field measurements, but its accuracy has not been assessed. This gap presents itself as an opportunity for contribution. As a result of the test circuit's design, the acquisition of self-reported power was trivial. The comparison between self-reported power and the actual power radiated by the UE was performed as a separate step in the analysis of the data.

Finally, the radiation pattern of a COTS UE will be measured as it relates to coupling into the test circuit. During pre-test activities, it was determined that there was sufficient interest in the community to warrant extending the radiation pattern measurements to full 3-D patterns.

1.3 Background

In the 2010 Presidential Memorandum on Unleashing the Wireless Broadband Revolution [3], the National Telecommunications and Information Administration (NTIA) was tasked to identify underutilized spectrum suitable for wireless broadband use. In the subsequent NTIA Fast Track Report [4], many federal bands were identified as commercially viable. From this report, the Federal Communications Commission (FCC) identified 1695 MHz to 1710 MHz, 1755 MHz to 1780 MHz, and 2155 MHz to 2180 MHz together as the AWS-3.

Through Auction 97 [5], the FCC auctioned the AWS-3 band for commercial mobile broadband usage in the United States. The auction raised \$41B in revenue for the United States Treasury and required federal agencies in the AWS-3 band to look for other ways to accomplish their missions. In the 1755 MHz to 1780 MHz portion of the AWS-3 band, the DoD is using a combination of sharing, compression, and relocation to other bands (including the 2025 MHz to 2110 MHz band).

From the AWS-3 auction proceeds, an spectrum relocation fund (SRF) was created. The DoD is using portions of the SRF to implement its approved transition plans. The SRF is also funding evaluation of early entry coordination requests from the auction winners in the AWS-3 band through the DoD early entry portal analysis capability (EEPAC), which is managed by DISA DSO. The portal receives requests from auction winners to enter band(s) before the DoD has transitioned out of the bands. These requests must be considered carefully and impartially to deliver a fair answer. If early entry is granted and there is interference to DoD users, it would be very costly to the DoD both financially and in terms of mission execution. If early entry is denied to a commercial carrier for overly conservative reasons, it could be very costly to their business model. To avoid these costs, it is crucial that the findings of the EEPAC are fair and based on a well-understood and openly documented methodology.

1.4 Overview

The goal of these measurements is to develop a methodology that enables a better understanding of UE emissions for use in interference assessments and other analyses. One way to enable a better understanding of emissions is with extensive in-field testing. Though in-field testing provides information on what is happening in live networks, many of

the parameters of interest are difficult to measure and control, making it difficult to understand which parameters have an influence on UE behavior. Laboratory-based measurements can be used as an alternative to in-field testing. The primary benefit of laboratory measurements is that many of the uncontrolled or unknown variables found in in-field measurements can be controlled. The challenge with laboratory testing is that there are many aspects of the network and environment that must be recreated.

The underlying concept of these measurements is simple: develop a list of factors that may have an impact on the uplink emissions of a UE, then test each of those factors in a laboratory experiment. An initial list of factors was proposed with the original NASCTN test plan. Through engineering analysis and public comment, this list was refined. Detailed descriptions of each of the factors examined can be found in Chapter 2. These factors can be placed into one of three categories: network settings, environment (e.g., radio frequency (RF) conditions, network loading), and use case (e.g., how the UE is used). The laboratory setup must be able to recreate each of these three aspects.

As discussed in Chapter 5, two extreme settings (high/low values) were specified for most factors to maximize the ability of the experiment to resolve factor effects. Settings were determined through careful consideration of potential effect size, operational use and limitations, and test stability.

One component of the environment category is the impacts from an adjacent LTE sector or cell. This geographically adjacent cell can be thought of as an independent LTE cell that does not coordinate with the primary serving cell. Previous work [1] posited that the emissions of UEs located in an adjacent cell can influence the radiated power level of a UE (or a group of UEs) in another sector. In essence, the adjacent cell UEs increases the noise floor in the cell-of-interest and causes the UEs to transmit more power to overcome the increased noise.

The concepts discussed above are illustrated in Figure 1.1. In this Figure, two cells are drawn: *A* and *B*. The two cells are adjacent, but not overlapping. Each cell is populated with UEs. These UEs are in the cell to load the cellular network in an effort to examine whether or not different loading conditions can impact emissions. These UEs are known as “loading UEs.” For completeness, the entire typical three cell diagram is shown. However, only the two individual cells of interest are populated with UEs.

Cell *A* also contains a device under test (DUT) UE. This UE is distinctly different from the loading UEs in that it is a COTS UE that is moved to different geographic locations within Cell *A*. At each location within Cell *A*, a measurement is taken. When the emitted spectrum is measured, it will be of this DUT UE, not of the loading UEs. The reason for this is discussed in subsection 3.2.3. The location of the loading UEs is a factor in the experiment, but they are placed in static locations and do not move dynamically during testing.

Figure 1.1 accounts for all three of the categories of interest. Different RF environments can be controlled by placing the DUT UE in different locations within Cell *A*. The influence of other UEs can be analyzed by changing the configuration of loading UEs in Cell *A* and/or *B*. The influence of an adjacent cell can be examined both from the perspective of network settings and from loading UE configuration. UE use cases can be considered by configuring the loading and DUT UEs to have different data rates, data types, or levels of data priority. By use of a COTS macro-cell eNB, an extensive test of network settings can be performed. Control over the cell radius, scheduling algorithms, power control mechanisms, and other network settings are all possible in a laboratory environment.

The loading UEs can be physically accounted for in one of two ways: through the use of additional COTS devices or through emulation. The use of additional COTS UEs would likely produce scenarios that are more realistic when compared to emulation. The spectrum of COTS loading UEs could be directly measured as part of these measurements, and their aggregate impact on the physical spectrum quantified. However, as the number of loading UEs and associated network configurations desired increases, the use of physical COTS UEs becomes more challenging. An alternative is to use a UE emulator or “traffic generator”, UE traffic generator (UTG), which is used in these measurements.

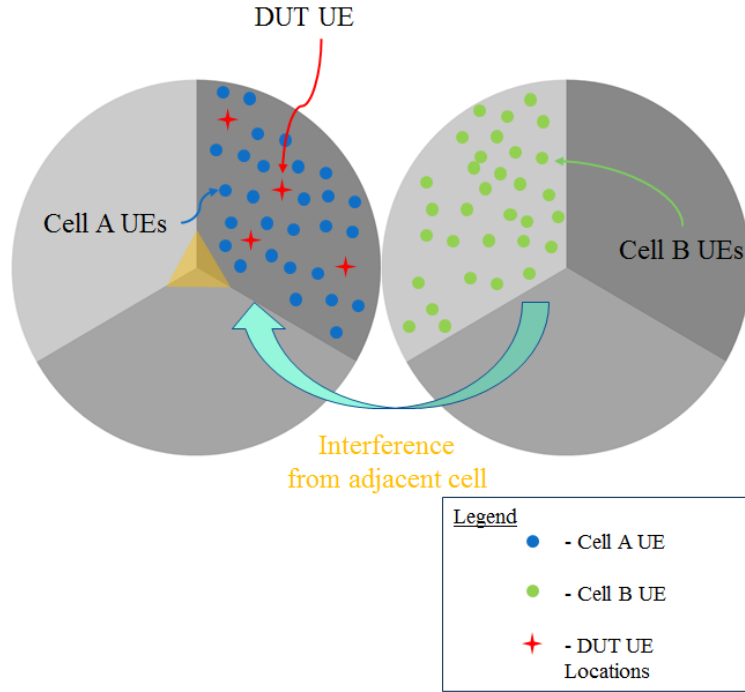


Figure 1.1: Conceptual illustration of the laboratory tests showing the DUT UE at various virtual locations within Cell A. An adjacent cell, Cell B, can have some influence on the behavior of Cell A.

A UTG is a single piece of hardware capable of emulating the full LTE stack of many UEs. This emulation is done in such a way that the eNB treats the emulated loading UEs as if they were COTS UEs. The UTG can be configured to change the location of the loading UEs within a cell, their data rate, traffic type, traffic priority, and more. The use of a UTG to emulate the loading UEs enabled the testing of many more configurations as the changes can be automated. The main drawback of the UTG is that the RF spectrum of the UTG should not be directly measured. The UTG is discussed in detail in Chapter 3¹.

Another way to represent the conceptual measurement diagram in Figure 1.1 is with Figure 1.2. This Figure shows the signal flow of the conceptual test diagram. Cells A and B are represented by their respective eNB blocks on the right side and the loading UEs for each cell are shown as a UTG on the left. Note that the arrows in the diagram are bi-directional, indicating both uplink and downlink traffic are exchanged. The physical layer RF influence between Cells A and B is shown by the two arrows crossing between the cells in the middle of the diagram. The COTS DUT UE is virtually inserted into Cell A via the dark blue arrow. Notice that a small portion of the DUT UE's signal is split off and injected into Cell B. This arrow is bi-directional, indicating that some of the Cell B signal is also injected into the DUT UE's signal path. Next to the DUT UE is a junction where part of the uplink signal is coupled off into a vector signal analyzer (VSA). It is at this point where the DUT UE's spectrum is captured. The setup depicted in Figure 1.1 and Figure 1.2 is realized in terms of laboratory equipment and discussed in detail in Chapter 3.

Measurement sequence and key assumptions. Once the network, environmental, and use case factors have been determined, individual measurement configurations are created. Each of these individual configurations is slightly different than the other, as determined by the experiment design. Once the test begins, a configuration consisting of settings for the eNB, UTG, and DUT UE is loaded. After the configuration is loaded, the network is given time

¹A UTG can also be referred to as an LTE radio access network (RAN) load tester.

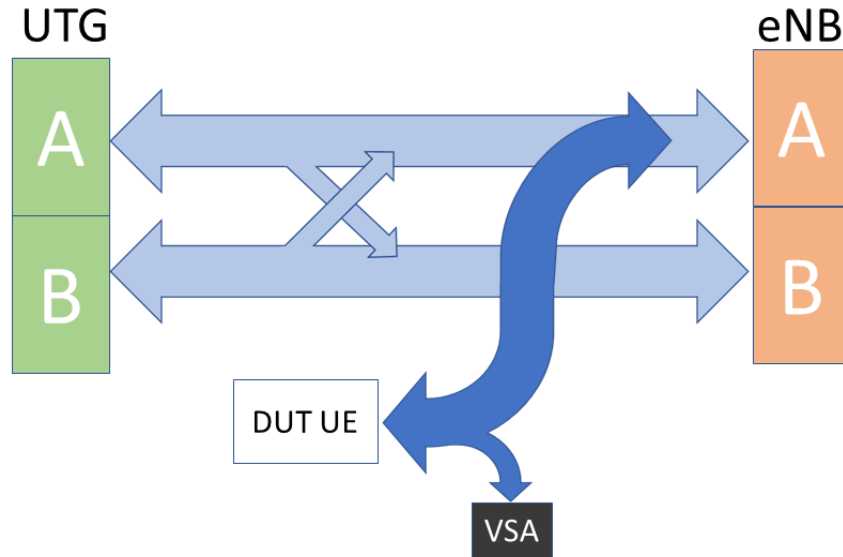


Figure 1.2: Conceptual view of the LTE signal flow in the factor-screening measurements.

to stabilize before two spectrograms of the DUT UE are acquired. As the spectrograms are acquired, additional parameters are recorded from the UTG and the DUT UE itself. The next configuration is then loaded. This repeats until the list of configurations is exhausted. Data are parsed and post-processed to separate the results into the effects of individual factors.

To help ensure the network and UEs are stable and constant before data are acquired, handovers and hand-offs between Cells *A* and *B* have been disabled. Further, it is assumed that there is no communication between the Cell *A* and *B* eNBs. The two eNBs used in these measurements exist independently of each other and are only subject to each other's actions through the cross-talk paths shown in Figure 1.2. Features such as inter-cell interference coordination (ICIC) have been disabled.

Each of the individual configurations has been carefully designed to prevent UEs from attaching or detaching from its eNB during the acquisition of data. Should a DUT or loading UE attach or detach during acquisition, it could skew the results. Because attach and detach sequences account for a small percentage of the overall emissions from an LTE UE, the measurement test intentionally excludes them. However, Chapter 8 outlines a follow-on experiment that specifically addresses attach and detach behavior.

These assumptions may appear to be an over-simplification since in real-world networks UE loading, UE data profiles, and UE location are dynamic and can be viewed more as distributions rather than single, fixed values. The objective in these measurements is not to replicate such distributions and dynamic changes, but rather to see what factors impact the emissions behavior of a DUT UE. Once the factors that influence the emissions behavior are identified, a future set of measurements can be performed to determine the impact given values derived from real-world network deployments. These derived values may be different depending on the morphology of interest.

Experimental Design and Data Analysis Results. The primary aim of this work is to determine which factors have a significant impact on the distribution of physical uplink shared channel (PUSCH) power per physical resource block (PRB). This type of experiment is called “factor screening” in the experimental design literature [6, 7]. As explained in Chapter 5, the experiment, which involved 28 factors, was designed to screen a large number of factors with a practical number of tests. Most factors had two settings, while a few had three. The settings were intended to

discover the maximum effect due to that factor varying in typical conditions.

The data analysis results consist of two main types: exploratory and inferential. The exploratory data analysis results, presented in Chapter 6, are graphical plots that summarize various aspects of the experimental observations. Namely, notable examples of LTE performance are given, as well as a comparison of UE-reported and measured PUSCH power. The inferential data analysis findings, presented in Chapter 7, resulted from a formal statistical analysis of the experimental measurements. Specifically, the results of the inferential analysis indicate which factors had a statistically-significant effect on PUSCH emissions.

Report overview. The remainder of this report is laid out as follows. Chapter 2 provides an in-depth discussion of each of the 28 experimental factors identified and considered in these measurements. The definition of each factor is given along with a hypothesis of how it may impact the uplink emissions of the DUT UE. Chapter 3 details the physical test circuit developed from Figures 1.1 and 1.2. The salient features of the hardware used in the measurement are provided along with basic information on how the data are acquired. The details of how the data are acquired and parsed ahead of statistical processing are given in Chapter 4. Chapter 5 discusses the statistical experiment design. Examples of notable results are given in Chapter 6. The inferential statistical analysis and its results are detailed in Chapter 7. The report concludes with a summary of the results, a discussion on their interpretation, and ideas for future work that expands on these measurements.

Chapter 2

Experimental Factors

The development of NASCTN test plan [1] began with an initial list of experimental factors composed of any factor thought to influence the uplink UE emissions. After inclusion in the initial test plan, feedback obtained in the public comment period informed the additional factors added to the list.

However, due to time constraints, not all of the factors could be examined via measurements. Other considered factors that were not included as part of the measurements are described in Appendix A. These factors were removed from the process after engineering discussions and analysis determined their impact to be minimal or negligible. Should those factors become of specific interest later, the methods described here can be used to evaluate them.

Most of the values of each factor are discussed in this chapter. A detailed summary table of all factors, including their values, can also be found in Chapter 5, Table 5.7.

2.1 Factor Descriptions

The factors that can contribute to changes in UE power emissions in a LTE system can be categorized into three different groups: eNB settings, network layout and environment, and UEs characteristics and service profiles. From here, NASCTN developed a list of all possible factors that *may* have an impact on emissions of a DUT UE. These factors, shown in Table 2.1¹, were then examined via a series of measurements.

The inclusion of eNB-related factors is complicated by the fact that eNBs from different manufacturers can have different parameters available for configuration. The factors selected and described here are a reflection of the eNB used in these measurements. Every effort is made to describe these factors in general terms to facilitate the identification of analogous parameters in other eNBs.

For each factor included in these measurements, NASCTN described its definition, outlined the reason it was included, and what element of the test circuit was manipulated as the variable was changed.

¹The color of the rows in Table 2.1 are shown only to delineate eNB factors from non-eNB factors.

Table 2.1: Factor List

Identifier	Testbed Component	Factor	# Levels
A	Variable Attenuator	Path Loss (Simulated DUT UE Position)	2
B	UTG	Spatial Size of Cell	2
C	UTG	Number of Loading UEs in Serving Cell (Cell A)	2
D	UTG	Number of Loading UEs in Adjacent Cell (Cell B)	2
E	UTG	Spatial Distribution of Loading UEs in Cell A	2
F	UTG	QCI Value of Loading UEs	2
G	DUT UE/UTG	Traffic Data Rate	2
H	DUT UE/UTG	Traffic Type (UDP/TCP)	2
I	eNB	UL Scheduling Algorithm Type	3
J	eNB	UL Scheduler FD Type	3
K	eNB	Power Control Type (Closed Loop/Open Loop)	2
L	eNB	SRS Config	2
M	eNB	SRS Offset	2
N	eNB	PUCCH Power Control: P_0	2
O	eNB	PUSCH Power Control: P_0	2
P	eNB	Power Control: α	2
Q	eNB	Receive Diversity	2
R	eNB	Filter coefficient for RSRP measurements	2
S	eNB	Maximum uplink transmission power (own cell)	2
T	eNB	Minimum PRB allocation for power-limited UEs	2
U	eNB	UL Improved Latency Timer Reaction	2
V	eNB	Initial Max # of Resource Blocks	2
W	eNB	Outer Loop Link Adaptation	2
X	eNB	Uplink link adaptation	2
Y	eNB	Cell Scheduling Request Periodicity	2
Z	eNB	Scheduling Weight UL for SRS	2
a	eNB	Blanked PUCCH Resources	2
b	eNB	Target UL Outer Scheduling	2

2.1.1 Factor A - Path Loss

The extent of path loss between the UE and eNB can impact the UE transmission power. That is, path loss and UE transmission power are generally positively correlated. The reason for this increase is that the UE is attempting to maintain the same power at the plane of the eNB receiver. The amount of power desired at the plane of the eNB is known as P_0 , represented as factors N and O. From a conceptual perspective, the eNB - UE RF link is designed to adapt to RF changes while maximizing the UE's battery life and minimizing the inter-cell interference for the data channel and control channel, respectively, by not transmitting more power than is necessary to close the link. As part of this process, the eNB and UE continuously exchange information and frequently attempt to predict the propagation channel conditions. This behavior occurs in real-world deployments as well as in the measurements described here.

In these measurements, the path loss was controlled by use of a variable attenuator. It is recognized that real RF propagation channels between a UE and eNB are almost always dynamically changing, involving some degree of RF fading. Fading can be described as a collection of path losses in various time, location and radio frequency dimensions. During fading, the propagation path can change rapidly, leading to rapid changes in the power emitted by the UE. Accurately capturing and statistically analyzing a rapidly changing UE power would have made these measurements impractical by increasing the number of factors. Path loss would no longer be a single variable, rather it would be several variables: free-space path loss, rate of change in dynamic fading, depth of RF fades, etc.

This path loss factor can also account for the eNBs antenna pattern. Given the hybrid radiated/conducted measurement circuit, there is no way to explicitly account for any antenna pattern of the eNB. In cases where a UE was in a null or side-lobe of an eNB antenna, it would artificially increase the path loss between the UE and eNB.

With indoor conditions excluded, the path loss variable represents the geographic distance between the UE and eNB. Here, the path loss is either set to a low (0 dB) or high (20 dB) value. These values correspond to the UE being close to the eNB (low) or far from the eNB (high). The 0 dB and 20 dB path loss values represent the amount of *additional* path loss caused by the variable attenuator.

The attenuator settings were determined empirically during pre-test activities. Increasing the attenuation beyond 20 dB resulted in the UE not attaching or being allocated resources in many of the test eNB configurations.

2.1.2 Factor B - Spatial Size of Cells

The spatial size of cells A and B representing the geographic boundaries of the loading UEs is implemented by specifying the path loss (location from eNB) between the loading UEs and the eNB. In real deployments, the spatial size of the cell is designed based on the surrounding morphology (e.g., urban, suburban, rural).

The factor screening measurements used cell radii of 100 m (replicating dense urban deployments) and 1000 m (replicating suburban/rural deployments). One of the secondary impacts of this factor is that UEs in the "far" condition may be allocated resources in a different fashion than UEs closer to the eNB.

In addition to controlling the size of the cell radius for the loading UEs, the cross-talk attenuation settings between the serving cell and adjacent cell were varied. In cases where the cell radius was set to 100 m, the attenuation between the cells was set to its low value to simulate a relatively lower free-space path loss between eNBs. Conversely, when the cell radius was 1000 m, and the simulated distance between eNBs was much higher, the cross-talk attenuator was set to its high value.

The hypothesis of this factor is that, in conjunction with factor E (Spatial Distribution of Loading UEs), it would cause more (or fewer) UEs to be near the cell edge, and thus scheduled differently by the eNB. This difference in scheduling would, in turn, have an impact on the behavior of the DUT UE.

The cell radius was implemented on the UTG as part of its configuration files. The cross-talk between cells was implemented by use of a variable attenuator. The spatial size of the cells was always equal. That is, both the serving cell and adjacent cell are either set to a radius of 100 m or 1000 m.

2.1.3 Factors C & D - Number of Loading UE

The number of loading UEs in the serving cell (Factor C) and the adjacent cell (Factor D) are thought to have an impact on the DUT UE's emissions through two possible effects, only one of which is tested here. In conjunction with Factors F, G, and H, these two factors play a significant role in loading the network.

One possible impact of a high number of loading UEs transmitting simultaneously could be the RF noise in the LTE channel is increased. To compensate for this, the DUT UE may increase its power to maintain a given signal to noise ratio (SNR). A potential secondary impact is that the loading UEs create a significantly different network loading condition that causes the eNB to change the way it allocates resources to the DUT UE. This change may affect the UEs uplink power.

These measurements only test the latter of these two cases because the UTG is simultaneously emulating the traffic associated with all of the loading UEs. Though the UTG is emulating the physical layer traffic of the loading UEs, it may not accurately reflect its combined spectrum. This effect is discussed in more detail in subsection 3.2.3. Since this spectral inaccuracy could potentially bias the results, the test circuit was designed to isolate the spectrum of the loading UEs from the DUT UE's spectrum.

In the "high" value condition, the number of loading UEs was selected to load the network to full capacity without pushing it into extreme/unusual behavior. During pre-test activities, it was noted that severely overloading the eNB's scheduler² resulted in behavior that was not consistent with its normal operation. When the number of loading UEs is set to its "low" value, there are 4 loading UEs emulated by the UTG, and when it is set to its "high" value, 52 loading UEs were used. The exact low and high values were influenced, in part, by the UTG's software, which creates UEs as a "group". The values of 4 and 52 made implementation and data logging simpler and practical.

2.1.4 Factor E - Spatial Distribution of Loading UEs

This factor controls the spatial distribution of loading UEs in both cells as implemented by the UTG. The UTG's application allows the location of the UEs to be set at any place inside the cell. Each location is associated with a predefined path loss, and therefore a predetermined reference signal received power (RSRP). A UTG adjusts UEs' downlink signal to replicate the path loss in the field and adjust SNR at eNB's receiver based on selected UEs' configuration model. Additional details on the UTG can be found in subsection 3.2.3.

There are two cases for the spatial distribution of UEs: near the cell center and along the cell edge. A function of this factor is the radius of the serving and adjacent cells. Table 2.2 outlines how the spatial distribution and RSRPs are linked. Note that the "In Cell" value represents the RSRP of all the loading UEs in a given cell.

The "Adjacent Cell" value represents the level of signal present in the neighboring cell. For example, if both cells have a radius of 100 m, and the loading UEs are in the near condition, the loading UEs in the serving cell will see the serving cell eNB at a level of -50 dBm. The loading UEs in the adjacent cell will also see the serving cell eNB at a level of -110 dBm. These adjacent cell signal levels are only within the UTG. They do not represent the value of the physical cross-talk attenuator between the cells, nor the level of the adjacent cell eNB present at the DUT UE.

Reasoning similar to that of factor B applies here as well. UEs that are in degraded RF conditions are likely to be

²Unusual behavior was observed with greater than 100 simultaneous active UEs in the cell. This behavior may also be present at lower values; extensive testing on this was not conducted.

Table 2.2: RSRP Linkage to Cell Radius.

Cell Radius [m]	Condition	In Cell RSRP [dBm]	Adjacent Cell RSRP [dBm]
100	Near	-50	-110
100	Far	-75	-110
1000	Near	-65	-127
1000	Far	-100	-127

handled differently by the eNB compared to UEs in favorable RF conditions. This difference, in turn, may create a significantly different network loading condition that impacts the DUT UE's emissions.

A UTG is one unit, which, as a whole, connects to an eNB. Although the eNBs' power to UTG stays constant, by placing the UEs at different location from the virtual UTG's base station, the UTG adjusts the path loss (virtually/re-al/combined) to each UE accordingly. Figures 2.1 and 2.2 show the UEs group in RF near condition or at eNB cell edge.

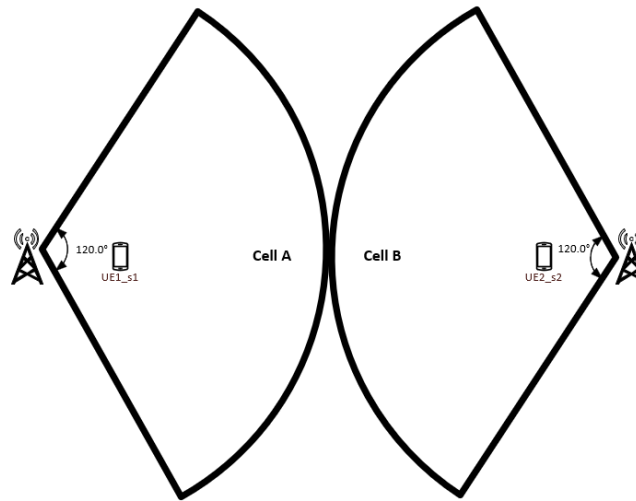


Figure 2.1: Two sectors with two groups of UEs in RF near condition are closer to eNBs with less path loss, and therefore with higher RSRP.

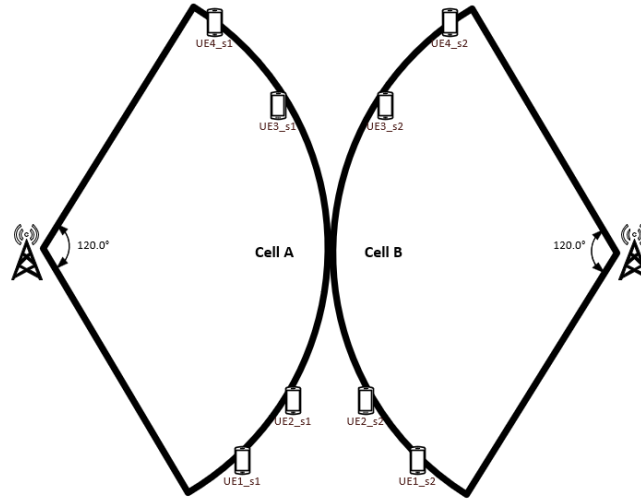


Figure 2.2: Two sectors with four groups of UEs at eNB’s cell edge with higher path loss, and therefore with low RSRP.

2.1.5 Factors F, G, & H - UE Traffic

Factors F, G, and H are all related to how the DUT and loading UEs transact data with the LTE network. In each case, the hypothesis is that a change in a UE’s traffic pattern may cause it to be scheduled by the eNB in a different manner, resulting in a change in the UE’s uplink emissions. All three traffic-related factors apply to both cells; cells are not adjusted individually.

Factor F. The quality of service (QoS) class identifier (QCI) of the loading UE traffic is controlled by factor F. Traffic QoS class identifier (QCI) is effectively the priority with which traffic is scheduled by the eNB. Table 2.3 shows the list of commonly used QCI values in an LTE network [8]. Resource type varies between guaranteed bit rate (GBR) and non-GBR. The QCI values selected for these measurements were QCIs 9 and 5.

Table 2.3: LTE Network Common QCI values.

QCI	Resource Type	Priority	Max. Packet Delay [milli second (ms)]	Max. Packet Error Loss	Example Services
1	GBR	2	100	10^2	Conversational voice
2		4	150	10^{-3}	Conversational video (live streaming)
3		3	50	10^{-3}	Real-time gaming
4		5	300	10^{-6}	Non-conversational video (buffered streaming)
5	Non-GBR	1	100	10^{-6}	IMS signaling
6		6	300	10^{-6}	TCP based video (buffered streaming)
7		7	100	10^{-3}	Voice/video (live streaming), interactive gaming
8		8	300	10^{-6}	TCP based data (web sites, chat, FTP, P2P file sharing)
9		9	300	10^{-6}	TCP based data (web sites, chat, FTP, P2P file sharing)

QCIs 5 and 9 were selected as a result of the network topology used. The measurements could have also been performed with traffic of two other QCI values. The goal is to create a stream of traffic that is scheduled at a higher priority. This higher priority traffic causes changes in the eNB’s behavior, which could lead to a change in the UE’s uplink emissions.

These two different QCIs were implemented by directing the traffic to two different access point names (APNs). Due to the way the DUT UE was integrated into the measurements, it was not possible to reliably control the QCI value of its traffic. Thus, QCI changes only impact the loading UEs. In the measurements, factor F is either set such that all of the traffic is QCI 9, or such that 25 % is QCI 5 and 75 % is QCI 9. During pre-test activities, it was determined that this was a sufficient mixture to create significantly different network loading condition.

Factor G. As with other factors, Factor G - the data rate of the DUT UE and loading UEs - was assigned a high and low value. During pre-test activities, an extremely high data rate was set for the UEs, causing unusual behavior from the eNB scheduling algorithm. Prior to the start of the formal measurements, a more reasonable high value was selected based on the theoretically and empirically determined cell-wide throughput rates.

The theoretical maximum throughput for a cell was calculated based on the physical layer parameters of the LTE signal. The equation is: Max. throughput = Available PRBs × # bits per Hertz (Hz) × [(Sub-carriers per PRB × # of symbols) - # reference symbols] × 1000 × # of antennae × coding rate. For the cells used in these measurements, this equates to an approximate theoretical maximum throughput of: $38 \times 4 \times [(12 \times 12) - 9] \times 1000 \times 1 \times 1 = 20.52 \text{ Mbits/s}$.

Empirically, the test found the maximum throughput for each cell to be 20.1 Mbit/s. The slight difference can be caused by the rounding in the estimation. For example, the coding rate is not exactly 1, sounding reference signal (SRS) may or may not be enabled, and depending on the eNB features enabled, some physical uplink control channel (PUCCH) resources may be allocated for PUSCH traffic.

Spreading the 20.1 Mbits/s across all 52 loading UEs yields a maximum data rate of 388 kilo bits per second (kbit/s) per UE. This value ensured that even when the maximum number of loading UEs was present, the eNB would be loaded, but not in an extreme fashion.

The low value for this factor was set to half the maximum data rate: 194 kbits/s. When 52 loading UEs are presenting, this translates to a maximum loading of approximately 10.09 Mbit/s and approximately 0.78 Mbit/s when only four loading UEs are present. This factor controlled the data rates in both cells, which always had identical data rates. The DUT UE was also configured to have the same data rate as the loading UEs.

This factor works in conjunction with the other eNB scheduling-related factors to create different network loading conditions, which could impact UE uplink emissions.

Factor H. Factor H specifies the type of traffic being sent by the DUT and loading UEs as either transmission control protocol (TCP) or user datagram protocol (UDP). UDP traffic is different from TCP traffic in that it doesn't require an acknowledgement on the receiving end. This factor is a product of the public comment period during the development of the original test plan. For the loading UEs, this was defined in the UTG configuration file. For the DUT UE, it was explicitly specified in the uplink data streaming application that was installed on the UE. In all cases, all UEs always had the same traffic type. No cases were examined where only a portion of the UEs had one type, and the rest another type.

The exclusive use of UDP and TCP traffic is not without its drawbacks. There is some indication [1] that the amount of power a UE will transmit varies based on whether the UE is in "voice mode" or "data mode." Though calls (voice or voice over LTE (VoLTE)) are still made, in terms of PRBs, they represent a small fraction of the total allocated PRBs. That is, the use of other data functions on UEs (e.g., video, web browsing, etc.) are so prolific that the clear majority of allocated PRBs are allocated for the use of data, rather than voice traffic [1].

2.1.6 Factors I, J, Y, & b - eNB Scheduling

Four factors related to the eNBs scheduling have been identified and analyzed in these measurements: I, J, Y, and b. These factors are uplink scheduling algorithm, uplink scheduler frequency domain (FD) type, cell scheduling request periodicity, and target uplink outer scheduling, respectively. Factors I and J are closely related.

Factor I. For factor I, there are three different uplink scheduling algorithms: channel unaware, interference aware, and channel aware. The objective of channel aware is to allocate more resources to UEs in favorable RF conditions while not starving the UEs in cell edge. Interference aware aims to reduce the effect of interference between UEs near the cell edge while distributing resources between UEs in the cell. Finally, the channel unaware method schedules resources evenly among (Round Robin) UEs in the cell. These scheduling methods use resources in time and frequency to fulfill the UE's need for resources.

Factor J. The uplink scheduler FD type (factor J) is closely related to the scheduling algorithm. This factor describes the algorithm the eNB scheduler uses to allocate resources. One algorithm allocates resources equally fair to the UEs selected by the time domain (TD) until the resources are exhausted or the number of resources is sufficient. This is commonly known as a "Round Robin" type scheduling algorithm. Another algorithm - an "exhaustive" method - assigns resources in a prioritized sequence set by the TD scheduler. In this case, the scheduler gives as many resources as possible to a given UE (beginning with the highest priority UE) until the UE no longer requires resources or the eNB's resources are exhausted. The final algorithm is a joint or "mixed" FD scheduler which assigns resources for signalling radio bearers (SRBs)³ and GBR⁴ bearers via the exhaustive method, and then uses a Round Robin approach to allocate the remaining resources to non-GBR bearers.

Factors I and J are related in that not all combinations of them are realizable. When either channel aware or interference aware algorithms are in use, the mixed allocation method must be used. Also, SRS must be used when the scheduler is operating in a channel-aware state. These limitations were identified during the pretest activities using empirical means.

Factors Y and b. The cell scheduling request periodicity (factor Y) and target uplink outer scheduling (factor b) are two additional scheduling-related features that can be enabled or disabled independent of the algorithms used.

The eNB has an optional feature (factor b) that will allow for scheduling PUSCH traffic in parts of the channel that would otherwise be reserved for physical random access channel (PRACH) and PUCCH resources. The benefit of this feature is that when the network is highly loaded, the eNB has additional resources at its disposal. The disadvantage of this configuration is that scheduling resources in the outer region of the channel increases their susceptibility to interference. In these measurements, only outer scheduling on the lower side of the channel was considered. Note that, even though the target uplink outer scheduling feature is enabled on the eNB, it does not necessarily mean that the feature is utilized. This feature is only actually utilized when the network loading is such that additional resources are required.

The final scheduling factor in these measurements is the cell scheduling periodicity (factor Y). This setting controls the frequency at which a UE may request resources from the eNB. A longer periodicity means that fewer uplink resources are used for scheduling requests, but it can also lead to higher buffer status report (BSR) values. These higher BSR values may in turn skew the way in which the eNB allocates resources (i.e., it may issue larger than normal grants in response to infrequent scheduling requests). Factor Y was either set to 20 ms or 80 ms. The range of possible values extends down to 5 ms, but 20 ms was selected because it is the factory default.

³The signaling radio bearer carries uplink and downlink radio resource control (RRC) and non-access stratum (NAS) messages

⁴Some services (i.e., QCIs) require guaranteed bit rates. When used, the bearer expects that enough resources will be made available at any time

2.1.7 Factor K - Power Control

In an LTE network, there are two methods that can be used to directly control a UE's uplink transmission power: open-loop and closed-loop. This method of power control is specified by the eNB when a UE first attaches to the cell. When open-loop power control is used, each UE in the cell is responsible for determining its own uplink transmit power depending on the conditions of the cell (e.g., the UE moves to/from a degraded RF condition). When closed-loop power control is used, the eNB will specify the UE's transmit power.

When the UE is left to determine its uplink transmission power, it will attempt to solve the open-loop power control equation specified in 3rd-generation partnership project (3GPP) TS 36.2.13 section 5.1 [9]:

$$P_{\text{OpenLoopPUSCH}} = \min [P_{cMax}, 10 \log_{10}(M_{\text{PUSCH}}(i)) + P_{0\text{PUSCH}}(i) + PL \alpha(i) + \Delta_{TF}] \quad (2.1)$$

In this equation, the UE will determine its transmission power at (i) instance of time by considering the number of resource blocks granted (M_{PUSCH}), the P_0 specified by the eNB, the channel path loss (PL), the fractional channel compensation factor (α), and the modulation coding scheme (MCS) being used in the transmission (Δ_{TF}). Most of these factors are specified by the eNB either when the UE attaches to the cell ($P_{0\text{PUSCH}}, \alpha$)⁵ or as part of the individual resource grant issued by the eNB ($M_{\text{PUSCH}}, \Delta_{TF}$). The remaining factor - PL - is derived from an estimate of the downlink path loss. To make this estimate, the UE measures the power it receives from the eNB's reference signal that is transmitted at a known power. Note that equation 2.1 is the minimum between the calculated value and the maximum allowable transmission power P_{cMax} . The transmit power of UEs is capped at +23 dB relative to 1 mW (dBm).

If closed-loop power control is in use, the power control equation has an additional term, $f(i)$, that accounts for the transmission power control (TPC) messages sent from the eNB. This equation is also specified in 3GPP TS 36.2.13 section 5.1 [9]⁶.

$$P_{\text{ClosedLoopPUSCH}} = \min [P_{cMax}, 10 \log_{10}(M_{\text{PUSCH}}(i)) + P_{0\text{PUSCH}}(i) + PL \alpha(i) + \Delta_{TF} + f(i)] \quad (2.2)$$

The TPC message is sent from the eNB and instructs the UE to increase or decrease the power of its uplink transmission. Under closed-loop power control, the eNB uses the lowest possible power to maintain a certain block error rate (BLER) given the ambient RF conditions. When the BLER exceeds a predefined threshold, the eNB sends a TPC message instructing the UE to increase its transmit power (assuming the UE is not already transmitting its maximum +23 dBm). Conversely, if the BLER drops below a threshold, it may instruct the UE to decrease its power.

Open-loop and closed-loop power control schemes each have advantages and disadvantages. In open-loop power control, the network is saving a small number of resources by not transmitting the TPC messages necessary for closed-loop power control. However, in open-loop cases, the UE is more susceptible to slow RF fades because of the longer time for open-loop power control to determine the UE power. If the rate of RF change is faster than the open-loop power adjustment calculation, the UE power may never be correctly determined or minimized. Both open- and closed-loop cases are examined in these measurements. The power control method specified applies to both the PUSCH and PUCCH channels⁷, and applies to both loading and DUT UEs. Additionally, both cells always have identical power control configurations.

⁵ $P_{0\text{PUSCH}}$ and α are also represented apart from the power control method by factors O and P. See subsection 2.1.9

⁶Equations 2.1 and 2.2 reference the PUSCH channel in their variables. The equations can also be solved for the power at instance (i) in the PUCCH channel.

⁷A similar power control equation exists for SRS. However, it is not controlled in these measurements.

2.1.8 Factors L & M - SRS

Factor L. The SRS feature is an explicit signal, when initiated by the eNB, that is transmitted by the UE in the PUSCH. This signal is used by the eNB to measure the uplink propagation channel. The eNB can then use this information when making scheduling decisions - prioritizing some resource blocks over others (e.g., frequency selective scheduling) or updating the UE's channel status information (CSI).

When SRS is used, the resource blocks allocated to the uplink SRS signals are filtered out of the data prior to any statistical analysis (for additional details, see section 4.2). Even with the actual emissions filtered out, there may still be an impact to the UE's uplink emissions, as the use of SRS consumes uplink resources, leaving fewer resources for data to be sent. This effect is compounded as the SRS feature applies to all UEs in a cell.

Factor M. Factor L simply toggles the SRS feature on or off, while factor M sets the SRS power offset. This power offset is used when a UE calculates the amount of power it will emit during an SRS transmission. The equation UEs use to calculate this power is similar to the power control equations shown in subsection 2.1.7, but with an additional offset value applied.

The use of SRS is dependent on the scheduling method (factor I), which must be set to "channel aware" when SRS is used. It is only possible to configure the SRS power offset when SRS is used. The serving and adjacent cells always have identical SRS configurations. Both the DUT UE and loading UEs from the UTG respond to SRS requests.

2.1.9 Factors N, O, & P - P_0 and Fractional Power Control

Factors N and O. Factors N and O represent the cell specific nominal power (also known as P_0) to be used in the power control equation that dictates the UE's uplink transmission power. This can also be described as the desired power level of uplink signals as they arrive at the eNB's receiver. The higher the P_0 value, the better the throughput and reception at eNB with the cost of increased inter-cell interference. This value is determined in field by the condition of RF and cell coverage.

Given that the goal of this screening experiment is to demonstrate what impact, if any, a factor has on the uplink power transmissions, values of P_0 were selected without regard for actual deployments. For the PUSCH, P_0 was either set to -85 dBm or +24 dBm. Since UE uplink transmit power is limited to +23 dBm, the +24 dBm setting for the PUSCH P_0 is not attainable in any circumstance. However, this setting would then cause the phone to transmit its maximum power regardless of other conditions. These P_0 values applied to both cells, as well as the loading and DUT UEs.

Factor P. The fractional power control factor, α , is used in the calculation of uplink power (in either closed- or open-loop). It is applied to the path loss value measured by the UE from the downlink reference signal. This compensation factor can mathematically have a range from 0.0 to 1.0, however in practice, the value is typically 0.8 to 1.0. When α is set to 1.0, fractional power control is said to be disabled. When fractional power control is disabled, the UE's power will attempt to maintain a constant signal to interference plus noise ratio (SINR) at the eNB. Under this scenario, if the path loss increases by 10 dB, so will the UE's transmit power.

When $\alpha < 1.0$, fractional power control is enabled. When fractional power control is enabled, the SINR at the eNB is allowed to decrease as path loss increases. In this scenario, as path loss between the UE and eNB increases, it is only compensated for by a fractional amount (mathematically between 0 % and 99 %). The specification for fractional power control can be found in 3GPP Technical Specification 23.213 [9].

For these measurements, α is either 0.5 and 1.0. Increasing the difference between the two settings would have resulted in configurations that were not practically realizable. For example, the UE may attach, but with no resource allocations.

2.1.10 Factor Q - Receive Diversity

This factor, when enabled, allows the eNB to utilize receive diversity. As discussed in subsection 3.1.1, the eNB can utilize up to two separate RF ports when receiving uplink signals from the UE.

This factor does not change any specific UE setting, but may still impact the UE's uplink emissions behavior. When receive diversity is enabled, the eNB may receive the UE's signal with a better SNR, potentially causing different TPC messages to be sent in closed-loop power control. In open-loop power control, no impact on UE emissions is expected.

2.1.11 Factor R - RSRP Filter Coefficients

Before RSRP measurements are used by the UE (e.g., in its calculation of path loss), they are passed through a filter that resides in the network layer [10]. Similar filters are applied to other values measured by the UE, but only the filter for the RSRP measurements is varied.

The filter can be described by the following equation:

$$F_n = \left(1 - \frac{1}{2}\right)^{\frac{k}{4}} \times F_{n-1} + \frac{1}{2} \times M_n. \quad (2.3)$$

In that equation, the filtered measurement output (F_n), is calculated from the filter coefficient k and the measured value (M_n). The filter coefficient can be set to 1 of 15 values that range from 0 to 19. When the filter coefficient is set to 0, the filter has no effect on the incoming measured values.

Adjusting this RSRP filter coefficient effectively changes how the UE estimates the path loss of the propagation channel in the power control equation, and thus can have an impact on the uplink transmission power. This filter coefficient is set by the eNB and received by the UEs when they attach. Since all UEs in a cell use the same filter coefficient, both the serving cell and adjacent cell were always configured as such in these measurements.

2.1.12 Factor S - Maximum UL Transmit Power

In the eNB's configuration it is possible to set the maximum allowable transmit power of all UEs attached to the cell. This parameter does not consider the UE's current RF condition, its resource allocations, nor other configuration parameters. This parameter is sent to the UE from the eNB during the initial attach process.

This factor was set to either 0 dBm or +24 dBm depending on the measurement configuration. According to the 3GPP User Equipment (UE) radio transmission and reception standard [11], Table 6.2.5-1, a UE needs to be able to manage its transmit power to ± 2 dB at its maximum transmit power and to ± 6 dB for a UE at a 0 dBm power.

Logically, this factor is expected to have a significant impact on the UE's uplink transmission power. Though there is a 24 dB difference between the high and low settings, there may be additional factors that cause the actual change to be less, as this factor only impacts the *maximum* power (not the minimum).

2.1.13 Factor T & V - Resource Allocation

These two factors involve the way in which PRBs are allocated to UEs. Factor V sets the minimum size of the initial PRB allocation and factor T sets the size of subsequent allocations. Both factors were set to a high value of 50 (the maximum possible number of PRBs in a 10 MHz channel) and a low value of 1.

Adjusting the minimum allocation size can be useful in cells with a significant amount of uplink traffic. Having a

large minimum allocation in these scenarios can reduce the number of resources spent on requests from the UE. If a UE is allocated more PRBs than it needs, the excess PRBs are filled with padding bits of data. Factors T and V can significantly alter the way in which resources are assigned, which could in-turn impact UE uplink emissions.

2.1.14 Factor U - Latency Reaction Timer

The latency reaction timer relates to the eNB proactively allocating resources to UEs. If a UE consistently requests resources, the eNB may schedule resources for the UE even before it requests them. When resources are scheduled in this manner, the UE has a limited time to use them. The length of time is controlled by the latency reaction timer. If the UE fails to use the pre-allocated resources, the eNB will no longer schedule resources in advance. This timer can be configured from zero (effectively disabling the feature) to 2000 ms. Regardless of the timer's value, both cells are identically configured and the timer can impact all UEs. Because this factor can have a direct impact on how resources are allocated, it may have an impact on the uplink emissions.

2.1.15 Factors W and X - Link Adaptation

Factor W. Two modes of link adaptation were considered and configured in the eNB. The goal of link adaptation is to make adjustments to the link (UE to eNB) parameters as conditions change. Factor W is an outer loop link adaptation algorithm that is used to prevent the eNB from missing a UE transmission as it comes out of discontinuous transmission (DTX) mode. DTX attempts to conserve battery power by deactivating the UE's transmitter when it is not actively sending data. Once the UE has data to send, DTX is disabled and the transmission is sent. It is possible for the eNB to miss the transition from disabling DTX to transmitting, causing a loss of data. To help ensure the transition is detected, the eNB will create a mapping between its SNR and the UE-reported QCI. Because this factor impacts how the eNB receives signals from the UE, it could affect any power control messages and decisions made concerning the UE's uplink emissions.

Factor X. Factor X is an eNB parameter that dictates the type of uplink link adaption (ULA) algorithm used for all UEs in a cell. This algorithm defines how the eNB reacts to changes in the UE's RF conditions. The "fast" version of this algorithm (fast uplink link adaption (FULA)) quickly instructs the UE to change its modulation and coding rate when the RF conditions change. The so-called "extended" version of the algorithm (EULA) is an improved version that better adapts to changing RF conditions. The exact details of these algorithms are proprietary to the eNB vendor.

Factor X is dependent on the eNB's scheduling method (factor I) and the state of SRS (factor L). Specifically, uplink link adaptation must be used when the scheduling method is either interference aware or channel unaware (options in factor I) and SRS is enabled. This dependency is accounted for in the experimental design described in Chapter 5. The eNB has options to use any of mentioned adaptation algorithms above or to turn off uplink link adaptation.

Regardless of the settings of Factor W and X, both cells always have identical configurations, and the settings impact all loading and DUT UEs.

2.1.16 Factor Z - SRB Uplink Scheduling Weight

Factor Z is an eNB feature that controls the scheduling weight of SRB messages that need to be sent from the UE to the eNB. These messages are sent either in the PUCCH or PUSCH. The larger the value of factor Z, the higher the priority that SRB messages carry when they are scheduled in the medium access control (MAC) layer by the eNB. By default, this value is set to 10 (range: 1 to 100). When configured in the factor screening measurements, the value is either 1 or 100.

2.1.17 Factor a - Blanked PUCCH Resources

When enabled on the eNB, factor a is a feature that will prohibit (i.e., blank) the use of a specified number of PUCCH resource blocks from being used by UEs. When PUCCH resources are blanked, the location of the channel quality indicator (CQI) and PRACH offset are also shifted. Resources are blanked equally from each side. For example, when factor a is set to its high value of 10 PRBs, five PUCCH PRBs from the high side and five from the low side of the channel are blanked. This blanking then forces the CQI and PRACH to begin five PRBs inward from its original location.

The primary benefit of this feature is that it aids in mitigating interference from adjacent channels. PUCCH PRBs are located on the outer edges of the LTE channel - the portion of the channel most susceptible to adjacent channel interference.

The low setting for this factor is zero PRBs, equivalent to disabling the feature. In all cases, both cells were identically configured, and the blanking impacted both the loading UEs and the DUT UE. As this factor changes the number of available resources for PUCCH and PUSCH information, it may impact how resources are allocated to UEs, thus potentially impacting uplink emissions.

2.2 Collateral eNB Factors

In the process of configuring the eNB with the factors above, additional factors were configured. Each of these factors were changed from their default value, but not considered as a factor in the screening experiment. Each of these variables remained the same across all measurement configurations.

Enhanced Inter-cell Interference Coordination (EICIC). The EICIC feature is designated to help to reduce interference from a UE located at the cell edge of two neighboring cells, as may be seen when UEs are handing over from one cell to another. This feature was disabled as it could unduly skew the eNB's scheduling algorithm.

eNB Cell Type. The cell type of an eNB determines the size of the LTE cell for the UE handover history and decision-making. The eNB cell type can be configured to be very small, small, medium, and large. In all factor-screening measurements, the cell size was set to large to reduce the chance of handover to the neighboring cell when the UEs are at the cell edge.

Maximum number of Uplink Users per transmission time interval (TTI). The two major factors which dictate the maximum number of uplink UEs per TTI are cell bandwidth and eNB manufacturer. There is a theoretical limit to the maximum possible number of UEs per TTI - equivalent to the number of available PUSCH PRBs - but eNB vendors typically set the limit much lower. To prevent this setting from having an impact on the results, the eNB was set to allow the maximum possible number of UEs per TTI: 14. Note that this setting does not force or encourage the eNB scheduler to reach this maximum. The scheduling algorithms are independent of this setting.

PUSCH Masking Feature. This masking provides an option to mask the frequencies used by the PUSCH sub-areas to prevent the eNB's scheduler from allocating resources in the masked region. This feature aids in preventing uplink interference at the price of bandwidth. This feature was disabled as the test team does not expect any interference from the loading UEs/UTG in the same or adjacent cells.

Maximum Aggregation of VoLTE Packets. This feature aggregates VoLTE packets together. This feature can be configured to various levels, but when the scheduling algorithm is set to Round Robin, this value has to be set to 1. For simplicity, it was set to 1 in all measurement configurations.

PRACH Parameters. The eNB required the configuration of several random access channel (RACH) related variables:

- **RACH frequency offset:** This parameter is a message sent to the UE indicating what frequency should be used to send its initial RACH request. This is set at three PRBs. That is, RACH requests should be sent on the third PRB from the end of the PUCCH.
- **CQI:** The CQI is sent by the UEs as a message to the eNB with information on the current RF condition of the channel. CQI values are between 15 to 0 (very good to very bad RF condition) requiring only four bits sent to the eNB via PUCCH channel.

In cases where PUCCH resources are blanked (factor a), the RACH and CQI values are offset accordingly. When factor a is set to its high value of 10, the RACH offset becomes 13, and the CQI offset becomes 12.

PRBs for CQI The CQI message conveys information about RF quality of channel as seen by a UE to eNB. This information helps the eNB's scheduler decide on PRBs allocations and modulation for each UE. The CQI was set to be wide-band in nature, covering the entire uplink channel, and was reported by the UEs every 40 ms. By default, the CQI message is allocated two PRBs at the beginning of the channel. This allocation had to be shifted by 10 PRBs to account for the occasional blanking of PUCCH resources (factor a). This shift was required by the eNB's configuration software; it was not optional.

Chapter 3

Test Implementation and Execution

3.1 Testbed Design

This chapter outlines the design and implementation of the test circuit. This circuit and implementation scheme realizes the measurement concept and flow diagrams discussed in section 1.4¹. The method, design, and equipment are discussed in detail both to enhance understanding of the measurements that NASCTN performed and to enable others to recreate the same or a similar test circuit for their measurements. Specifications not enumerated here are not thought to have a meaningful impact on the test results.

3.1.1 Test Circuit

To realize the testing of factors described in Chapter 2, NASCTN developed the test circuit in Figure 3.1. In general, the two eNB cells can be seen on the right side of the diagram and the UTG generating the loading UEs on the left. In the lower left, a small shielded chamber is shown housing the DUT UE. The circuitry immediately to the right is responsible for inserting the DUT UE into Cell A. The circuitry in the middle of the diagram is used to control the cross-talk between cells and shift the level of the downlink signal to a level appropriate for the UTG. The components shown in Figure 3.1 are summarized in Table 3.1. Note that this table only shows the primary purpose of each component. Each component has one (if not more) secondary impacts, as described below.

This realization involves two commercial macro-cell eNBs and a UE UTG to simulate the loading UEs. The cells can be serviced with two separate commercial eNBs or with a single eNB capable of supporting two cells. A controlled DUT UE will be inserted into Cell A. This DUT UE is a real, commercially available UE that attaches to the same cell as the loading UEs and is assigned resources from the eNB's scheduling algorithm. Both the loading UEs and the DUT UE will transact a specified data rate and protocol. It is important to note that the ability of the eNB and UE to handover or handoff from one cell to another has been disabled.

The DUT UE is drawn as being placed inside a small shielded chamber with a horn antenna to capture the uplink signal and transmit the downlink signal. A directional coupler (component #5) was used with the side-arm port connected to an RF switch (component #6). This switch toggles between a matched RF termination (for noise reference measurements) and the VSA. The output port of coupler #5 is connected to a variable attenuator (component #10). The VSA is used to collect emission spectrograms of the DUT UE during each test configuration. The variable attenuator connected to the output of the coupler is used to change the path loss between the DUT UE and the eNB as a way of simulating changes in the DUT UE's position within the cell.

Also shown in the small chamber is a connection from the DUT UE to a personal computer (PC). During the measurement process, the DUT UE will run diagnostic monitoring software capable of capturing the self-reported transmit power along with a variety of other parameters. The data will be transferred to a computer, recorded, and timestamped

¹The LTE infrastructure that the eNB is connected to is, for simplicity, omitted here as it is not the subject of this testing. This infrastructure is described in section 3.2.1

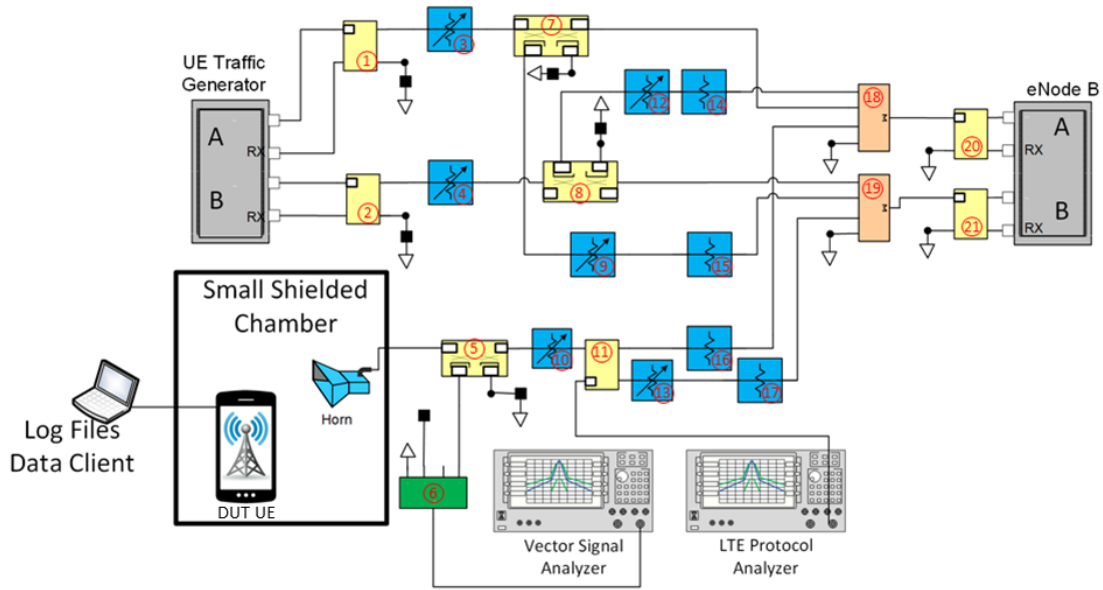


Figure 3.1: NASCTN Laboratory Testbed

for alignment with the VSA spectrograms. The timestamping and alignment process is detailed in section 6.1.

The DUT UE portion of the test circuit is inserted into Cells *A* and *B* via the splitters/combiners labeled as components 18 and 19. These components bring together signals from the eNB, UTG, and DUT UE. A small portion of the DUT UE signal is split off via the #11 hybrid coupler and added to Cell *B* via #19. The Cell *A* signals from various components are combined (uplink) and split (downlink) in component #18.

The cross-talk between cells *A* and *B* are controlled by couplers 7 and 8 and attenuators 9, 12, and 13. These attenuators control the level of influence of Cell *B* loading UEs on Cell *A* UEs and vice versa. The three variable attenuators were always changed at the same time; the amount of influence between the cells was always reciprocal. The value of the attenuators was tied to the spatial size of the cell (factor *B*). When the cell radius was set to the low value of 100 m, the attenuators were set to zero to simulate an increased amount of cross-talk which may be caused by eNBs being closer together. Conversely, when the cell radius was set to 1000 m, the cross-talk attenuators were set high (approximately 100 dB) to simulate a large amount of path loss between the eNBs of the cells.

The four hybrid couplers (components 1, 2, 20, and 21) were placed immediately adjacent to the UTG and eNB. Both of these components were designed with two RF ports per cell: one duplex port and one receive-only port. The receive-only port is utilized when receive diversity is enabled. For the eNB, factor *Q* controlled receive diversity, and it was always enabled on the UTG and DUT UE.

NASCTN exercised care in designing the test circuit, accounting for the lowest possible transmit power from the eNB being +39 dBm with a reference signal power level of +11 dBm. This power level far exceeded the maximum input level of the UTG, and would have constituted an unreasonable RSRP to the DUT UE inside the chamber. To shift the downlink signal to a more reasonable level, a series of fixed (components 14, 15, and 16) or manually variable attenuators (components 3 and 4) were used. These attenuators shifted the downlink signal level down to -68 dBm (assuming the path loss attenuator - #10 - is set to zero) for both the DUT UE and the UTG. Specifically, attenuators 3 and 4 were set to 54 dB and 58 dB, respectively.

Table 3.1: Summary of test circuit components.

#	Item	Primary Purpose
1	Hybrid coupler	Shift phase of downlink Cell A signal into diversity RX port of UTG
2	Hybrid coupler	Shift phase of downlink Cell B signal into diversity RX port of UTG
3	Fixed attenuator	Adjust downlink signal level of Cell A
4	Fixed attenuator	Adjust downlink signal level of Cell B
5	Directional coupler	Couple a small portion of the DUT UE signal for sompling by the VSA
6	RF switch	Toggle between an RF load (for noise reference measurements) and the input signal
7	Directional coupler	Couple a small portion of the Cell A signal for insertion into Cell B
8	Directional coupler	Couple a small portion of the Cell B signal for insertion into Cell A
9	Variable attenuator	Adjust the amount of Cell A signal inserted into Cell B
10	Variable attenuator	Adjust the path loss between the DUT UE and the eNB
11	Hybrid coupler	Couple a portion of the DUT UE signal for insertion into Cell B
12	Variable attenuator	Adjust the amount of Cell B signal inserted into Cell A
13	Variable attenuator	Adjust the level of DUT UE signal inserted into Cell B
14	Fixed attenuator	Shift the level of Cell B signal being inserted into Cell A
15	Fixed attenuator	Shift the level of Cell A signal being inserted into Cell B
16	Fixed attenuator	Shift the level of Cell A signal to/from the DUT UE
17	Fixed attenuator	Shift the level of DUT UE signal being inserted into Cell B
18	Splitter/Combiner	Sum/split the Cell A signals
19	Splitter/combiner	Sum/split the Cell B signals
20	Hybrid coupler	Shift the phase of the Cell A uplink signal into the diversity RX port of the eNB
21	Hybrid coupler	Shift the phase of the Cell B uplink signal into the diversity RX port of the eNB

To aid in troubleshooting and system verification, an LTE protocol analyzer is inserted into the system. Connected to one of the arms of the #11 hybrid coupler, this analyzer is capable of capturing, decoding, and recording the uplink and downlink LTE traffic. Future measurement setups could elect to integrate this protocol analyzer into the test circuit as another source of data. As an additional troubleshooting tool, test points were added to various stages of the circuit. The test ports on components 1, 7, 18, and 20 provide access to the path between Cell *A* of the UTG and UE and 2, 8, 19, and 21 provide access to the Cell *B* path between the UTG and eNB. The DUT UE path can be accessed from ports on 5, 18, and 20.

Figure 3.2 shows a photo of the actual test circuit used in the factor screening measurements. This circuit contains all of the couplers, attenuators, and splitters shown in Figure 3.1.

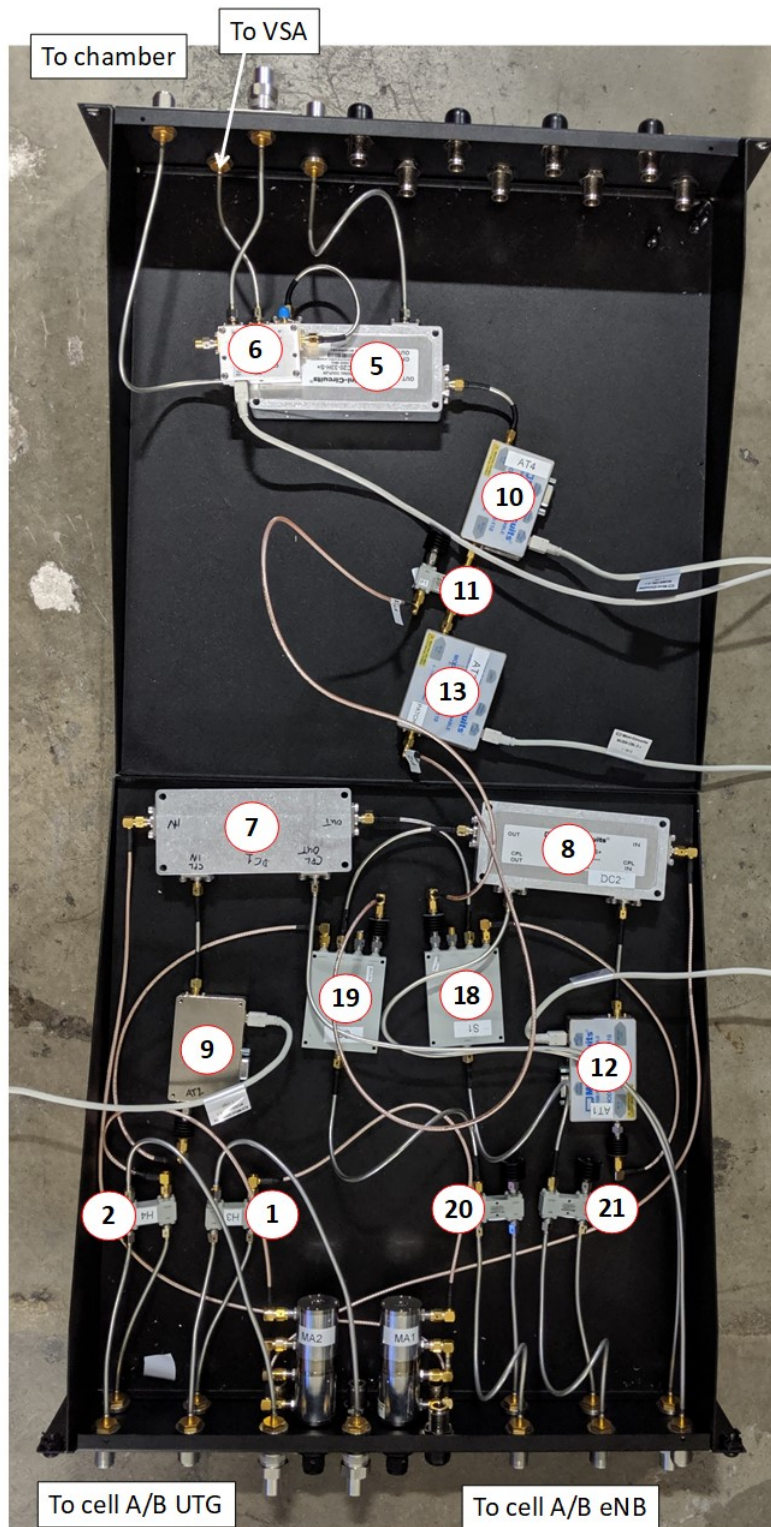


Figure 3.2: A photo of the realized test circuit used in the factor screening measurements.

3.1.2 Data and Control Connections

There are two different types of data controlled in the factor-screening measurements: measured and transacted. Measured data includes data acquired during the measurement and communications with the test instrumentation. Transacted data is data sent over the radiated or conducted air interface of the LTE network, typically in the uplink direction. The type (i.e., TCP or UDP) and rate of these data are carefully controlled as factors F, G, and H.

Once acquired, measured data are transported via the network shown in Figure 3.3. These connections are either universal serial bus (USB) or wired Ethernet local area network (LAN). No measured data are sent via the LTE interface.

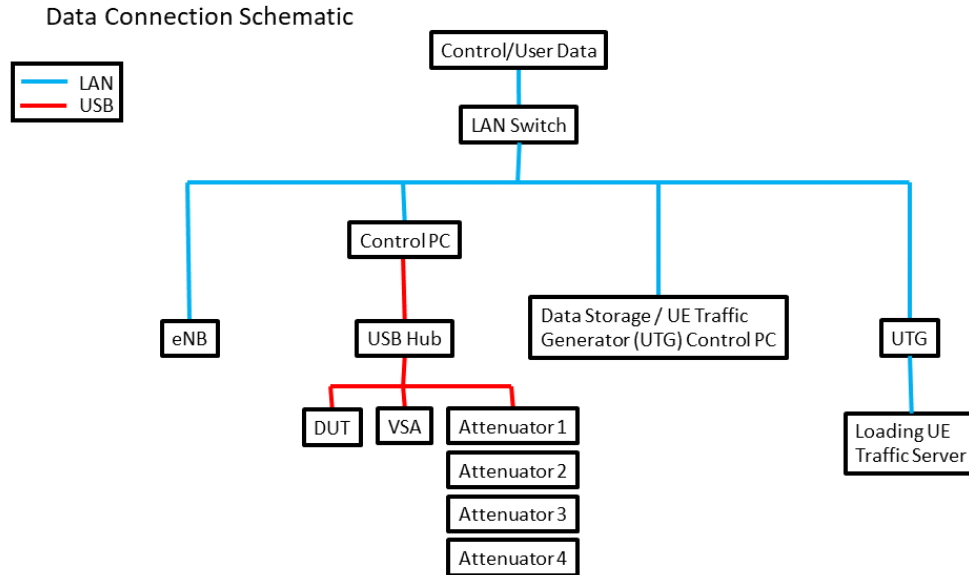


Figure 3.3: Data and control connections between the PC and the rest of the testbed.

3.1.3 Test Automation

The experimental design of Chapter 5 was executed by automated testing. The automation was implemented in Python test scripts running on a PC. The role of the scripted automation was to 1) collect and log data stream(s) from instruments and the DUT, and 2) coordinate the measurement system with the DUT UE. These capabilities were linked to source code designed to ensure test parameters and processes match the specifications in Chapter 2. Investment of time and effort into test automation before collecting data can reduce human intervention during tests. The resulting benefits include:

- improvements in test throughput by concurrency and rapid progression through test states
- running unattended tests for several hours or days, operating overnight or during weekends
- less dependency on the person operating the testbed during test executions
- reducing human error in repetitive tasks such as iterating between test cases

These benefits are substantial in this testing because of the required large-scale coordination between many instruments and runs for extended periods. Test parameters and processes require control of up to 12 different test devices, and a typical test runs several hours and spans multiple days. The alternative to automation strains human focus and patience, limits test output, and risks data corruption through mistakes.

3.2 Equipment

3.2.1 LTE Infrastructure

These measurements were supported by the laboratory's existing LTE infrastructure. This infrastructure consists of a virtual evolved packet core (EPC) that performs several functions. The virtual EPC has all of the same nodes as a larger, separate core network, including: mobility management entity (MME) (the main LTE signaling node), serving gateway (SGW) (for forwarding and routing user data packets), and packet gateway (PGW) (for internet protocol (IP) routing of data). A separate home subscriber server (HSS) is used for provisioning and authenticating the UEs. Each of the loading and DUT UEs were individually provisioned for service in the HSS.

To support the use of two different traffic QCIs, two separate APNs were configured in the PGW and SGW. All traffic for QCI 9 was sent to one APN while traffic for QCI 5 was routed to the other. The configuration of two APNs ensured that QCI 5 traffic was scheduled accordingly by the eNB and remained a priority throughout the LTE network.

3.2.2 LTE eNB

The eNB manages the RAN, scheduling of resource allocations, and handover decisions on the LTE network. eNBs typically consist of at least one radio head and a controller unit. The eNB selected for these measurements was a COTS eNB with a single radio-head that supported two distinct LTE cells. Each cell can be configured independent of the other. This eNB was loaded with firmware from the manufacturer that was compliant with all the major features of the 3GPP release 9. The eNB was a macro-cell product, as opposed to a small-cell or indoor product. This eNB was a Band 3 FDD unit. Band 3 was selected because it was already deployed in the NASCTN lab (decreasing start-up time) and its uplink frequency overlaps with Band 66.

Any multiple-input multiple-output (MIMO) functionality on the eNB is disabled. Though MIMO functionality is deployed for use in commercial networks, including it in this testing is difficult. To include it here, one would need to ensure that the MIMO functionality is either consistently implemented and utilized across test cases or that enough control over the MIMO functionality is available to include it as an individual variable in the test.

The eNB was configured through software provided by the manufacturer. To aid in automating the measurements, configuration files were pre-made based on the experimental design described in Chapter 5. These files were created in the software, then saved as extensible markup language (XML). These files were then pushed to the eNB as required. Each time a new configuration file was loaded, the eNB was rebooted (i.e., power cycled).

3.2.3 LTE UE Traffic Generator

The UTG is a piece of laboratory equipment designed to load the network to which it is connected by emulating COTS UEs. As it emulates UEs in a user-specified scenario (static or dynamic), the UTG records a large variety of information from multiple network layers and stores them in files for later analysis. One of the advantages of a UTG is that it enables the emulation of a large number of UEs (possibly thousands, depending on configuration) in a controlled, laboratory setting. The UTG provides a full-stack implementation of LTE. In general, the eNB does not know the UEs are emulated and treats them as a COTS UE.

Nearly every aspect of the emulated UEs can be configured in the UTG's user interface: the RF condition of individual UEs, dynamic channel fading, traffic type, data rate, location in a cell, and traffic QCI. The UTG is also capable of emulating separate cells and facilitating the UE side of handover process from one cell to another. To create a test configuration, a graphical user interface (GUI) is used to draw cell boundaries, place emulated UEs, configure their traffic profile, and specify their RF condition. This configuration is then saved and sent as a series of command line

interface (CLI) messages as the factor-screening measurements are executed.

The UTG is comprised of a chassis with a common communications back-plane into which RF “cards” are inserted. Manufacturers make a variety of cards for different purposes and frequency ranges. Because this test is interested in emulating UEs in two cells, two separate radio cards were used and configured.

Though the UTG is a capable and complex piece of equipment, the way it implements some of its emulation could be problematic for some types of measurements. When possible, the UTG will implement its emulation directly in the physical, network, and MAC layers in exactly the same way as a real UE would respond. However, in many cases, the UTG is unable to implement all of the UE behavior in the physical layer. In these cases, the UTG will continue correctly emulating UEs’ data traffic in the other network layers, but its physically-emitted spectrum will not be accurate. This limitation requires no mitigation as it has a minimal impact on these measurements since the main purpose of the UTG is to load eNB scheduler, and not to accurately emulate details of the process in the physical layer.

To demonstrate this behavior, consider a case where the UTG is emulating 52 UEs in a cell. Given the RF cards installed, the maximum power output from the UTG is +20 dBm per cell. This +20 dBm is spread across *all* emulated UEs. This total power is quickly exceeded when multiple UEs are transmitting in the same subframe. As soon as the limit is reached, the UTG becomes less accurate in its physical-layer emulation. In some cases, the UTG may inject noise into the physical layer to intentionally degrade the uplink signal to the eNB and achieve an appropriate SNR. Examples of network and protocol layer emulation include sending desired power headroom report (PHR) (as opposed to measured PHR) and continuing to respond to TPC messages regardless of the actual power output from the UTG.

For the UTG to function properly, some supporting hardware that is not shown in Figure 3.1 is required. This hardware includes a server for generating the loading UE traffic and a server that acts as a destination for the loading UE traffic. The traffic servers are configured in such a way as to not interfere with the physical layer testing being performed. That is, the servers do not create a throughput bottleneck.

To match the DUT UE and eNB specifications, all of the loading UEs were configured to be Category 4 and Release 9 of 3GPP. Both the UE category and release number are configurable within the UTG. When appropriate, the UTG was configured to send SRS messages (factors L & M).

As shown in Figure 3.1, the UTG is connected to the test circuit over cables in a conducted manner. This is important because it could potentially obscure real-world effects caused by the pattern of base station antennas, their height, and their down-tilt. The UTG assumes that the antenna pattern is isotropic and not configurable. With respect to antenna patterns and down-tilt, the closest way of accounting for these parameters is with the cell radius. The cell radius is specified in the UTG and is controlled by factor B.

3.2.4 Vector Signal Analyzer

The signal analyzer produces the spectrogram used as the basis for the physical measurement of DUT UE emissions. This spectrogram needs to give the power distribution binned into time aligned to 1 TTI (1 ms resolution) and binned frequency aligned to the 50 LTE UL PRBs. The spectrogram needs to produce continuous stream of this data in time for several seconds or more. Modern instruments achieve this in practice by real-time analysis of in-phase and quadrature (IQ) data.

The ideal test instrument for this purpose would align the spectrogram data by demodulating the uplink waveform and synchronizing to symbols in the LTE waveform. Unfortunately, the NASCTN test team did not have an instrument available that could both support this function and acquire continuously for several seconds. In order to avoid this problem, the team collected samples that were unsynchronized and oversampled the spectrogram time resolution. The test team aligned and downsampled this spectrogram as detailed in subsection 4.2.3.

The key specification of the instrument's spectrogram acquisition is that the time-domain oversampling ensure time resolution at least a factor of 10 smaller than the 1 ms TTI. This is necessary, because the alignment and downsampling needs to throw away samples that straddle the boundary between TTIs. The test team sampled at approximately 53 μ s resolution, which was approximately a factor of 19. The VSA was set to a center frequency of 1.77 GHz with a span of 9 MHz.

3.2.5 DUT UEs - Devices and Traffic

The factor-screening measurements were done with two category 4² COTS LTE UE devices that were released to the United States (US) market in 2016. Both devices were the same model, but with different serial numbers, and contained a software image provided by a major commercial carrier. The devices were "unlocked" such that they were not locked to a commercial network and could be used on the NASCTN laboratory network.

In 3GPP, the UEs are grouped based on their hardware and software capabilities in both uplink and downlink directions. Each UE category has a higher throughput than the previous one, and it may be able to do higher modulation or support greater numbers of antennas or both.

Though the measurements were done in Band 3, the DUT UEs supported Band 66 (AWS-3). In order to prevent the UEs from attempting to handover or search for other cells, software on a PC was used to write the nonvolatile random-access memory (NVRAM). This forced the DUT UEs to stay locked on Band 3 and not search for other available frequency bands or cells.

To control the uplink traffic of the DUT UEs, an application designed for generating and sending IP traffic was installed on each DUT UE. This application was controlled through a developer bridge between the DUT UE and the control PC. The connection from the control PC was independent of the wireless LTE connection. Depending on the measurement configuration, the application was setup to send TCP or UDP traffic (factor H) at a specified data rate (factor G) to a server running on the control PC. A log of the data stream and its throughput was collected from the application, but only used for troubleshooting purposes.

3.2.5.1 USRD Monitoring Software

Most major manufacturers of LTE chipsets provide some type of UE self-reported diagnostics (USRD) tool for accessing information directly from the chipset of a COTS UE. There are also some third-party vendors who market a similar product. In either case, the result is a variety of information from the the current state and behavior of a UE. This software tool can be used to troubleshoot system issues, debug new features, or collect metrics on performance. To get this information, the software forces the UE into a mode where it will echo the LTE protocol stack messages to an output port (e.g., USB) on the UE. The type of USRD software used here is different from other applications (or "apps") that can be installed on top of a UE's operating system. Some apps may be able to provide the same or similar information as the USRD software, but it may consume more of the UE's computing resources. In rare cases, this could impact the UE's performance or ability to maintain a desired data rate during a measurement.

This software can be configured to collect all or some of the protocol messages from the phone. Due to the high number of messages, events, and status indicators available in the LTE protocol stack, a filter is used to only collect pertinent messages during acquisition. If the filter is too broad and too many messages are collected, it can cause adverse effects, potentially biasing the results. During pre-test activity, it was noted that periodic drop outs of information from the UE were occurring. These dropouts were traced back to collecting too many parameters.

In the factor-screening measurements, this software was primarily used to gather self-reported metrics from the DUT

²LTE UE category 4 is specified as maximum downlink data rate of 150 mega bits per second (Mbit/s) and a maximum uplink rate of 50 Mbit/s. 64 quadrature amplitude modulation (QAM) in the uplink is not supported.

UEs. These metrics were used for cross-checking against parameters recorded, for comparing the self-reported power to the measured power, and for time-aligning data streams as described in section 6.1. Among the metrics collected from this software were: BSR, MCS, number of PRBs and transmit power. The full list of parameters can be found in Appendix B.

3.3 Shielded Enclosure

As shown in Figure 3.1, the DUT UE was placed inside a small, shielded, anechoic chamber during measurements. The use of an anechoic chamber isolated the DUT UE from any ambient signals present in the laboratory, and enables the controlled insertion of the DUT UE into cells *A* and *B*. Figure 3.4 shows a DUT UE placed in a machined foam holder and placed in the center of the small shielded anechoic chamber.

One concern with using a small anechoic chamber, as opposed to a larger chamber, is that caution must be exercised to ensure the chamber and antenna placement do not impact the radiation of the DUT UE. Detailed verification measurements of the shielded chamber and its environment impact on the measurements is highlighted in Appendix C. Through these measurements, it was determined that the distance between the horn antenna and DUT UE was sufficient and did not result in any significant undue interaction. Figure C.9 shows a small impact on the test antenna's self-reflection characteristics, beyond that, however, the test team did not experience a large impact when placing the DUT UE into the test chamber, see Figure C.11.

3.4 Data Acquisition

A valid implementation of the experiment defined in Chapter 5 needs to produce repeatable, meaningful, and applicable data. This means that the test must proceed through clearly-defined states. The full test state for each factor screening test case is defined as follows:

1. The settings for a test case are active as defined by one of the rows in Table 5.5.
2. All other configuration settings defined in controlled nuisance factor section Table 5.8 are also active.
3. All devices in the testbed are finished initializing to ensure steady state operation.

The initialization requirement helps to ensure that the system is operating in steady state (though the data may still be dynamic).

This section defines these states, to serve as specifications for the testbed implemented in Chapter 3. The testbed must implement these requirements strictly and query its constituent devices to validate at runtime. This requires waiting for each component to confirm that it has achieved the desired state whenever possible.

3.4.1 Test Sequence

The test sequence to implement the experimental design is specified in Figures 3.5 and 3.6. The test sequence iterates through all test cases in the defined order. In each test case, a configuration is applied to the hardware in the test setup, and data is acquired and recorded. The iteration is defined as two levels of nested loops:

- an outer loop that sets the eNB test parameters
- an inner loop that sets the other test parameters that are not determined by the eNB

An important practical aspect of this measurement campaign is the overall test execution time. Test execution is most efficient when slow operations are executed in the outer loop. In this implementation, changing the eNB configuration is the slowest single operation, so it is specified in the outer loop. Other test implementations may consider swapping

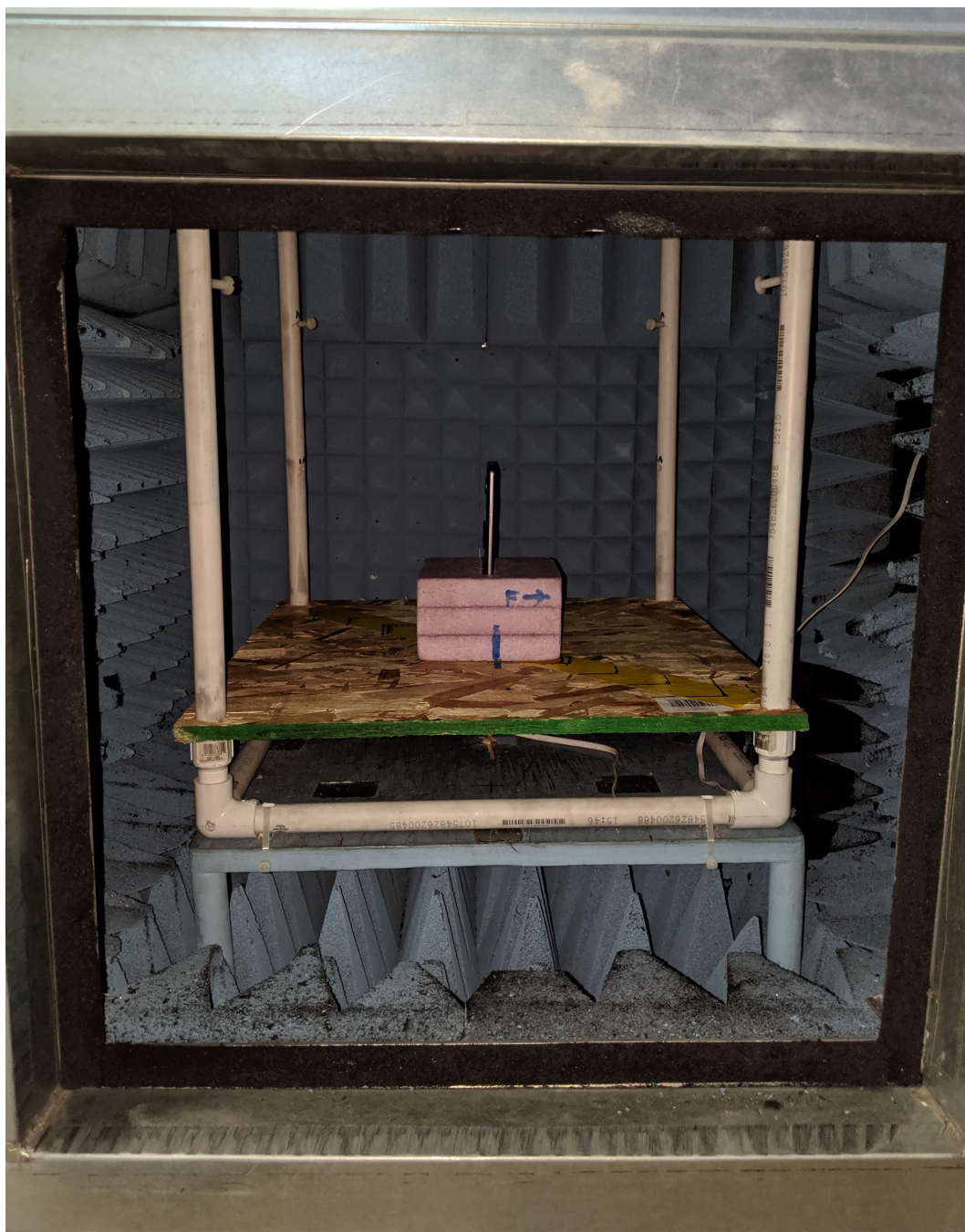


Figure 3.4: Photo showing a DUT UE in a machined foam holder inside the small shielded enclosure

the inner and outer loops if different instruments take longer to configure.

The testbed improves throughput by using multi-threaded concurrency. The benefits are most significant in the inner loop. The timing specifications in Figure 3.6 show the instruments that can be configured concurrently along the y -axis of inner-loop functional blocks used in Figure 3.5.

The following threads execute in the inner loop:

- **PC:** The PC executes the scripts that run the test sequence and manages the resulting data and dispatches input and output (*I/O*) to and from all testbed devices. In order to increase test throughput, the spectrogram data transfer from the signal analyzer is concurrent with spectrogram downsampling from the *previous* spectrogram capture. Processing is on the previous dataset, because the current spectrogram capture is in the process of transfer.
- **Signal analyzer:** The 5 s capture defined in this specification is driven by limitations of the instruments in this implementation as discussed in subsection 3.2.4. Future implementations of this test may consider longer capture times if the signal analyzer is sufficiently capable.
- **DUT UE:** This includes (for brevity) the DUT UE itself, the diagnostic software running on the UE, traffic generating software running on the UE, operating system (OS) queries about LTE link condition, and programmable attenuation between the DUT UE and the eNB. The configuration steps for these were much shorter than the operations in the other devices, so they are chained together serially instead of concurrently.
- **UTG:** Configuration time needed by the UTG may be larger than other inner-loop devices because it emulates and logs behavior of all loading UEs.

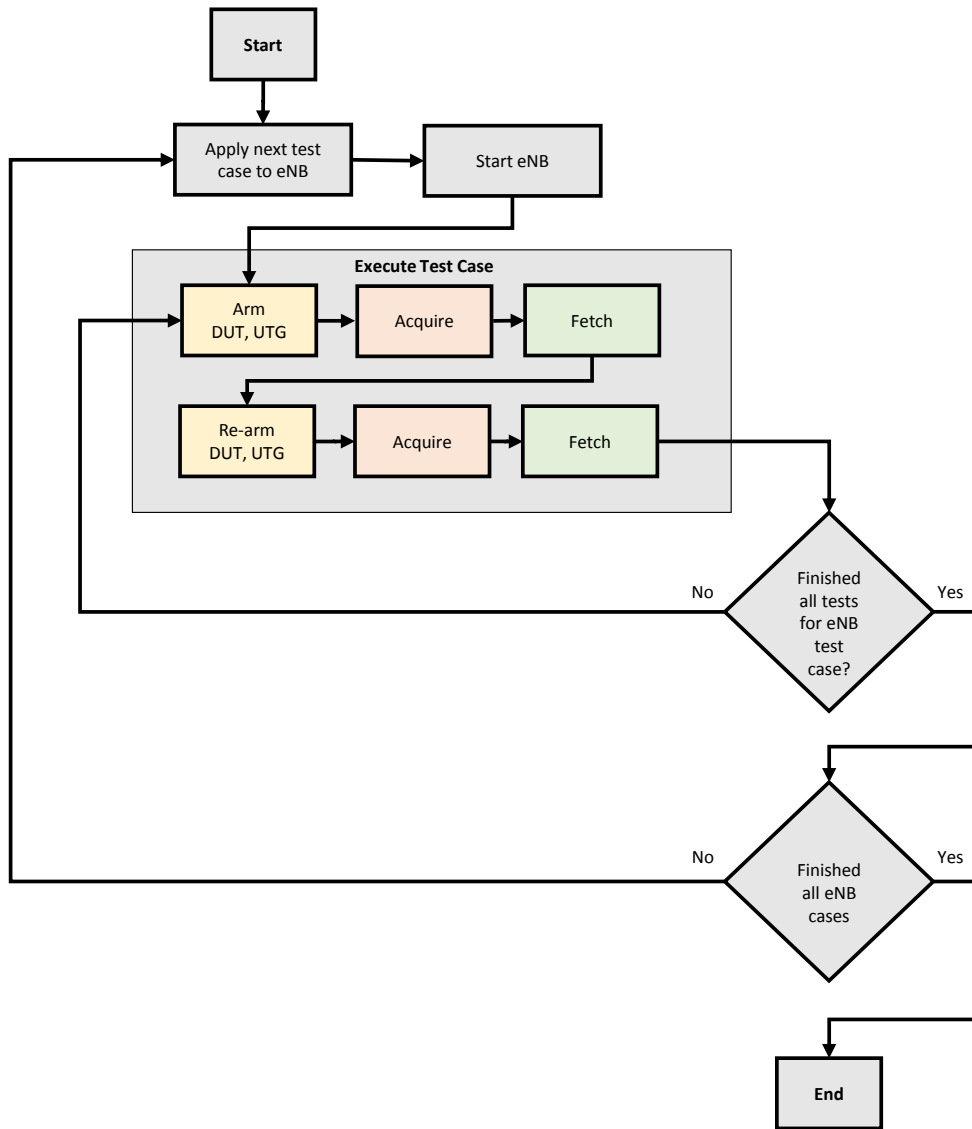


Figure 3.5: High-level test sequence specification for the experiment design specified in chapter 5.

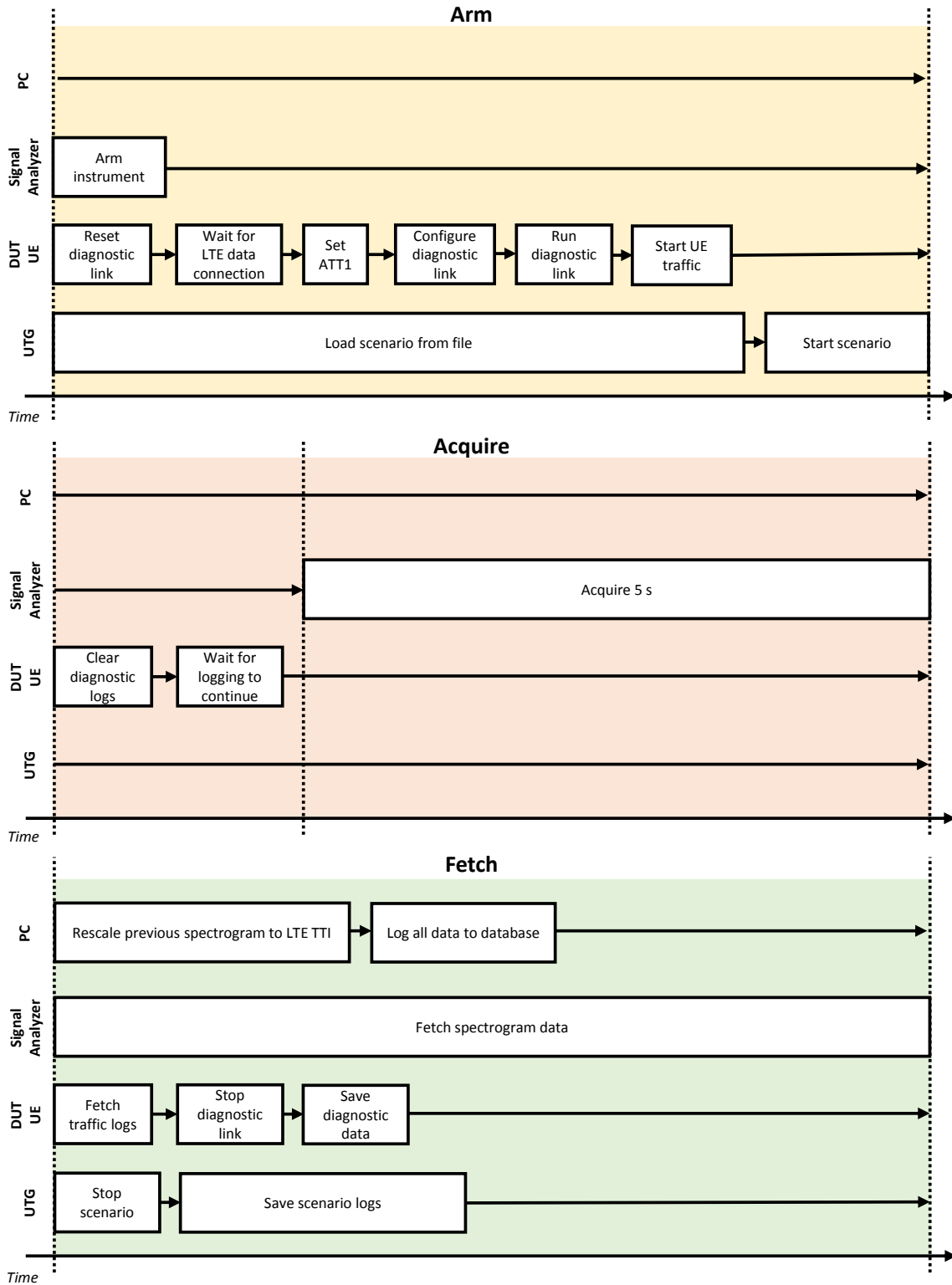


Figure 3.6: Test sequence specifications to arm, acquire, and fetch within a single eNB configuration. Threads that control different devices synchronize at the dotted lines.

3.4.2 Device Checks Prior to Data Collection

To produce valid results, the state of each instrument and piece of equipment in the testbed needs to match that of the experimental design. In order to ensure this, the system needs to confirm that each piece of equipment is in the proper state that aligns with the experimental design. To this end, the team undertook the measures in Table 3.2 for each device.

Table 3.2: Validation Checks During Testing to Confirm Steady State Operation

Function	Checks
LTE eNB	Configuration applied to fit test case in Table 5.5 Active and ready to accept attach from UEs
Simulated UEs	Configuration applied to fit test case in Table 5.5 Radios active All UEs are attached Logging is running
DUT UE	DUT has rebooted Attached to eNB for LTE data Uplink traffic configured to fit test case in Table 5.5 Uplink traffic transmission is active Data debug logging is active
Signal analyzer	Armed for spectrogram capture and ready to acquire
Attenuators	Set to attenuation defined the test case in Table 5.5

3.5 Reference Measurements

As detailed in Appendix C, the test team carried out several reference measurements, which are summarized below. These measurements encompassed the following components of the test architecture:

- the radiated environment,
- the conducted RF signaling chain,
- the UE placement, and
- the overall system path loss, and uncertainty.

The radiated environment included a small, mobile anechoic chamber with exterior dimensions of 94 cm in width, 94 cm in depth, and 182 cm in height. The interior of the chamber was lined with RF absorber material. The test antenna, a dual ridge horn antenna was suspended from the ceiling of the chamber. The DUT UE was placed into the chamber at a nominal separation distance of 78 cm from the aperture of the test antenna. The team investigated the RF chamber for its shielding effectiveness, and also for its effect on the radiative performance of the test antenna. The shielding was better than 105 dB ensuring that errant coupling between the UE and outside entities was minimized. The chamber's effect on the radiative performance of the test antenna was minimal, as the test antenna's effective gain was similar to gain measurements obtained in a 3 m quiet zone anechoic chamber. The antenna gain was calculated using a two antenna method.

The RF signaling chain was verified through a series of measurements of the primary signal paths for their path loss. This gave confidence in the RF circuit's ability to appropriately isolate and control cross-talk between cells. Furthermore, this series of measurements enabled balancing the test set-up in terms of intra-cell and a cross-cell path loss.

The team also investigated the effect of UE placement on DUT UE transmit power and end-to-end eNB to DUT

UE path loss of the overall system. These measurements indicated the expected variability and uncertainty in the observations of UE reported power and VSA spectrogram captured power. Namely, the overall path loss of the system within the LTE Band 3 was found to be 73.2 dB from the plane of the DUT UE to the input to the eNB. Moreover, a 54.1 dB path loss was measured between the DUT UE and the VSA. The combined uncertainty was calculated to be ± 2.3 dB. See Appendix C for further details.

Chapter 4

Data Processing

The raw data produced by instruments and DUTs require preparation and statistical analysis to produce the final test results. This chapter details these processes.

4.1 LTE UE Data Acquisition

In this experiment, a dataset was defined as a series of data captures corresponding to one particular choice of eNB experimental parameters. The data from each capture consisted of files acquired simultaneously from the DUT-UE diagnostic monitoring software (i.e., USRD), the UTG, and the VSA. A given dataset typically contained two captures with each of the 32 sets of non-eNB experimental parameters. Figure 4.1 shows schematically the files generated during each capture that are relevant to post-acquisition parsing and subsequent data analysis. A full list of parameters collected in this experiment can be found in Appendix B.

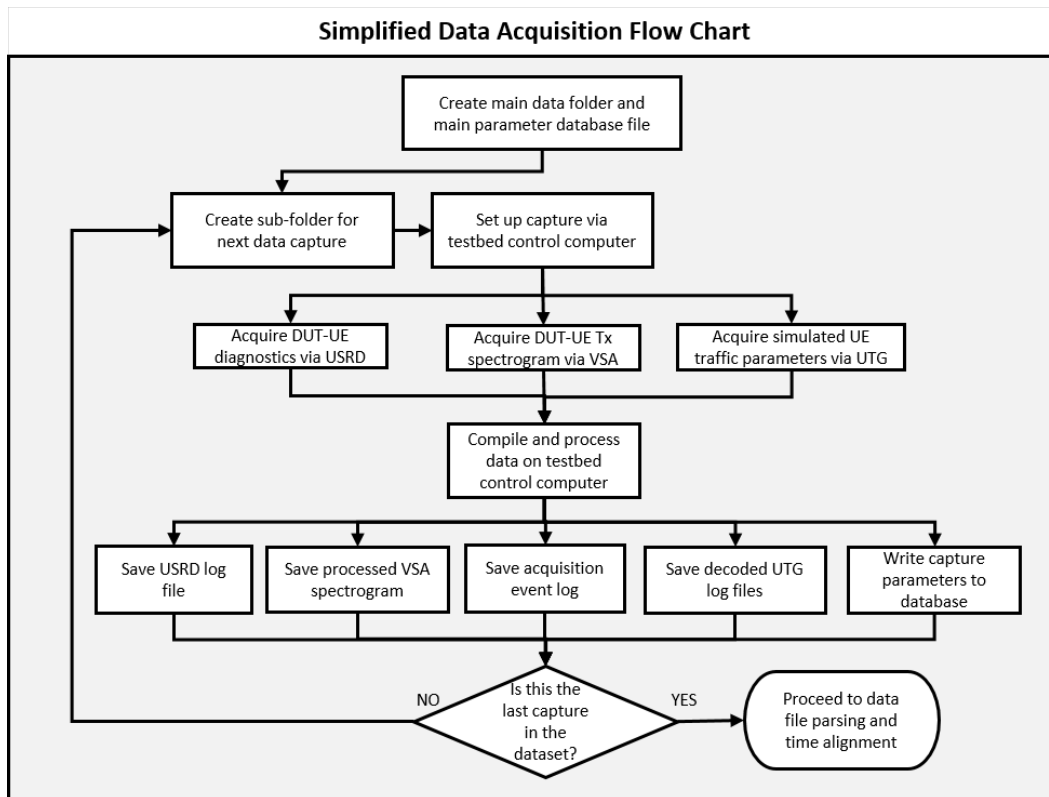


Figure 4.1: A simplified flow chart depicting the data files generated for each capture during acquisition of a dataset.

4.1.1 DUT Data Output

While some performance and RF status information is available to users, more detailed data is available through diagnostic access on the phone. The user data accessed includes qualitative information about LTE connection status and benchmark information about data throughput rate. The diagnostic logs for LTE stack provide more detailed RF and protocol status information, such as universal terrestrial access network (UTRAN) protocol messages, control and data traffic statistics, and RSRP estimated for each PRB. The test team obtained this information by software licensed from the chip-set manufacturer.

4.1.2 Data Output by the Traffic Generator

The UTG is capable of implementing and running different morphologies and configurations. As the UTG is emulating UEs in a particular configuration, several different parameters can be logged. These logs capture parameters from all layers of the network; from the physical layer through the application layer. Once the logs are collected, they can be used in troubleshooting or data analysis.

The UTG collects these logs in a binary format. Once the measurement has been concluded, the measurement files are converted to a comma separated value (CSV) format by use of software provided by the UTG manufacturer. Many of the logs available in the UTG were not enabled as they are outside the scope of this project.

The most relevant parameters collected were:

- Attached Loading UEs, Cell *A*
- Attached Loading UEs, Cell *B*
- Mean UEs Signalled per TTI (500 ms average)
- Mean PRBs Used (500 ms average), Cell *A*
- Mean PRBs Used (500 ms average), Cell *B*

4.2 Parsing and Spectrogram Analysis

Preliminary post-processing of the VSA spectrogram and decoding of the binary-format UTG data files were performed during acquisition. However, in order to minimize computer processing time on the testbed control computer, extraction and integration of the parameters of interest were performed by standalone parsing code in a separate step after the acquisition of each complete dataset.

The main task of post-acquisition processing was to automatically extract the particular parameters of interest from each data file and compile them in a format convenient for data analysis. For example, if the self-reported transmission power of the DUT-UE during a particular PUSCH subframe is to be compared against the measured power in the VSA spectrogram while a known number of simulated UEs simultaneously signal the eNB via the UTG, those parameters from the USRD log, the VSA spectrogram, and the UTG log must be compiled into tables of the same format with a shared time index. However, in this experiment, there was no hardware-based timing synchronization between between the different components of the test apparatus. As a result, the timestamps generated by each piece of equipment and attached to its reported parameter values were subject to inconsistencies between the on-board clocks—inconsistencies much larger than the 1 ms agreement required to align individual subframes. Hence, a key component of data parsing was to correct the timestamps in order to achieve time alignment between the parameters from different data files. An overview of the post-acquisition data file parsing and time alignment process is depicted in Figure 4.2. The details of individual processing steps are described later in section.

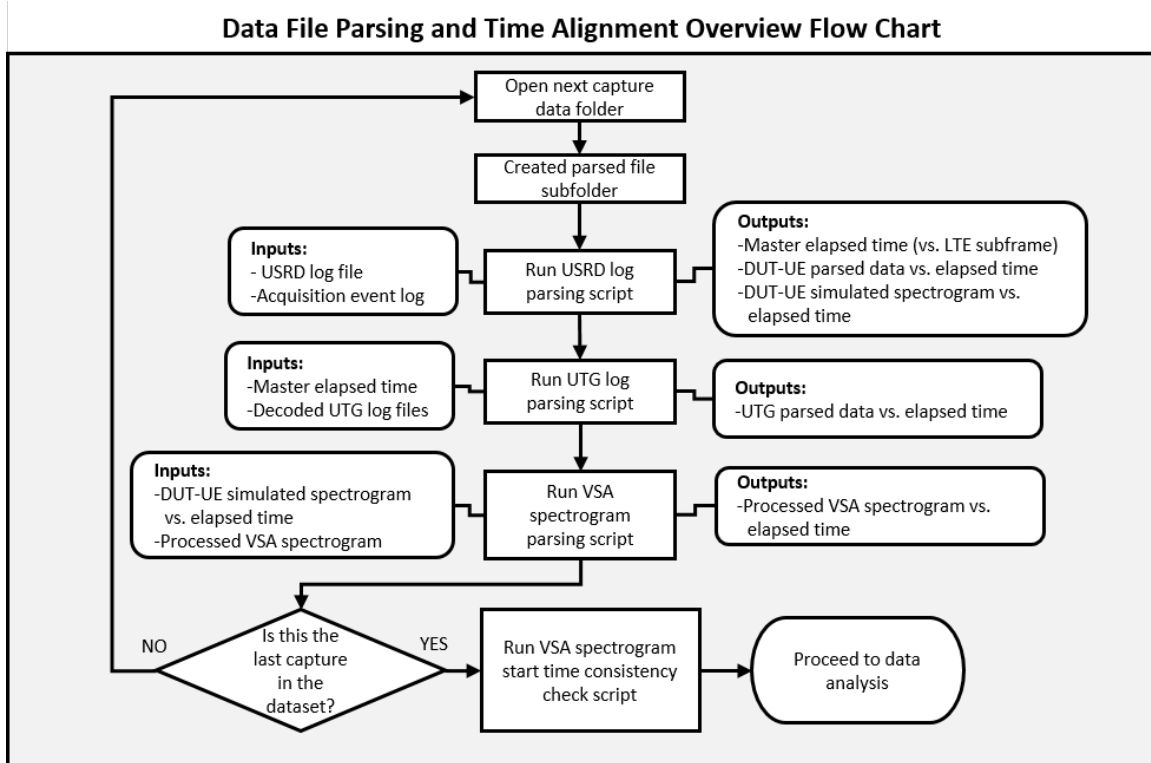


Figure 4.2: High-level flow chart of post-acquisition data file parsing and time alignment process.

4.2.1 DUT Diagnostic Monitoring Data Parsing

The first step in post-acquisition data file processing was to parse the DUT-UE diagnostic monitoring data (i.e., the USRD log file). The goal in parsing the USRD data was twofold: to assemble the data into a single table of DUT-UE self-reported parameter values organized chronologically, and to define a master relative elapsed time—based on a running count of LTE system frame and subframe numbers—that could be used to self-consistently align the USRD, VSA, and UTG data with one another.

During acquisition, the USRD log is saved in a database-like file format. Each entry in this database file is referred to as a "packet". A packet comes in one of many formats, depending on its contents, and contains UE-reported data corresponding to between 1 and 20 individual subframes. There were three main challenges encountered when trying to assemble the data chronologically and define the master elapsed time via subframe counting:

1. A single packet might contain data from up to 20 DUT-UE transmission subframes, but each packet as a whole has only a single timestamp. Because of this, there was often a high degree of uncertainty as to which reported combination of LTE system frame and subframe numbers corresponded to the packet timestamp.
2. There was occasional anomalous behavior in which the data from a DUT-UE transmission subframe seemed to have been held over from a previous capture and aggregated into a packet in the current capture. This further added to the ambiguity in the relationship between packet timestamps and the reported system frame and subframe numbers therein.
3. The packet timestamp behavior was often unpredictable. While the packet timestamps were mostly self-consistent across a given USRD log file—that is, timestamps from packets containing data from single consecutive subframes reliably differed by 1 ms—the set of timestamps as a whole was typically shifted by anywhere from a few seconds

to several minutes relative to the clock on the testbed control computer.

Addressing these challenges in a general way added considerable complexity to the USRD log file parsing process. Figure 4.3 shows the USRD file parsing procedure. The first step was to find a combination of timestamp, system frame number, and subframe number that could be used to define $t = 0$ in the master relative elapsed time. Due to issues (1) and (2) described above, care had to be taken to avoid selecting a packet timestamp that might be inconsistent with the system frame and subframe numbers in the rest of the log. To minimize this risk, the timestamp used for reference was selected to be the timestamp from the packet among the first 50 in the USRD log file that had the smallest non-zero total elapsed time between the packet timestamps of the previous and next chronologically neighboring packets. Selecting a reference timestamp closely surrounded in time by neighboring log entries reduces the chances of accidentally picking an outlier as the reference.

Once a suitable reference USRD packet timestamp was selected, however, there was still the problem of unpredictable timestamp offsets (i.e., issue (3) described above). To compensate for the unpredictable offset between the set of USRD packet timestamps and the clock on the testbed control computer, a correctional shift was applied to the timestamps in the USRD log such that the chosen reference timestamp was set to be the same as the testbed control computer acquisition log timestamp corresponding to the USRD initialization command. Once this correction was applied, the corrected reference USRD packet timestamp and its corresponding system frame and subframe numbers were defined as $t=0$ in the master relative elapsed time.

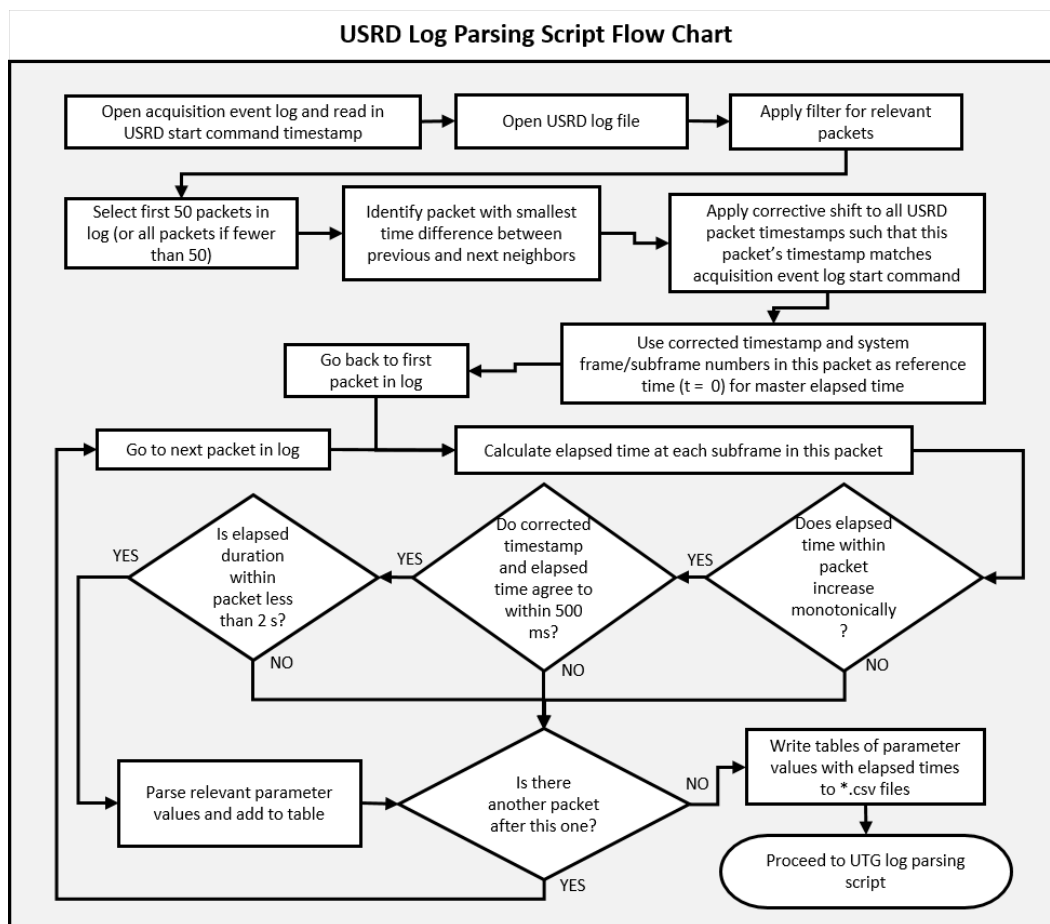


Figure 4.3: Flow chart of USRD log file parsing procedure.

After defining $t = 0$, the relevant parameters from each packet in the USRD log were parsed and assigned an elapsed time based on the reported system frame and subframe numbers. Note that the USRD log packets used here did not report an LTE hyperframe number. Hence, the combination of system frame and subframe numbers for a row of data within a packet did not, on its own, yield a unique elapsed time, since the system frame numbers recycle every 10.24 s. So, an artificial hyperframe number, defined as 0 at $t = 0$, was added to each system frame/subframe number combination in the USRD log by calculating the time difference between each packet timestamp and the reference packet timestamp and determining how many hyperframes (i.e., cycles of system frame numbers) should have elapsed in that time.

During early debugging, occasional cases were encountered in which the calculation of elapsed time resulted in data points being put in the wrong order. This typically occurred in cases where an outlying data point was held over in a packet (i.e., issue (2) described above), or during an interval in which DUT-UE uplink activity was particularly infrequent. To avoid such errors, log packets that showed any of the following were automatically omitted from parsed datasets:

- Non-monotonic elapsed time within the packet (i.e., calculation of elapsed time resulted in items within the packet being re-ordered)
- Large discrepancy between the approximate elapsed time according to the corrected packet timestamp and the elapsed time calculated from system frame/subframe number
- Excessive total duration between the first subframe and last subframe that were included in the packet

In practice, the USRD data from very few datapoints (less than 0.1 % of active DUT-UE subframes on average) were omitted based on these criteria in each dataset.

4.2.2 Traffic Generator Data Parsing and Time Alignment

The post-acquisition parsing of relevant parameters from the UTG logs in each capture was significantly simpler. UTG data were reported at 500 ms intervals. Data points were put into separate tables based on whether they came from the simulated UE traffic in the DUT-UE serving cell (Cell *A*), or the adjacent cell (Cell *B*). Each data point included a LTE system frame and subframe number, as well as a timestamp provided by the UTG on-board clock. To achieve time alignment, the elapsed time at each UTG reporting subframe was calculated relative to $t = 0$ as defined during USRD log parsing. Once again, LTE hyperframe was not reported, so the artificial hyperframe number was calculated based on the time difference between the UTG timestamp and the corrected reference timestamp at $t = 0$ — with the inclusion of the artificial hyperframe number, the unique elapsed time of each UTG datapoint with respect to the USRD parsed data was obtained. A flow chart of the UTG log file parsing process is shown in Figure 4.4.

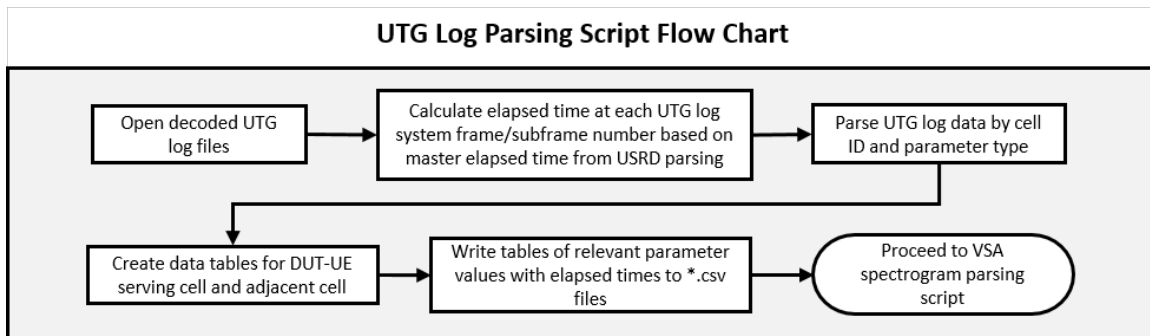


Figure 4.4: Flow chart of UTG log file parsing procedure.

4.2.3 Spectrogram Re-binning to LTE Resource Block and Subframe

Compared to the time and frequency grid defined by LTE resource blocks, spectrograms acquired by the signal analyzer are both 1) asynchronous in time and 2) oversampled in both time and frequency, with respect to LTE resource block time and frequency.

Post-processing the spectrogram must downsample the spectrogram into power bins that are aligned with LTE resource blocks. The acquisition and LTE time and frequency grids are illustrated in Figure 4.5. The post-processing for this transformation is made possible by a combination of oversampling and the assumption that the LTE data and control PRBs under study transmits in all resource elements (REs) in each PRB.

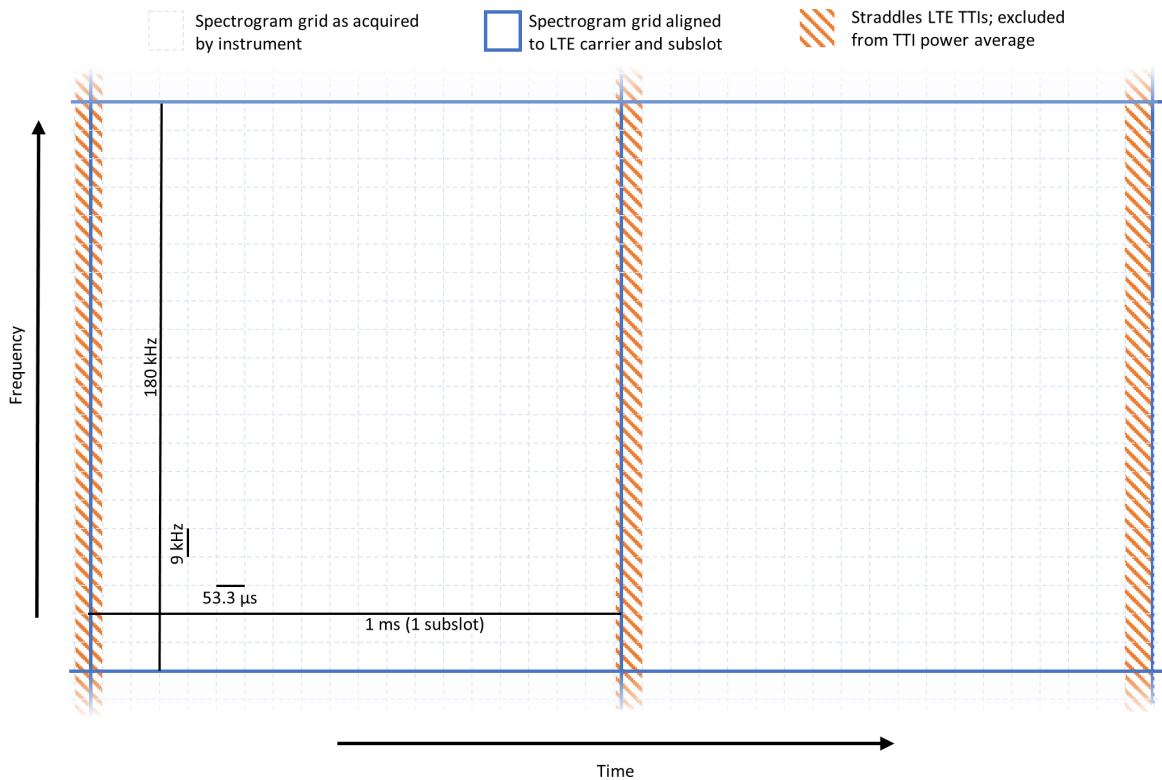


Figure 4.5: Grid of the acquired (dashed lines) and LTE-aligned (solid lines) spectrograms. The postprocessing procedure produces power averages in each LTE-aligned block of the spectrogram, consisting of all acquired data except the excluded orange dashed lines.

The eNB time base is tied to atomic clocks via Global Positioning System (GPS), and the signal analyzer uses its internal standard for time and frequency. The following assumes that the relative drift between these two time bases is negligible through the 5 s duration of each spectrogram, and that the two devices agree on the frequencies of the 50 LTE PRBs.

4.2.3.1 Re-binning in Time

The time grid is more complicated, because the instrument does not support alignment to the any integer divisor of the LTE TTI, which is 1 ms. The time resolution of the spectrogram acquired by the instrument is slightly greater than 18 compared to 1 TTI. The team resampled this in the power domain by making new time bins that are the average of

spectrogram time bins acquired during each TTI.

The average power computation in the LTE power bin rejects acquired spectrogram bins that cross a subframe boundary in time. This means that these bins represent “dead time,” in which energy detected by the instrument is not included in the measurement results. The average fraction of dead time in each LTE subframe is $0.75/18$ (4.2 %). In performing the averaging, the calculations assume that the average power during this dead time is equal to that of the remaining 95.8 % of the TTI. This is a source of error if the uplink waveform exhibits some other behavior. A worst-case error scenario is for the uplink transmit waveform turns off exactly during this dead time. In this case, replacing 4.2 % of the transmit power P_{tx} (linear units) with 0 suggests that the spectrogram overestimates the physical power by $-10 \log_{10}((P_{tx} - 0.042P_{tx})/P_{tx}) = 0.19$ dB.

Identifying the time bins to exclude from the power measurements is a minimum mean-squared error (MMSE) estimator.

4.2.3.2 Re-binning in Frequency

The signal analyzer is configured to align frequency acquisition to place exactly 20 frequency bins in each of the 50 PRBs.

The orthogonality realized by single-carrier frequency division multiple access (SC-FDMA) in each LTE uplink symbol is only coarsely visible in the spectrogram. Each SC-FDMA sub-carrier bleeds some energy into its neighboring frequency bin [12]. This is the expected behavior for SC-FDMA demodulation without carrier or time synchronization or LTE windowing functions. Because the victim receiver under study is not an SC-FDMA receiver, it is appropriate to show the energy that bleeds into neighboring frequency bins, because it will also not be synchronized to the LTE carrier, baseband timing, or windowing.

There is no frequency synchronization to correct for differences between the local oscillator (LO) frequencies of the eNB and signal analyzer. This produces slight imbalance between the energy that bleeds to the PRBs directly below and above any given active PRB. The bleeding serves to mitigate this effect, however. Since the bleeding is already at -13 dB (1 part in 20), the frequency output of the two LOs only need to agree to within 1 part in 400 in order to reduce errors to within ± 0.01 dB. Further, by Parseval’s relation, the average power integrated across frequency bins in the spectrogram is not affected by any imbalance.

An example of an acquired spectrogram is shown in Figure 4.6. The frequency domain is on the vertical axis, numbered by LTE resource block number; the time domain is the horizontal axis, in steps of one LTE subframe. The expected bleeding about 13 dB below the active PRBs is visible along the vertical axis. The energy in these spectrogram bins is physically present, but as expected, only a small fraction of the total energy received in each subframe.

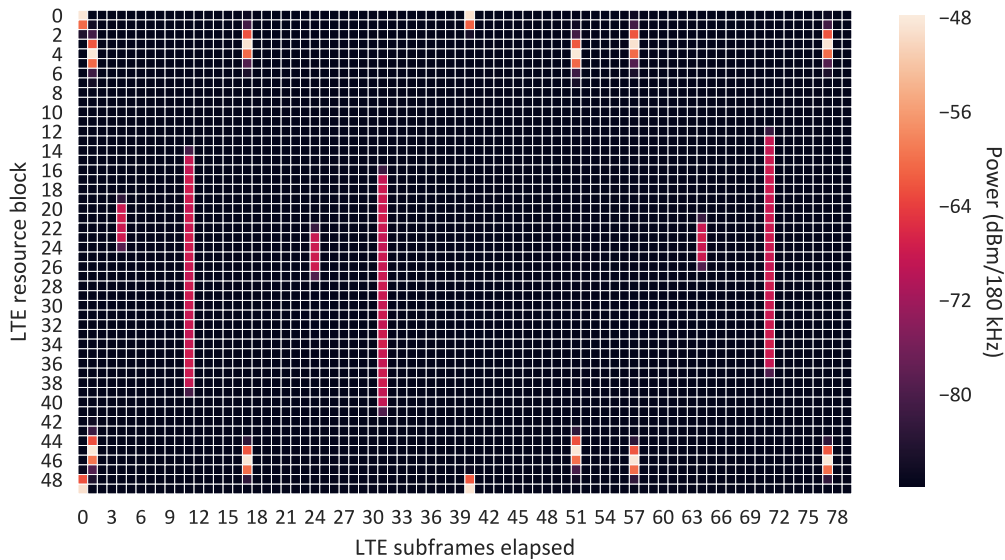


Figure 4.6: Example of spectrogram re-binned to the LTE time and frequency grid. The frequency domain bleeding between PRB is visible between active and inactive blocks.

4.2.3.3 Limitations

A full LTE measurement receiver that aligns to the UE clock and downconverts to IQ baseband waveforms is required for any future work that seeks to characterize features on the scale of LTE REs. Some potential use cases for this include

- statistics based on spectrogram data aligned to LTE symbols, currently 1/12 ms or 1/14 ms, and
- measurement of PRBs that mainly consist of symbols aligned at the beginning or end of the subframe.

The approach described in this section is impossible for these use cases because the required simultaneous oversampling in both time and frequency is forbidden by the Nyquist sampling theorem.

4.2.4 Spectrogram Timestamp Alignment

The final task in parsing the data from each capture was aligning the VSA spectrogram in time with the parsed USRD data (and thus with the UTG data as well). The processed VSA spectrogram that was saved for each capture during acquisition consisted of a two-dimensional matrix that was binned along the frequency axis into PRBs (180 kHz intervals) and along the time axis into subframes (1 ms intervals). However, the starting time of the VSA spectrogram relative to the clock on the acquisition control computer was subject to the unknown offset of the VSA on-board clock. In addition, because the VSA was not set up to synchronize with the LTE signal, LTE system frame and subframe numbers were not recorded in the spectrogram. Hence, the VSA spectrogram relative elapsed time could not simply be calculated from the reference USRD start time by use of system/subframe numbers in the manner of the USRD and

UTG data.

Instead, time alignment between the VSA spectrogram and the USRD parsed data was achieved by an image-matching method, which can be summarized as follows:

1. Assemble an approximate simulated spectrogram from the USRD-reported PRB allocation information. Each active PRB was given a power level equal to the USRD-reported total transmission power in that subframe divided by the number of PRBs. Inactive PRBs were assigned a power of 0 mW.
2. Pad the USRD simulated spectrogram in time with zeros at the beginning and end, in order to allow for the possibility that the VSA spectrogram began before or ended after the reported USRD data.
3. Perform a one-dimensional time-domain cross-correlation between the VSA spectrogram and the padded USRD simulated spectrogram.

The cross-correlation yielded an array of correlation values versus proposed starting time of the VSA spectrogram (relative to the USRD elapsed time); the VSA relative starting time of highest correlation was likely to be the position of time alignment between the VSA spectrogram and the USRD parsed data. Figure 4.7 shows a portion of an example USRD simulated spectrogram plotted next to a measured VSA spectrogram prior to aligning in time; Figure 4.8 shows portions of the simulated and measured spectrograms after time alignment.

While this simple algorithm would be sufficient to achieve subframe-level time alignment in the majority of cases, it was possible for the proposed VSA spectrogram start time of maximum correlation to be an erroneous solution. Because the duration of the acquired USRD data in a given capture was typically significantly longer than the duration of the VSA spectrogram, there were opportunities for the correlation value at a proposed VSA spectrogram start time outside of the actual overlap interval to be higher than the correlation at the true start time if, for example, the DUT-UE transmission power was significantly higher in some of the subframes in which USRD data was being recorded but the VSA spectrogram had not yet begun. Other potential correlation pitfalls occurred when the sequence of PRB allocations was highly periodic over time, when the DUT-UE transmissions were infrequent, or when the DUT-UE transmission power was particularly low.

To try to avoid false-positive time alignment, several redundancies and diagnostics were built into the VSA spectrogram parsing/alignment routine. These include:

- **Image correlation with both raw and normalized spectrograms.** In addition to the cross-correlation calculated using the as-measured power levels in the processed VSA spectrogram, a repeat cross-correlation was run using a normalized version of the VSA spectrogram in which the power in each PRB in each active subframe was divided by the maximum PRB power in that subframe. A discrepancy in the VSA spectrogram proposed start times of maximum correlation between the raw and normalized versions triggered additional alignment verification steps.
- **Testing the uniqueness of the proposed VSA start time solution.** In cases where the sequence of PRB allocations was highly periodic over time, multiple proposed VSA start times with very similar correlation values were possible; the maximum correlation point may not have been a unique solution. If the next-highest correlation value exceeded 99.9% of the highest value, the 10 highest-correlation possible VSA spectrogram start times were all tested as proposed solutions.
- **Checking the amount of spread in measured VSA spectrogram power versus USRD-reported power.** The total DUT-UE transmission power that was reported by USRD in a given subframe was given in integer dBm increments. At each discrete USRD-reported transmission power, there was a range of total power measured in the corresponding active PRBs in the VSA spectrogram. Because the USRD-reported PRB allocations were used to identify the active PRBs in the VSA spectrogram, erroneous time alignment between the USRD parsed data and the VSA spectrogram generally resulted in a much larger spread (i.e., the ratio between the maximum and minimum values) in the measured VSA spectrogram power at each given USRD-reported transmission power value than the

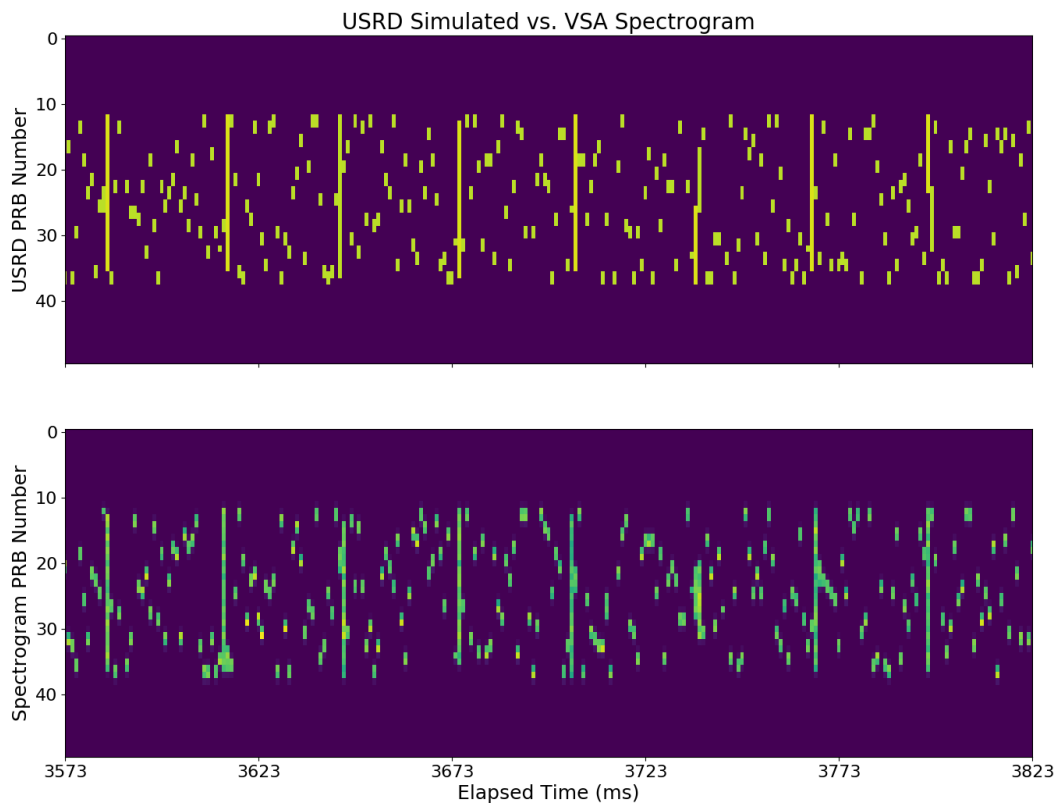


Figure 4.7: (Top) A portion of a simulated spectrogram constructed from DUT UE self-reported PRB allocations (via USRD); (bottom) a portion of the measured VSA spectrogram (on a mW power scale) from the same capture, prior to time alignment with the USRD data.

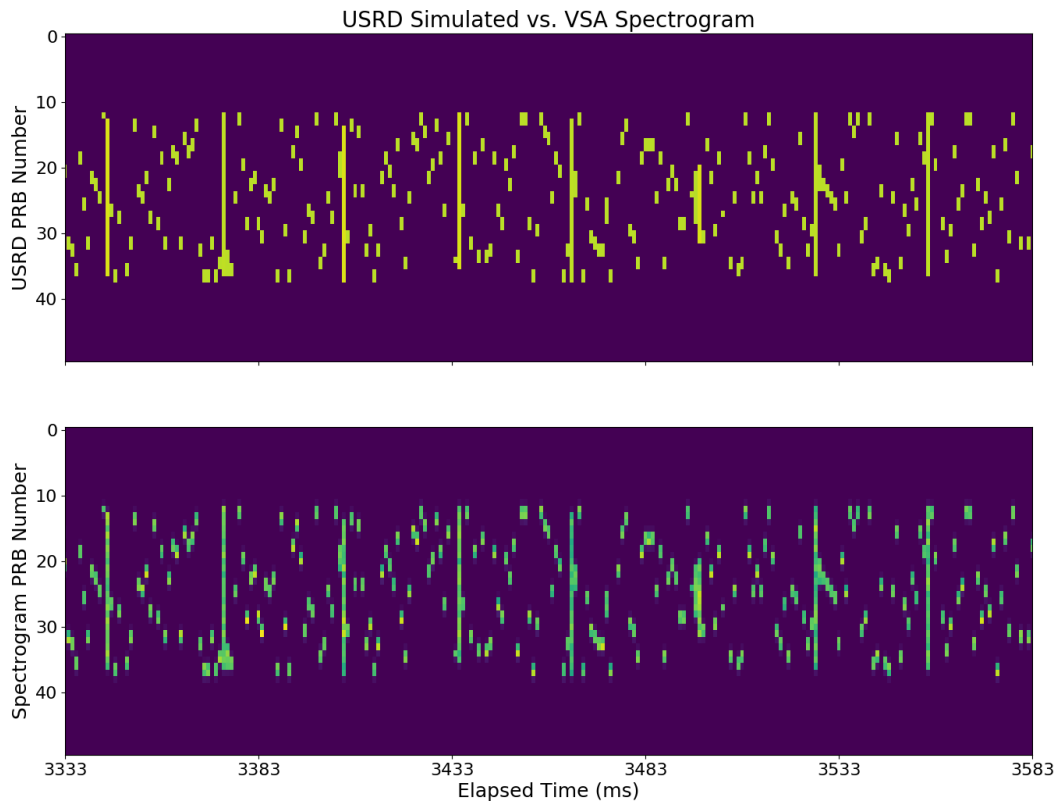


Figure 4.8: (Top) Portion of a simulated spectrogram constructed from DUT UE self-reported PRB allocations (via USRD); (Bottom) Portion of the measured VSA spectrogram (on a mW power scale) from the same capture, after time alignment with the USRD data.

spread in properly time-aligned data. Therefore, the maximum spread in VSA power among the USRD-reported power levels in a capture was a useful time alignment diagnostic; a maximum spread larger than 3 dB triggered additional alignment verification steps. If no VSA relative start time was found that passed the power spread test, or if multiple start times passed the power spread test, the capture was flagged as having ambiguous time alignment. Figure 4.9 shows a typical plot of USRD-reported transmission power versus measured VSA spectrogram power without proper alignment in time; Figure 4.10 shows data from a capture after time alignment.

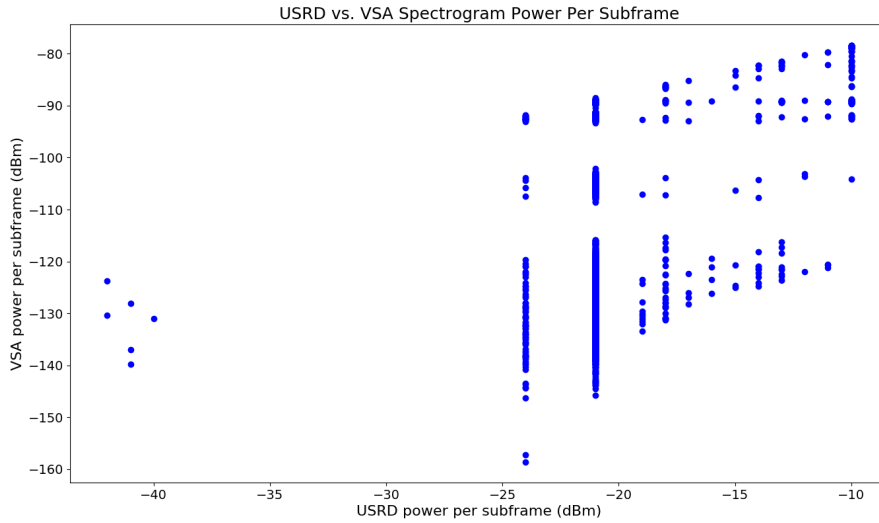


Figure 4.9: DUT UE self-reported transmission power (via USRD) versus total power in corresponding PRBs in the measured VSA spectrogram, without alignment in time between the VSA and USRD. The largest spread in measured VSA power at a given USRD power is nearly 60 dB (at a reported USRD power of -21 dBm).

Once the best relative start time for the VSA spectrogram was found, a column of elapsed time based on this starting time was added to the VSA spectrogram file so that it shared a common time index with both the USRD and the UTG parsed data files. A flow chart of the steps followed during the alignment of each VSA spectrogram capture is shown in Figure 4.11.

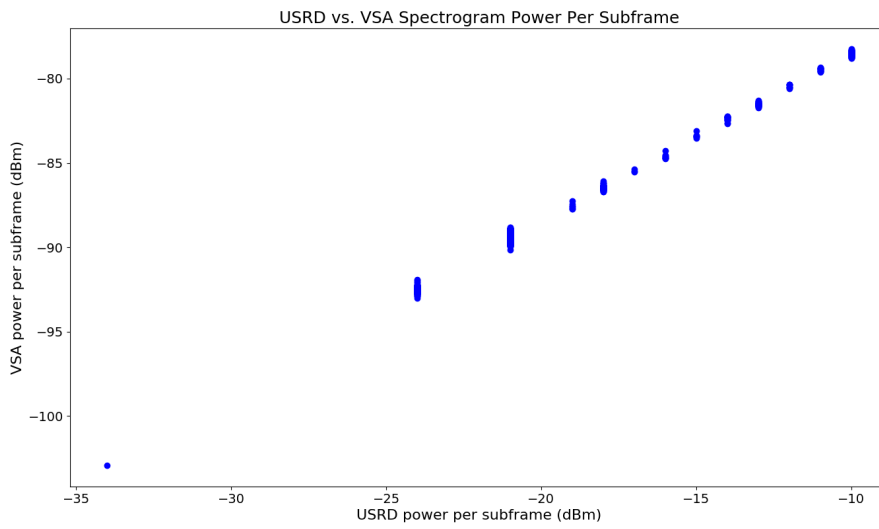


Figure 4.10: DUT UE self-reported transmission power (via USRD) versus total power in corresponding PRBs in the measured VSA spectrogram, after alignment in time between the VSA and USRD. The largest spread in measured VSA power at a given USRD power is less than 2 dB (at a reported USRD power of -21 dBm).

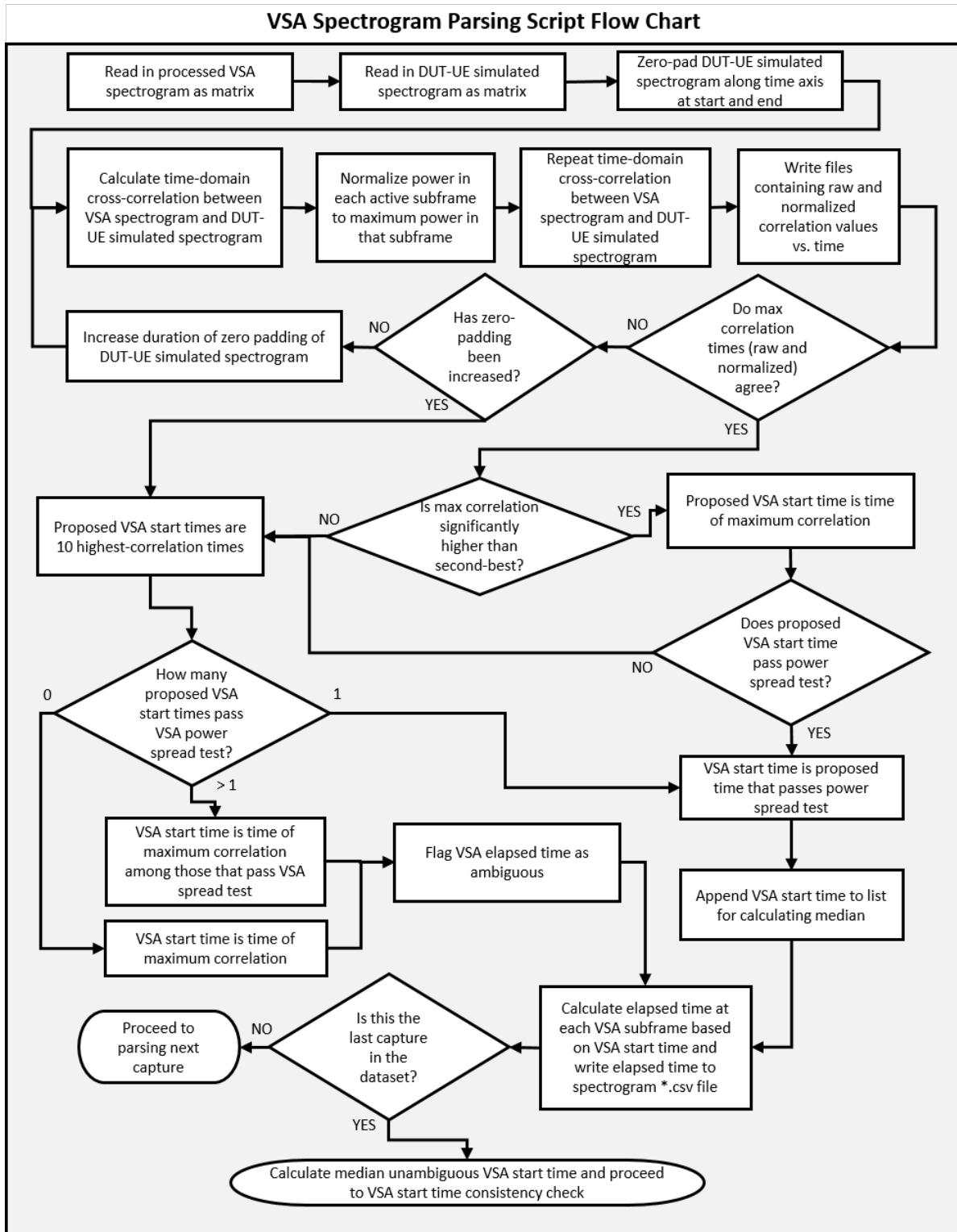


Figure 4.11: Flow chart of VSA spectrogram time alignment procedure.

4.2.5 Time Alignment Consistency Checks

Due to variations in the time between DUT-UE transmissions, the time required for the DUT-UE to initially attach to the eNB, and other variability in the timing of hardware and software operations with different test conditions, some scatter was to be expected in the start time of the VSA spectrogram relative to the USRD log. However, because the nominal time between control computer commands was intended to be the same during the acquisition of each capture, the relative VSA spectrogram start times were not likely to differ by more than one second or so across a given dataset. So, once each complete dataset was parsed, an additional check was performed to verify that the VSA spectrogram start times were consistent with one another. First, the median relative VSA time-aligned spectrogram start time was calculated from among the captures in which the time alignment had not been flagged as ambiguous. Then, in each capture that either (a) was flagged as ambiguous during parsing, or (b) resulted in a VSA spectrogram relative start time that fell outside of the median ± 600 ms, an additional check was performed. In this check, the proposed VSA spectrogram start times with the 10 highest correlation values that were within 600 ms of the dataset median were subjected to the VSA spectrogram power spread test. If exactly one VSA spectrogram proposed start time within this interval passed the power spread test, this proposed start time was used to calculate the elapsed time index for the VSA spectrogram. If no VSA spectrogram proposed start time within this interval passed the power spread test, or if multiple start times passed, the capture was flagged as having ambiguous time alignment. A flow chart depicting the VSA spectrogram start time consistency check is shown Figure 4.12

A complete round of testing, which included all of the experimental configurations, consisted of on the order of 2000 data captures. The portion flagged as having ambiguous time alignment by the automated parser was less than 1%. After parsing, each flagged capture was subjected to human inspection to determine whether the VSA spectrogram elapsed time solution found by the parser was valid, and whether there were anomalies in the measurement that contributed to the ambiguity. Once this manual data review step was complete, the parsed and time-aligned data in each dataset were aggregated into a summary for further evaluation and analysis.

4.3 Data Aggregation and Cleaning

The power from active PRBs in the shared channel was extracted from VSA measurements of the UE emissions by first identifying occupied bands at the aligned time using the diagnostic software self report after the time alignment procedure. The self report contains a resource block start and number of resource blocks allocated. This information is used to extract the power in resource blocks of interest from the processed (time aligned) VSA spectrogram. The power in each active PRB is summed and divided by the number of active PRBs to give a mean measured power per PRB. The mean self reported power per PRB was calculated by dividing the total transmitted power by the number of active PRBs.

After extracting the mean self reported power and measured power from parsed data captures of shared channel activity, the data were aggregated and linked to the appropriate eNB and non-eNB states excluding any capture that was flagged as having a major parsing exception. Three major exceptions were excluded from the aggregated dataset. The first major parsing exception is triggered when active TTIs during the overlap time were missed by the UE diagnostic software. The second major exception is an incomplete coverage of VSA spectrogram duration by the UE diagnostic software. The final exception is ambiguous time alignment between the VSA and UE diagnostic software report.

As a final processing step, summary statistics, consisting of 99 percentiles, were estimated for the measured and reported power per PRB. The percentiles comprised a general, but succinct, description of the distribution shape that was used for the inferential data analysis presented in Chapter 7.

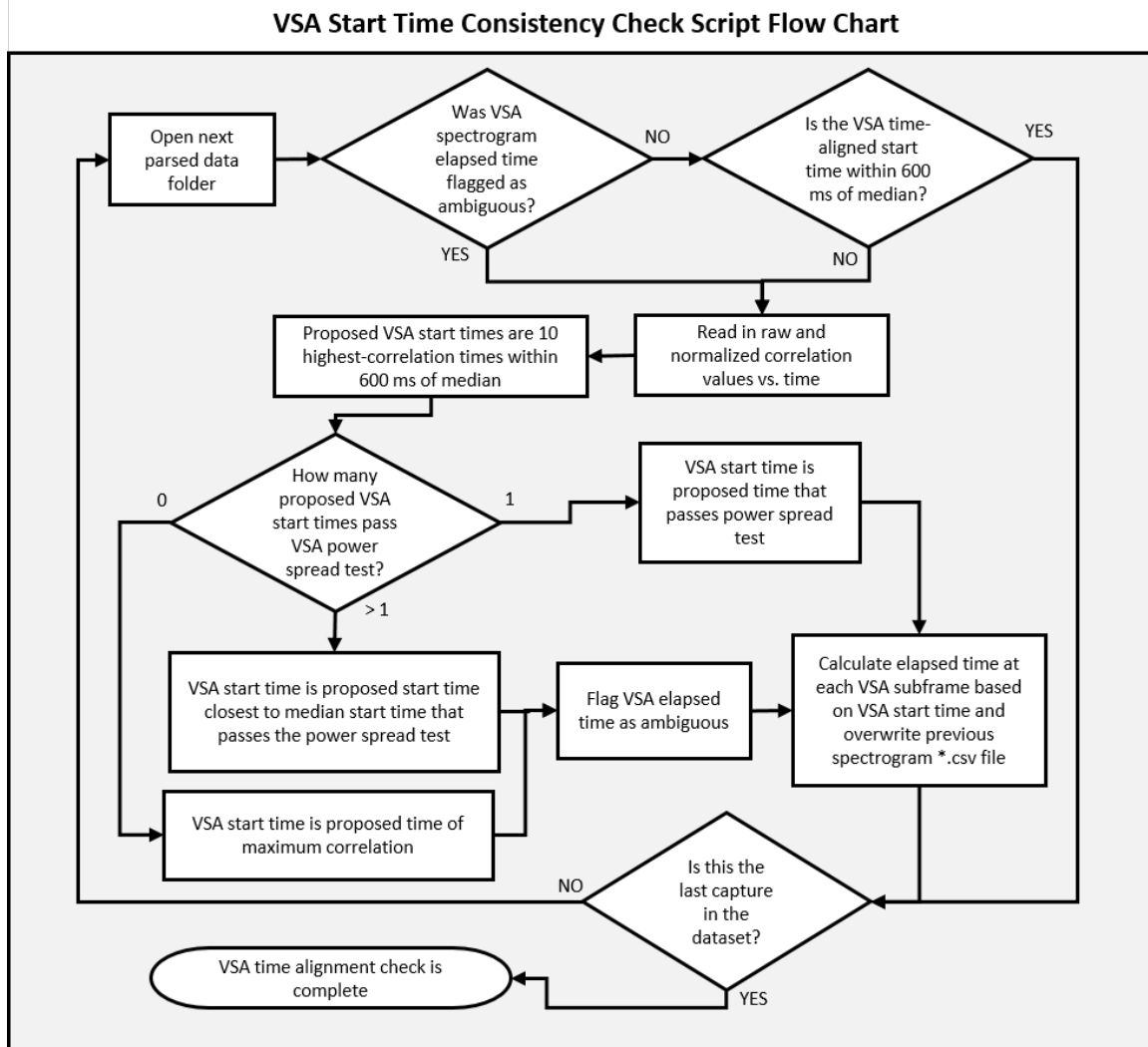


Figure 4.12: Flow chart of VSA spectrogram starting time consistency check procedure.

Chapter 5

Experimental Design

5.1 Statistical Design

5.1.1 Overview

A summary list of the controlled experimental factors (or variables) considered is shown in Table 5.1. Overall, there were 28 factors: eight non-eNB factors (shown in green) and 20 for the eNB (shown in gray). Two settings (levels) were specified for most factors, except for the scheduling factors, I and J, for which three categorical settings were specified. Details on the factor settings are provided later in this chapter.

Because the goal of the factor screening experiment was to determine which factors had the most influence on the response, it was important to ensure that estimates of main effects due to individual factors were uncorrelated (i.e., orthogonal). Namely, main effects were not allowed to be confounded with other main effects. However, to enable an efficient design that would screen a large number of factors with a practical number of tests (runs), main effects were allowed to be confounded with effects due to interactions between two or more factors. This approach is typical in screening designs [6, 7].

Two additional considerations played key roles in the design. First, because eNB factor changes required much more time than non-eNB factor changes, the NASCTN test team sought a design that minimized the number of eNB configuration changes. For this reason, the test team chose a split-plot design that is well-suited to experiments with hard-to-change factors [6, 7]. Specifically, the design was organized into 32 groups of 32 tests each, where each group of tests had the same eNB configuration and consisted of the same set of 32 non-eNB factor configurations.

A second important design consideration arose from the fact that not all combinations of settings were possible for five eNB factors (i.e., I, J, L, M, and X) due to eNB configuration constraints, as described in section 2.1. Because I and J were three-level factors, and L, M, and X were two-level factors, there would ideally have been $3^2 \times 2^3 = 72$ possible setting combinations among these factors. However, only 20 setting combinations were possible. This issue was addressed by incorporating 16 of the valid setting combinations for I, J, L, M, and X into a single 16-level factor, called Ω .¹ This choice enabled the construction of an orthogonal design with a practical number of eNB test configurations (runs).

Following good experimental practice, the fundamental principles of randomization, replication, and blocking were employed [6, 7]. Specifically, to alleviate the influence of uncontrolled factors, the 32 eNB configuration groups were tested in a random order and the 32 non-eNB configurations were tested in a different random order for each eNB configuration. Also, to improve estimates of experimental variability, and consequently, to increase the power to detect real effects, four replicates of the design were collected, i.e., the entire design was repeated four times (two times for each of the two UEs). Finally, to improve experimental precision, the eNB design was organized into eight blocks, where each block was executed with one of two UEs (same model, different serial numbers); details are provided

¹The four excluded combinations corresponded to the $(I, J) = (0, 1)$ case, which was covered by tests of the default eNB configuration.

Table 5.1: Factor List

Identifier	Testbed Component	Factor	# Levels	
A	Variable Attenuator	Path Loss (Simulated DUT UE Position)	2	
B	UTG	Spatial Size of Cell	2	
C	UTG	Number of Loading UEs in Serving Cell (Cell A)	2	
D	UTG	Number of Loading UEs in Adjacent Cell (Cell B)	2	
E	UTG	Spatial Distribution of Loading UEs in Cell A	2	
F	UTG	QCI Value of Loading UEs	2	
G	DUT UE/UTG	Traffic Data Rate	2	
H	DUT UE/UTG	Traffic Type (UDP/TCP)	2	
I	*	eNB	UL Scheduling Algorithm Type	3
J	*	eNB	UL Scheduler FD Type	3
K		eNB	Power Control Type (Closed Loop/Open Loop)	2
L	*	eNB	SRS Config	2
M	*	eNB	SRS Offset	2
N		eNB	PUCCH Power Control: P_0	2
O		eNB	PUSCH Power Control: P_0	2
P		eNB	Power Control: α	2
Q		eNB	Receive Diversity	2
R		eNB	Filter coefficient for RSRP measurements	2
S		eNB	Maximum uplink transmission power (own cell)	2
T		eNB	Minimum PRB allocation for power-limited UEs	2
U		eNB	UL Improved Latency Timer Reaction	2
V		eNB	Initial Max # of Resource Blocks	2
W		eNB	Outer Loop Link Adaptation	2
X	*	eNB	Uplink link adaptation	2
Y		eNB	Cell Scheduling Request Periodicity	2
Z		eNB	Scheduling Weight UL for SRS	2
a		eNB	Blanked PUCCH Resources	2
b		eNB	Target UL Outer Scheduling	2

* These five factors were grouped together as factor Ω .

in section 5.2. (The blocks used for keeping track of experimental runs are not the same as the blocking variables described in Chapter 7.) This arrangement captured experimental variability due to UE serial number and physical placement of the UE, but kept the conditions within each block homogeneous with respect to these nuisance factors.²

To monitor testbed stability and repeatability, a test with a default eNB configuration was executed at the start of every test day. Namely, all 32 runs of the non-eNB design were tested with the default eNB configuration.

5.1.2 Technical Details

The overall design consisted of a 32-run design for the eNB factors crossed with a 32-run design for the non-eNB factors. As mentioned above, to minimize the number of eNB configuration changes, a split-plot design was used.

The 32-run non-eNB design tested eight two-level factors. For this design, the test team selected a resolution IV fractional factorial design, denoted 2_{IV}^{8-3} . Resolution IV means that main effects are not confounded with two-factor interactions, but two-factor interactions can be confounded with other two-factor interactions [6, 7]. This design is

²In experimental design terminology, a nuisance factor may influence the experimental response, but is not of direct interest [6].

shown in Table 5.2, where each row denotes a different non-eNB factor configuration and the -1 and $+1$ values are labels for the two-factor levels. The specific settings for the non-eNB factor levels are given in section 5.3.

Table 5.2: Experimental design for the non-eNB factors.

Configuration	A	B	C	D	E	F	G	H
1	-1	-1	-1	-1	-1	-1	1	-1
2	1	-1	-1	1	-1	-1	-1	1
3	-1	-1	-1	1	1	-1	1	1
4	1	-1	-1	-1	1	-1	-1	-1
5	-1	-1	-1	1	-1	1	-1	-1
6	1	-1	-1	-1	-1	1	1	1
7	-1	-1	-1	-1	1	1	-1	1
8	1	-1	-1	1	1	1	1	-1
9	-1	1	-1	-1	-1	-1	-1	1
10	1	1	-1	1	-1	-1	1	-1
11	-1	1	-1	1	1	-1	-1	-1
12	1	1	-1	-1	1	-1	1	1
13	-1	1	-1	1	-1	1	1	1
14	1	1	-1	-1	-1	1	-1	-1
15	-1	1	-1	-1	1	1	1	-1
16	1	1	-1	1	1	1	-1	1
17	-1	-1	1	-1	-1	-1	-1	-1
18	1	-1	1	1	-1	-1	1	1
19	-1	-1	1	1	1	-1	-1	1
20	1	-1	1	-1	1	-1	1	-1
21	-1	-1	1	1	-1	1	1	-1
22	1	-1	1	-1	-1	1	-1	1
23	-1	-1	1	-1	1	1	1	1
24	1	-1	1	1	1	1	-1	-1
25	-1	1	1	-1	-1	-1	1	1
26	1	1	1	1	-1	-1	-1	-1
27	-1	1	1	1	1	-1	1	-1
28	1	1	1	-1	1	-1	-1	1
29	-1	1	1	1	-1	1	-1	1
30	1	1	1	-1	-1	1	1	-1
31	-1	1	1	-1	1	1	-1	-1
32	1	1	1	1	1	1	1	1

Using the R software package ‘FrF2’ [13], the non-eNB design was constructed so that the following two-factor interactions were estimable and not confounded with other two-factor interactions: AG, BG, CG, EG, FG, AC, CE, CF. These unconfounded, “clear” two-factor interactions were selected based on technical judgement and the aim of maximizing the number of clear two-factor interactions between A, C, E, F, and G. The two-factor interaction aliasing relations for the design are: AB=EH, AD=EF, AE=FD=BH, AF=ED, AH=EB, FB=DH, FH=BD, e.g., AB is confounded by EH.

The 32-run eNB design tested fifteen two-level factors and one 16-level factor, named Ω , that was used to code 16 valid combinations of I, J, L, M, and X, as explained earlier. The design is a mixed-level, orthogonal array, denoted OA(32, $2^{15}16^1$), obtained by deleting one column from the standard OA(32, $2^{16}16^1$) design [14, 15]. Because it is a strength 2 orthogonal array, this design has resolution III [14, p. 281], implying that main effects are confounded with two-factor interactions, but not with other main effects [6].

The eNB design is shown in Table 5.3, where each row denotes a different eNB factor configuration. In this table,

levels for two-level factors are labeled with -1 and $+1$ and levels for the 16-level factor, Ω , are labeled with integers between 0 and 15. Table 5.4 gives the mapping between levels of Ω and the levels of I, J, L, M, and X. Here, levels for the three-level factors I and J are labeled as -1 , 0, and $+1$, respectively, and factors that are not applicable are indicated by “N/A.” Applying this mapping yields the expanded design shown in Table 5.5. The specific settings for the eNB factor levels are provided in section 5.3.

Table 5.3: Experimental design for the eNB factors.

Configuration	K	N	O	P	Q	R	S	T	U	V	W	Y	Z	a	b	Ω
1	-1	-1	-1	-1	-1	-1	-1	-1	-1	-1	-1	-1	-1	-1	-1	0
2	1	-1	-1	-1	-1	-1	-1	-1	-1	1	1	1	1	1	1	8
3	1	-1	-1	-1	-1	1	1	1	1	-1	-1	-1	-1	1	1	4
4	-1	-1	-1	-1	-1	1	1	1	1	1	1	1	1	-1	-1	12
5	1	-1	-1	1	1	-1	-1	1	1	-1	-1	1	1	-1	-1	2
6	-1	-1	-1	1	1	-1	-1	1	1	1	1	-1	-1	1	1	10
7	-1	-1	-1	1	1	1	1	-1	-1	-1	-1	1	1	1	1	6
8	1	-1	-1	1	1	1	1	-1	-1	1	1	-1	-1	-1	-1	14
9	-1	-1	1	-1	1	-1	1	-1	1	-1	1	-1	1	-1	1	1
10	1	-1	1	-1	1	-1	1	-1	1	1	-1	1	-1	1	-1	9
11	1	-1	1	-1	1	1	-1	1	-1	-1	1	-1	1	1	-1	5
12	-1	-1	1	-1	1	1	-1	1	-1	1	-1	1	-1	-1	1	13
13	1	-1	1	1	-1	-1	1	1	-1	-1	1	1	-1	-1	1	3
14	-1	-1	1	1	-1	-1	1	1	-1	1	-1	-1	1	1	-1	11
15	-1	-1	1	1	-1	1	-1	-1	1	-1	1	1	-1	1	-1	7
16	1	-1	1	1	-1	1	-1	-1	1	1	-1	-1	1	-1	1	15
17	-1	1	-1	-1	1	-1	1	1	-1	-1	1	1	-1	1	-1	15
18	1	1	-1	-1	1	-1	1	1	-1	1	-1	-1	1	-1	1	7
19	1	1	-1	-1	1	1	-1	-1	1	-1	1	1	-1	-1	1	11
20	-1	1	-1	-1	1	1	-1	-1	1	1	-1	-1	1	1	-1	3
21	1	1	-1	1	-1	-1	1	-1	1	-1	1	-1	1	1	-1	13
22	-1	1	-1	1	-1	-1	1	-1	1	1	-1	1	-1	-1	1	5
23	-1	1	-1	1	-1	1	-1	1	-1	-1	1	-1	1	-1	1	9
24	1	1	-1	1	-1	1	-1	1	-1	1	-1	1	-1	1	-1	1
25	-1	1	1	-1	-1	-1	-1	1	1	-1	-1	1	1	1	1	14
26	1	1	1	-1	-1	-1	-1	1	1	1	1	-1	-1	-1	-1	6
27	1	1	1	-1	-1	1	1	-1	-1	-1	-1	1	1	-1	-1	10
28	-1	1	1	-1	-1	1	1	-1	-1	1	1	-1	-1	1	1	2
29	1	1	1	1	1	-1	-1	-1	-1	-1	-1	-1	-1	1	1	12
30	-1	1	1	1	1	-1	-1	-1	-1	1	1	1	1	-1	-1	4
31	-1	1	1	1	1	1	1	1	1	1	-1	-1	-1	-1	-1	8
32	1	1	1	1	1	1	1	1	1	1	1	1	1	1	1	0

Table 5.4: Mapping between levels for Ω and I, J, L, M, and X.

Ω	I	J	L	M	X
0	-1	1	-1	N/A	-1
1	-1	1	-1	N/A	1
2	-1	1	1	-1	1
3	1	1	1	-1	-1
4	1	1	1	-1	1
5	-1	1	1	1	1
6	1	1	1	1	-1
7	1	1	1	1	1
8	0	-1	-1	N/A	-1
9	0	-1	-1	N/A	1
10	0	-1	1	-1	1
11	0	-1	1	1	1
12	0	0	-1	N/A	-1
13	0	0	-1	N/A	1
14	0	0	1	-1	1
15	0	0	1	1	1

Table 5.5: Expanded experimental design for the eNB factors including constrained factors.

Configuration	I	J	K	L	M	N	O	P	Q	R	S	T	U	V	W	X	Y	Z	a	b
1	-1	1	-1	-1	N/A	-1	-1	-1	-1	-1	-1	-1	-1	-1	-1	-1	-1	-1	-1	-1
2	0	-1	1	-1	N/A	-1	-1	-1	-1	-1	-1	-1	-1	1	1	-1	1	1	1	1
3	1	1	1	1	-1	-1	-1	-1	-1	1	1	1	1	-1	-1	1	-1	-1	1	1
4	0	0	-1	-1	N/A	-1	-1	-1	-1	1	1	1	1	1	1	-1	1	1	-1	-1
5	-1	1	1	1	-1	-1	-1	1	1	-1	-1	1	1	-1	-1	1	1	1	-1	-1
6	0	-1	-1	1	-1	-1	-1	1	1	-1	-1	1	1	1	1	1	-1	-1	1	1
7	1	1	-1	1	1	-1	-1	1	1	1	1	-1	-1	-1	-1	-1	1	1	1	1
8	0	0	1	1	-1	-1	-1	1	1	1	1	-1	-1	1	1	1	-1	-1	-1	-1
9	-1	1	-1	-1	N/A	-1	1	-1	1	-1	1	-1	1	-1	1	1	-1	1	-1	1
10	0	-1	1	-1	N/A	-1	1	-1	1	-1	1	-1	1	1	-1	1	1	-1	1	-1
11	-1	1	1	1	1	-1	1	-1	1	1	-1	1	-1	-1	1	1	-1	1	1	-1
12	0	0	-1	-1	N/A	-1	1	-1	1	1	-1	1	-1	1	-1	1	1	-1	-1	1
13	1	1	1	1	-1	-1	1	1	-1	-1	1	1	-1	-1	1	-1	1	-1	-1	1
14	0	-1	-1	1	1	-1	1	1	-1	-1	1	1	-1	1	-1	1	-1	1	1	-1
15	1	1	-1	1	1	-1	1	1	-1	1	-1	-1	1	-1	1	1	1	-1	1	-1
16	0	0	1	1	1	-1	1	1	-1	1	-1	-1	1	1	-1	1	-1	1	-1	1
17	0	0	-1	1	1	1	-1	-1	1	-1	1	1	-1	-1	1	1	1	-1	1	-1
18	1	1	1	1	1	1	-1	-1	1	-1	1	1	-1	1	-1	1	-1	1	-1	1
19	0	-1	1	1	1	1	-1	-1	1	1	-1	-1	1	-1	1	1	1	-1	-1	1
20	1	1	-1	1	-1	1	-1	-1	1	1	-1	-1	1	1	-1	-1	-1	1	1	-1
21	0	0	1	-1	N/A	1	-1	1	-1	-1	1	-1	1	-1	1	1	-1	1	1	-1
22	-1	1	-1	1	1	1	-1	1	-1	-1	1	-1	1	1	-1	1	1	-1	-1	1
23	0	-1	-1	-1	N/A	1	-1	1	-1	1	-1	1	-1	-1	1	1	-1	1	-1	1
24	-1	1	1	-1	N/A	1	-1	1	-1	1	-1	1	-1	1	-1	1	1	-1	1	-1
25	0	0	-1	1	-1	1	1	-1	-1	-1	-1	1	1	-1	-1	1	1	1	1	1
26	1	1	1	1	1	1	1	-1	-1	-1	-1	1	1	1	1	-1	-1	-1	-1	-1
27	0	-1	1	1	-1	1	1	-1	-1	1	1	-1	-1	-1	-1	1	1	1	-1	-1
28	-1	1	-1	1	-1	1	1	-1	-1	1	1	-1	-1	1	1	1	-1	-1	1	1
29	0	0	1	-1	N/A	1	1	1	1	-1	-1	-1	-1	-1	-1	-1	-1	-1	1	1
30	1	1	-1	1	-1	1	1	1	1	-1	-1	-1	-1	1	1	1	1	1	-1	-1
31	0	-1	-1	-1	N/A	1	1	1	1	1	1	1	1	-1	-1	-1	-1	-1	-1	-1
32	-1	1	1	-1	N/A	1	1	1	1	1	1	1	1	1	1	-1	1	1	1	1

5.2 Test Execution

The test matrix summarizing the overall execution plan is shown in Table 5.6. For reasons explained in subsection 5.1.1, the overall design was independently repeated over four rounds, with each round divided into eight blocks. Each block was executed with one of two UEs, which were the same model but with different serial numbers, as indicated in the test matrix. Note that every UE change required physically re-positioning the UE in the test chamber, which added variability to the measurement.

The same random order of eNB test configurations was used for Rounds 1 & 2, and Rounds 3 & 4, respectively, with the UE swapped for each block. This arrangement ensured that both UEs were tested twice with every eNB configuration. For each eNB configuration, the full 32-run non-eNB design was executed in a randomized order. Due to issues arising from unstable test configurations or problems with the testbed, it was necessary to retest some eNB configurations in each round. Consequently, retests were executed out of the preplanned order shown in Table 5.6.

To support a review of testbed stability, at the start of every test day, a test with the default eNB configuration was carried out for the full 32-run non-eNB design. For Rounds 1 & 3, the default tests used UE #1, whereas Rounds 2 & 4 used UE #2.

Table 5.6: Test matrix for factor screening experiment.

Round 1			Round 2			Round 3			Round 4		
Block	Run Order	eNB Config									
1	UE #1		1	UE #2		1	UE #1		1	UE #2	
	1	32		1	32		1	27		1	27
	2	22		2	22		2	3		2	3
	3	6		3	6		3	23		3	23
	4	3		4	3		4	16		4	16
2	UE #2		2	UE #1		2	UE #2		2	UE #1	
	5	16		5	16		5	31		5	31
	6	11		6	11		6	25		6	25
	7	30		7	30		7	19		7	19
	8	7		8	7		8	5		8	5
3	UE #1		3	UE #2		3	UE #1		3	UE #2	
	9	14		9	14		9	17		9	17
	10	8		10	8		10	11		10	11
	11	28		11	28		11	7		11	7
	12	17		12	17		12	9		12	9
4	UE #2		4	UE #1		4	UE #2		4	UE #1	
	13	5		13	5		13	4		13	4
	14	29		14	29		14	32		14	32
	15	21		15	21		15	24		15	24
	16	25		16	25		16	15		16	15
5	UE #1		5	UE #2		5	UE #1		5	UE #2	
	17	31		17	31		17	2		17	2
	18	27		18	27		18	8		18	8
	19	26		19	26		19	21		19	21
	20	19		20	19		20	1		20	1
6	UE #2		6	UE #1		6	UE #2		6	UE #1	
	21	15		21	15		21	10		21	10
	22	1		22	1		22	12		22	12
	23	23		23	23		23	13		23	13
	24	2		24	2		24	14		24	14
7	UE #1		7	UE #2		7	UE #1		7	UE #2	
	25	4		25	4		25	28		25	28
	26	18		26	18		26	6		26	6
	27	24		27	24		27	29		27	29
	28	13		28	13		28	20		28	20
8	UE #2		8	UE #1		8	UE #2		8	UE #1	
	29	9		29	9		29	30		29	30
	30	20		30	20		30	18		30	18
	31	10		31	10		31	26		31	26
	32	12		32	12		32	22		32	22

5.3 Factor Settings

The eNB and non-eNB factor settings are shown in Table 5.7. The settings were selected to maximize the response effect for each factor. However, these settings may produce cases that aren't found in the real-world, it should help increase the chance of observing a difference in emissions, should one be caused by a given factor.

Each factor used by the eNB and non-eNB has a set of values and limits to choose from. These values may simply be enabling or disabling a factor or numerical upper and lower boundary limits. Some factors also had a hard dependency on other factors (e.g., SRS offset is dependent on SRS being enabled). These dependent factors require that other factors be configured in order to have meaning. The factors that have dependencies on other experimental factors are shown in Table 5.4. This table outlines all realizable combinations of the factors I, J, L, M, and X. These dependencies were found by reviewing the eNB's documentation and empirical testing. Aside from the numerical limits of each factor, values had to be selected that would still allow for UEs to attach, be scheduled for resources, and send/receive data.

Challenges were encountered in overcoming all of the above mentioned limitations while keeping the factor limits far enough apart to see their effect on the UEs's uplink power. To do so, the hard dependencies were resolved first and then balanced with the values of the other factors to create a functional system with large differences between and low and high factors settings. The most challenging limitation was to balance between path loss, alpha, UE maximum power, nominal PUCCH and PUSCH powers.

Table 5.8 lists settings of controlled nuisance factors that were not of direct interest. These factors had to be changed from their default settings in order to configure the other 20 screened eNB factors. Descriptions of these factors can be found in section 2.2.

Table 5.7: Design Factor Settings

ID	Testbed Component	Factor	# Levels	Low Value (-1)	Int. Value (0)	High Value (+1)	Default Value
A	Variable Attenuator	Path Loss (Simulated DUT UE Position, dB)	2	0	X	20	N/A
B	UTG	Spatial Size of Cell (m)	2	100	X	1000	N/A
C	UTG	Number of Loading UEs (Cell A)	2	4	X	52	N/A
D	UTG	Number of Loading UEs (Cell B)	2	4	X	52	N/A
E	UTG	Spatial Distribution of Loading UEs in Cell A	2	Near eNB	X	Cell edge	N/A
F	UTG	Traffic QCI (Loading UEs)	2	100 % 9	X	25 % 5; 75 % 9	N/A
G	DUT UE/UTG	Traffic Data Rate	2	194 kbit/s/UE	X	388 kbit/s/UE	N/A
H	DUT UE/UTG	Traffic Type (UDP/TCP)	2	All UDP	X	All TCP	N/A
I	eNB	UL Scheduling Method	3	Interference Aware	Channel Unaware	Channel Aware	Channel Unaware
J	eNB	UL Scheduler FD Type	3	Round Robin	Exhaustive	Mixed	Mixed
K	eNB	UL Power Control Method*	2	Closed-Loop	X	Open-Loop	Open-Loop
L	eNB	SRS	2	Deactivated	X	Activated	Deactivated
M	eNB	SRS Power Offset (dBm)	2	0	X	15	7
N	eNB	PUCCH P0 (dBm)	2	-117	X	-96	-117
O	eNB	PUSCH P0 (dBm)	2	-85	X	24	-85
P	eNB	Alpha	2	0.5	X	1	0.8
Q	eNB	Receive Diversity	2	Deactivated	X	Activated	Activated
R	eNB	RSRP Filter Coefficient	2	"fc0"	X	"fc19"	"fc4"
S	eNB	Max. UL Transmit Power/UE (dBm)	2	0	X	24	23
T	eNB	Minimum PRB Allocation (Power Limited UEs)	2	1	X	50	3
U	eNB	UL Improved Latency Reaction Timer	2	0	X	2000	0
V	eNB	Initial # of UL PRBs	2	1	X	50	10
W	eNB	Outer Loop Link Adaptation	2	Deactivated	X	Activated	Activated
X	eNB	UL Link Adaptation	2	eUILa	X	fUILa	eUILa
Y	eNB	SRS UL Scheduling Weight	2	1	X	100	10
Z	eNB	Scheduling Request Periodicity	2	20	X	80	20
a	eNB	Blanked PUCCH Resources	2	0	X	10	0
b	eNB	Target UL Outer Scheduling	2	Lower Edge	X	None	None

*Applies to both PUSCH and PUCCH

Table 5.8: Controlled Nuisance Factor Settings

ID	Collateral Factor	Test Case Value	Default Value
aa	Inter-Cell Interference Coordination	X	Off
bb	Cell Size	X	Large
cc	Max. number of UEs per TTI	X	14
dd	Activate PUSCH PRBs Masking	X	Off
ee	Maximum Uplink Packet Aggregation	1	2
ff	PRACH Frequency Offset during Attach	12	7
gg	Number of PRBs reserved for CQI	13	6

Chapter 6

Exploratory Data Analysis

This chapter presents exploratory graphical plots that illustrate noteworthy aspects of these observations. It can be viewed as a complement to the formal statistical analyses presented in Chapter 7. In addition to highlighting notable examples of LTE system performance, this chapter contains plots indicating the overall span of the laboratory observations, and presents an investigation into the agreement between measured EIRP and UE-reported uplink transmission power. Data underlying all of the plots in this chapter are publicly-available at <https://doi.org/10.18434/M32130>.

As explained in section C.4, the conversion factor between measured VSA spectrogram power and DUT EIRP was found to be $61.8 \text{ dB} \pm 2.3 \text{ dB}$. This factor was used to make all of the measured EIRP plots presented here.

6.1 Data Verification Plots

A key step of the experimental workflow was data verification, which included checks for parsing and time-alignment failures, missing data, and acquisition anomalies. To aid the data verification process, software was developed to automatically produce a 294 page “data summary packet” for each 32-run test of an eNB configuration. The data summary packets were inspected manually to identify anomalous or unusual results. When a problem was identified, the affected eNB configuration was flagged for retesting.

In addition to being useful for data verification, the plots produced for the summary packets lend insight into LTE system performance. Examples of the different types of data summary plots are given in Figures 6.1-6.6. These plots summarize results for a test of non-eNB configuration #19 with the default eNB configuration that was collected in Round 4 of the experiment on 1/24/2019. The settings for this test are summarized in Table 6.1; see section 5.3 for the full list of default eNB settings. Figures 6.1-6.6 are shown only to give an example of the types of plots contained in the summary data packets.

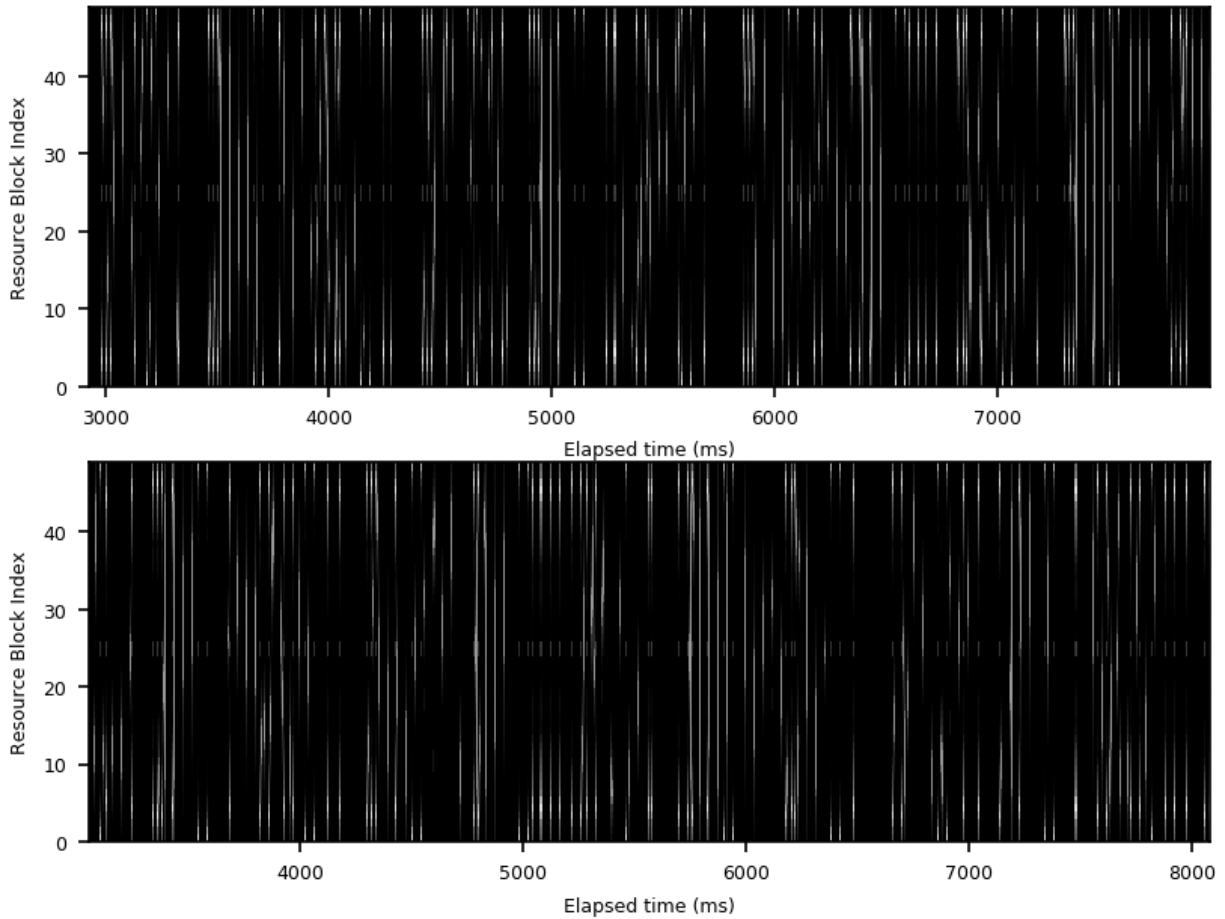


Figure 6.1: Example VSA spectrogram captures. Grayscale range: $[-58, 23]$ dBm.

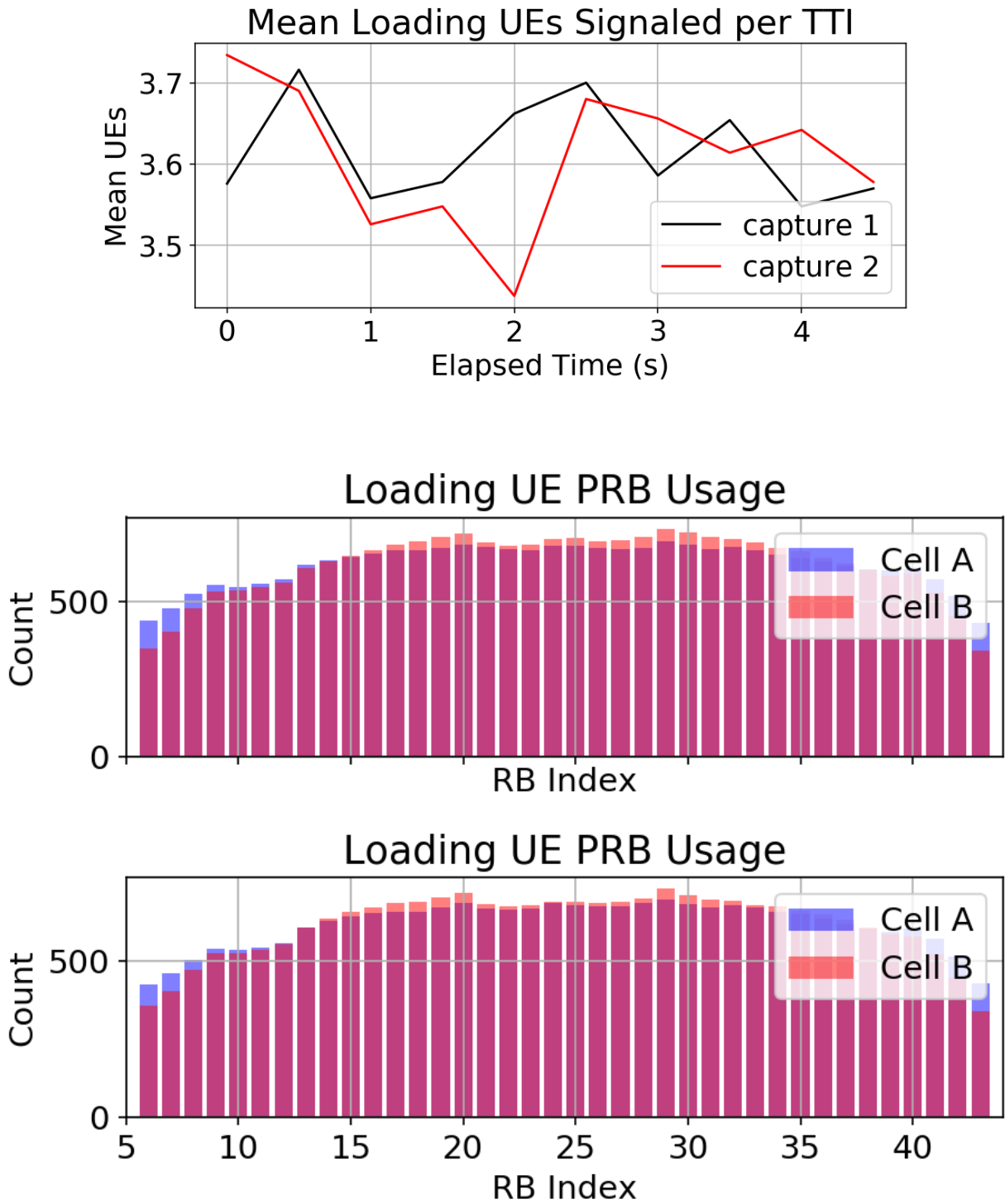


Figure 6.2: Example loading UE activity time-series (Top) and PUSCH PRB allocation distributions (Bottom) for the two captures. Note: The PUSCH PRB usage values are reported by the UTG as 500 ms averages.

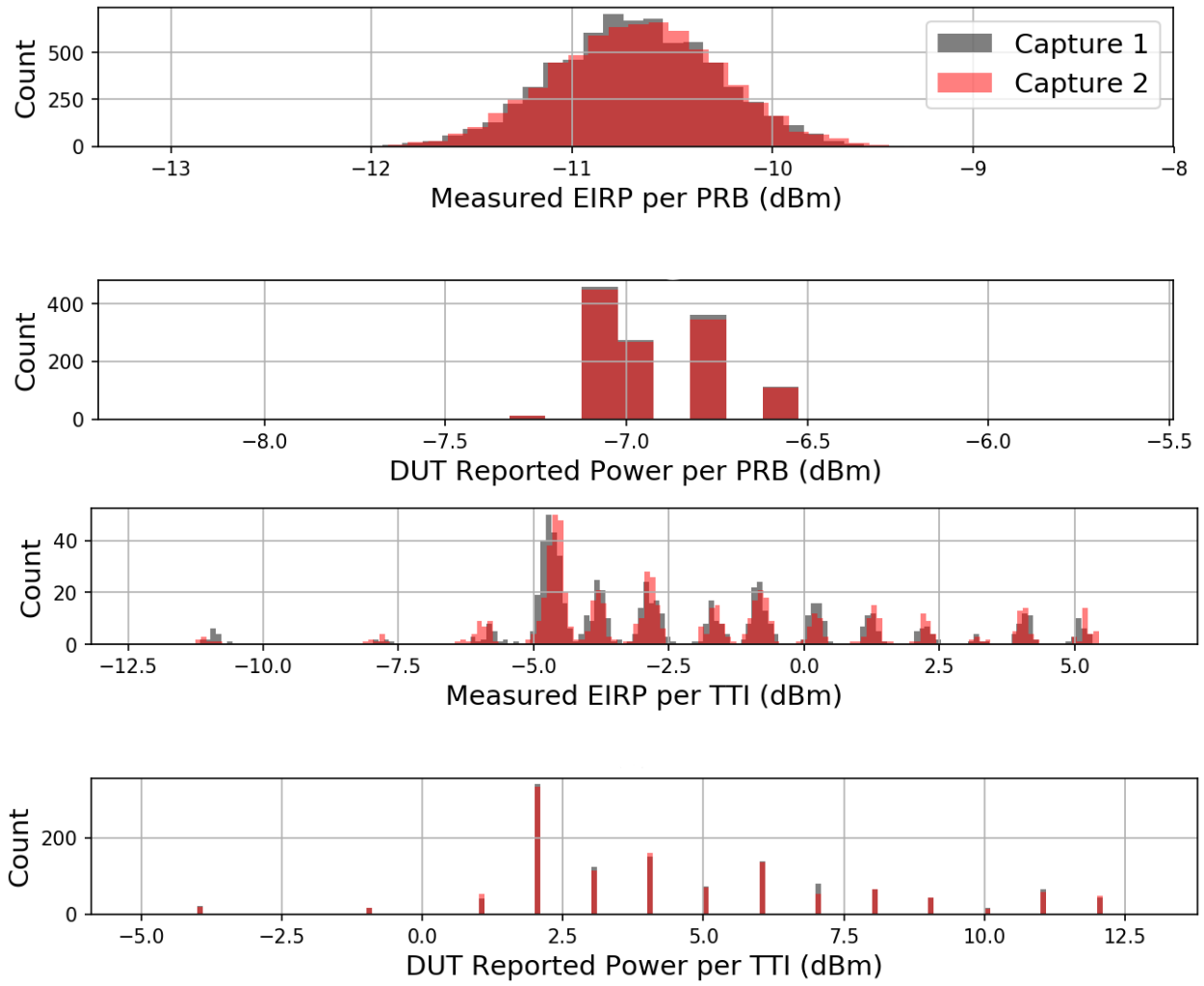


Figure 6.3: Example PUSCH Power histograms.

Table 6.1: Settings for the example plots in section 6.1 (default eNB configuration, non-eNB configuration #19).

Factor	Setting
Path Loss Attenuation	0 dB
Spatial Size of Cell	100 m
Number of Loading UEs in Cell A	52
Number of Loading UEs in Cell B	52
Spatial Distribution of Loading UEs in Cell A	Cell Edge
QCI Value of Loading UEs	100 % 9
Traffic Data Rate	194 kbit/s/UE
Traffic Type	TCP
PUSCH Power Control Type	Open-Loop
PUSCH Power Control: P_0	-85 dBm
PUCCH Power Control: P_0	-117 dBm
Fractional Power Control: α	0.8

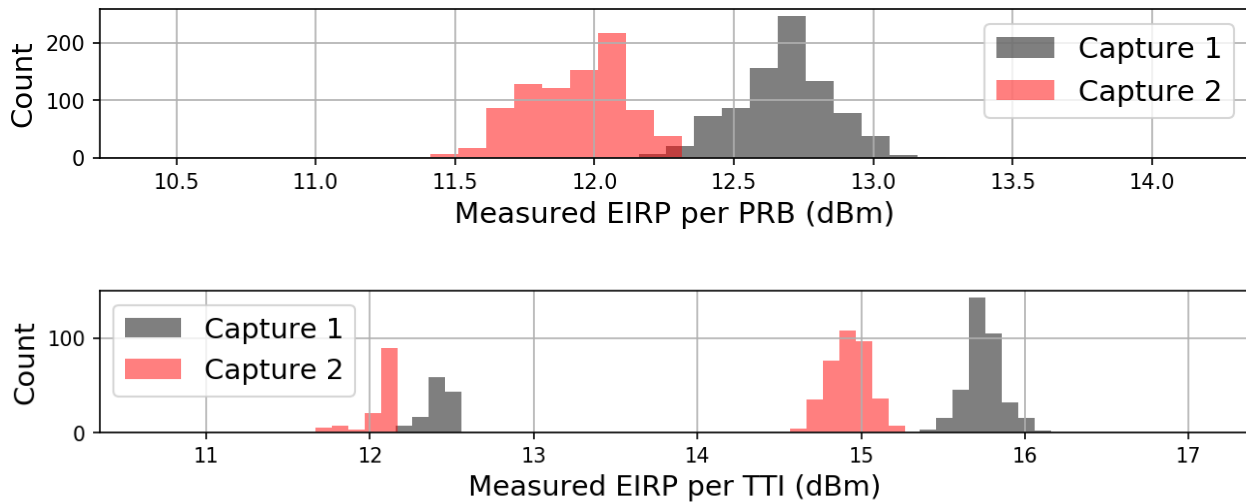


Figure 6.4: Example PUCCH Power histograms.

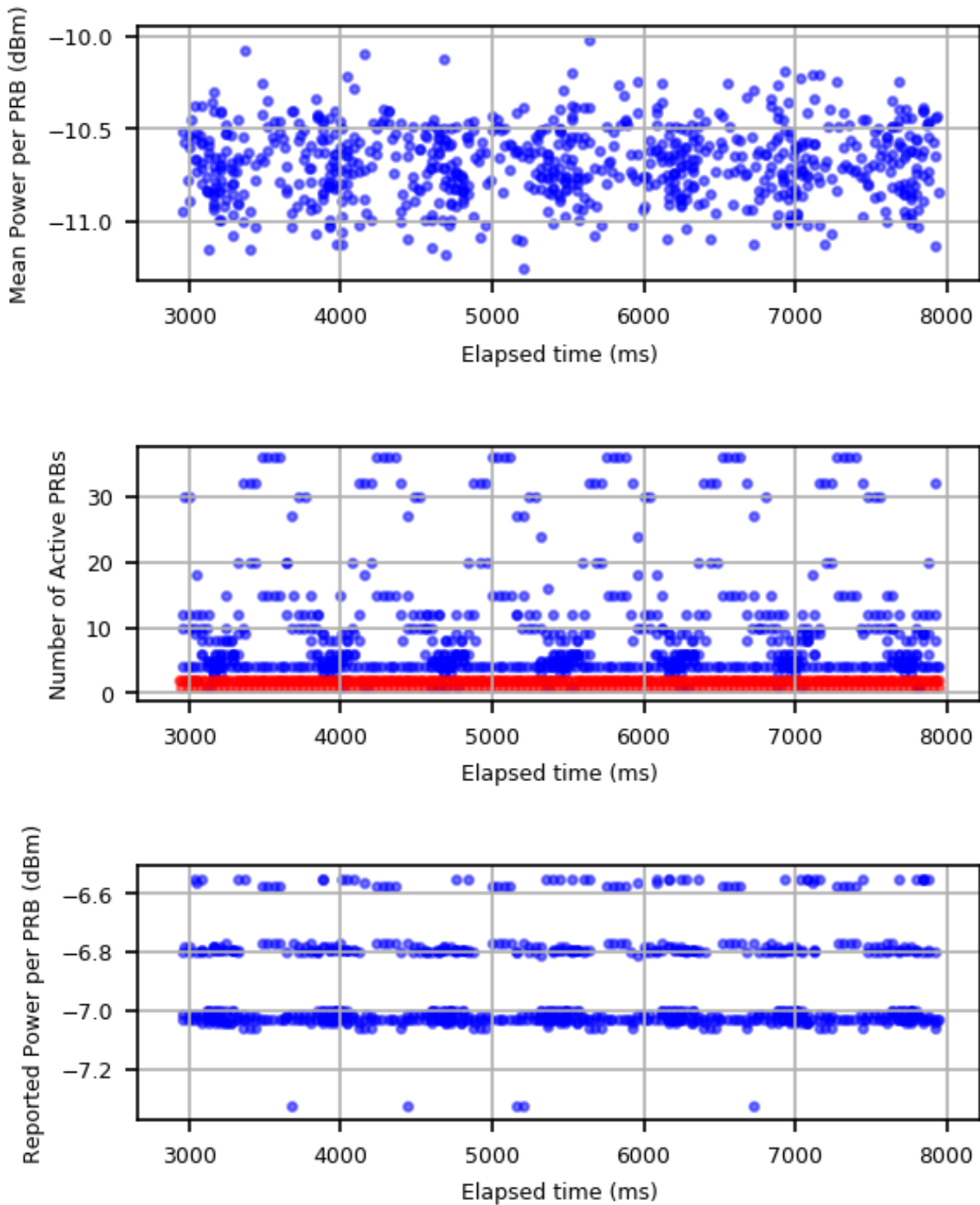


Figure 6.5: Example time-series plots. Top: Mean measured PUSCH EIRP per PRB. Middle: Number of active PRBs for PUSCH (blue) and PUCCH (red). Bottom: DUT-reported power per PRB.

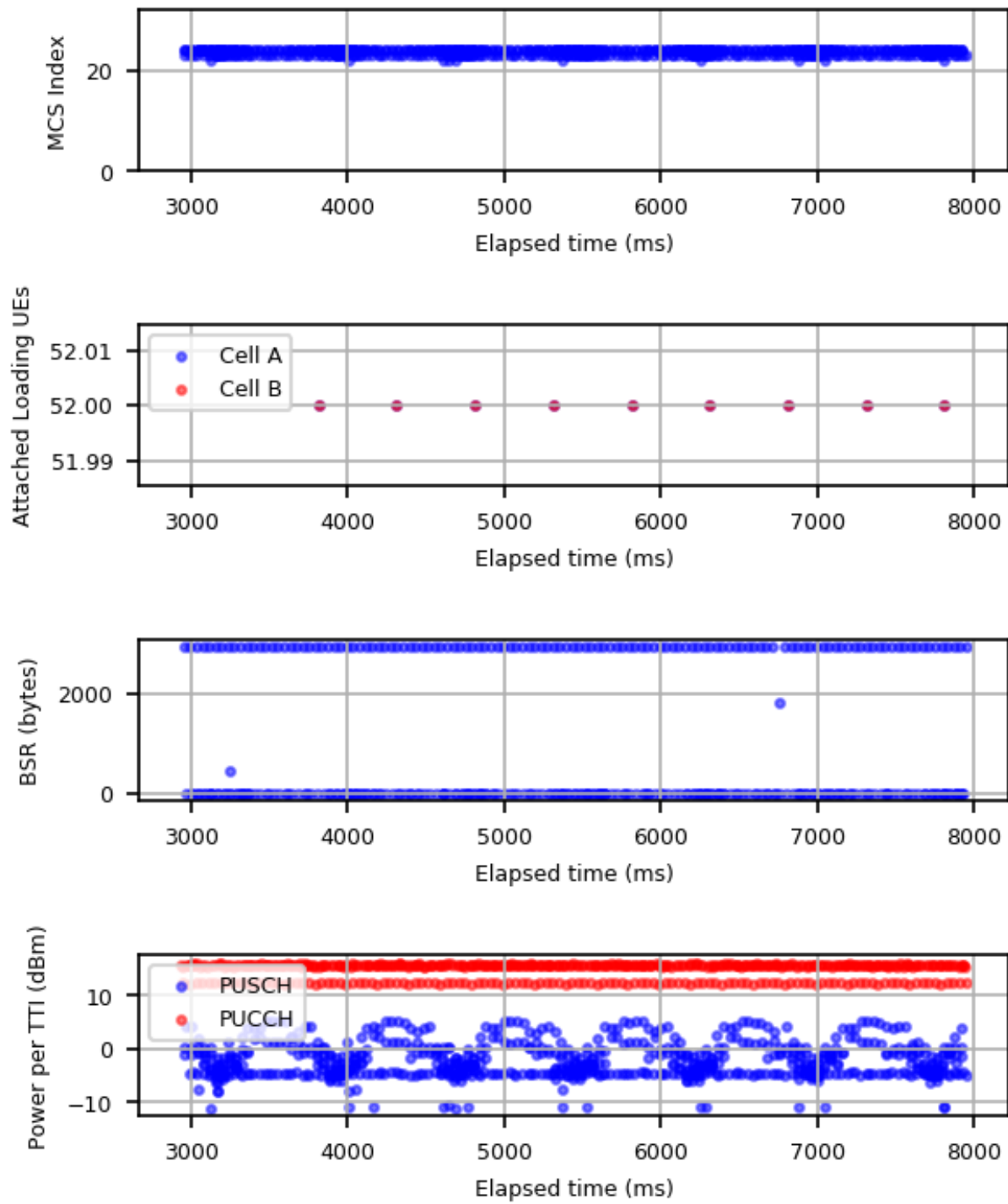


Figure 6.6: Example time-series plots. Top: MCS Index. Upper-Middle: Number of attached loading UEs. Lower-Middle: BSR. Bottom: Measured EIRP per TTI.

6.2 Notable Examples

This section presents several test examples that illustrate the richness of data collected by the experiment and provide insight into important aspects of LTE systems. In particular, these examples demonstrate situations that may be of interest for modeling LTE uplink emissions. All of the example results were collected during Round 4 of the experiment.

6.2.1 Power-Constrained and Resource-Constrained UEs

To better understand UE uplink performance, it is useful to consider if the UE is power-constrained or resource-constrained. Specifically, a UE is said to be power-constrained if its uplink data rate is limited by the amount of power that it can transmit. Alternatively, a UE is said to be resource-constrained if its uplink data rate is limited by the number of available uplink resource blocks. Test results for an example of a power-constrained DUT UE are provided in Figures 6.7a-6.11a. These results are for a test of non-eNB configuration #12 with the default eNB configuration. The test settings are summarized in Table 6.2a; see section 5.3 for the full listing of default eNB settings. When it is able to successfully close the link with the eNB, a power-constrained UE often receives large PUSCH PRB grants, as shown in the PRB time-series in Figure 6.10a, and has a frequently empty buffer, as indicated by the BSR plot in Figure 6.11a.

Test results for an example of a resource-constrained DUT UE are provided in Figures 6.7b-6.11b. These results are for a test of non-eNB configuration #21 with the default eNB configuration. The test settings are summarized in Table 6.2b; see section 5.3 for the full listing of default eNB settings. A resource-constrained UE receives PUSCH PRB grants with a limited size, as shown in the PRB time-series in Figure 6.10b. In this testing, since the eNB settings implied that the PUSCH consisted of 38 PRBs and since the maximum number of active UEs in a TTI was set to 14, and since the loading UEs and the DUT all had the same specified data rate, the maximum number of PUSCH PRBs that were granted to the DUT was three, since $38/14 \approx 2.7$. Because a resource-constrained UE is competing for a pool of limited resources, its buffer is never empty, as indicated by the BSR plot in Figure 6.11b.

Another notable aspect of LTE is illustrated by the plots in this subsection. Namely, the distributions for PUSCH power per PRB and PUSCH power per TTI can be either unimodal (one peak) or multimodal (multiple peaks). For instance, in Figure 6.9a for the power-constrained example, PUSCH power per PRB is multimodal, but PUSCH power per TTI is unimodal. By contrast, in Figure 6.9b for the resource-constrained example, PUSCH power per PRB is unimodal, but PUSCH power per TTI is multimodal. These examples show that multimodality can occur regardless of whether or not PUSCH power is normalized by PRB or TTI.

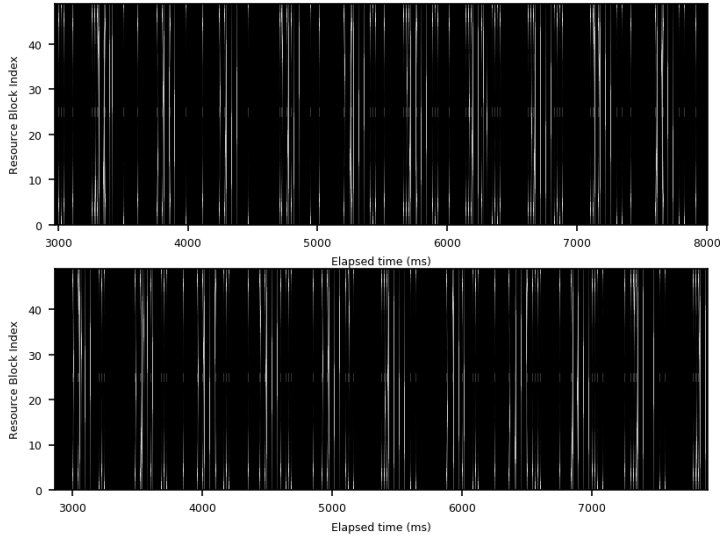
(a) Power-constrained example (non-eNB configuration #12).

Factor	Setting
Path Loss Attenuation	20 dB
Spatial Size of Cell	1000 m
Number of Loading UEs in Cell <i>A</i>	4
Number of Loading UEs in Cell <i>B</i>	4
Spatial Distribution of Loading UEs in Cell <i>A</i>	Cell Edge
QCI Value of Loading UEs	100 % 9
Traffic Data Rate	388 kbit/s/UE
Traffic Type	TCP
PUSCH Power Control Type	Open-Loop
PUSCH Power Control: P_0	-85 dBm
PUCCH Power Control: P_0	-117 dBm
Fractional Power Control: α	0.8

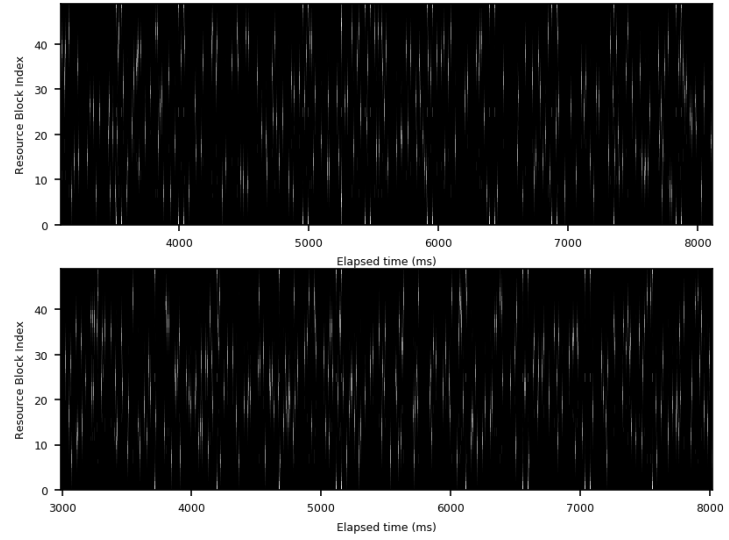
(b) Resource-constrained example (non-eNB configuration #21).

Factor	Setting
Path Loss Attenuation	0 dB
Spatial Size of Cell	100 m
Number of Loading UEs in Cell <i>A</i>	52
Number of Loading UEs in Cell <i>B</i>	52
Spatial Distribution of Loading UEs in Cell <i>A</i>	Near Edge
QCI Value of Loading UEs	25 % 5; 75 % 9
Traffic Data Rate	388 kbit/s/UE
Traffic Type	UDP
PUSCH Power Control Type	Open-Loop
PUSCH Power Control: P_0	-85 dBm
PUCCH Power Control: P_0	-117 dBm
Fractional Power Control: α	0.8

Table 6.2: Settings for the power-constrained and resource-constrained examples. Both examples were collected with a default eNB configuration.

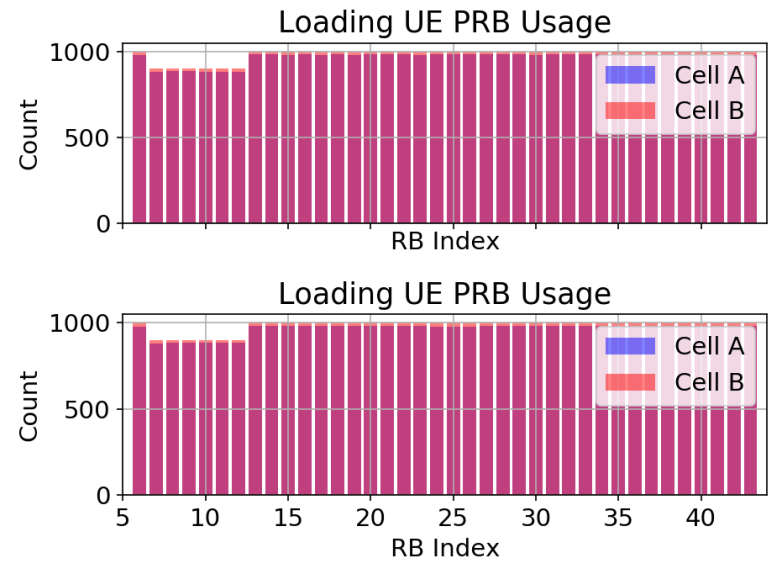
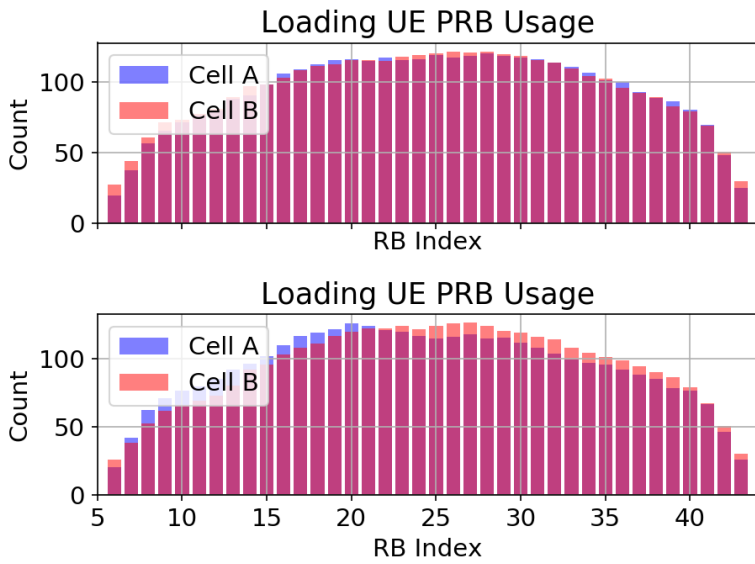
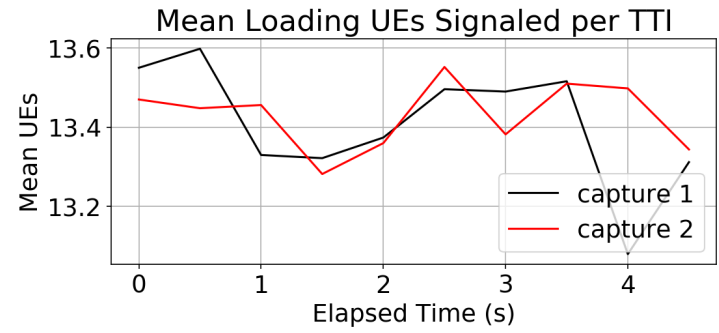
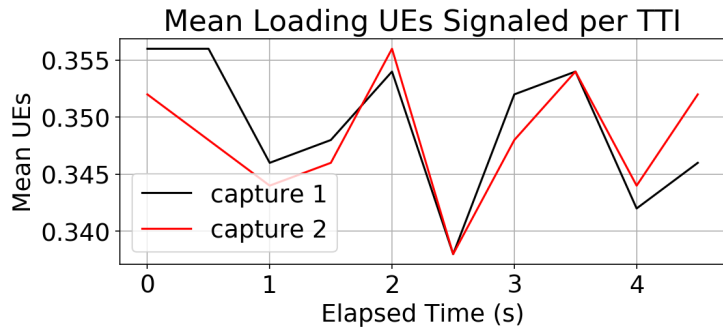


(a) Power Constrained



(b) Resource Constrained

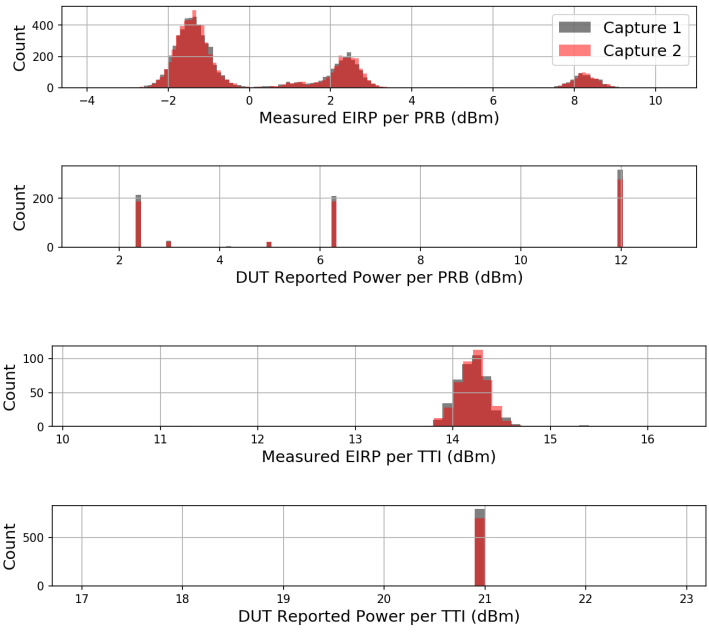
Figure 6.7: Power-constrained versus Resource-constrained UE Example: VSA spectrogram captures. Grayscale range: $[-58, 23]$ dBm.



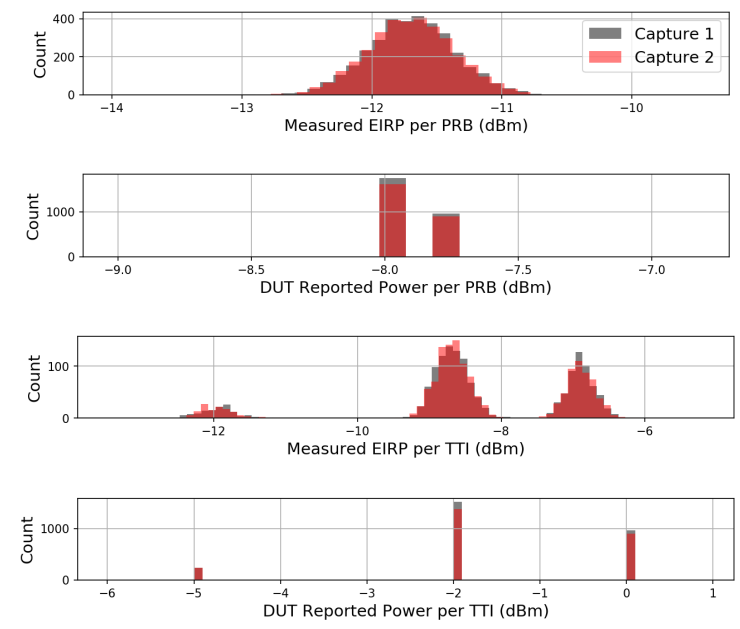
(a) Power Constrained

(b) Resource Constrained

Figure 6.8: Power-constrained versus Resource-constrained UE Example. Top: Loading UE activity time-series. Bottom: PRB allocation distributions.

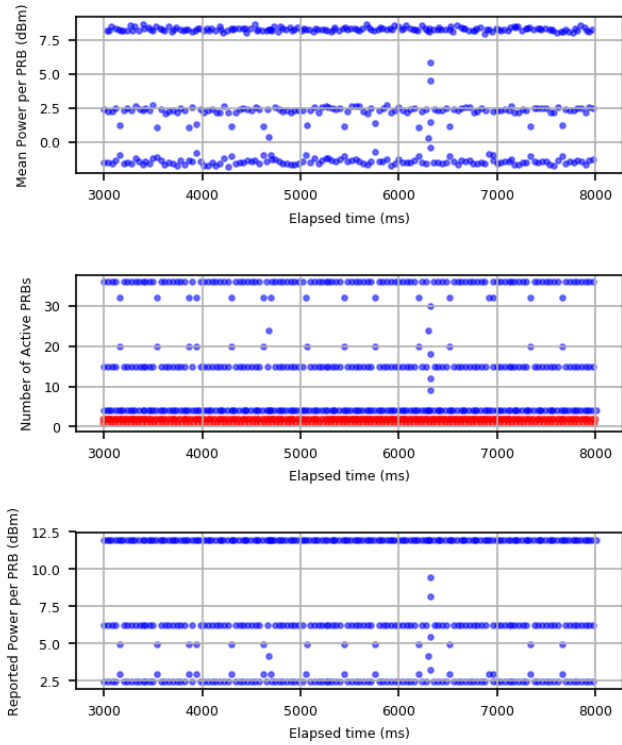


(a) Power Constrained

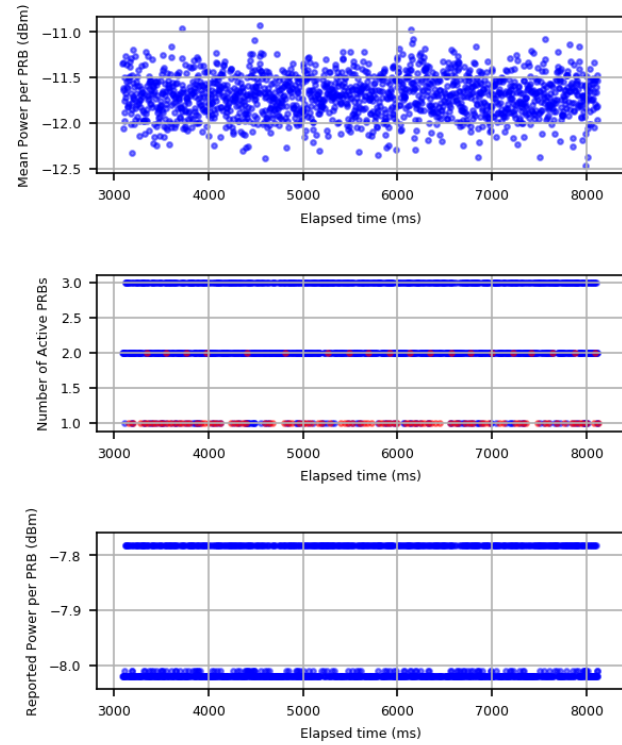


(b) Resource Constrained

Figure 6.9: Power-constrained versus Resource-constrained UE Example: PUSCH Power Histograms

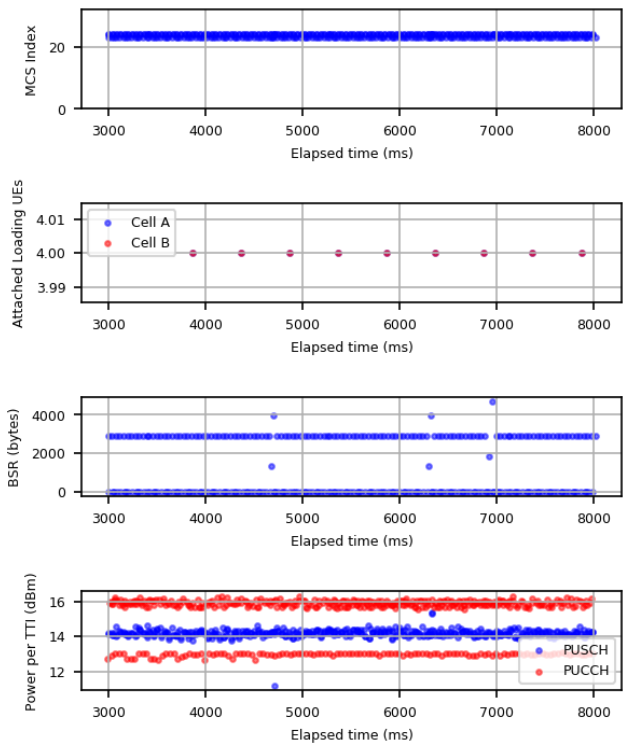


(a) Power Constrained

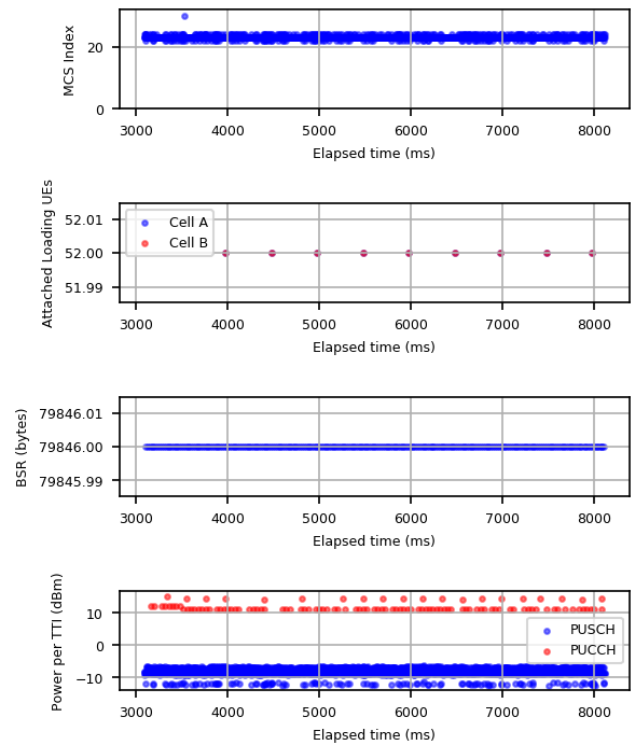


(b) Resource Constrained

Figure 6.10: Power-constrained versus Resource-constrained UE Example: PUSCH Time Series.



(a) Power Constrained



(b) Resource Constrained

Figure 6.11: Power-constrained versus Resource-constrained UE Example: Additional KPI Time Series.

6.2.2 Negative Power Headroom

A UE is said to be in negative power headroom for a given TTI if the open-loop component of the PUSCH power control equation, omitting the MCS-dependent offset, is greater than P_{\max} , the maximum allowable transmission power from the UE, expressed in dBm. Mathematically, this condition is

$$10 \log_{10}(M_{\text{PUSCH}}) + P_{0 \text{ PUSCH}} + \alpha \text{ PL} > P_{\max}, \quad (6.1)$$

where M_{PUSCH} is the grant size, $P_{0 \text{ PUSCH}}$ (expressed in dBm) and α are power control parameters, and PL , expressed in dB, is the path loss between the UE and eNB. See subsection 2.1.7 and subsection 2.1.9 for additional details on power control.

When the negative power headroom condition is satisfied, the open-loop component of the power control equation is not, by itself, a useful predictor of UE emission levels. Moreover, it indicates that the UE has been scheduled at a higher data rate than it can support given its current power availability. For these reasons, the range of UE emissions in negative power headroom conditions are of particular interest to those attempting to predict or model UE emissions. In particular, the factors affecting UE emissions in negative power headroom cases could potentially differ from pertinent factors in other conditions.

For every test, the proportion of active TTIs for which the DUT UE was in a negative power headroom condition was calculated. Specifically, for each TTI in which the DUT UE was actively transmitting, the left side of inequality (Equation 6.1) was evaluated, where the path loss was estimated by taking the difference between the reference signal power (11 dBm in these tests) and the RSRP reported by the DUT, and compared to the maximum transmission power, set to 23 dBm.

Test results for an example when the DUT UE was in a negative power headroom condition for a large proportion of its active TTIs are shown in Figures 6.12-6.16. Specifically, in this example, the DUT UE was in negative power headroom for 42.5 % of its active TTIs. These results are for a test of eNB configuration #8 with non-eNB configuration #28. The settings are summarized in Table 6.3; see section 5.3 for the full listing of the eNB settings.

Table 6.3: Settings for the negative power headroom example (eNB configuration #8, non-eNB configuration #28).

Factor	Setting
Path Loss Attenuation	20 dB
Spatial Size of Cell	1000 m
Number of Loading UEs in Cell A	52
Number of Loading UEs in Cell B	4
Spatial Distribution of Loading UEs in Cell A	Cell Edge
QCI Value of Loading UEs	100 % 9
Traffic Data Rate	194 kbit/s/UE
Traffic Type	TCP
PUSCH Power Control Type	Open-Loop
PUSCH Power Control: P_0	-85 dBm
PUCCH Power Control: P_0	-117 dBm
Fractional Power Control: α	1.0

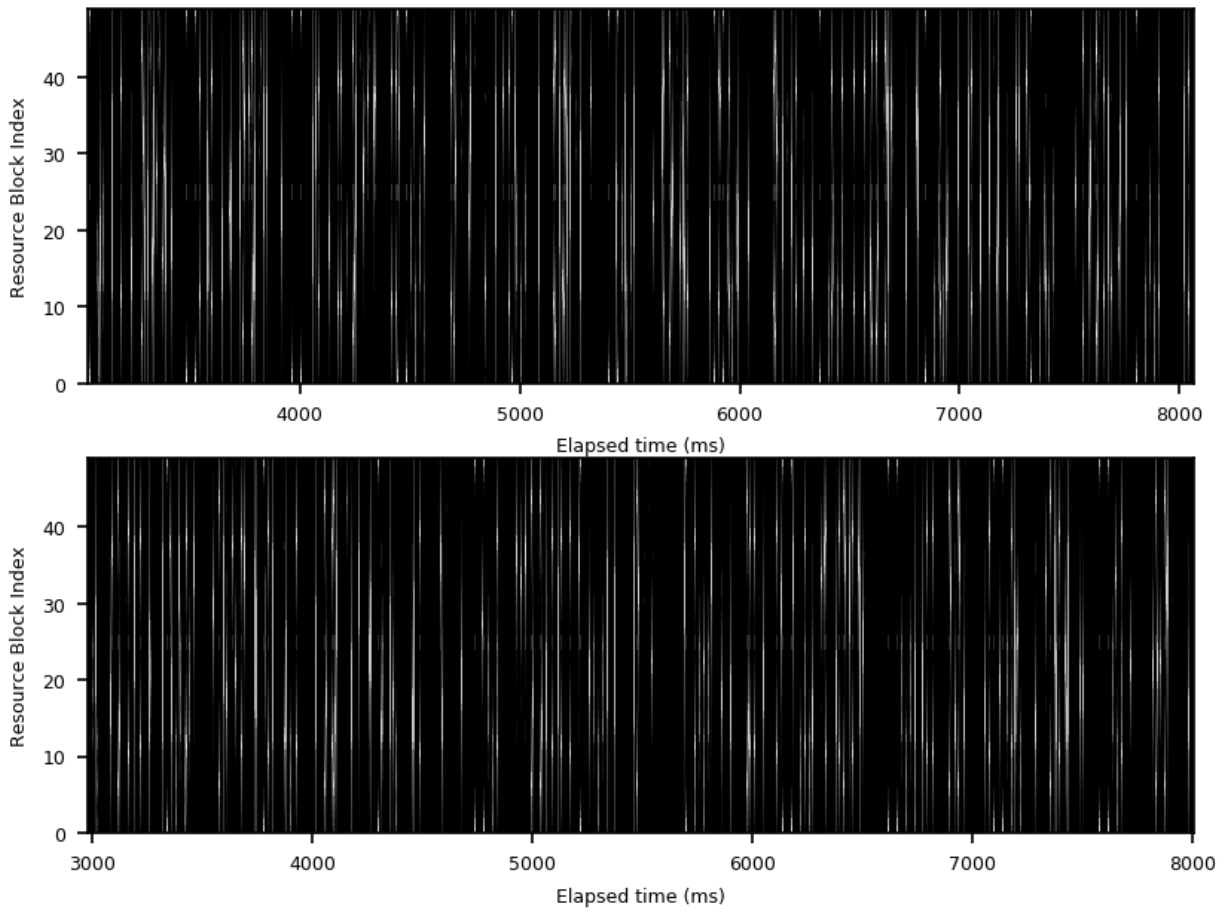


Figure 6.12: Negative Power Headroom UE Example: VSA spectrogram captures. Grayscale range: $[-58, 23]$ dBm.

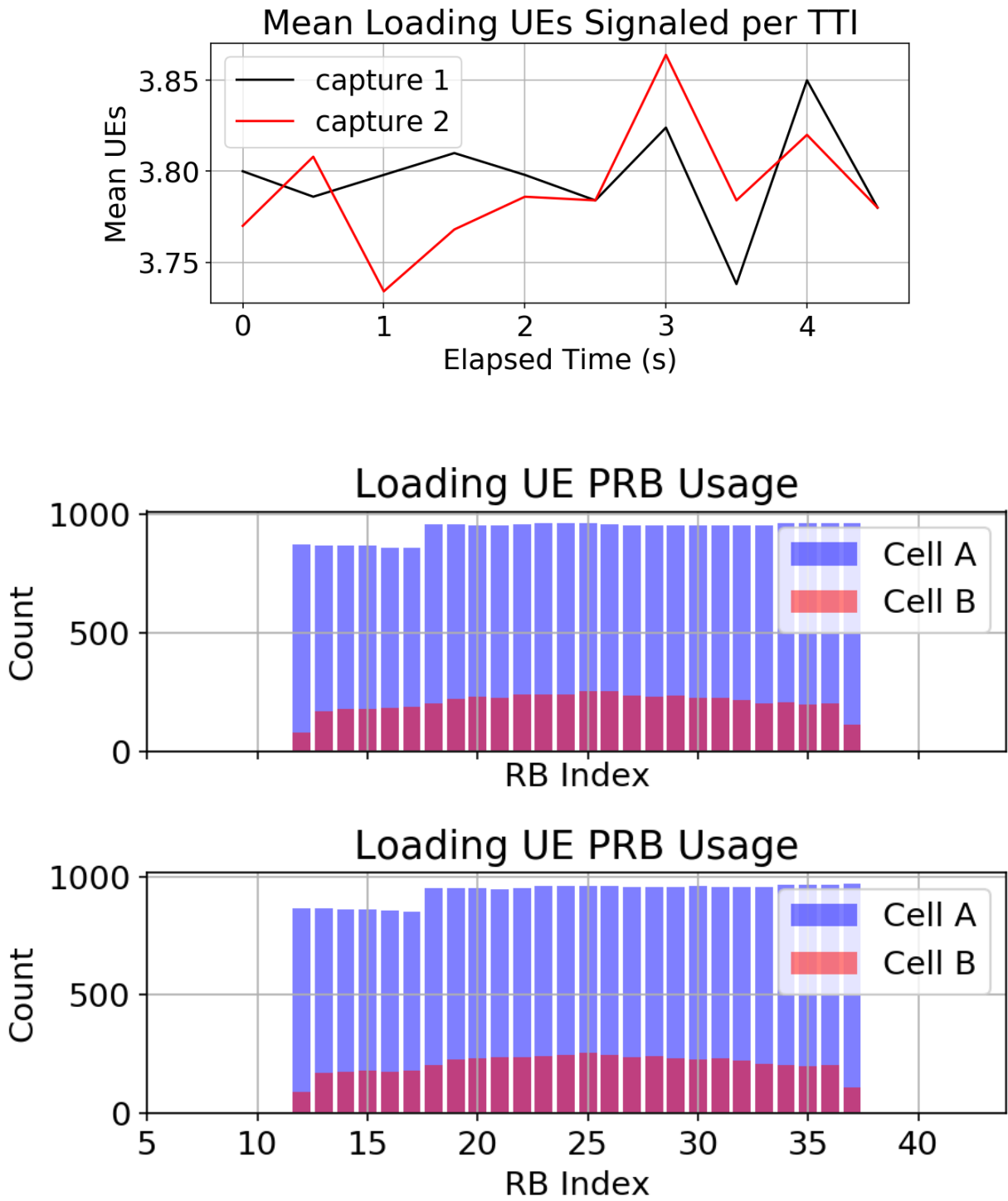


Figure 6.13: Negative Power Headroom UE Example: loading UE activity time-series (Top) and PRB allocation distributions (Bottom).

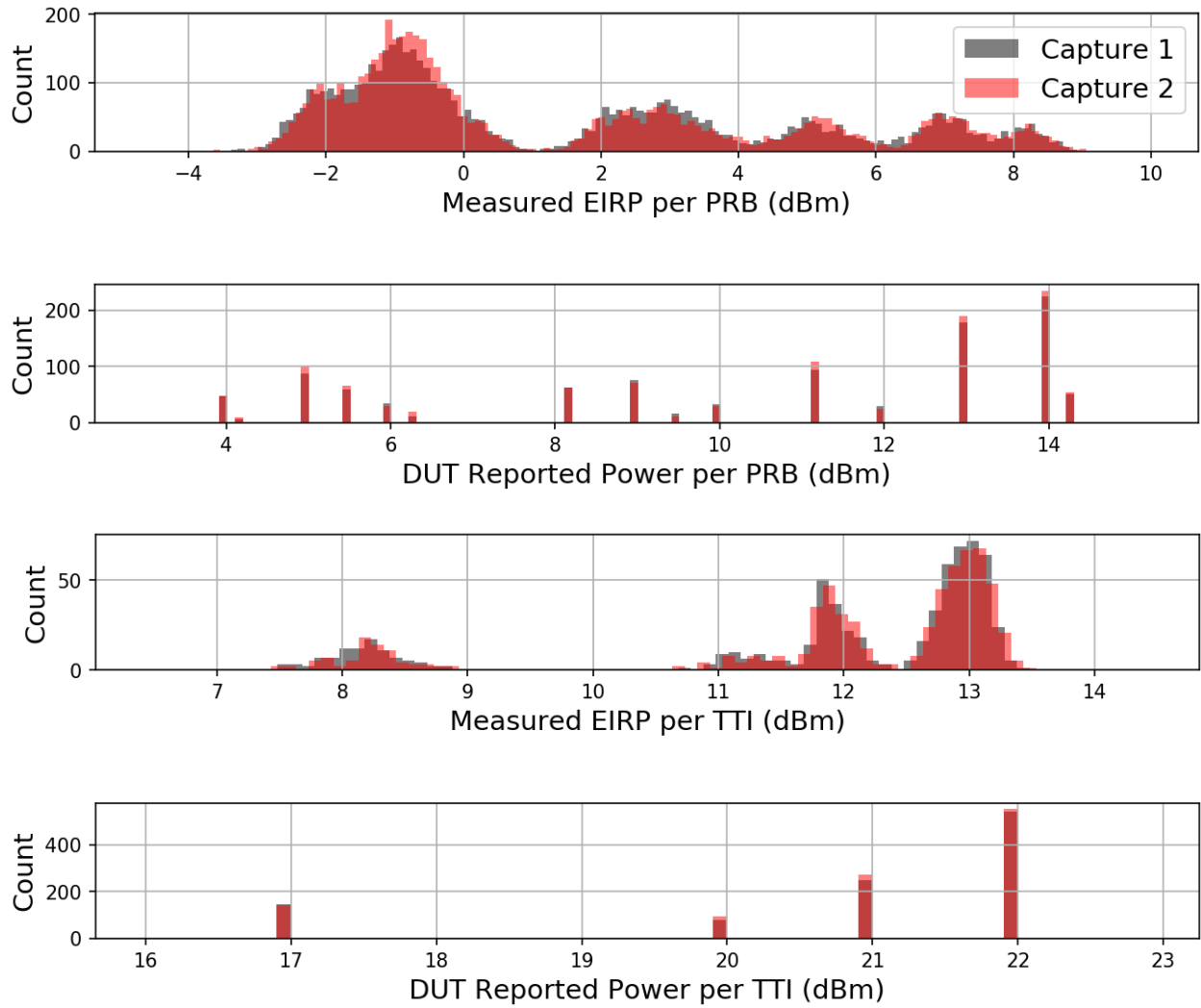


Figure 6.14: Negative Power Headroom UE Example: PUSCH Power histograms.

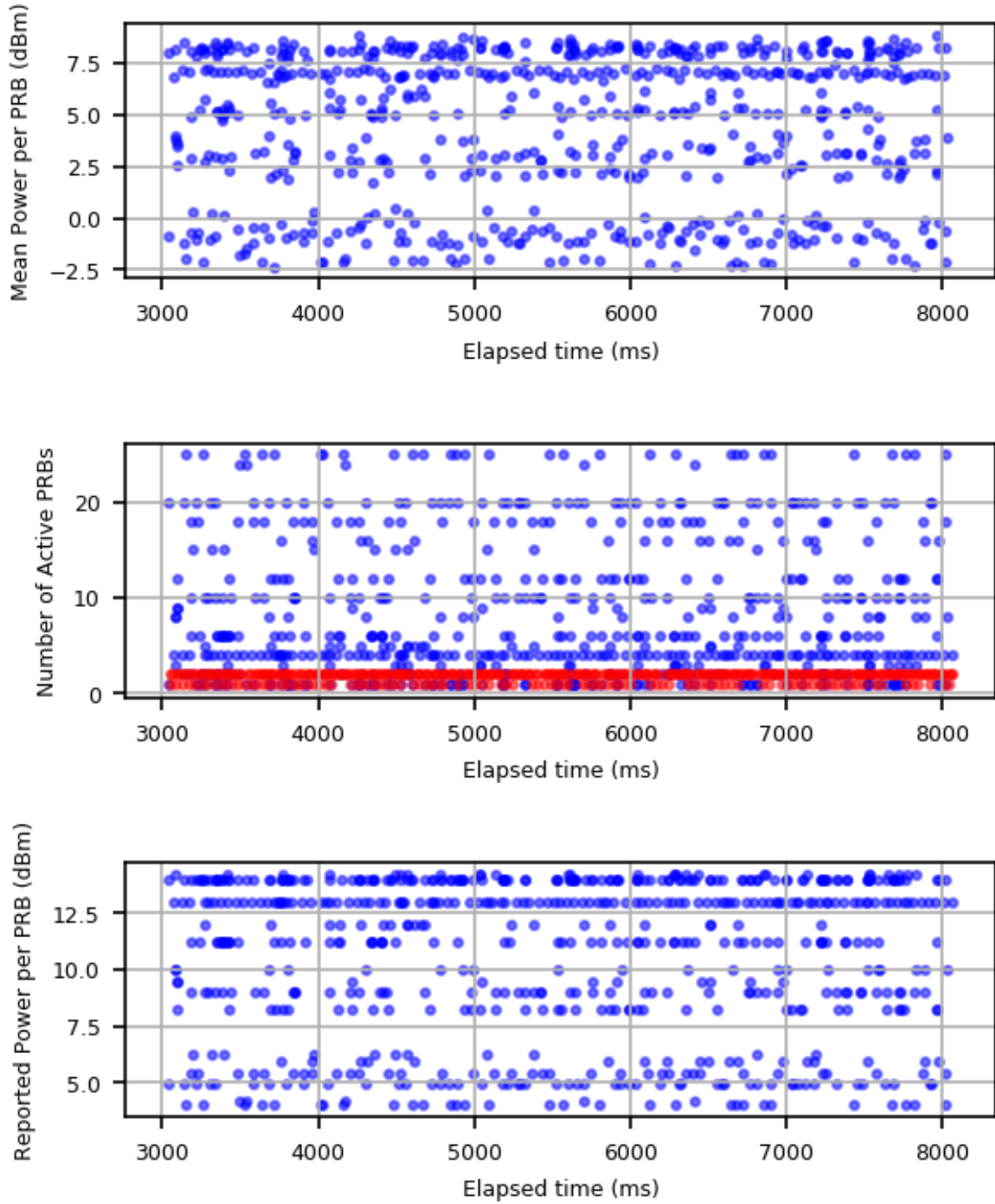


Figure 6.15: Negative Power Headroom UE Example: time-series PUSCH power per PRB and allocation size.

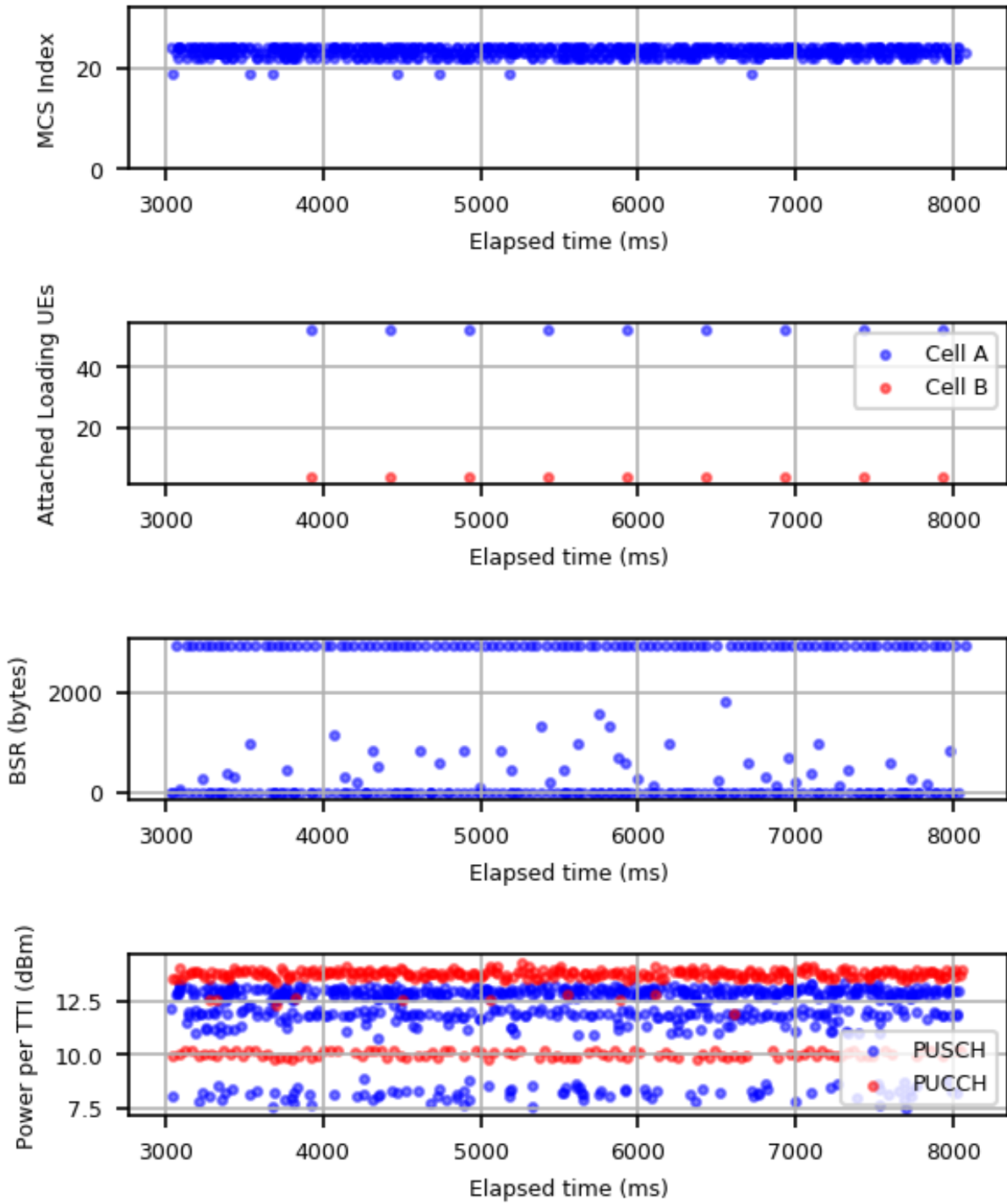


Figure 6.16: Negative Power Headroom UE Example: time-series for additional KPIs.

6.2.3 Interference Aware Scheduling

Test results for an example with interference-aware scheduling are shown in Figures 6.17-6.21. These results are for a test of eNB configuration #5 and non-eNB configuration #14. The test settings are summarized in Table 6.4; see section 5.3 for the full listing of the eNB settings.

This example illustrates the sensitivity of interference-aware scheduling to interference (or cross talk) from an adjacent cell. As shown in Figure 6.18, the loading UE PRB distributions are notably different for cells *A* and *B*. For example, when interference-aware scheduling is activated, PRB indices 20 and 21 were scheduled less frequently in Cell *A* than in Cell *B*. By contrast, PRB indices 16 and 23 were scheduled more frequently in Cell *A* than in Cell *B*.

Table 6.4: Settings for the Interference Aware scheduling example (eNB configuration #5, non-eNB configuration #14).

Factor	Setting
Path Loss Attenuation	20 dB
Spatial Size of Cell	1000 m
Number of Loading UEs in Cell <i>A</i>	4
Number of Loading UEs in Cell <i>B</i>	4
Spatial Distribution of Loading UEs in Cell <i>A</i>	Near eNB
QCI Value of Loading UEs	25 % 5; 75 % 9
Traffic Data Rate	194 kbit/s/UE
Traffic Type	UDP
PUSCH Power Control Type	Open-Loop
PUSCH Power Control: P_0	-85 dBm
PUCCH Power Control: P_0	-117 dBm
Fractional Power Control: α	1.0

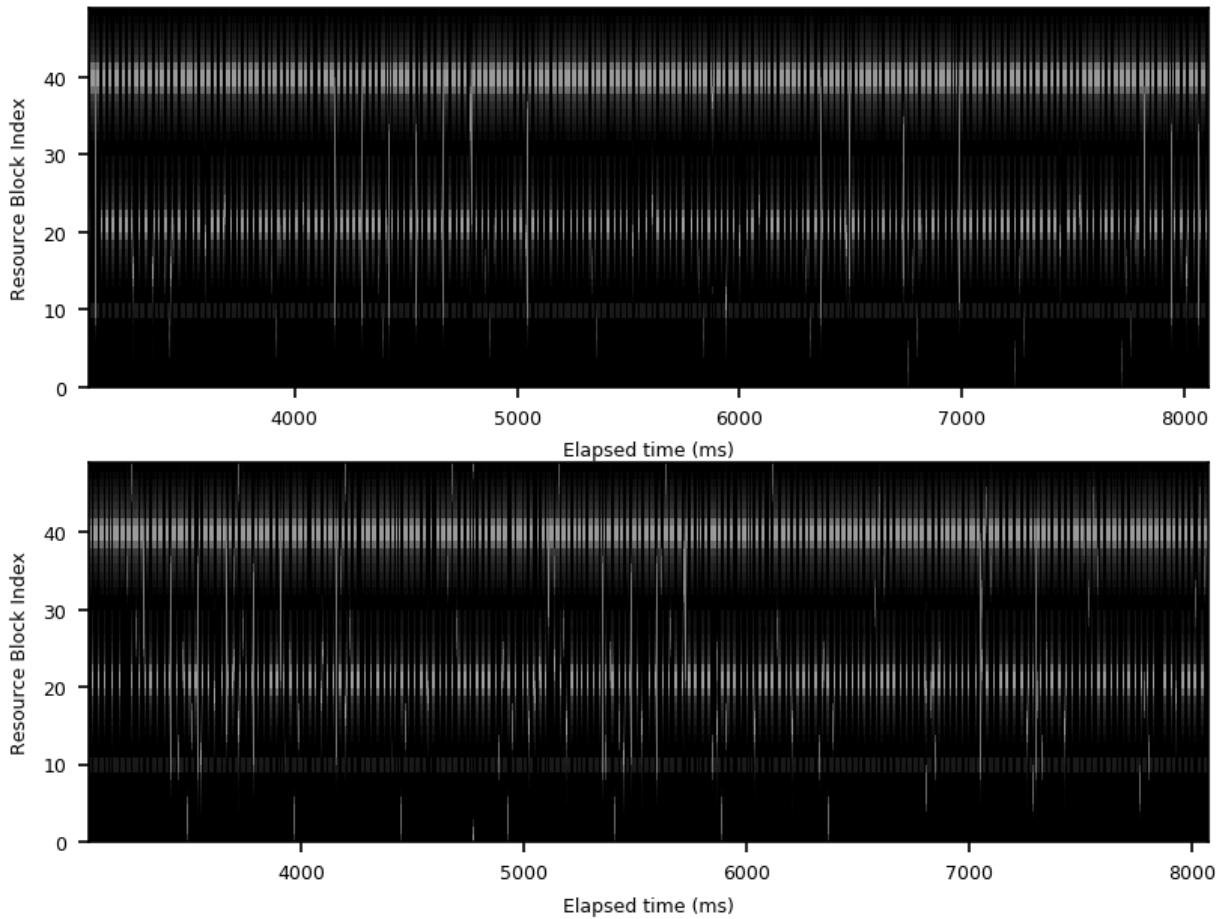


Figure 6.17: Interference Aware scheduling Example: VSA spectrogram captures. Grayscale range: [-58, 23] dBm.

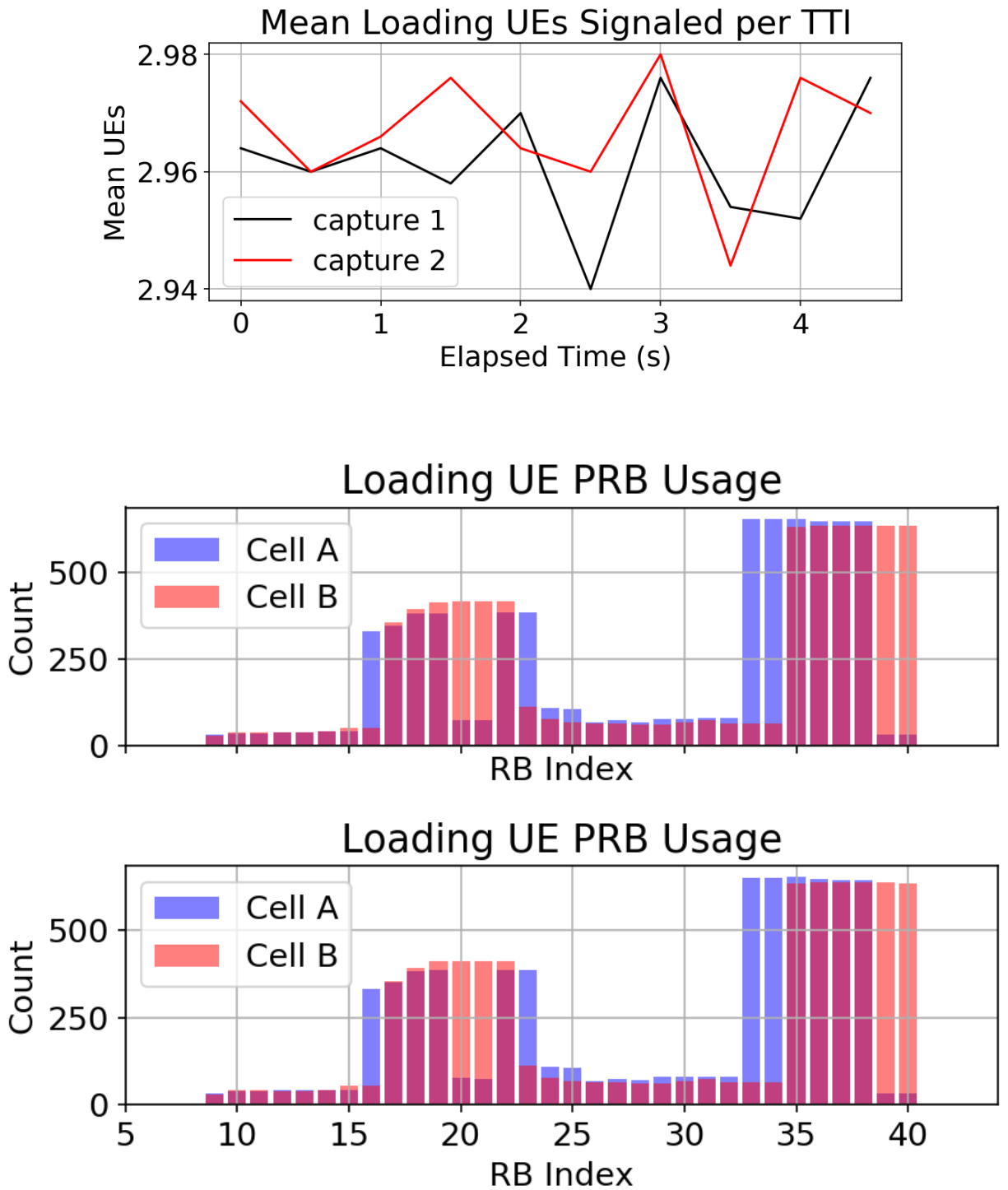


Figure 6.18: Interference Aware scheduling Example: loading UE activity time-series (Top) and PRB allocation distributions (Bottom).

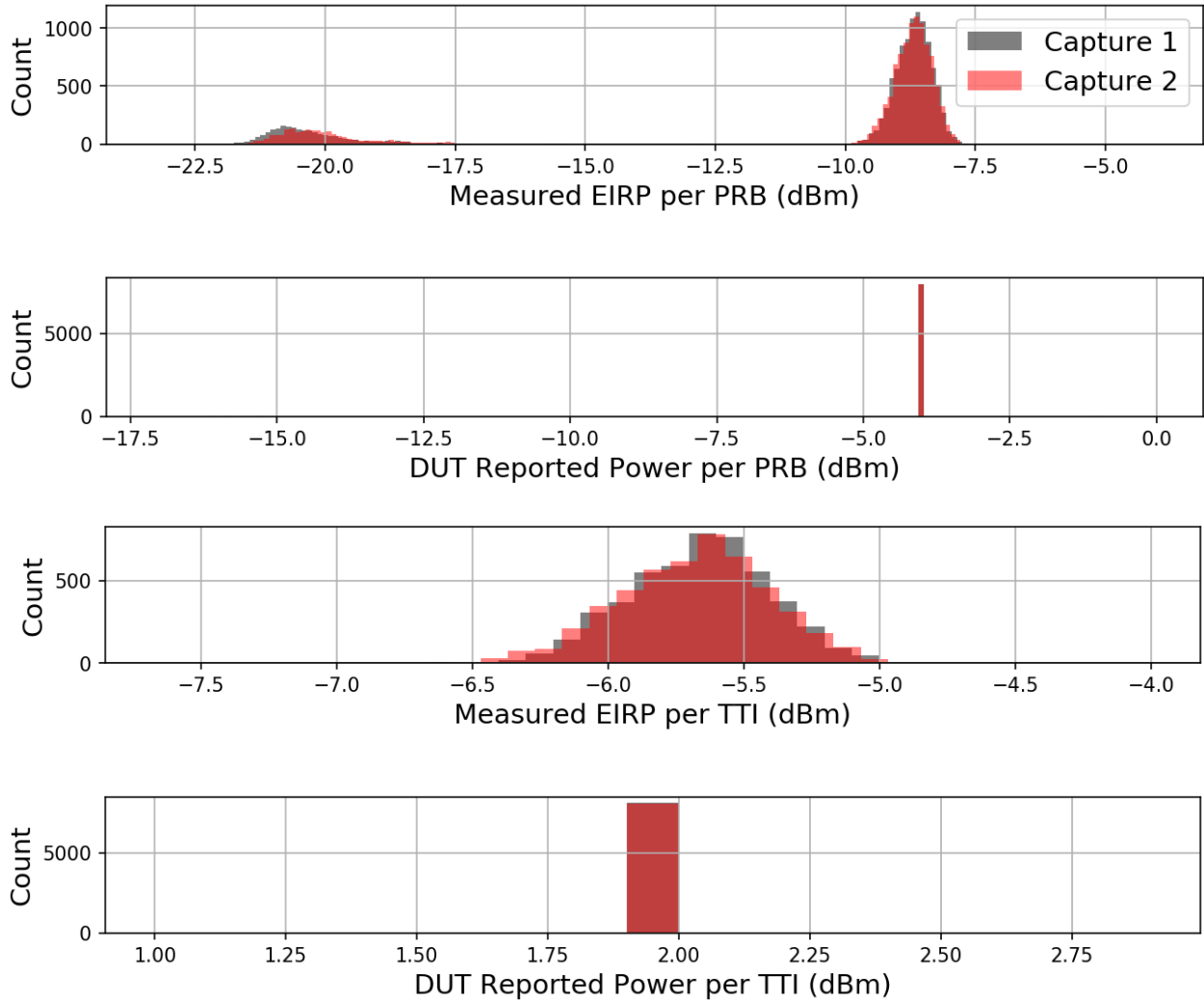


Figure 6.19: Interference Aware scheduling Example: PUSCH Power histograms.

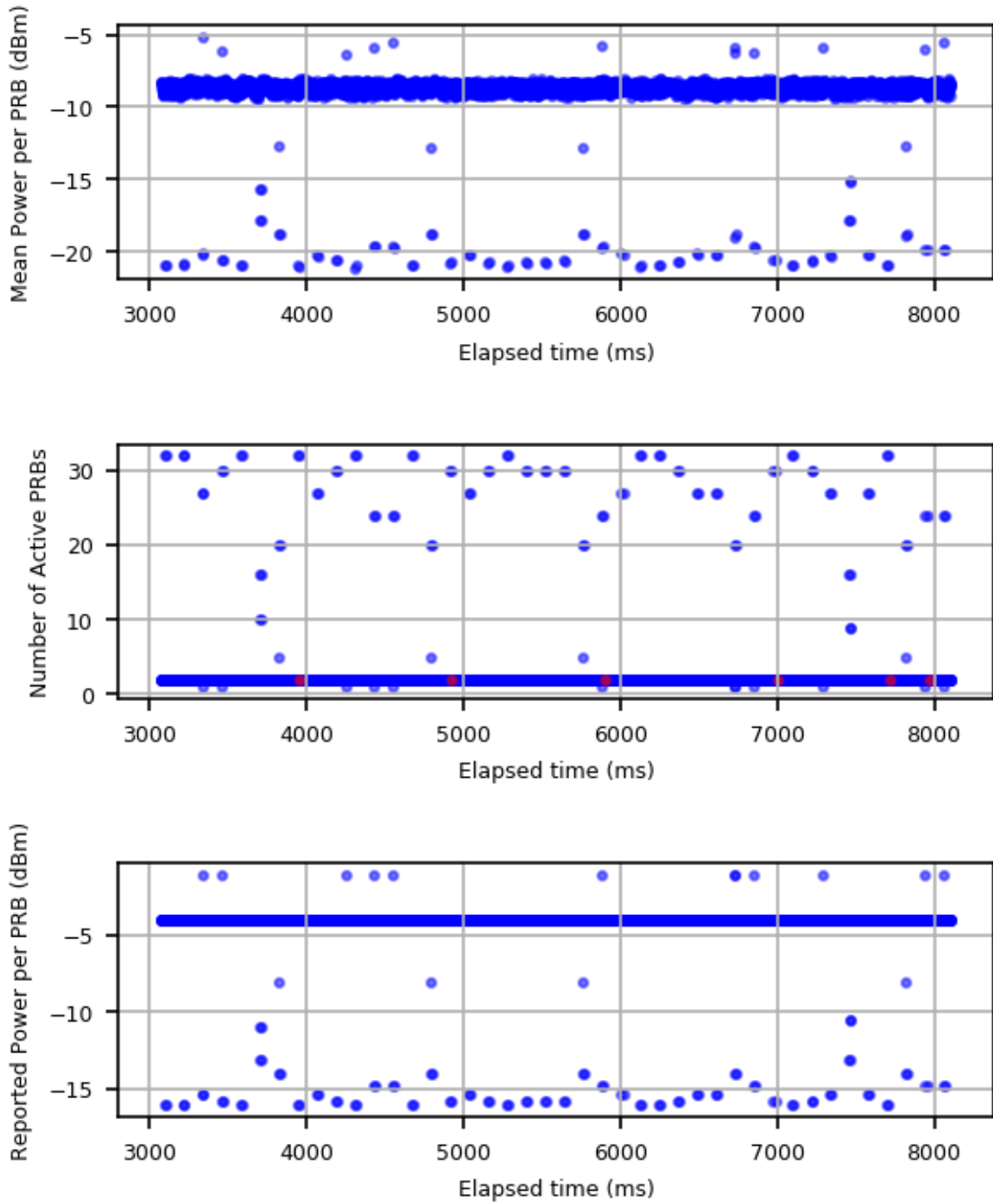


Figure 6.20: Interference Aware scheduling Example: time-series PUSCH power per PRB and allocation size.

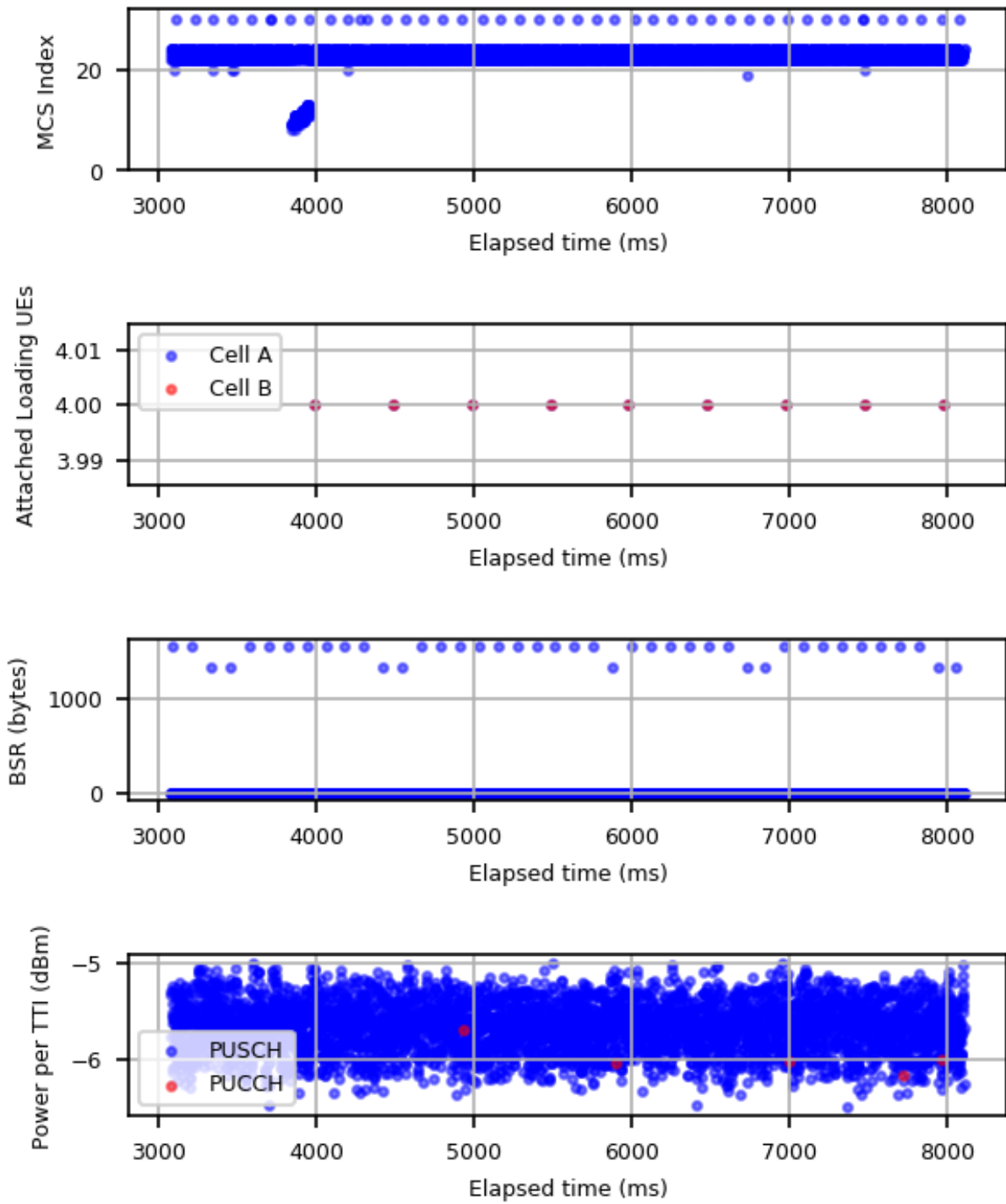


Figure 6.21: Interference Aware scheduling Example: time-series for additional KPIs.

6.2.4 Large Variation in MCS Index

Test results for an example with large variations in MCS index are shown in Figures 6.22-6.26. These results are for a test of eNB configuration #26 and non-eNB configuration #2. The test settings are summarized in Table 6.5; see section 5.3 for the full listing of the eNB settings.

From Figure 6.26, observe that the MCS time-series periodically ramps between roughly 7-18, until an MCS index of 30 is reported, indicating retransmissions at the previous MCS index value. After multiple retransmissions, the MCS index is then substantially reduced.

Note that in this example, since the PUSCH P_0 was set to 24 dBm, the DUT UE was in a negative power headroom condition for the entirety of the test.

Table 6.5: Settings for the MCS variation example (eNB configuration #26, non-eNB configuration #2).

Factor	Setting
Path Loss Attenuation	20 dB
Spatial Size of Cell	100 m
Number of Loading UEs in Cell A	4
Number of Loading UEs in Cell B	52
Spatial Distribution of Loading UEs in Cell A	Near eNB
QCI Value of Loading UEs	100 % 9
Traffic Data Rate	194 kbit/s/UE
Traffic Type	TCP
PUSCH Power Control Type	Open-Loop
PUSCH Power Control: P_0	24 dBm
PUCCH Power Control: P_0	-96 dBm
Fractional Power Control: α	0.5

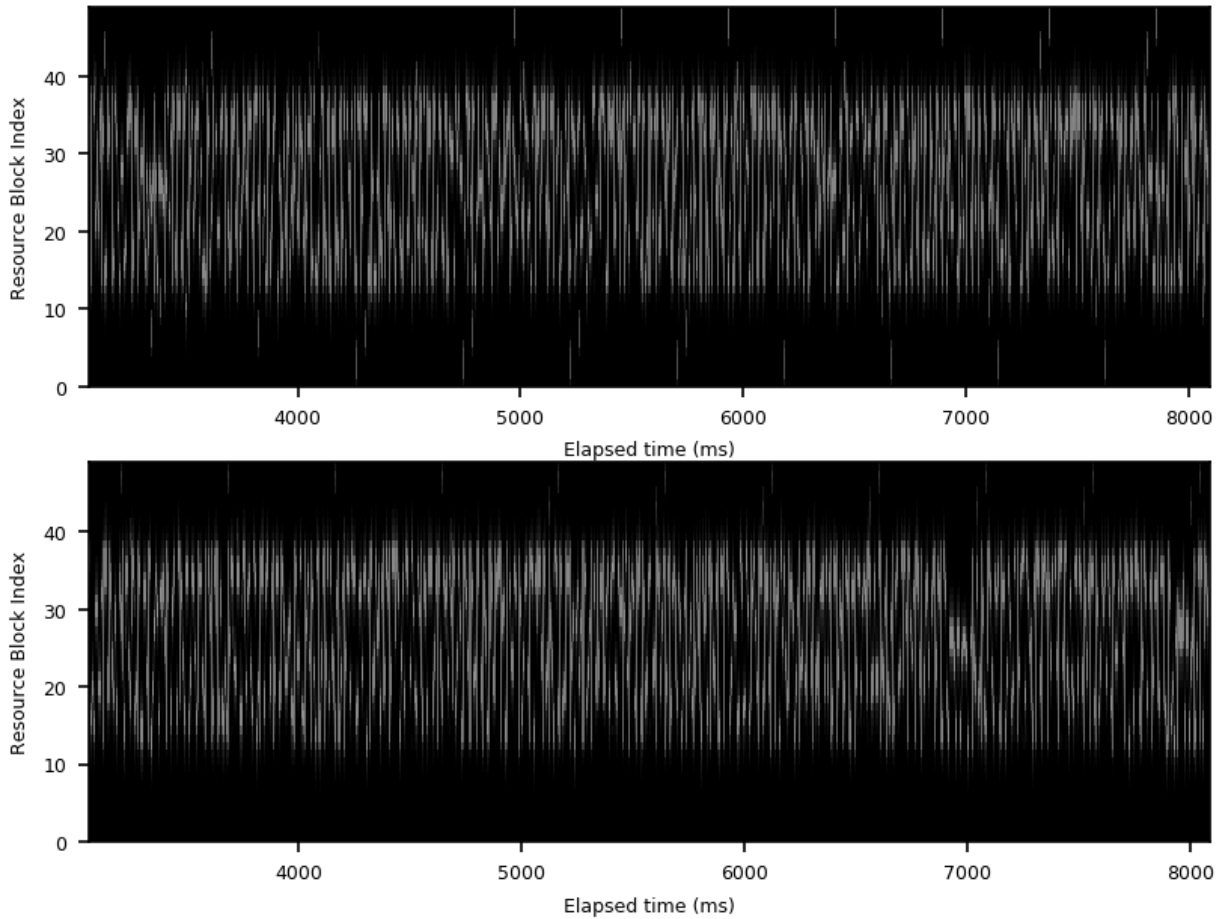


Figure 6.22: MCS variation example: VSA spectrogram captures. Grayscale range: $[-58, 23]$ dBm.

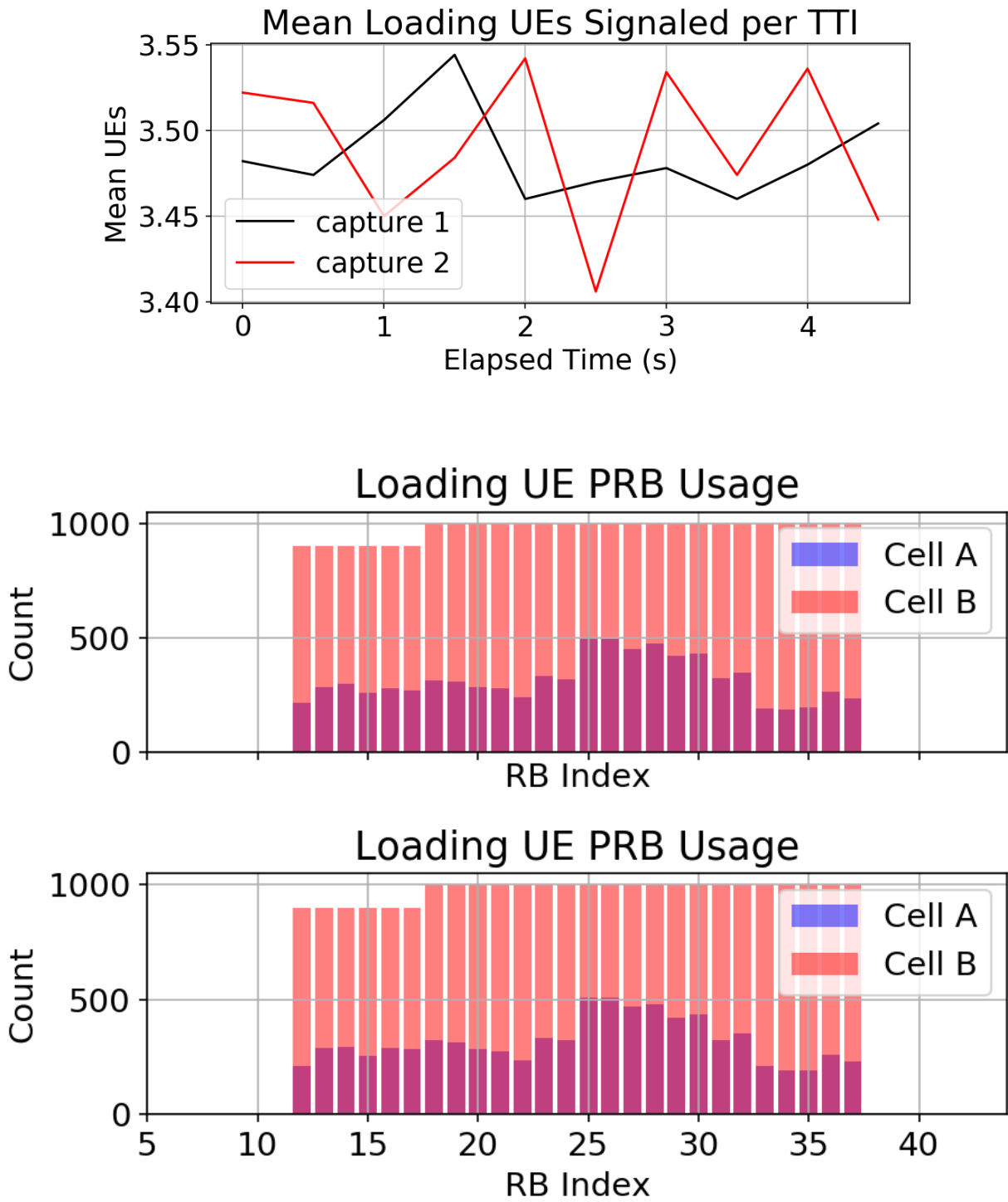


Figure 6.23: MCS variation example: loading UE activity time-series (Top) and PRB allocation distributions (Bottom).

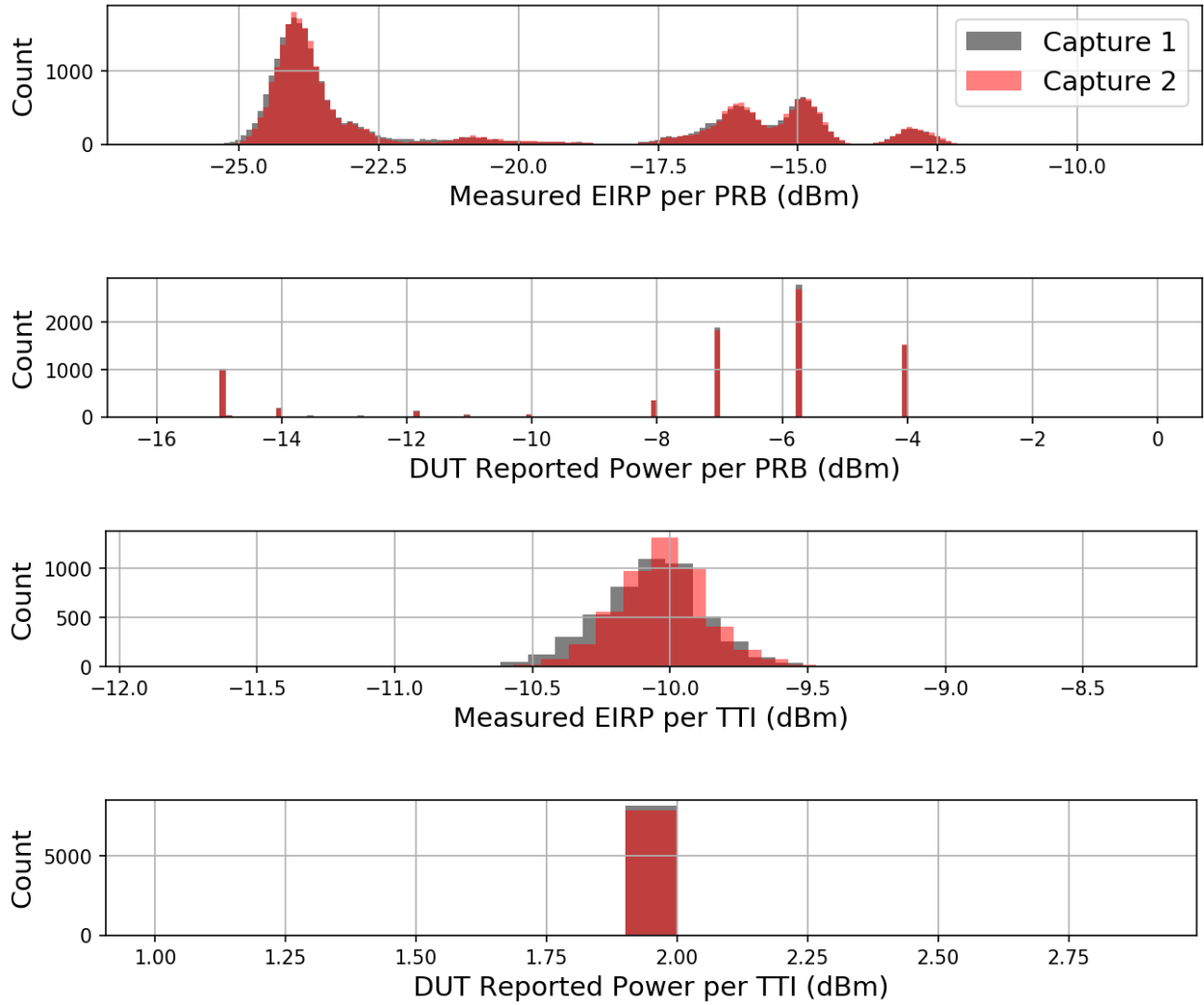


Figure 6.24: MCS variation example: PUSCH Power histograms.

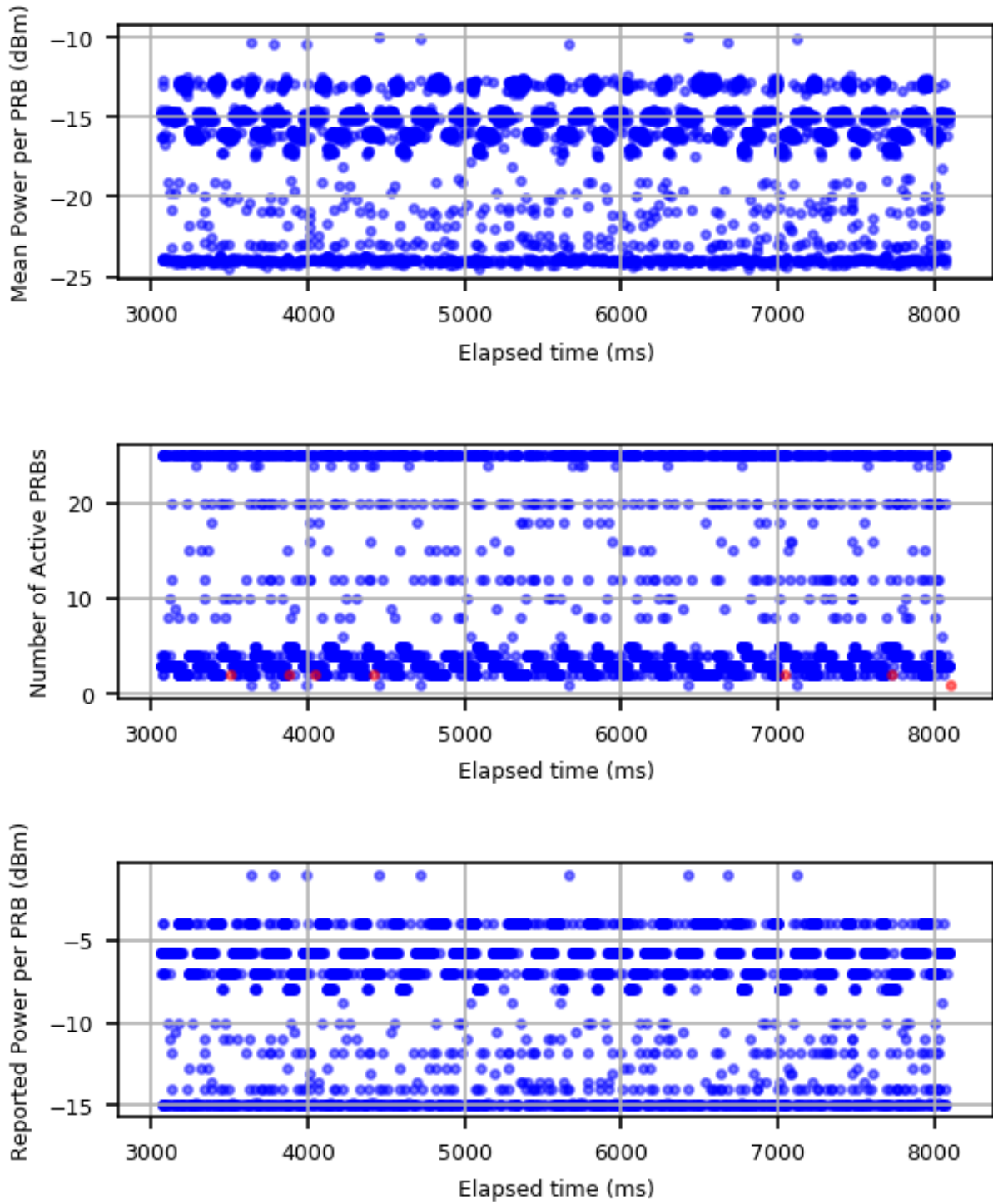


Figure 6.25: MCS variation example: time-series PUSCH power per PRB and allocation size.

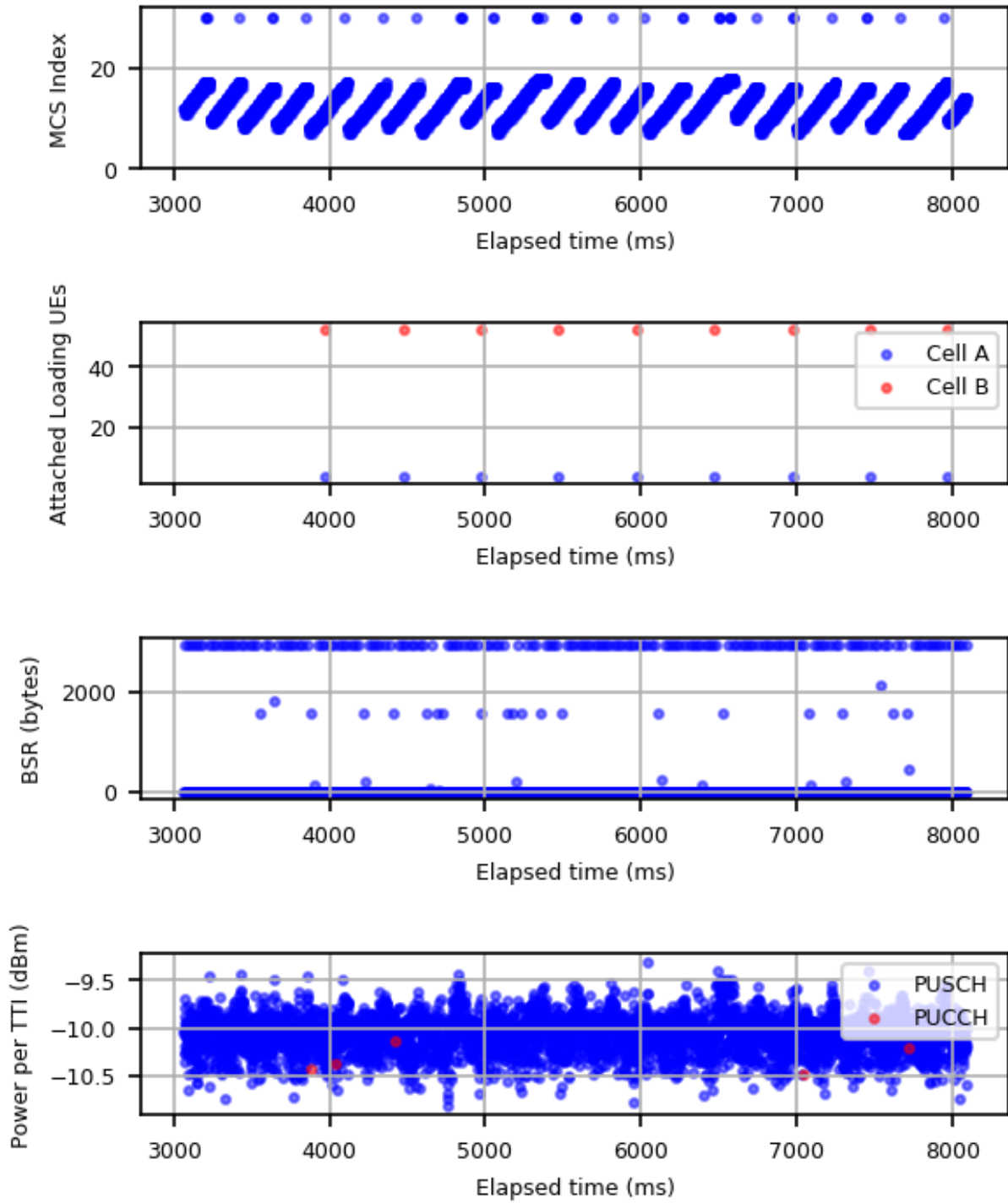


Figure 6.26: MCS variation example: time-series for additional KPIs.

6.3 Global Summary Plots

6.3.1 RSRP stability

Since LTE power control depends directly on the RSRP, it was important to verify that the DUT-reported RSRP was consistent across the duration of the testing and to assess variability. To assess RSRP stability, the test team used data from the default eNB tests, which were collected at the start of each test day. Figure 6.27 plots the median DUT-reported RSRP across all test days for each testbed attenuation setting. This plot aggregates results from 45 default eNB tests, where 30 were executed with UE #1 and 15 were executed with UE #2. (Recall from section 5.2 that For Rounds 1 & 3, the default tests used UE #1, whereas Rounds 2 & 4 used UE #2.)

The inset text boxes on Figure 6.27 contain inter-day and intra-day summary statistics. Specifically, the interquartile range (IQR), defined as the difference between the 75th and 25th percentiles, provides a robust measure of variability (or spread). The range, defined as the difference between the maximum and minimum, characterizes the full extent of the observations. From these statistics, note that the variations in RSRP were typically very small for the same day, whereas the variations across days were much larger. Namely, the intra-day IQR was approximately 0.2 dB, whereas the inter-day IQR was roughly 2 dB. For both attenuation settings, the overall inter-day range of median RSRP values was nearly 5 dB.

The dashed lines in Figure 6.27 correspond to the overall inter-day median for each attenuation setting. The lower and upper dotted lines for each attenuation setting are the length of typical boxplot whiskers, which can be used to assess outliers. Namely, the dotted lines correspond to the 25th percentile minus 1.5 times the IQR, and the 75th percentile plus 1.5 times the inter-day IQR, respectively.

A plot of the difference in the median RSRP for the two testbed attenuation settings versus test day is shown in Figure 6.28. As expected, the difference in median RSRP was very close to 20 dB across test days, with a median difference of 19.7 dB. The IQR for the median RSRP difference was 0.3 dB, and the range was 0.7 dB.

Figure 6.29 contains RSRP stability plots for UE-specific subsets of the data in Figure 6.27. While the intra-day IQR was roughly the same for both UEs (≈ 0.2 dB), the inter-day IQR differed by 0.5 dB, with a larger variation for UE #1.

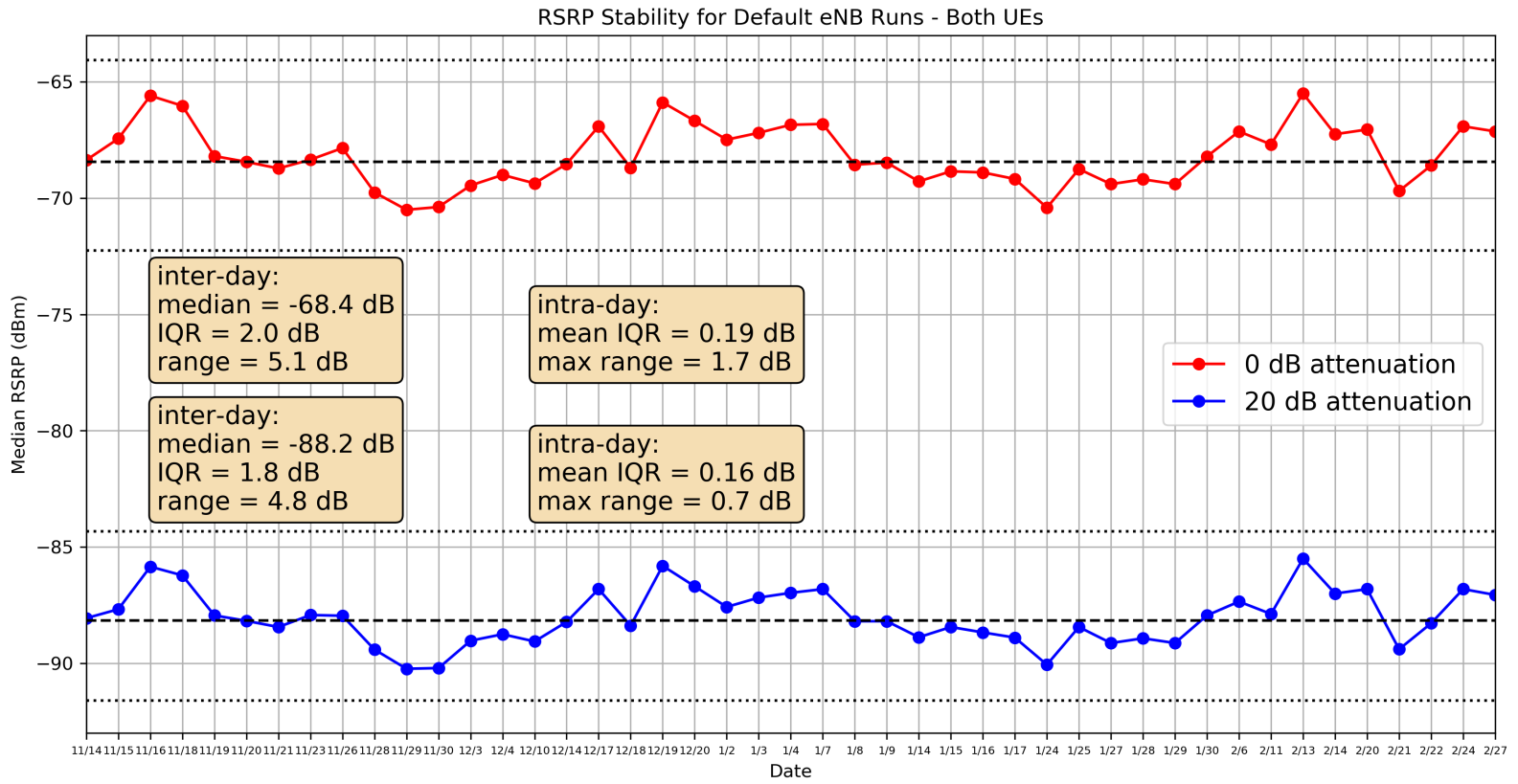


Figure 6.27: RSRP stability plot - both UEs.

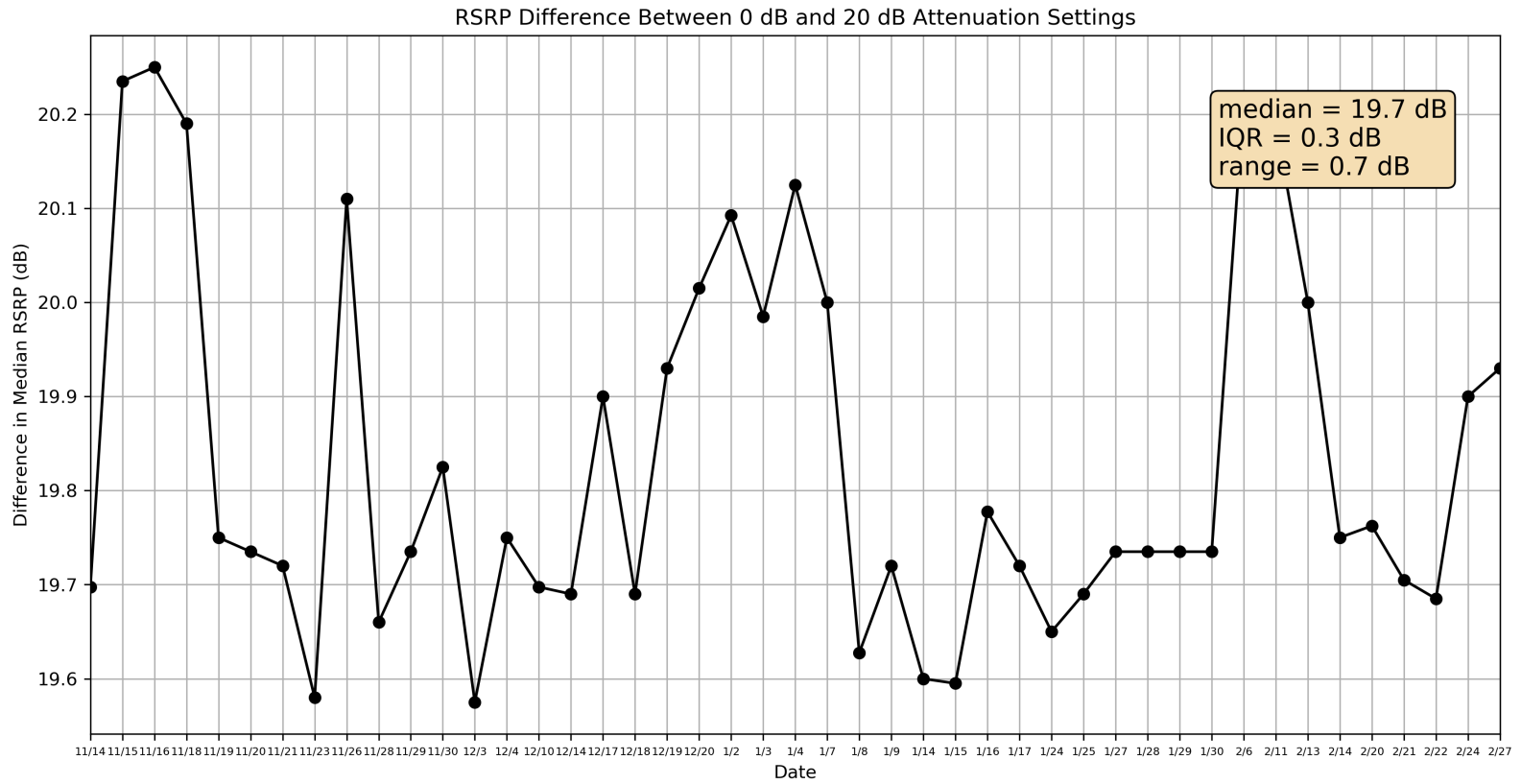


Figure 6.28: Difference in median RSRP between attenuator settings.

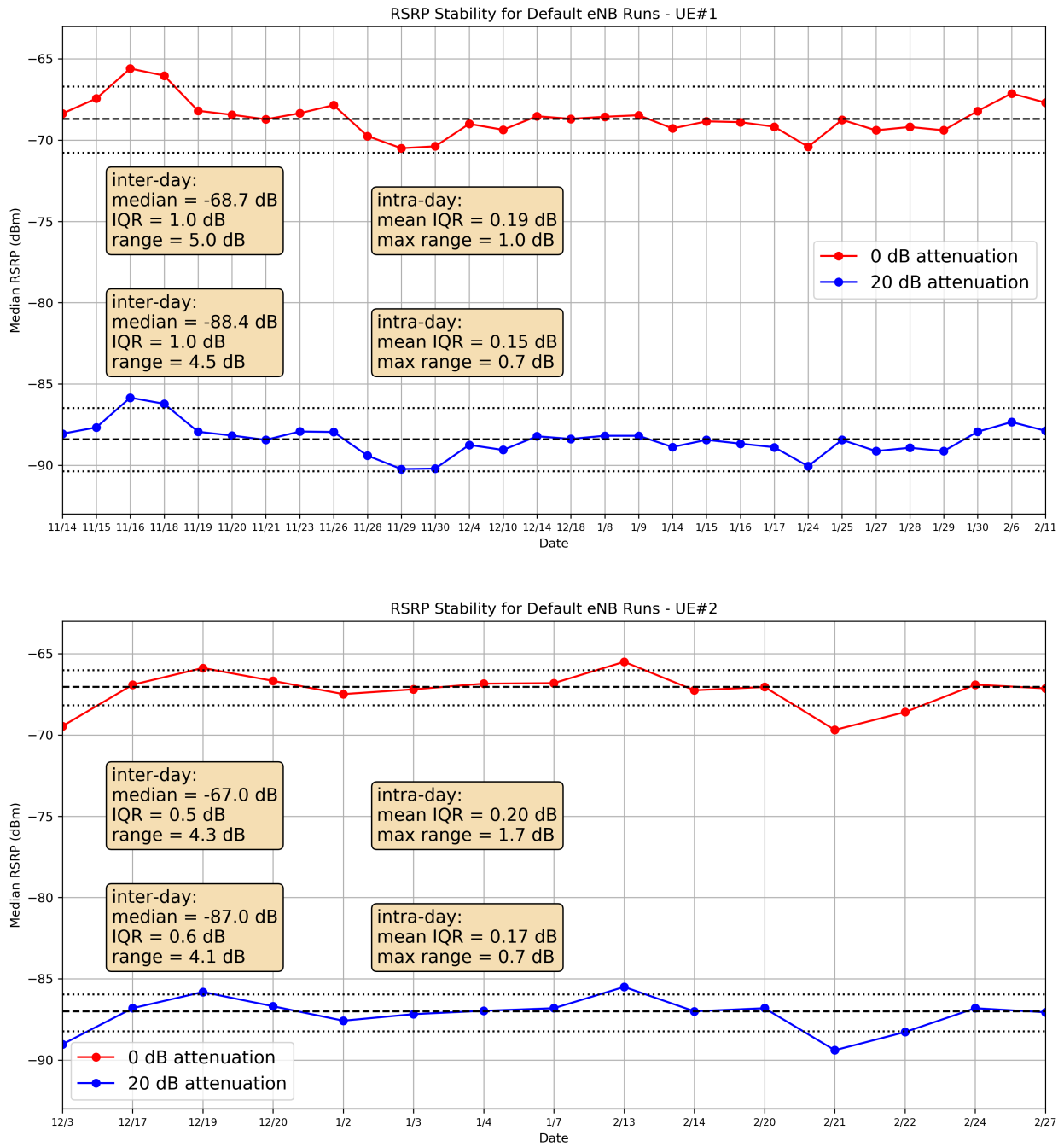


Figure 6.29: RSRP stability plots by UE.

6.3.2 Empirical CDFs for measured PUSCH EIRP per PRB

For every test configuration in the factor screening experiment, Figure 6.30 plots the empirical cumulative distribution functions (CDFs) for the measured PUSCH EIRP per PRB. Since there were 32×32 test configurations tested over four rounds, this plot summarizes approximately 4000 empirical CDFs. Overall, a nearly 70 dB range was covered by the measured distributions.

To lend more insight, Figure 6.31 presents summary plots of the empirical CDFs of all tests separated by power control type and testbed attenuation setting. Here, each graph summarizes one quarter of all tests, e.g., roughly 1000 empirical CDFs are plotted.

Observe that the PUSCH power per PRB distributions with open-loop power control spanned a much larger range than the distributions with closed-loop power control. Interestingly, for the closed-loop power control case, the overall range of distributions was approximately 10 dB greater with the 20 dB attenuation setting.

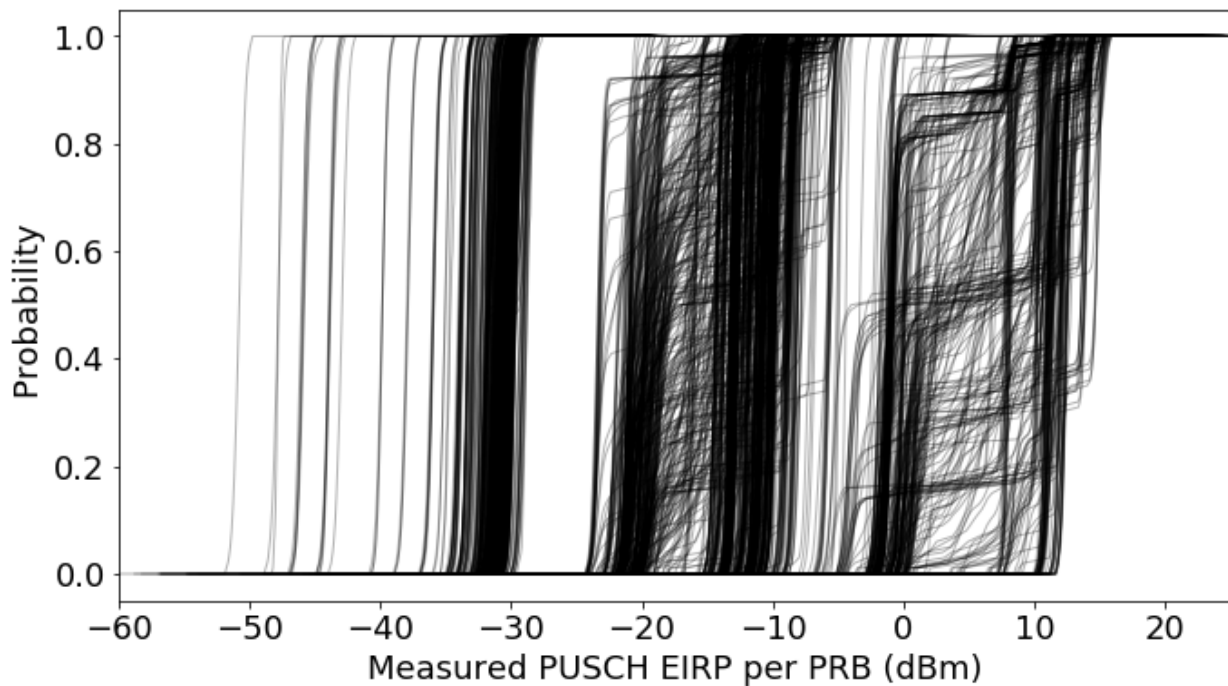


Figure 6.30: Summary of empirical CDFs for measured PUSCH power per PRB for all test configurations in the screening experiments. This plot contains approximately 4000 unique CDFs.

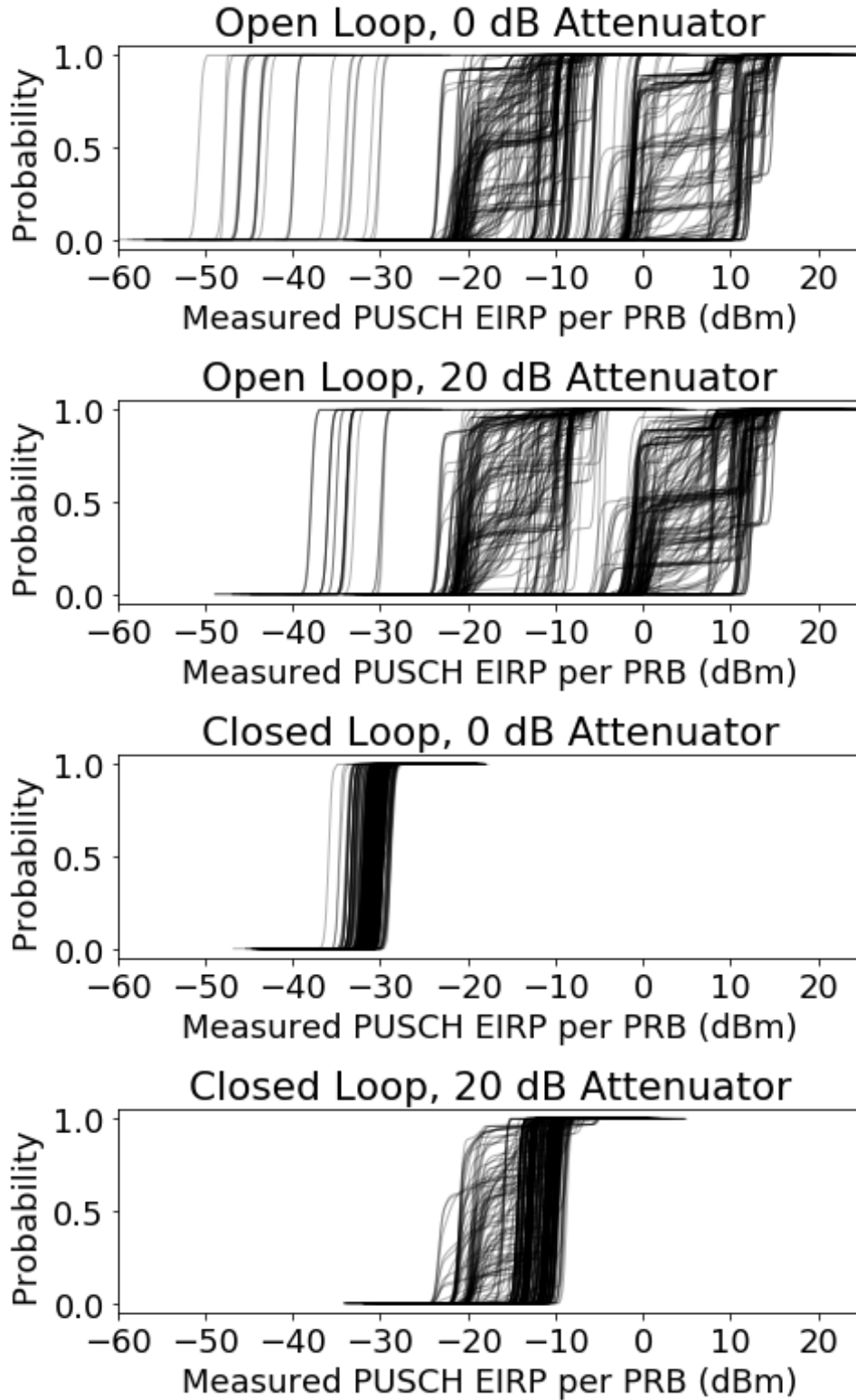


Figure 6.31: Summary of empirical CDFs for measured PUSCH power per PRB for all test configurations organized by power control type and testbed attenuation setting.

6.3.3 Empirical CDFs for measured PUCCH power per PRB

The global summary plots of all empirical CDFs for measured PUCCH power per PRB are given in Figures 6.32 and 6.33. Overall, the range of measured PUCCH power per PRB spanned roughly 70 dB, consistent with the PUSCH measurements. Also, as shown in Figure 6.33, the PUCCH power per PRB distributions with open-loop power control spanned a much larger range than the distributions with closed-loop power control.

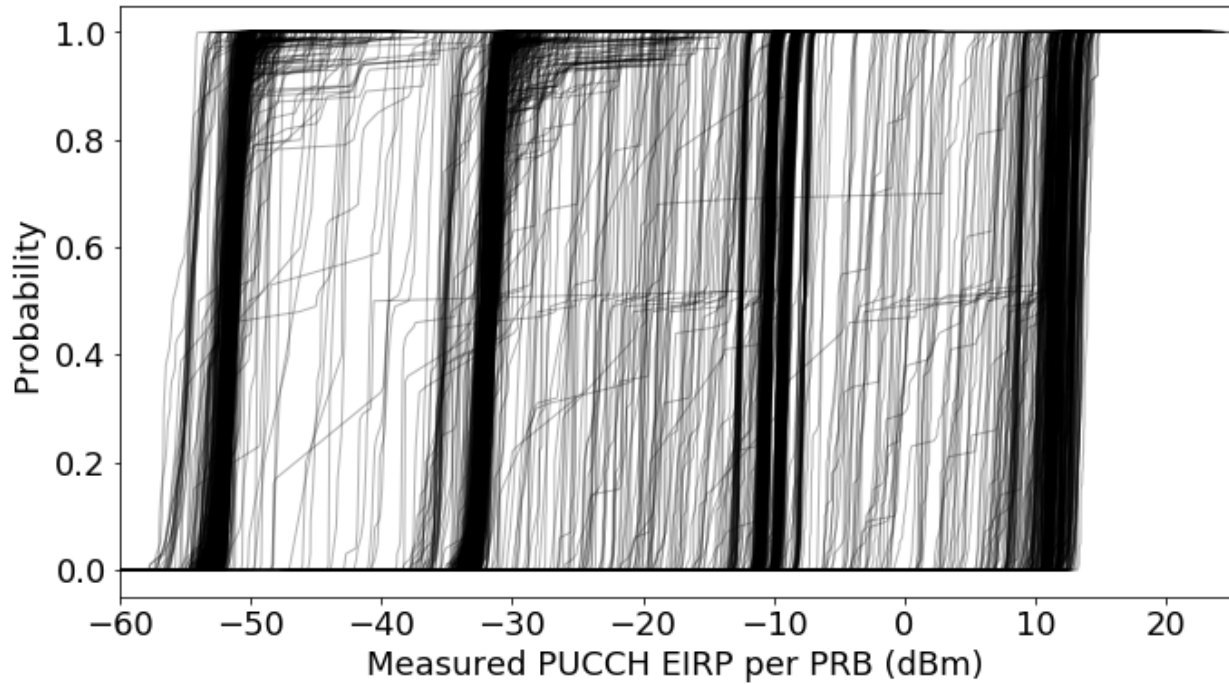


Figure 6.32: Summary of empirical CDFs for measured PUCCH power per PRB for all test configurations in the screening experiments. This plot contains approximately 4000 unique CDFs.

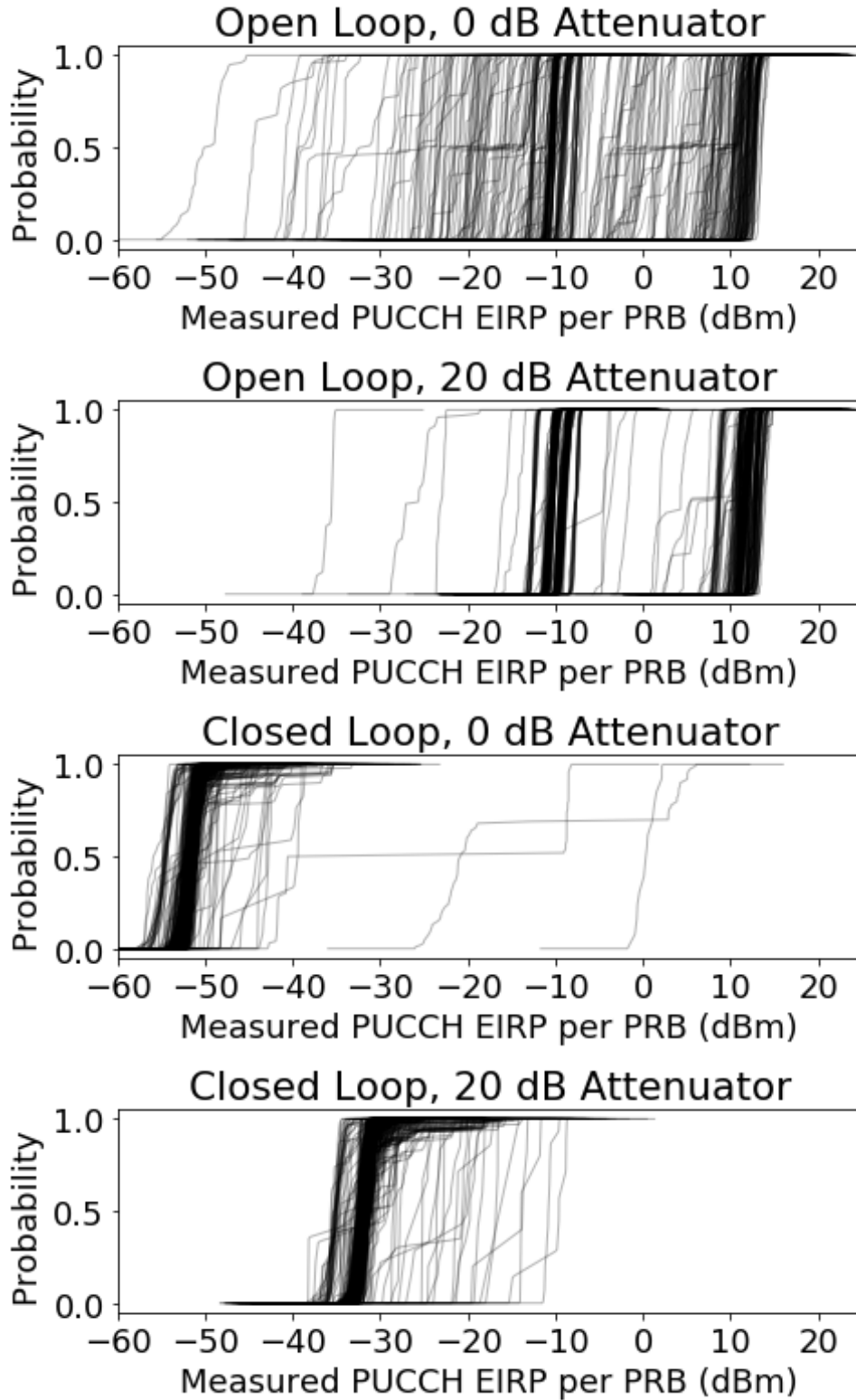


Figure 6.33: Summary of empirical CDFs for measured PUCCH power per PRB for all test configurations organized by power control type and testbed attenuation setting.

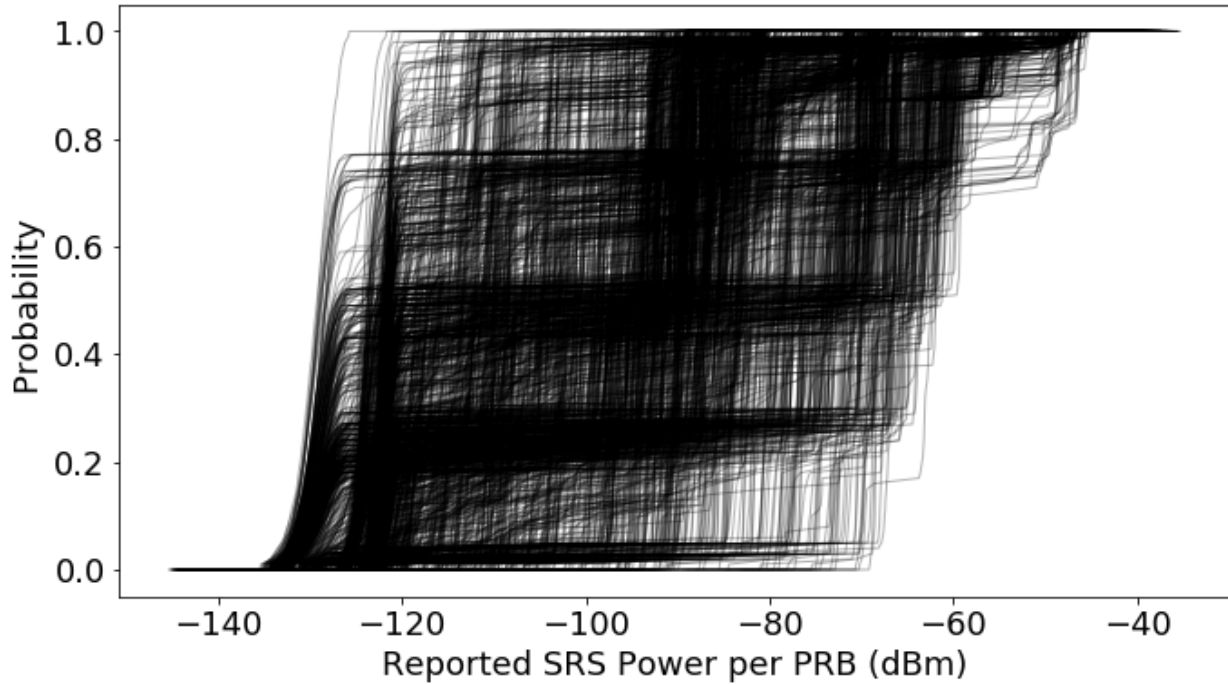


Figure 6.34: Summary of empirical CDFs for UE-reported SRS power per PRB for all test configurations in the screening experiments. This plot contains approximately 2000 unique CDFs.

6.3.4 Empirical CDFs for reported SRS power per PRB

Because the VSA spectrograms were processed and aligned into 1 ms bins, the measurements did not have enough time-resolution to capture SRS activity cleanly, since SRS transmissions occupy only one orthogonal-frequency division multiplexing (OFDM) symbol. Nonetheless, UE-reported SRS power was collected by the diagnostic monitoring software. Because the factor screening experiment was not specifically designed to assess the factors impacting SRS transmissions, a formal analysis of the reported SRS power data was not attempted. A global summary plot of empirical CDFs for the UE-reported SRS power per PRB across all test configurations is shown in Figure 6.34. Since half of all test configurations had the SRS feature enabled, there are roughly 2000 unique CDFs in this plot.

6.3.5 Comparison of Measured EIRP and UE-Reported PUSCH Power per PRB

In this section, for PUSCH, the test team compared the measured DUT EIRP per PRB to the UE-reported power per PRB. Note that there is no expectation that these values are the same. Namely, since the UE-reported power is not clearly defined by the 3GPP LTE standard or by the documentation for the USRD monitoring software, the reference plane is unknown. Ideally, the expected relationship between measured EIRP and UE-reported power is a linear trend with unit slope and an intercept equal to the equivalent offset.

Figure 6.35 contains plots comparing the median UE-reported and measured EIRP per PRB (in dBm) across all non-default experimental runs. Namely, Figure 6.35a shows a histogram of the difference between the median UE-reported and measured EIRP per PRB, and Figure 6.35b shows a scatter plot comparing median UE-reported and measured EIRP per PRB. The histogram displays three distinct regions, indicated with different colors. The first, identified as Region I, is tightly clustered with a mean of 4.4 dB and a standard deviation of 1.0 dB. The second, identified as Region II, is similarly narrow with mean of 8.1 dB and standard deviation of 0.9 dB. The third region, labeled

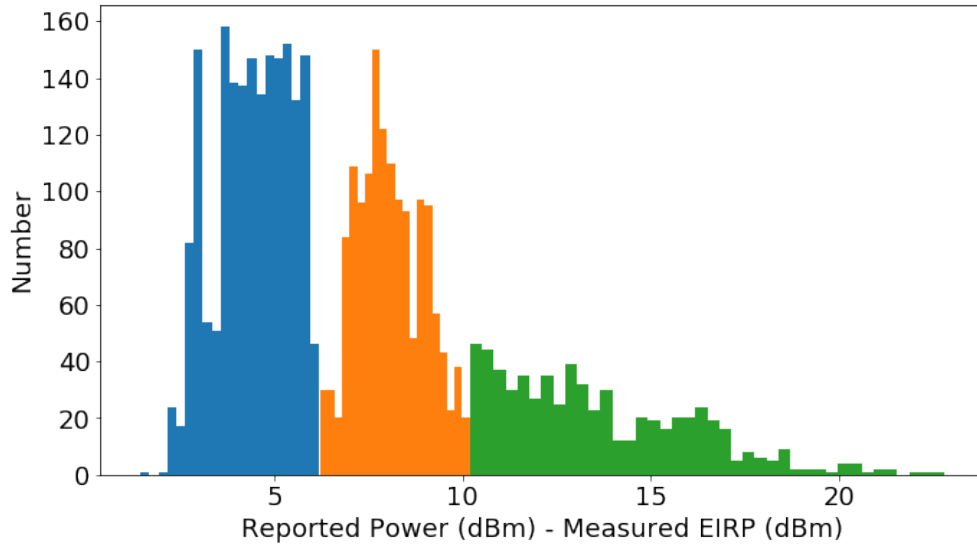
Region III, is much broader, with a mean of 13.1 dB and a standard deviation of 2.6 dB. Although this region deviates from the expected relationship, note that the UE-reported power per PRB is always less than measured EIRP, i.e. the UE never transmitted more power than it reported.

Across the roughly 4000 configurations tested in the factor screening experiment, approximately 47 % were in Region I, 37 % were in Region II, and 16 % were in Region III. Although these percentages are informative in the context of this experiment, please note that they are not indicative of the proportions expected in field, since the factor screening experiment was designed to test extremes, not to replicate realistic field conditions.

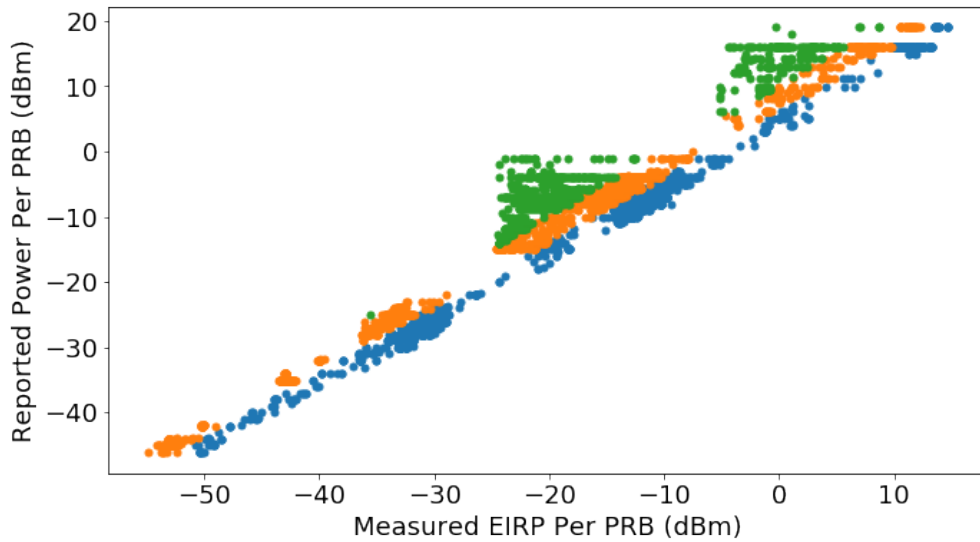
Figure 6.36 shows scatter plots of Region I, Figure 6.36a, and Region I together with Region II, Figure 6.36b, with best fit lines for Region I and Region II, respectively. The regression lines confirm the expected relationship between UE-reported and measured EIRP, with a unit slope and an intercept approximately equal to the offset between the UE-reported power and measured EIRP.

By contrast, the points in Region III clearly did not follow a linear relationship, as shown in Figure 6.35b. Region III behavior is further illustrated in Figure 6.37, which contains a scatter plot summarizing results for all tests of eNB configuration #10. This plot shows that for many tests of eNB configuration #10, the median UE-reported power was constant over a large range of measured EIRP values.

Careful investigations of the eNB and non-eNB configurations with results in Region III revealed that no single factor was responsible, and that these cases likely arose from complex interactions between the eNB and non-eNB factors. Figure 6.38 presents a bar chart showing the composition of tests in each region by eNB configuration number. Note that since there were $4 \times 32 = 128$ tests of each eNB configuration, the maximum height for each bar is 128; values less than 128 indicate missing data. This chart shows that all configurations with region III tests also had some tests in region I or region II. In addition, there were many eNB configurations (#2,3,4,7,9,14,17,18,19,22,28,31) with no anomalous Region III tests.

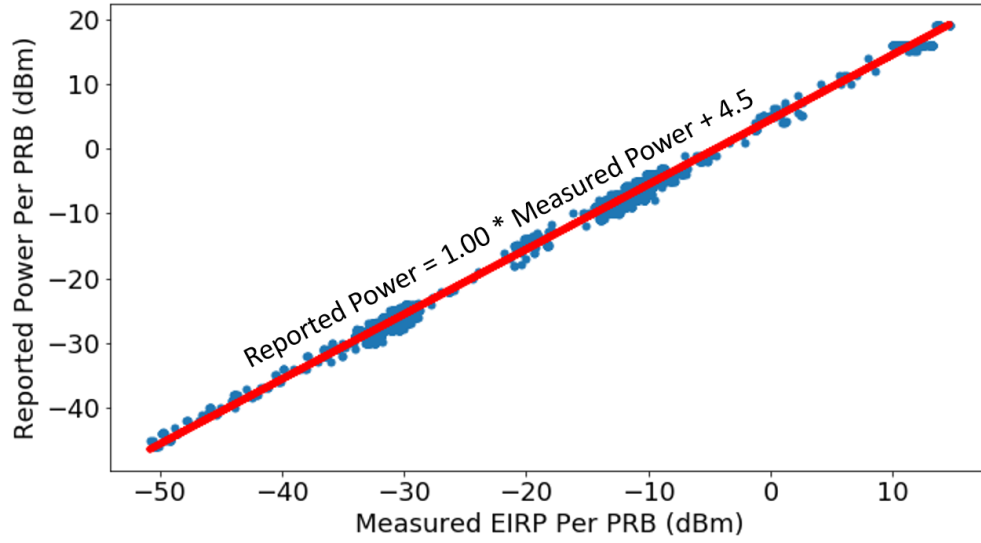


(a) Histogram of difference.

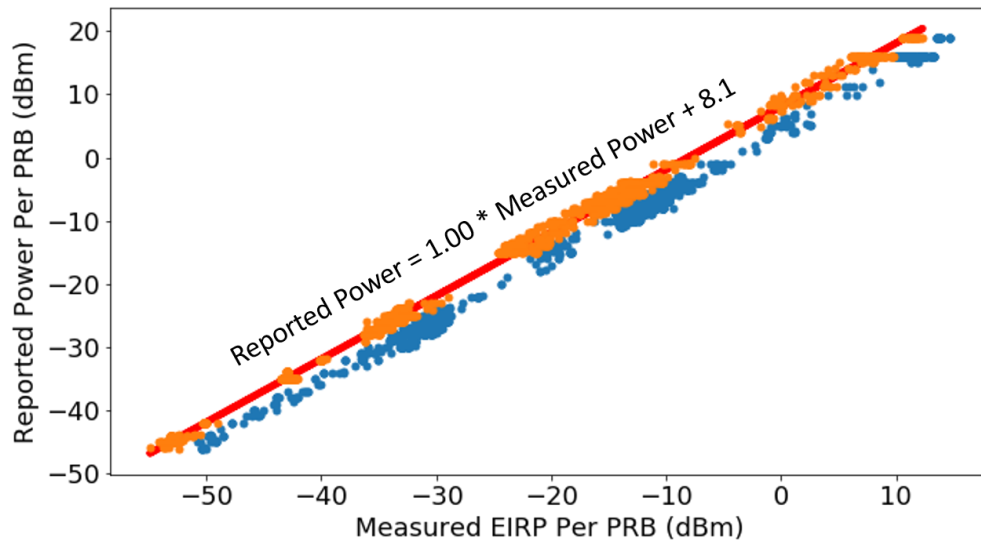


(b) Scatter plot.

Figure 6.35: Overall comparisons of median UE-reported and measured PUSCH EIRP per PRB. The approximate conversion factor between measured EIRP and reported power at the DUT UE is $7.5 \text{ dB} \pm 2.3 \text{ dB}$.



(a) Scatterplots for Region I only



(b) Scatterplots for Region I together with Region II

Figure 6.36: Scatterplots with best-fit lines through Region I and Region II.

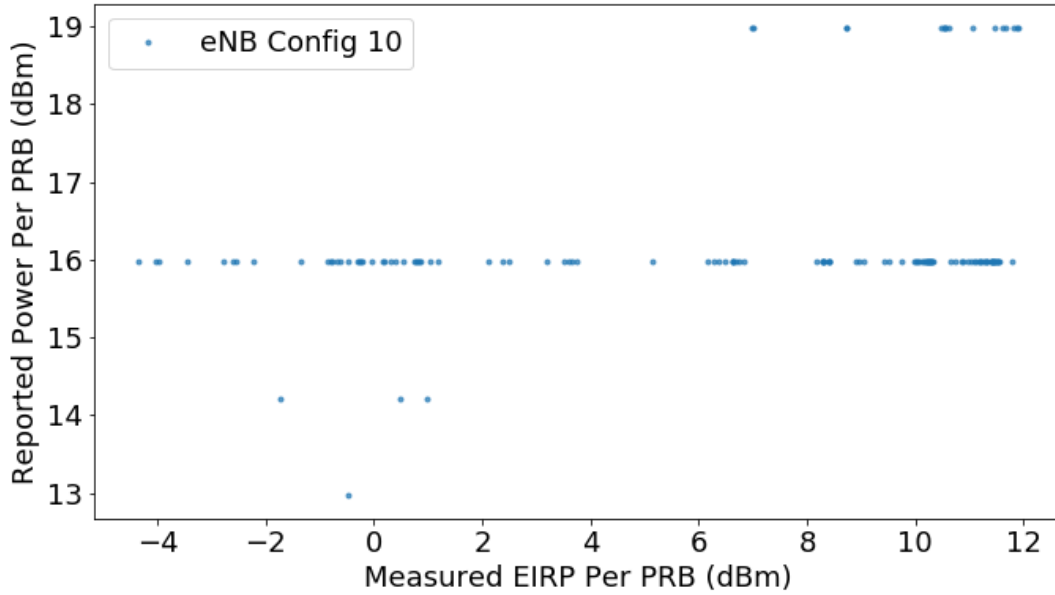


Figure 6.37: Aggregate results for all tests of eNB configuration #10. Scatterplot of median reported power per PRB versus median measured EIRP per PRB.

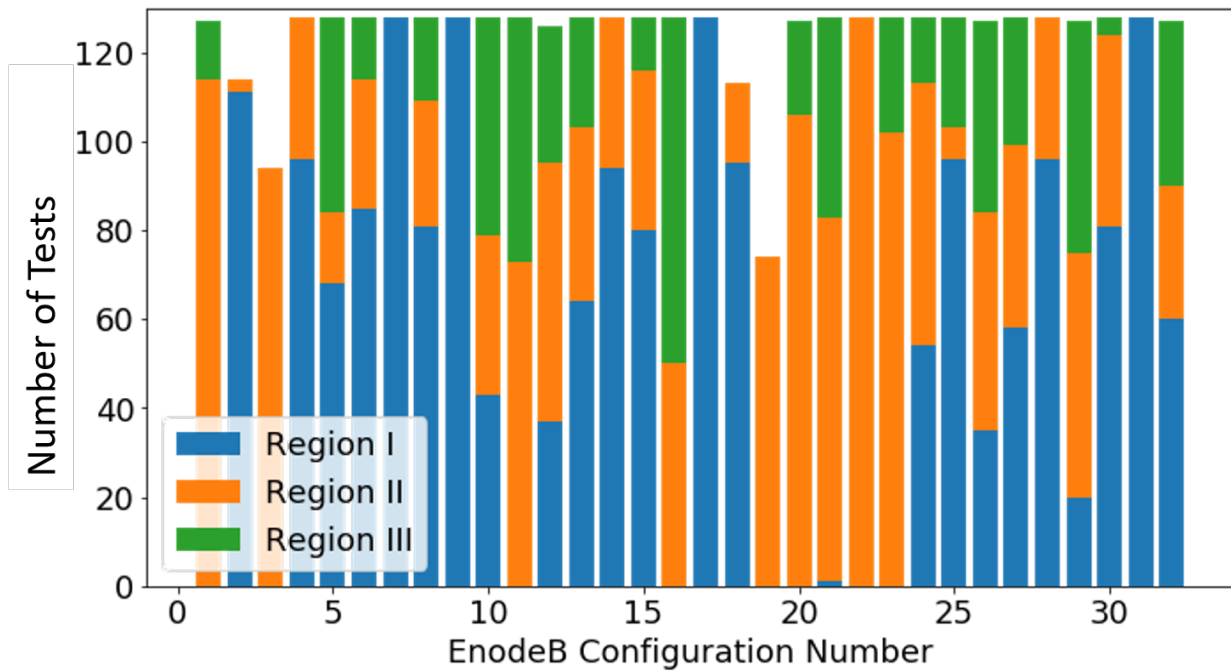


Figure 6.38: Breakdown of tests falling in Regions I, II, or III for each eNB configuration.

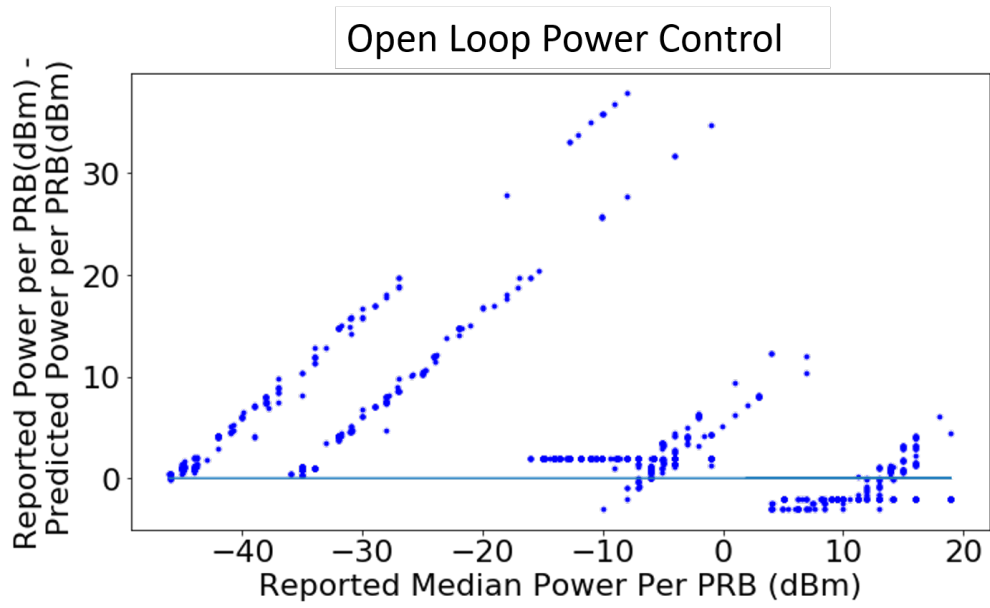
6.3.6 Comparison of Open-Loop Power Control Prediction and UE-Reported Power

As discussed in subsection 2.1.7, LTE PUSCH power control can be rather complicated. Therefore, it is natural to ask if a simplified model of LTE power control can be used to predict PUSCH emissions. To investigate this question, the test team evaluated the predictive power of the open-loop power component of the LTE power control equation, excluding the MCS-dependent term using the model

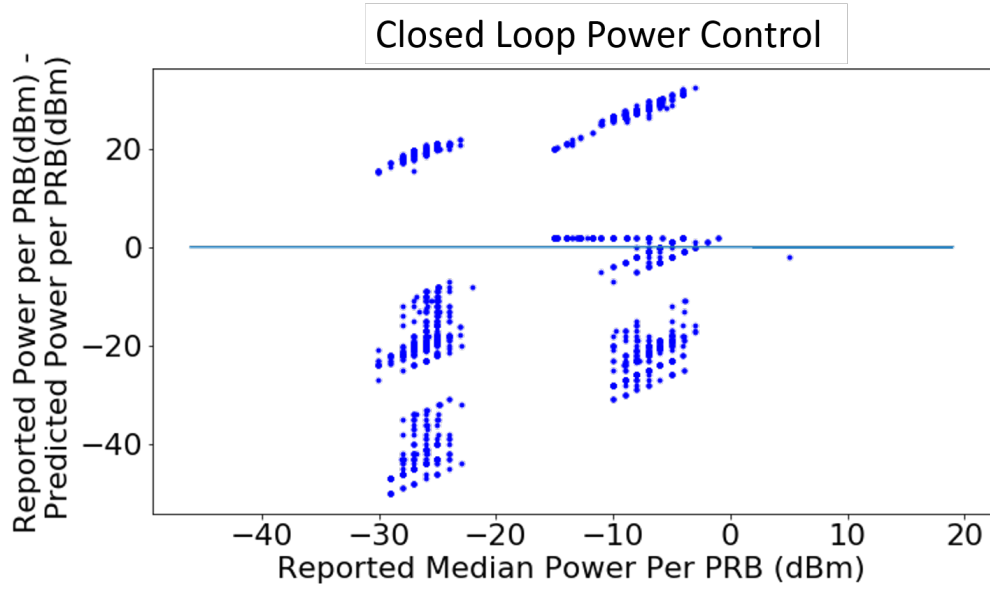
$$P_{\text{PredictedPower}} = \min[P_{cMax}, 10 \log_{10}(M_{\text{PUSCH}}(i)) + P_{0 \text{ PUSCH}}(i) + \text{PL } \alpha(i)], \quad (6.2)$$

where the notation is as defined in subsection 2.1.7.

In Figure 6.39 the difference of median UE-reported and predicted PUSCH power per PRB is plotted for all tests against the UE-reported power. The open-loop cases are shown in Figure 6.39a and closed-loop power control cases are shown in Figure 6.39b. Note that when the prediction and the UE-reported power agree, the value is 0 dB. In both cases, the Equation 6.2 has little predictive utility. In the open-loop case, it can be seen that the UE-reported power generally exceeded the prediction.



(a) Open-loop power control tests.



(b) Closed-loop power control tests.

Figure 6.39: Comparison of reported PUSCH power per PRB to prediction from the open-loop component of the LTE power control equation.

Chapter 7

Inferential Data Analysis

The previous chapter identified and explored noteworthy post-hoc features in the collected data. The present chapter makes an inferential analysis of the experiment data to answer the formal, planned statistical questions associated with a screening experiment. Specifically, this chapter addresses for each screening factor whether its main effect is statistically significantly non-zero and, where so, estimates the main effect's size and direction. The chapter is organized into two sections, the first section introducing the methods used and the second presenting the inferences drawn for each of the screening factors.

7.1 Methods

This section presents the methods used to test factor main effects, presenting the multivariate analysis of variance (MANOVA) model in the first subsection and the test for non-zero significance in the second subsection. The MANOVA model and its associated test for main effect are standard and well-known and only briefly presented in these two subsections. The screening experiment presented two significant inferential analysis challenges, the distributional nature of the measured PUSCH power response and the multiple comparisons required in this setting. Subsection 7.1.3 details the issue of the PUSCH power distribution response measured in this experiment and the way this distributional response is treated in this analysis. Subsection 7.1.4 addresses the multiple comparisons required for factors with more than two levels, noting the potential for inflated error rates. The relatively technical discussion in this subsection describes a new statistical procedure, a permutation-based multivariate Tukey test, that was developed to solve this multiple comparisons problem. Finally, subsection 7.1.5 discusses the trade-off between type I error (false alarm) and type II error (missed detection) that was considered by the analysis team in its selection of significance level for factor main effect testing.

7.1.1 Analysis of Variance

An analysis of variance (ANOVA) and MANOVA are used to analyze the data from the split-plot screening experiment. The general MANOVA model for a split-plot experiment is

$$\mathbf{Y} = \mathbf{D}\mathbf{b} + \boldsymbol{\delta} + \boldsymbol{\epsilon} \quad (7.1)$$

where \mathbf{Y} is an $n \times q$ response matrix (n is the number of observations and q is the number of response variables), \mathbf{D} is an $n \times p$ experiment design matrix (p is the number of factors), and \mathbf{b} is the $p \times q$ matrix of factor effects to be estimated. Model (7.1) is called an ANOVA model when $q = 1$. The terms $\boldsymbol{\delta}$ and $\boldsymbol{\epsilon}$ represent $n \times q$ whole-plot and sub-plot error matrices, respectively [16].

The design matrix, \mathbf{D} , reflects all screening factors, Table 7.1, as well as two random blocking variables, UE (a whole-plot blocking variable) and path loss (a sub-plot blocking variable). The effects of the two blocking variables are not

of interest since they are considered nuisance¹ variables; however, the blocking variables are included in the model to account for variability due to both path loss and different UEs used in the study. Blocking allows improved precision of the experiment by controlling and accounting for nuisance variables [6].

Table 7.1: Experiment design factors. All factors have two levels except Ω .

Whole-Plot (eNB)	K	Power control (closed v. open-loop)	
	N	PUCCH power control	
	O	PUSCH power control	
	P	Power control, alpha	
	Q	Receive diversity	
	R	Filter coefficient for RSRP measurements	
	S	Maximum uplink transmission power (own cell)	
	T	Minimum PRB allocation for power-limited UEs	
	U	UL improved latency timer reaction	
	V	Initial maximum number of PRBs	
	W	UL link adaptation	
	Y	Cell scheduling request periodicity	
	Z	Scheduling weight UL for SRS	
	a	Blanked PUCCH resources	
	b	Target UL outer scheduling	
	Ω	Amalgam of I,J,L,M,X (16 levels) I - UL scheduling algorithm type J - UL scheduler FD type L - SRS configuration M - SRS offset X - Extended link adaptation	
	Split-Plot (non-eNB)	A	Path Loss (Simulated DUT UE Position)
		B	Spatial size of cell
C		Number of loading UEs in serving cell	
D		Number of loading UEs in adjacent cell	
E		Spatial distribution of loading UEs in serving cell	
F		QCI value of loading UEs	
G		Traffic data rate	
H		Traffic data type (UDP/TCP)	

Two error terms, δ and ϵ , are needed for hypothesis testing because of the special structure of the split-plot design [17]. The interaction among all whole-plot factors and the UE serves as the whole-plot error term, while the residual mean-squared-error serves as the sub-plot error term.

Model (7.1) in its ANOVA form assumes that the measurement errors ϵ are independent and identically $N(0, \sigma^2)$ distributed with constant variance σ^2 (homoscedasticity) across all factor combinations. Model (7.1) in its general MANOVA form assumes measurement errors ϵ are independent and identically multivariate normally distributed with zero mean vector and covariance matrix Σ with constant covariance matrix across all factor combinations. MANOVA models apply only for interval data, as is the case in this experiment with measured power.

¹In experimental design terminology, a nuisance factor is a factor that may influence the experimental response, but that is not of direct interest [6].

7.1.2 Hypothesis Testing

The ANOVA and MANOVA assumptions are required for hypothesis testing. The null and alternative hypotheses are formally written:

$$H_0 : \text{Factor Main Effect} = 0,$$

$$H_a : \text{Factor Main Effect} \neq 0,$$

where "Factor Main Effect" is the difference in the mean responses at the factor's two levels being compared. The means at each level are understood to be averages over all points in the experiment design space with the factor under test set to that particular level. An F test was used for univariate responses (ANOVA) to determine the statistical significance of each main effect. The test statistic is

$$F = \frac{\text{MS Factor}}{\text{MS Error}}, \quad (7.2)$$

where MS Factor is the sum-of-squares for the factor divided by the degrees of freedom for the factor, and MS Error is the sum-of-squares for the error term divided by the degrees of freedom for the error term. The denominator of the test statistic depends on whether a whole-plot or sub-plot factor is being tested. The degrees of freedom for a factor is the number of levels minus 1. For this study, all factors except Ω have one degree of freedom. There are 15 degrees of freedom for testing Ω . The test statistic is compared to an F distribution with degrees of freedom for the factor and degrees of freedom for the error term. The null hypothesis is rejected if the p-value associated with the test statistic is less than $\alpha = 0.05$. (See [6] for information regarding analysis of variance F tests.) In other words, if the p-value is less than 0.05, there is a statistically significant effect due to that factor.

Factor effects for multivariate responses (MANOVA) were tested using Wilks' Lambda.² Other multivariate tests such as: Pillai's Trace, Hotelling-Lawley Trace, and Roy's Greatest Root are available; however, they produce p-values that are identical to those observed for Wilks' Lambda.

7.1.3 Response Variables

A designed experiment typically has a univariate response, and its purpose is to model central tendency. The present screening experiment aimed to screen factors not just on central tendency but on the full observed PUSCH power distribution. This type of analysis is rarely attempted, and the present screening experiment offers the further complication that many of the PUSCH power distributions under investigation have multiple modes and are not well-described by, say, the mean and standard deviation. To address the distributional nature of PUSCH power, the analysis team decided to work in terms of the 99 centiles C_1, C_2, \dots, C_{99} of each distribution, making the response a 99-component vector. The challenge of this approach led the analysis team to:

1. Introduce new summary center, spread, and skew statistics C_{50} , C_S , and C_Q to summarize C_1, C_2, \dots, C_{99} . This has the simple advantage of basing the analysis on just a small number of intuitive statistics, making the results more accessible to scientists and engineers.
2. Develop a new statistical procedure to treat multiple comparisons of multivariate responses. A Tukey test for multivariate multiple comparisons is known for a few combinations of dimension and number of levels, but it does not apply generally nor, in particular, is it applicable to the present experiment. Using a modern, computationally-driven approach, the inferential analysis team developed an innovative permutation-based multivariate Tukey test (described in 7.1.4). This procedure has the potential to become a standard statistical tool for multivariate multiple comparisons.

²Details regarding Wilks' Lambda are beyond the scope of this paper. See [18] for more information.

- Use principal component analysis (PCA) to confirm the effective use of the experiment data. PCA is a powerful tool for investigating the information content in a collection of variables, and PCA naturally finds use in various ways in conjunction with MANOVA. PCA is used here in a novel way to show that little is lost by the reduction of the response to C_{50} , C_S , and C_Q .

The success of this innovative combined approach to the analysis of this screening experiment recommends its use in similar experiments.

The 99 centiles of each PUSCH power distribution were used as a conceptual representation of the distribution. To make the experiment analysis computationally and statistically tractable, though, a subset of three centiles and their combinations were used for analysis. Specifically, the analysis used the median (C_{50}), centile spread ($C_S = C_{95} - C_5$), and centile skew ($C_Q = (C_{95} - C_{50}) - (C_{50} - C_5)$) as response variables for analysis. Note that any linear combination of these three summary statistics would yield the same results within the context of the linear model (7.1). In particular, analysis based around (C_5, C_{50}, C_{95}) instead of (C_{50}, C_S, C_Q) would yield the same results; however, the median, centile spread and centile skew are more intuitive and easier to interpret than the three centiles. This data reduction strategy — using (C_{50}, C_S, C_Q) instead of the full 99-centile response — potentially entails information loss. To assess this loss, a principal components analysis [19] using scores based on linear combinations of the 99 centiles was done. This analysis with principal component scores shows (presented in 7.2.3) that very little information is lost by the use of (C_{50}, C_S, C_Q). This is important for similar experiments where PUSCH power is being studied as a distribution: the trivariate statistic (C_5, C_{50}, C_{95}) captures the fundamental elements, center, spread, and shape, of a distribution and is relatively easily to interpret, it is relatively amenable to analysis, and very little distributional information is lost by its use.

7.1.4 Multiple Comparisons

For two level factors, F tests of MANOVA model (7.1) test for differences between the two factor level means. When a factor has more than two levels, the F test only indicates whether at least one pair of the factor level means are different; it does not identify which pair(s) are significantly different. For factors with more than two levels, multiple comparisons of the factor level means are required, potentially inflating overall error rate. Tukey's studentized range test (or honest significant difference test) accomplishes these multiple comparisons while controlling the family-wise error rate. The null and alternative hypotheses for the Tukey test are

$$\begin{aligned} H_0 : \quad & \mu_i - \mu_j = 0 \\ H_a : \quad & \mu_i - \mu_j \neq 0, \end{aligned}$$

for all $i \neq j$. Significant differences are identified by comparing mean studentized differences to the minimum significant difference as defined by the studentized range distribution [6].

While the univariate Tukey test is widely used, a Tukey test for multivariate data is not readily available. Thus, the analysis team developed a multivariate Tukey test based on simulating the null distribution of the multivariate studentized range [20]. A single value from the null distribution of the multivariate studentized range statistic is simulated by permuting the rows of the response matrix, fitting the MANOVA model (7.1), and computing distances between factor level means, d_{ij} , over all possible pairs. The multivariate studentized range statistic, R_{max} , is the maximum of the d_{ij} values. The procedure is repeated for many different permutations of the response matrix to obtain the null distribution of the multivariate studentized range.

Distances between pairs of factor level means are computed using

$$d_{ij} = \sqrt{(\mathbf{x}_i - \mathbf{x}_j)' \mathbf{L}^{-1} (\mathbf{x}_i - \mathbf{x}_j)}, \quad (7.3)$$

where \mathbf{x}_i and \mathbf{x}_j represent the vectors of means for the i th and j th factor levels. The \mathbf{L} matrix is analogous to a multivariate mean-squared error. For example, in the trivariate case, the \mathbf{x}_i vector contains the i th factor level means of the C_{50} , C_S and C_Q , and the \mathbf{L} matrix has the form

$$\mathbf{L} = \begin{bmatrix} \sigma_{C_{50}}^2 & \sigma_{C_{50},C_S} & \sigma_{C_{50},C_Q} \\ \sigma_{C_{50},C_S} & \sigma_{C_S}^2 & \sigma_{C_S,C_Q} \\ \sigma_{C_{50},C_Q} & \sigma_{C_S,C_Q} & \sigma_{C_Q}^2 \end{bmatrix}, \quad (7.4)$$

where the elements of the matrix correspond to error variances and covariances of the three responses. The only multi-level factor in this study, Ω , is a whole-plot factor so the \mathbf{L} matrix is based on the δ error term instead of the mean-squared error, ϵ .

For $\alpha = 0.05$, the critical value is defined as the 95th percentile of the simulated null distribution of R_{max} . Values of distance for the observed data larger than the critical value are significant, indicating that the corresponding two factor level means are different. The simulated studentized range distributions are displayed in Figure 7.1 for the univariate, bivariate, and trivariate cases.

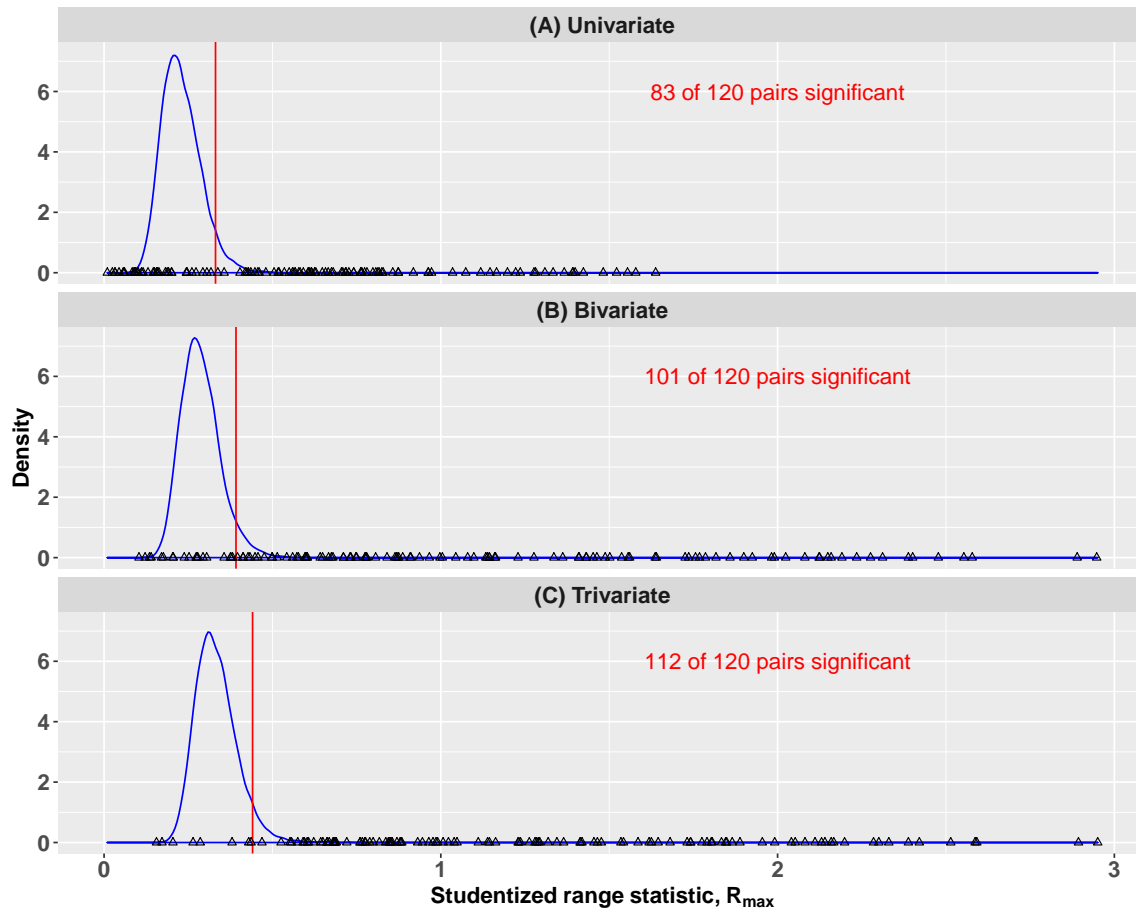


Figure 7.1: Simulated studentized range (R_{max}) densities for (a) univariate, (b) bivariate, and (c) trivariate cases. The vertical red lines indicate critical values associated with $\alpha = 0.05$. The black triangles represent all possible pairs of observed differences (d_{ij}) between factor levels. Since Ω has 16 factor levels, there are 120 computed differences. Critical values are 5.26, 0.39, and 0.44 for the univariate, bivariate, and trivariate cases, respectively.

7.1.5 Significance Level

This experiment was planned to screen 27 factors. Five of these factors, I, J, L, M, and X, were combined into the single 16-level factor Ω , so the experiment's design and ANOVA models effectively involved 23 factors. The statistical analysis of the experiment therefore required 23 decisions (hypothesis tests) about statistical significance of factor main effect. Depending on the true nature of the factor effect, each of these tests is vulnerable to either Type I error (i.e., false positive) or type II error (i.e., false negative). The (conditional) probabilities of these errors are α and β , respectively, where α is, in fact, the significance level of the test. These error probabilities are inversely related, necessitating a trade-off between them. The significance level α is set by the analyst, allowing direct control of the test's type I error probability. A test's type II error probability β is determined by a host of parameters, including α , sample size, type of inference, and the degree of random variation present in the data, so α effectively determines the trade-off made between the test's type I and type II error probabilities.

In an experiment involving multiple statistical decisions — 23 tests in this screening experiment — each decision has its own risk. These risks accumulate with the number of tests, and the overall error in the experiment has to be considered. This overall error is quantified by the family-wise type I error probability α_F and the number of type I errors N_I . The mean number $E[N_I]$ of type I errors satisfies $E[N_I] = M\alpha$, where M is the number of tests to be made in which the factor effect is zero. The family-wise type I error probability α_F is the probability of making *any* type I errors in the experiment analysis and is given approximately by

$$\alpha_F = 1 - (1 - \alpha)^M. \quad (7.5)$$

Factor Ω has 16 levels, and as noted earlier, its 120 pairs of levels amount to 120 effect tests. However, the Tukey analysis of factor Ω has the property that the chosen significance level $\alpha = 0.05$ is the family-wise error rate for the analysis. In budgeting for error among the 23 factors in the experiment, the Tukey analysis counts for just one inference.

The test and analysis teams chose in planning for the screening experiment to use $\alpha = 0.05$. This is a standard choice for statistical inference. For the screening experiment $\alpha = 0.05$ was chosen based on a consideration of α_F and N_I . The analysis team judged conservatively that maybe $M = 10$ of the 23 factors would have zero effect, in which case with $\alpha = 0.05$, the number of type I errors is approximately binomially distributed (Figure 7.2), with $E[N_I] = 0.5$ and family-wise type I error probability 0.6. The analysis team deemed $E[N_I] = 0.5$ to be an acceptable number of type I errors in a screening experiment with 23 factors.

The preceding analysis of type I error probability and the choice $\alpha = 0.05$ does not account for type II error. The judgment of the test team's LTE engineers was that with factor levels chosen to be widely separated and the planned amount of data collection, few missed detections (type II errors) would occur among the 23 tests. A missed detection is only possible where a factor effect is judged to be zero. In fact, because most of the factors in the experiment were found in testing to have non-zero effects, the opportunities for missed detections are few and the number of type II errors among the results of the screening experiment is necessarily small.

7.2 Results

This section is organized into seven subsections. The first subsection sets out as a preliminary matter the number of design points from which data were obtained and the sample sizes those design points yielded. Subsection 7.2.2 presents the inferential conclusions reached with respect to measured PUSCH power, discussing MANOVA results for main effects in the case of the two-level experiment factors and the Tukey results for the one sixteen-level factor. These measured PUSCH power results are based on the summary power distribution statistics C_{50} , C_S , and C_Q . Sub-

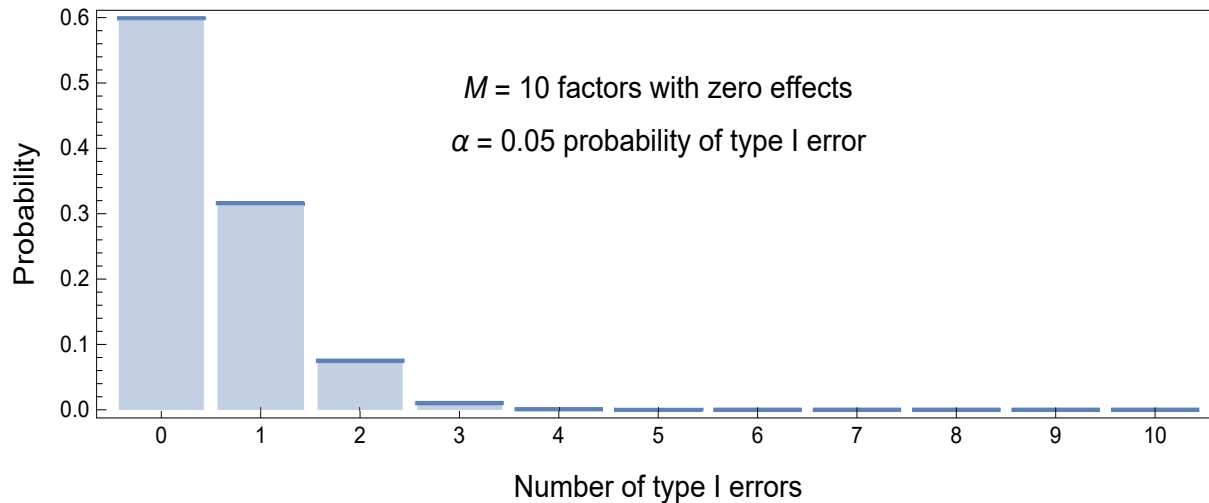


Figure 7.2: Approximate distribution of the number of type I errors in an experiment with 23 factor effect tests, each with $\alpha = 0.05$ significance level, in which ten of the 23 factors are assumed to have zero effect. Under these conditions the probability of no more than one type I error is 92 %.

section 7.2.3 presents a principal components analysis to validate the use of this restricted set of statistics. Subsection 7.2.4 makes an analysis of reported PUSCH power paralleling that given for measured PUSCH power, comparing the results from the two analyses. Using the same analysis approach from subsection 7.2.2, subsection 7.2.5 treats measured PUCCH power. The last two subsections offer cautions and suggest best practices for the conduct of screening experiments.

7.2.1 Sample Size

In this study, each of the 1024 factor combinations was measured on four separate occasions, so the experiment-wise sample size should be 4096. Some factor combinations did not produce viable data, so the sample sizes are less than 4096. The actual sample sizes for measured PUSCH, reported PUSCH, and measured PUCCH are 3978, 3973, and 3748, respectively.

A secondary sample size reflects the number of measurements used to create the response distribution for a single factor combination. Response distribution sample sizes vary widely among factor combinations. Figure 7.3 displays sample sizes obtained for measured PUSCH response distributions corresponding to each eNB and non-eNB factor combination for the four rounds of measurements. Response distribution sample sizes for measured PUSCH range from 18 to 227 633. For reported PUSCH (Figure 7.4), response distribution sample sizes are generally smaller than for measured PUSCH and range from 6 to 18 802. Measured PUCCH response distribution sample sizes are displayed in Figure 7.5. No measured PUCCH response distributions were obtained for 348 factor combinations, and response distribution sample sizes range from 1 to 2084.

The centiles derived from response distributions with small sample sizes have much higher variability than centiles derived from large samples. Homogeneity of variance is a key assumption in ANOVA and the method is fairly robust to violations. For some cases, which are noted, the variability among the response distribution can differ by a factor of 100.

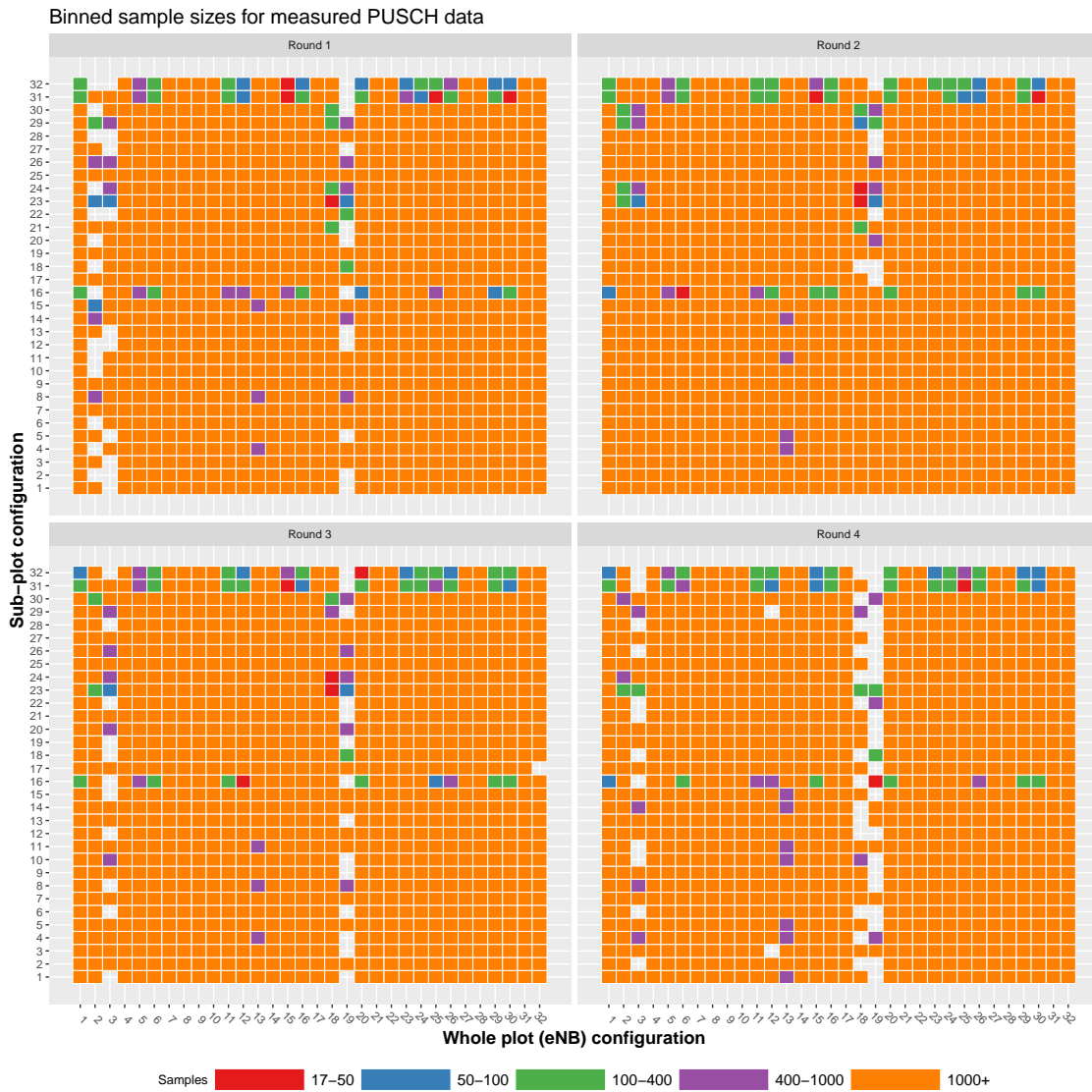


Figure 7.3: Heat map of measured PUSCH response distribution sample sizes obtained for each eNB and non-eNB factor combination for each round of measurements. Data is missing (grey boxes) for 118 factor combinations. Response distribution sample sizes range from 18 to 227 633.

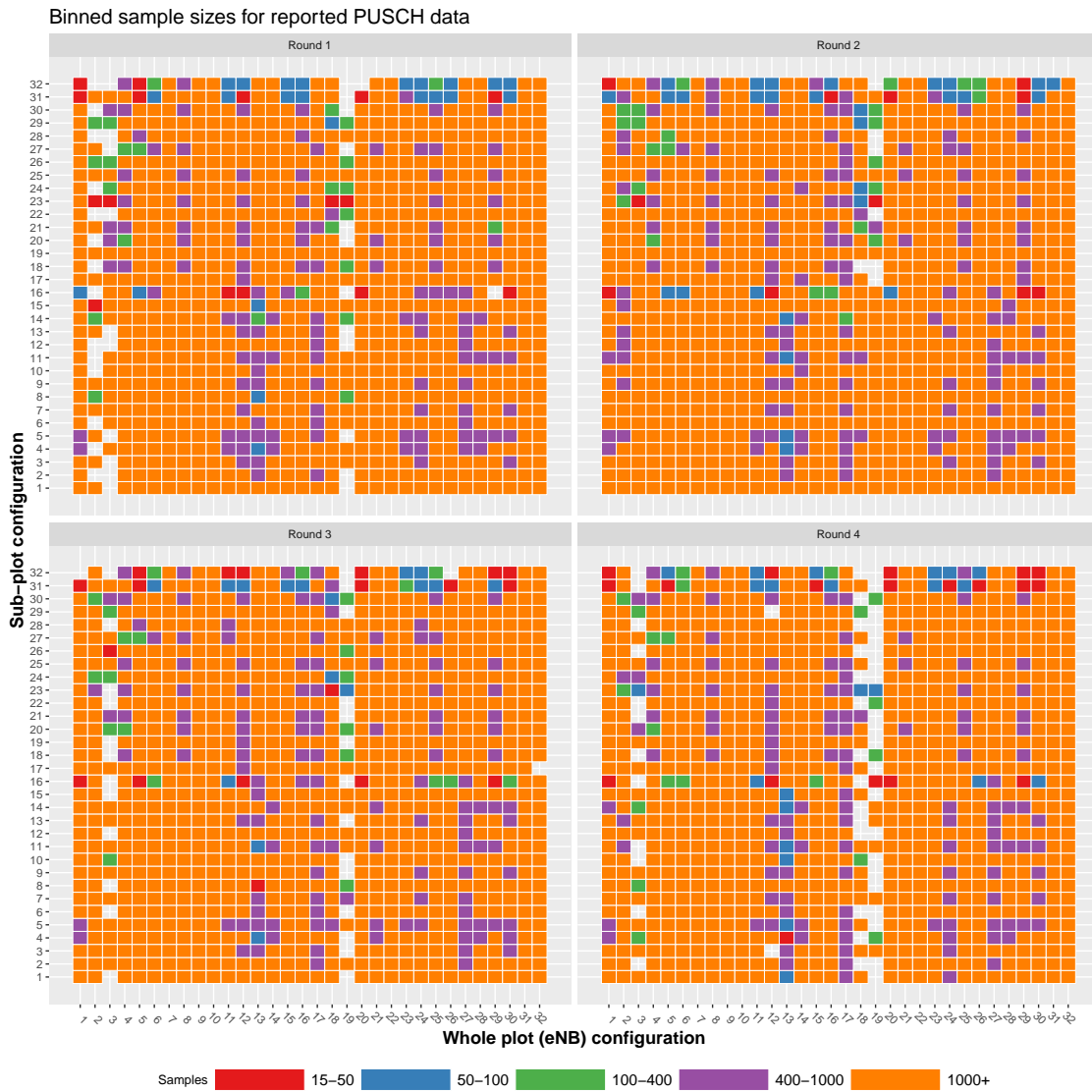


Figure 7.4: Heat map of reported PUSCH response distribution sample sizes obtained for each eNB and non-eNB factor combination for each round of measurements. Data is missing (grey boxes) for 123 factor combinations. Response distribution sample sizes range from 6 to 18 802.



Figure 7.5: Heat map of measured PUCCH response distribution sample sizes obtained for each eNB and non-eNB factor combination for each round of measurements. Data is missing (grey boxes) for 348 factor combinations. Response distribution sample sizes range from 1 to 2084

7.2.2 Measured PUSCH Power

This section presents the results of statistical analyses of the full set of measured PUSCH power data from the four rounds of the 23-factor screening experiment. The statistical analyses are based on measured PUSCH power centile statistics using the ANOVA and MANOVA models described in the previous section. Specifically, the results are of an ANOVA of the median measured PUSCH power C_{50} as well as results from MANOVAs of (C_{50}, C_S) and (C_{50}, C_S, C_Q) .

Statistical analysis of a screening experiment has the primary purpose of estimating effects of the different factors on the system response. The intent is to identify those factors that have large effects with, in the judgment of the system engineer, consequences for characterizing and predicting system performance. Screening experiments are important in this regard when working with complex natural or engineered systems so that experimental resources can subsequently be efficiently directed at the most important and interesting aspects of the system under study. Statistical analysis has the supporting purpose of identifying those factor effects that statistically significantly differ from zero. The p-values from this aspect of the analysis ensure that system scientists are not misled by effect sizes due just to random chance variation in the experiment results. This section reports p-values (Table 7.2) and factor effects for each of the 23 factors in this experiment.

Table 7.2: ANOVA and MANOVA p-values for the measured PUSCH data set.

Source	C_{50}	PC_1	(C_{50}, C_S)	(PC_1, PC_2)	(C_{50}, C_S, C_Q)	(PC_1, PC_2, PC_3)
B	.23	.32	.47	.57	.60	.48
C	.00	.00	.00	.00	.00	.00
D	.81	.70	.75	.14	.01	.03
E	.14	.32	.17	.36	.04	.08
F	.33	.40	.28	.65	.46	.83
G	.09	.07	.00	.00	.00	.00
H	.00	.02	.00	.00	.00	.00
K	.00	.00	.00	.00	.00	.00
N	.33	.33	.07	.00	.01	.00
O	.00	.00	.00	.00	.00	.00
P	.00	.00	.00	.00	.00	.00
Q	.98	.98	.07	.00	.00	.00
R	.03	.03	.09	.08	.04	.00
S	.00	.00	.00	.00	.00	.00
T	.01	.01	.00	.00	.00	.00
U	.50	.36	.00	.00	.00	.00
V	.00	.00	.00	.00	.00	.00
W	.00	.00	.00	.00	.00	.00
Y	.00	.00	.00	.00	.00	.00
Z	.04	.04	.00	.00	.00	.00
a	.36	.42	.65	.31	.00	.00
b	.00	.00	.00	.00	.00	.00
Ω	.00	.00	.00	.00	.00	.00

To determine the statistical significance of the measured effects of the 23 factors in the screening experiment, three increasingly comprehensive statistical analyses were conducted, based first on C_{50} alone, then on (C_{50}, C_S) , and then (C_{50}, C_S, C_Q) . The effect p-values from these three analyses are shown in Figure 7.6, grouped by factor. The red line in Figure 7.6 is the reference $\alpha = 0.05$ significance level. The results in Figure 7.6 reflect that adding components to the analyzed response tends to increase the power to resolve differences in factor levels. Figure 7.6 shows that

factors C through b have significant median effects, with R and Z having marginally significant effects. Factors G and U's median effects are not significant, but the factors are significant when their median and spread effects are jointly considered. Factors E, a, N, D, and Q become significant only when their median, spread, and skew effects are all jointly considered. Factors F and B are not significant even when median, spread, and skew effects are jointly considered. The MANOVAs of the bivariate and trivariate responses (C_{50}, C_S) and (C_{50}, C_S, C_Q) account for the correlations present in C_{50}, C_S , and C_Q , essentially by estimating their covariance matrices and using Mahalanobis distance to compare factor levels.

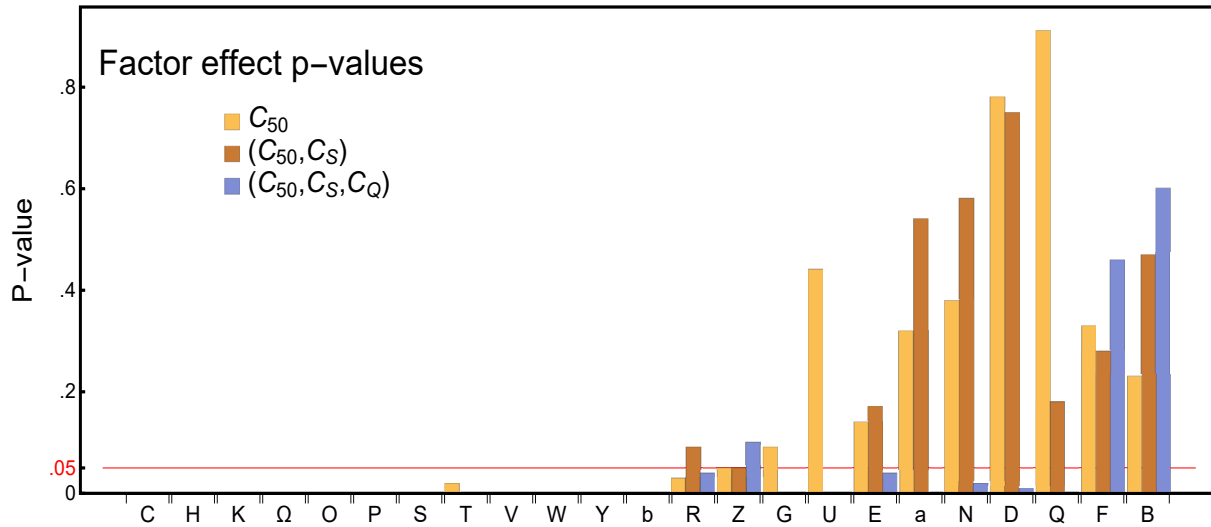


Figure 7.6: Factor effect p-values for 23 experiment factors from three increasingly comprehensive analyses based on C_{50} , (C_{50}, C_S) , and (C_{50}, C_S, C_Q) .

All the experiment factors had two levels (coded as (+1) and (-1)) except the 16-level factor Ω . For the 22 two-level factors in the experiment, their main effect is unambiguous; it is the difference in the means at their two levels ((+1) level minus (-1) level). Figures 7.7–7.9 show the estimated main effects of each of the 22 two-level factors with respect to each of the centile statistics C_{50} , C_S , and C_Q . In each plot, the main effects are shown in the same order as the p-values in Figure 7.6; main effects marked in red are not significant. Of course, a main effect considered to be statistically significant may have no practical engineering significance. For example, factor G was not statistically significant (Figure 7.7) with respect to C_{50} , but became statistically significant when (C_{50}, C_S) is considered (Figure 7.8); G's -1 dB effect on spread was sufficient to detect a difference in its two levels. However, this small -1 dB spread effect may not be practically meaningful.

Increasing the dimension of an experiment's response does not necessarily increase the experiment's resolving power. Factor R showed a weak effect (Figure 7.7) that was significant with respect to C_{50} . When factor R was considered with respect to (C_{50}, C_S) , though, its weak C_{50} effect and its even weaker C_S effect (Figure 7.8) yielded a joint effect that was not significant. The tale of factor Z is similar: Z is significant when just C_{50} is considered; it is still significant with (C_{50}, C_S) , but no longer significant when C_Q is involved.

The 16-level factor Ω is an amalgam of five pre-factors I, J, L, M, and X, jointly representing combinations of eNB settings. These five factors have dependencies; for example, $I = 0, J = 1$ is not physically realizable, and M only comes into play when $L = -1$. Also, two of the factors, I and J, have three levels that were tested. Because of these dependencies and complications, coding I, J, L, M, and X into Ω simplified the experiment's design.

The main effect of a factor in an experiment is the difference in response that results from changing the factor from

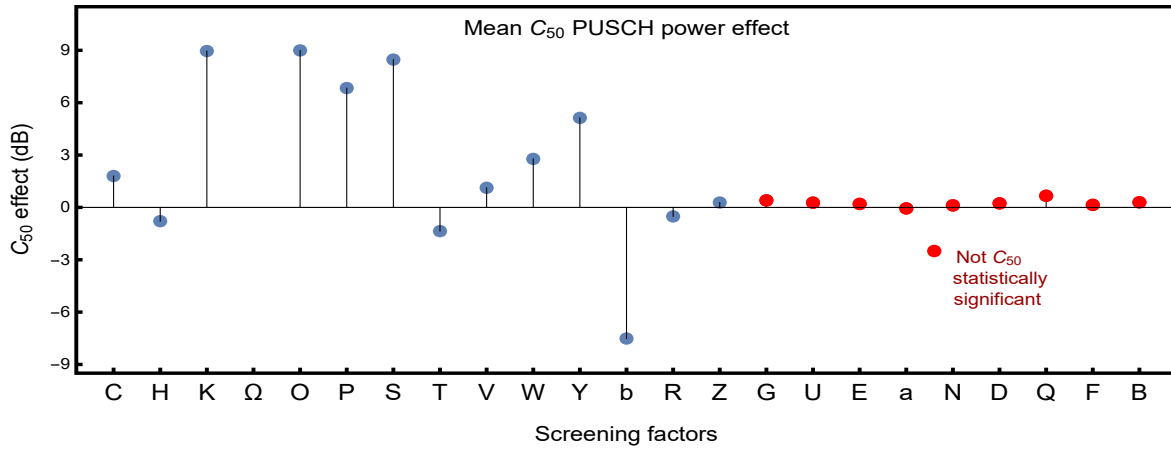


Figure 7.7: Mean factor effects on C_{50} (PUSCH power median). Factor Ω has 16 levels; its C_{50} level means are shown in Table 7.3. Effects marked in red are not statistically C_{50} -significant.

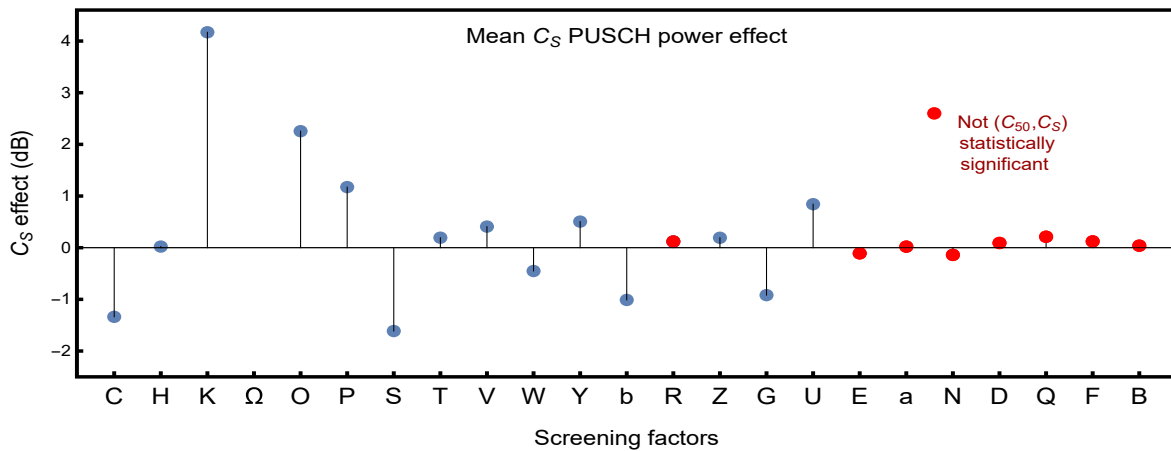


Figure 7.8: Mean factor effects on C_S (PUSCH power spread). Factor Ω has 16 levels; its C_S level means are shown in Table 7.3. Effects marked in red are not statistically (C_{50}, C_S) -significant.

one level to another. Unlike the two-level factors in this experiment, factor Ω with its sixteen levels has many (120) different effects to consider, some effects potentially significant while others not. Tukey groupings are presented in Table 7.3 to show which differences in Ω 's levels are not significant ($\alpha = .05$). The blue-colored Tukey groupings for C_{50} show, for example, that levels 7 and 11 of Ω belong commonly to group A, meaning that the mean difference in C_{50} power in levels 7 and 11 is not statistically significant. As another example, levels 2 and 12 each belong to C_{50} Tukey groups, but they do not share a group in common so they are statistically significantly different.

To the right of the levels of Ω in Table 7.3 are the levels' corresponding combinations of the factors I, J, L, M, and X. When, for example, two levels of Ω differ significantly in the C_{50} Tukey analysis, this means that the median powers of the corresponding combinations of levels of I, J, L, M, and X are significantly different. This requires careful interpretation: the effect of factor X on C_{50} is not significant when $I = J = L = M = 1$, because levels 2 and 6 of Ω are not significantly different (2 and 6 are together in group D). On the other hand, factor X's effect is significant when $I = 0, J = 0$, and $L = -1$ because levels 7 and 8 of Ω are significantly different.

The Tukey analyses presented in Table 7.3 show that the effect of basing the analysis on a multivariate response such

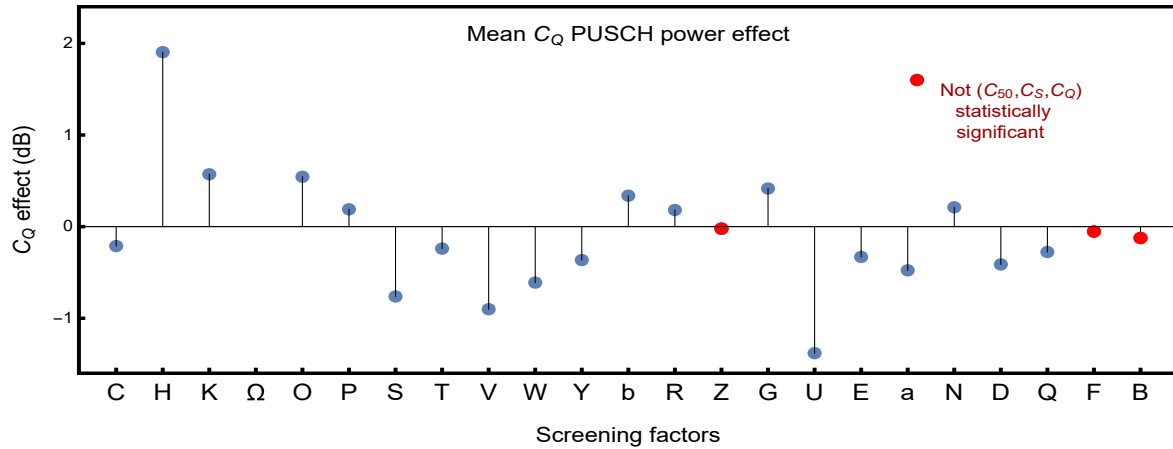


Figure 7.9: Mean factor effects on C_Q (PUSCH power skew). Factor Ω has 16 levels; its C_Q level means are shown in Table 7.3. Effects marked in red are not statistically (C_{50}, C_S, C_Q) -significant.

as (C_{50}, C_S) or (C_{50}, C_S, C_Q) instead of on just the univariate response C_{50} is to increase the resolving power of the experiment. Among Ω 's sixteen levels are 120 pairs of levels, corresponding to 120 factor effects. The Tukey analysis based on C_{50} alone can discern differences among 83 of the 120 pairs; 31 pairs of levels were found not to be significantly different at $\alpha = 0.05$. With (C_{50}, C_S) , differences between levels of Ω can be resolved in 101 of the 120 pairs, and 112 of the 120 pairs can be resolved with (C_{50}, C_S, C_Q) .

7.2.3 Principal Components Analysis

The three analyses of the measured PUSCH power data used the median C_{50} to describe the power distributions' centers, the spread $C_S = C_{95} - C_5$ to describe the power distributions' spreads, and the skew $C_S = (C_{95} - C_{50}) - (C_{50} - C_5)$ to capture the distributions' shapes through the differences in their tail lengths. These three statistics are standard and intuitive measures of the fundamental features—center, spread, and shape—of distributions, and each is measured in the same physical units (dB) as the original data. As a check to better understand whether and how these three statistics performed in the present experiment, a parallel set of three analyses was done on the first three principal components of the same response data. In this section this parallel set of analyses is described and compared with the C_{50} , (C_{50}, C_S) , and (C_{50}, C_S, C_Q) analyses presented in Figures 7.6–7.9.

A PCA of D -dimensional data—the 99-dimensional space of centiles in this experiment—linearly transforms the data, rotating it so that the largest possible fraction of the variability in the data is aligned with the first principal axis, as much as possible of the remaining variability is aligned with a second principal axis orthogonal to the first, and so on [19]. Each principal component PC_1, PC_2, \dots, PC_D of a D -dimensional data set is a linear combination of the original data vector components C_1, C_2, \dots, C_D , and all D principal components are needed to fully represent a set of D -dimensional data. Often, though, just a few principal components suffice to capture almost all of the variability in the original data. In these cases, the PCA-transformed data can be much easier than the data in original form to characterize and interpret.

PCA of the measured PUSCH power data found that 99.72 % of the measured PUSCH power data falls within a three-dimensional subspace of the 99-dimensional space of power centiles, with the first principal component PC_1 accounting for 98.71 % of the total variability in the measured power, PC_2 accounting for 0.76 % of the total variability, and PC_3 accounting for 0.25 %. The remaining 96 principal components (ie. other possible features) reflect just 0.18 % of the total variability in measured PUSCH power.

Table 7.3: Tukey groupings based on PUSCH C_{50} , (C_{50}, C_S) , and (C_{50}, C_S, C_Q) power responses for the sixteen levels of factor Ω . Two levels in the same Tukey group are not significantly different in their responses. The C_{50} means for Ω 's levels are reported relative to -100 dB. The levels of factor M labelled "na" indicate cases where factor M did not logically apply ("not applicable").

16 levels of Ω	Subfactors					C_{50} (dB)	C_S (dB)	C_Q (dB)	Tukey C_{50} groups	Tukey (C_{50}, C_S) groups	Tukey (C_{50}, C_S, C_Q) groups
	I	J	L	M	X						
4	1	1	1	-1	1	4.6	2.55	0.35	A	A	A
11	0	-1	1	1	1	7.0	1.40	-0.01		B	B
7	1	1	1	1	1	8.4	2.73	-0.24	B	A	A
8	0	-1	-1	na	-1	10.1	1.36	0.02		B	B
12	0	0	-1	na	-1	16.7	4.53	2.57	C	C	C
5	-1	1	1	1	1	17.2	4.27	1.09		D	D
15	0	0	1	1	1	18.1	6.00	0.97	D	E	E
1	-1	1	-1	na	1	19.5	4.10	0.60		F	F
2	-1	1	1	-1	1	19.6	5.05	0.03	E	C	C
6	1	1	1	1	-1	21.2	5.03	-0.22		D	D
13	0	0	-1	na	1	21.9	5.40	1.90	F	G	G
14	0	0	1	-1	1	26.1	5.54	0.31		H	H
3	1	1	1	-1	-1	28.2	5.67	0.81	I	I	I
9	0	-1	-1	na	1	28.7	7.38	0.23		J	J
0	-1	1	-1	na	-1	29.0	6.34	-0.46	J	I	I
10	0	-1	1	-1	1	30.0	5.85	1.06		J	J

An ANOVA of PC_1 paralleling (same statistical model) the analysis described earlier for C_{50} yielded the p-values shown in Figure 7.10 and in Table 7.2. Also shown for comparison in Figure 7.10 are the p-values given in Figure 7.6 from the C_{50} ANOVA. The PC_1 ANOVA p-values for the 23 screening experiment factors are consistent with those from the C_{50} ANOVA. Both analyses found factors C through R in Figure 7.10 to have significant effects ($\alpha = 0.05$), factors Z and G to be borderline significant, and the remaining factors to not be significant with p-values that tended to match up in size. Figure 7.11 compares the results of a bivariate MANOVA of (PC_1, PC_2) with the results found from the earlier bivariate (C_{50}, C_S) MANOVA. Figure 7.11 shows in this comparison that the two bivariate MANOVAs are broadly consistent. Figure 7.12 compares the p-values from trivariate MANOVA of (PC_1, PC_2, PC_3) with those from MANOVA of (C_{50}, C_S, C_Q) . Again, there is broad consistency in the sets of p-values. These comparisons in Figures 7.10–7.12 support the validity of the statistical results reported from the C_{50} , (C_{50}, C_S) , and (C_{50}, C_S, C_Q) analyses of the screening factor effects.

Beyond confirming the results from the C_{50} , (C_{50}, C_S) , and (C_{50}, C_S, C_Q) analyses, the parallel PCA-based analyses help justify using C_{50} , C_S , and C_Q as bases for analysis. To see this, recall that the principal components of a D -dimensional data set are linearly weighted combinations of the D original data components. For the power data in terms of $D = 99$ centiles, for example, the k th principal component is

$$PC_k = \sum_{i=1}^{99} w_{ik} C_i, \tag{7.6}$$

where C_i is the i th centile and w_{ik} is the relative weight given to that centile by PC_k . Figure 7.13 shows the relative weights associated with the first three principal components. Figure 7.13 shows that PC_1 gives nearly uniform weight to all the centiles; this means that PC_1 is effectively the mean power and could be expected to perform very similarly to the median C_{50} , both being measures of centrality. This specifically supports the focus on the center (mean/median) of the power distribution as the primary gauge of the effects of the 23 experiment factors. Now look in Figure 7.13 at the relative weights of the centiles in PC_2 . Here the weights in the upper half of the distribution are positive and those in the lower half are negative; PC_2 is measuring the spread in the distribution, supporting the choice of C_S as the next statistic for consideration after C_{50} . Turning now to the centiles' relative weights in PC_3 shown in Figure 7.13, there is justification for following C_{50} and C_S with the skew statistic C_Q . C_Q is the difference in the lengths of the upper and lower tails of the power distribution, meaning in the standard sense of skew [21] that the power distribution is more skewed when $|C_Q|$ is larger, positively so when C_Q is positive and negatively so when C_Q is negative. PC_3 with its relative weights shown in Figure 7.13 is measuring skew in this same sense. Its positive weights above C_{80} with its negative weights between C_{50} and C_{80} work to represent the length of the upper tail. Similarly its weights for the centiles below C_{50} encode (the negative of) the length of the lower tail. The PC_3 weights of all 99 centiles taken together reflect the difference in the two tail lengths.

The relative weights shown in Figure 7.13 support using C_{50} , C_S , and C_Q for the analyses of measured PUSCH power for screening the 23 experiment factors. The principal components PC_1 , PC_2 , and PC_3 encompass almost all of the variability in the data. Had the relative weights of the centiles in these three components not had forms recognizable as center, spread, and skew statistics, the decision to base the analyses on C_{50} , C_S , and C_Q might have warranted reconsideration. As it is, in addition to being intuitive summary statistics of power, C_{50} , C_S , and C_Q encompass almost all of the information content (variability) in the centiles of the measured PUSCH power data.

7.2.4 Reported PUSCH Power

UE-reported PUSCH power was captured in parallel with measured PUSCH power in the four rounds of the screening experiment. This section presents results of the statistical analysis of these UE-reported powers, with results summarized in Figure 7.14, Table 7.4, and Table 7.5. The factors in Figure 7.14 and Table 7.5 are presented in the same order as in Figures 7.6–7.9. Measured and UE-reported PUSCH power differ in interesting ways that are discussed elsewhere in this report. Here, the interest is in whether, and to what extent, a screening analysis based on reported PUSCH power results agrees with the screening analysis of the corresponding measured PUSCH powers. Figure 7.14 shows p-values for the factors' effects on the responses C_{50} , (C_{50}, C_S) , and (C_{50}, C_S, C_Q) . Comparing Figure 7.14 to Figure 7.6 shows that the p-values from the reported and measured PUSCH power data are in close agreement, the largest discrepancy being the C_{50} -based p-value for factor H. Specifically, the analyses based on the two sets of data broadly agree with respect to $\alpha = 0.05$; bear in mind that large p-values, being associated with no factor effect, are uniformly randomly distributed and can only be expected to agree in distribution.

Table 7.5 shows the differences $\delta_j(C_{50})$, $\delta_j(C_S)$, and $\delta_j(C_Q)$ in the effects of the 22 factors $j = C, H, \dots, B$ as estimated by UE-reported PUSCH power compared to the factor effects in Figures 7.7–7.9 estimated from measured PUSCH power. The differences $\delta_j(C_{50})$, $\delta_j(C_S)$, and $\delta_j(C_Q)$ are almost all less than 1 dB in absolute magnitude. Also, the differences $\delta_j(C_{50})$ in reported and measured C_{50} averaged across all 22 two-level factors is $\bar{\delta}(C_{50}) = 0.04$ dB, with the corresponding averages for C_S and C_Q being $\bar{\delta}(C_S) = 0.04$ dB and $\bar{\delta}(C_Q) = 0.13$ dB, respectively. These averages indicate no bias in the reported results relative to the measured results, meaning that neither the measured nor the UE-reported data produce estimates of C_{50} , C_S , and C_Q that tend to be larger than the other. To summarize, the estimates in C_{50} , C_S , and C_Q factor effect sizes as derived from measured data versus UE-reported data differ little and for these small differences no bias is present.

Table 7.4: ANOVA p-values for the reported PUSCH data set.

Source	C_{50}	PC_1
B	.15	.53
C	.00	.00
D	.56	.62
E	.33	.50
F	.33	.64
G	.81	.13
H	.76	.76
K	.00	.00
N	.21	.24
O	.00	.00
P	.00	.00
Q	.50	.49
R	.04	.05
S	.00	.00
T	.00	.00
U	.38	.84
V	.00	.00
W	.00	.00
Y	.00	.00
Z	.01	.02
a	.75	.83
b	.00	.00
Ω	.00	.00

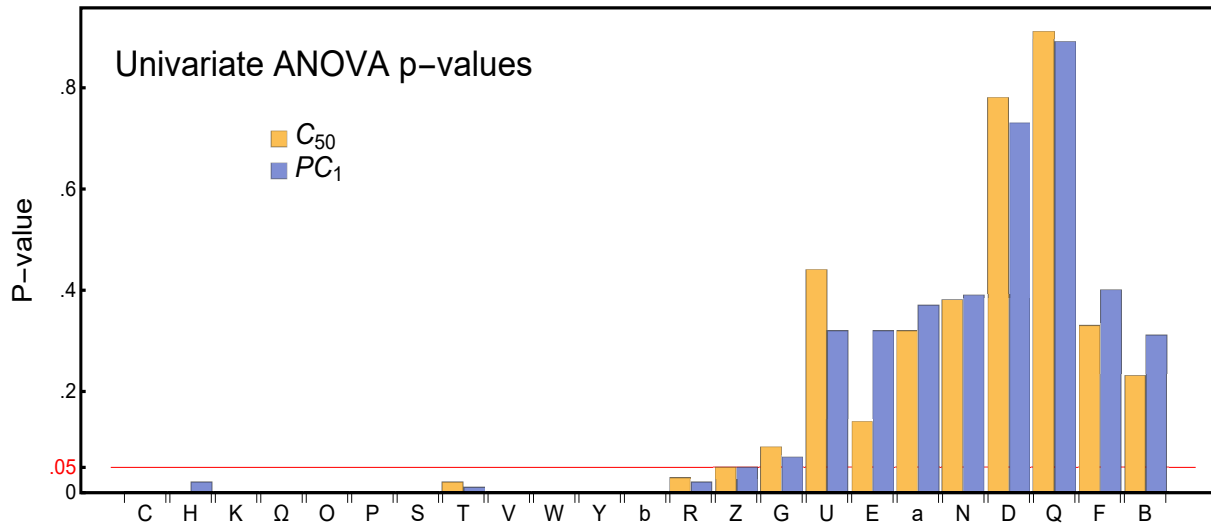


Figure 7.10: Comparison of factor effect p-values from two univariate ANOVAs, one ANOVA based on the median C_{50} and the other based on the first principal component of the power distribution. The first principal component of the power distribution should line up with the center of the distribution, in which case the results of the two analyses should be consistent with one another.

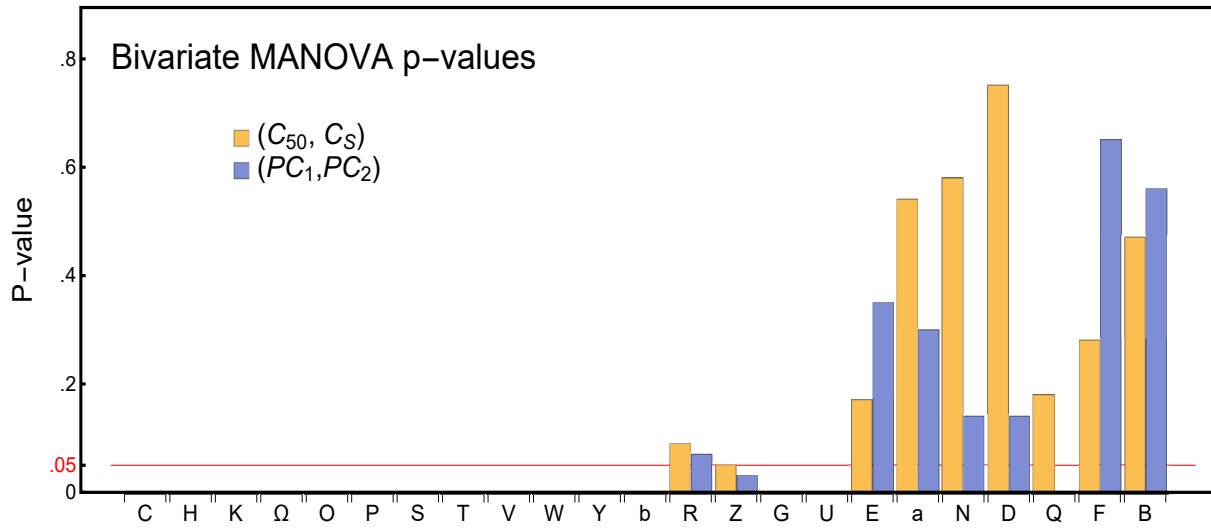


Figure 7.11: Comparison of factor effect p-values from two bivariate MANOVAs, one based on the pair of centile statistics (C_{50}, C_S) and the other based on the first two principal components (PC_1, PC_2) .

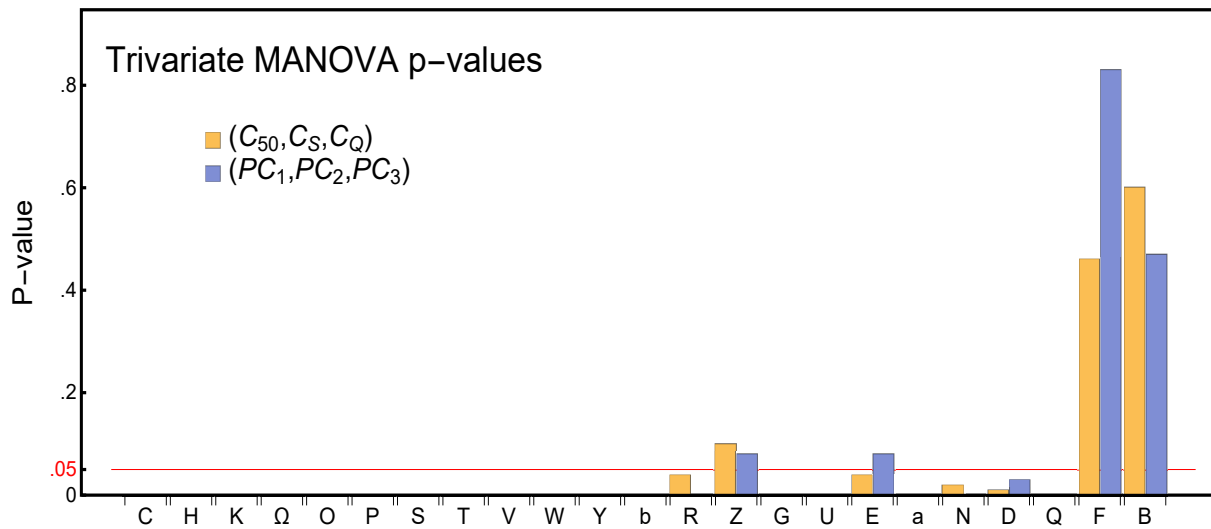


Figure 7.12: Comparison of factor effect p-values from two trivariate MANOVAs, one based on the trio of centile statistics (C_{50}, C_S, C_Q) and the other based on the first three principal components (PC_1, PC_2, PC_3) .

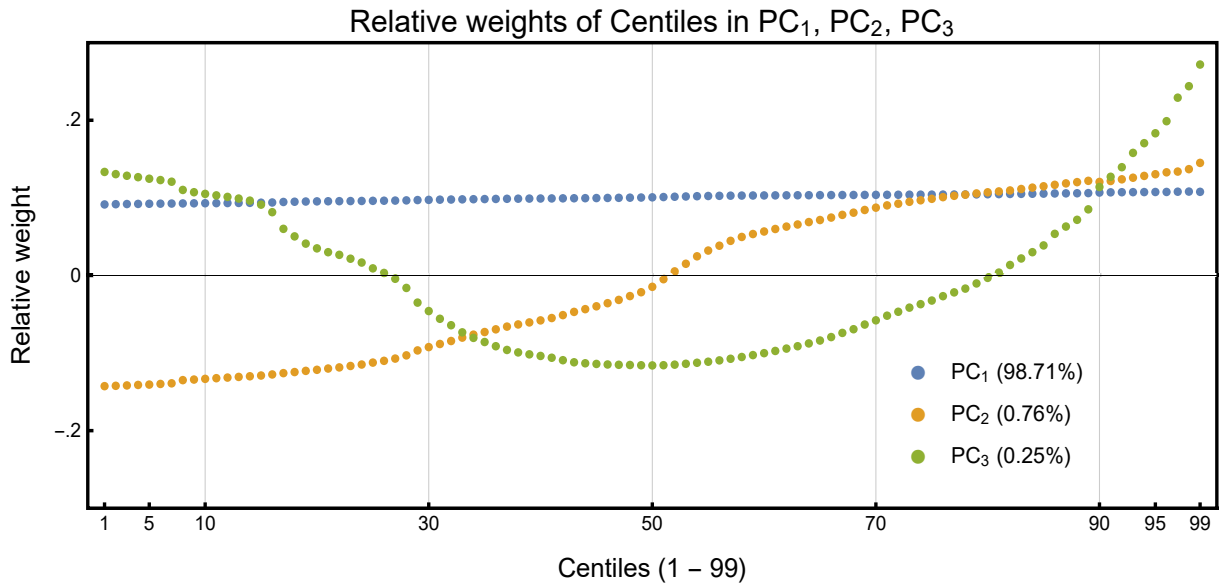


Figure 7.13: Relative weights of the 99 power centiles in the first three principal components of the measured PUSCH power. The first principal component is functioning as a measure of center, the second as a measure of spread, and the third as a measure of skew. The percentages are the amount of the total variability in the measured PUSCH power data explained by each principal component. Together PC_1 , PC_2 , and PC_3 explain 99.72 % of the variability in the data.

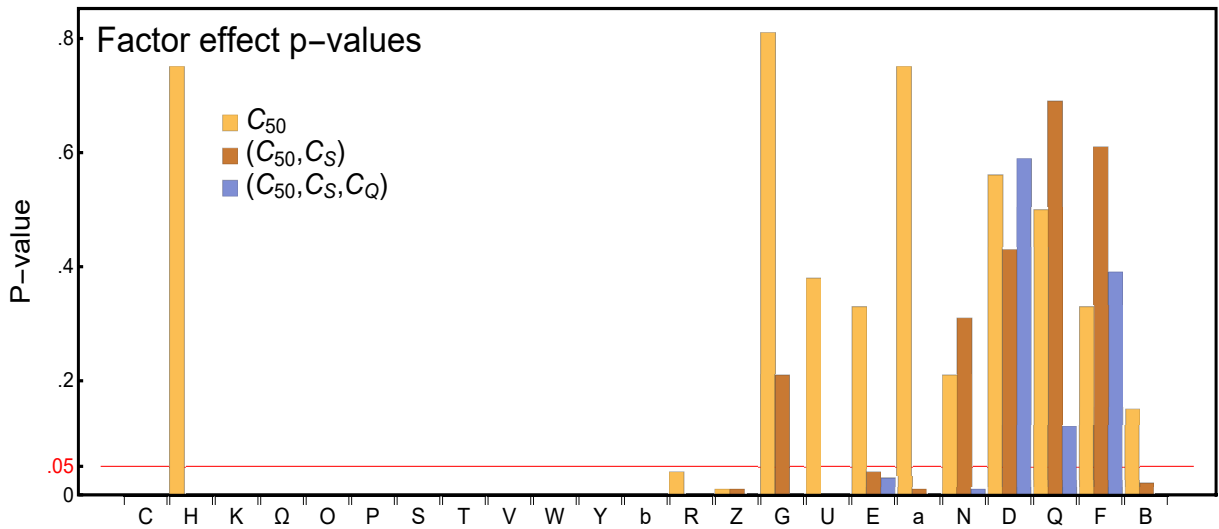


Figure 7.14: Factor effect p-values for 23 experiment factors from three increasingly comprehensive analyses based on C_{50} , (C_{50}, C_S) , and (C_{50}, C_S, C_Q) . Compare these p-values for reported PUSCH power with those in Figure 7.6 based on measured PUSCH power.

Table 7.5: Differences ($\delta_j(C_{50}), \delta_j(C_S), \delta_j(C_Q)$) in estimated PUSCH power distribution effect sizes based on reported power versus measured power for 22 two-level screening factors.

		Difference in effect sizes (dB)										
		C	H	K	O	P	S	T	V	W	Y	b
C_{50}		-0.5	0.9	2.3	0.7	0.5	-1.8	-0.6	-0.1	-1.0	-1.0	-0.1
C_S		0.7	0.9	0.0	0.3	0.0	-0.6	-0.1	-0.4	-0.4	-0.4	0.4
C_Q		0.6	-2.6	-1.5	-0.5	-0.4	0.3	0.5	0.1	0.4	0.2	0.5
		R	Z	G	U	E	a	N	D	Q	F	B
C_{50}		0.4	0.1	-0.2	0.8	-0.1	-0.3	-0.2	-0.2	-0.5	0.0	0.0
C_S		0.4	-0.1	0.7	-1.4	-0.1	-0.3	0.2	0.0	-0.2	-0.2	-0.3
C_Q		0.1	-0.4	0.1	-1.0	0.1	0.2	0.1	0.4	0.1	-0.1	-0.2

7.2.5 Measured PUCCH Power

The primary focus of this experiment is factor screening with respect to measured PUSCH power, and a full set of PUSCH power statistical analyses were presented in the previous section. PUCCH power was measured along with PUSCH power for each experiment configuration, so a PUCCH power-based screening analysis is also possible. This section presents the results of a statistical analysis of the full set of measured PUCCH power data from the four rounds of the 23-factor screening experiment. Because PUCCH power is of lesser interest for factor screening, only an abbreviated analysis is given, focusing on just PUCCH median power C_{50} . The ANOVA p-values are listed in Table 7.6. The effect sizes of the 22 two-level screening experiment factors are shown in Figure 7.15, color-coded according to significance ($\alpha = 0.05$). For ease of comparison, the factors in Figure 7.15 are presented in the same order as in Figures 7.6–7.9. Results of a Tukey analysis of the sixteen-level factor Ω are given in Table 7.7. Any two levels of Ω not members of the same Tukey group are significantly different, with estimated effect size given by the difference in their mean PUCCH C_{50} responses. Among the 120 Ω factor effects in Table 7.3, 61 are shown to be statistically significant.

Table 7.6: ANOVA p-values for the measured PUCCH data set.

Source	C_{50}	PC_1
B	.89	1.00
C	.02	.02
D	.38	.43
E	.14	.14
F	.39	.39
G	.68	.67
H	.38	.44
K	.00	.00
N	.01	.01
O	.00	.00
P	.00	.00
Q	.20	.19
R	.13	.11
S	.00	.00
T	.20	.22
U	.10	.10
V	.28	.26
W	.01	.01
Y	.00	.00
Z	.02	.02
a	.31	.30
b	.01	.01
Ω	.00	.00

Table 7.7: Tukey groupings based on PUCCH C_{50} power responses for the sixteen levels of factor Ω . Two levels in the same Tukey group are not significantly different in their responses. The C_{50} means for Ω 's levels are reported relative to -100 dB. The levels of factor M labelled "na" indicate cases where factor M did not logically apply ("not applicable").

16 levels of Ω	Subfactors					C_{50} (dB)	Tukey PUCCH C_{50} groups
	I	J	L	M	X		
11	0	-1	1	1	1	5.0	
4	1	1	1	-1	1	6.3	
5	-1	1	1	1	1	9.0	
15	0	0	1	1	1	9.4	
8	0	-1	-1	na	-1	9.9	
2	-1	1	1	-1	1	10.2	
6	1	1	1	1	-1	10.7	
12	0	0	-1	na	-1	11.3	
1	-1	1	-1	na	1	12.3	
9	0	-1	-1	na	1	14.4	
13	0	0	-1	na	1	15.8	
0	-1	1	-1	na	-1	19.7	
7	1	1	1	1	1	22.0	
14	0	0	1	-1	1	22.0	
10	0	-1	1	-1	1	22.7	
3	1	1	1	-1	-1	22.7	

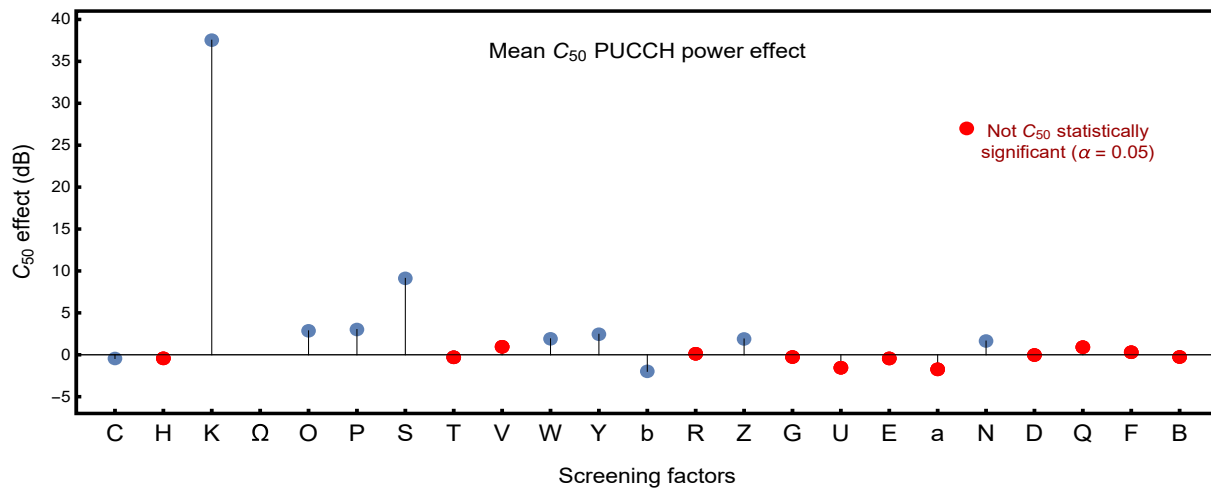


Figure 7.15: Mean factor effects on C_{50} (PUCCH power median). Factor Ω has 16 levels; its C_{50} level means are shown in Table 7.7. Effects marked in red are not statistically C_{50} -significant.

7.2.6 Testbed Stability

To monitor the stability of the experiment testbed, measured PUSCH power data were collected for 32 testbed configurations, called default configurations, created from 32 non-eNB configurations (those used in the screening experiment) and a single common eNB configuration (not used in the screening experiment, but centrally located in the space of eNB configurations). This set of default data contains PUSCH power measurements collected 45 times over the course of the testbed's 106 days of operation. These default data were collected to detect possible systematic biases or anomalies that might have compromised testbed operation in the screening experiment.

Exploratory statistical analysis of the measured C_{50} PUSCH power in the default data raises two concerns: testbed differential droop and a covariant day effect. Testbed droop is the total systematic drop in measured power for a given non-eNB configuration over 106 days of testbed operation. Figure 7.16 shows timeplots of the observed measured PUSCH power medians for each of the 32 default configurations. Each plot in Figure 7.16 shows median PUSCH power at each of 45 times in 106 days of testbed operation. A downward, constant-rate trend is present in every time plot, as evidenced by linear regression. For each of the 32 default configurations, the total drop in mean C_{50} PUSCH power is estimated by the difference at days 0 and 105 in the regression lines' heights. The 32 testbed droops in Figure 7.17 grouped by attenuation level have estimated means 2.8 and 4.2 dB for $A = -1$ and $A = +1$, respectively.

The testbed droop clearly varies (p-value = 0.00) by attenuation level. Groupings with respect to other non-eNB factors similarly reveal significant dependencies on factor level. This phenomenon in which the testbed droop depends on factor settings is referred to as differential droop. The testbed clearly exhibits differential droop over the set of non-eNB factors in the screening experiment. Because the default configuration included only one combination of eNB factor settings, whether the testbed also experienced droop differentially over the different eNB factor settings used in the experiment is unknown. Because this is unknown, the impact of any differential droop on the experiment results cannot be assessed. The analysis team, based on previous experience with similar experiments, considers that to whatever degree this phenomenon may have been present, it did not significantly impact the experiment's results. The differential nature of the testbed droop in the default configuration complicates the search for the source(s) of this test bed instability and/or the LTE system under study.

Some degree of chance variation is inevitably present in collected data, even after accounting for, as with the default data, systematic trends like droop. The variation about the droop in each of the 32 testbed monitoring configurations is shown in Figure 7.18 by plots of the residuals from the regressions in Figure 7.16. Visual examination of that variation suggests that it is random and homoscedastic over time. Visual examination also indicates that the random variation is heteroscedastic over configuration with estimated PUSCH C_{50} regression standard errors averaging 1.8 dB and 3.7 dB for $A = -1$ and $A = +1$, respectively (see Figure 7.19). Close visual comparison of the residual plots in Figure 7.18 further suggests that the different configurations' droop residuals track one another, even though the default data that yielded those plots were collected at different times on the days when data were taken. This covariant day effect is sometimes very strong; for example, the random variation in time plots of configurations 4 and 8 appear to strongly positively covary. In fact the estimated cross-correlation is 0.96 in these two configurations' droop residuals. The array plot in Figure 7.20 shows the cross-correlations in the droop residuals of all pairs of the 32 default configurations. The cross-correlations in the array plot are consistently positive³. These positive cross-correlations suggest the presence, in the testbed at the times of the default measurements, of unidentified underlying variables that tend to push measurements for all configurations in the same direction. The structure evident in Figure 7.20 in the amount of cross-correlation may be pointing to variables relating to non-eNB screening factors.

³ Figure 7.20 contains six negative cross-correlations. None of these are statistically significantly negative.

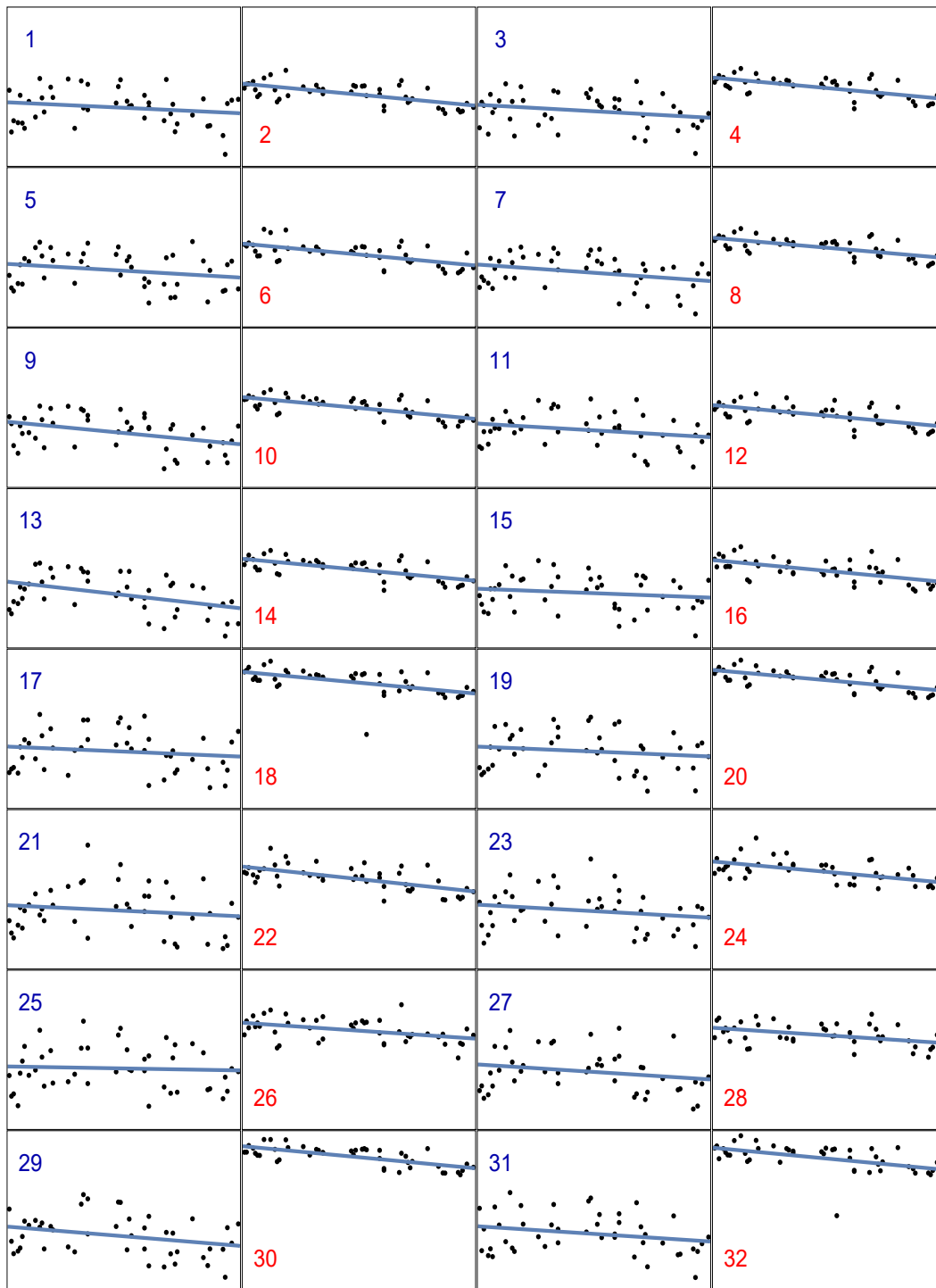


Figure 7.16: Median PUSCH power C_{50} at each of 45 times in 106 days of testbed operation, for each of 32 default configurations. Each configuration has a systematic downward trend, modeled by linear regression. The blue- and red-colored configuration numbers correspond to $A = -1$ and $A = +1$ attenuation levels, respectively.

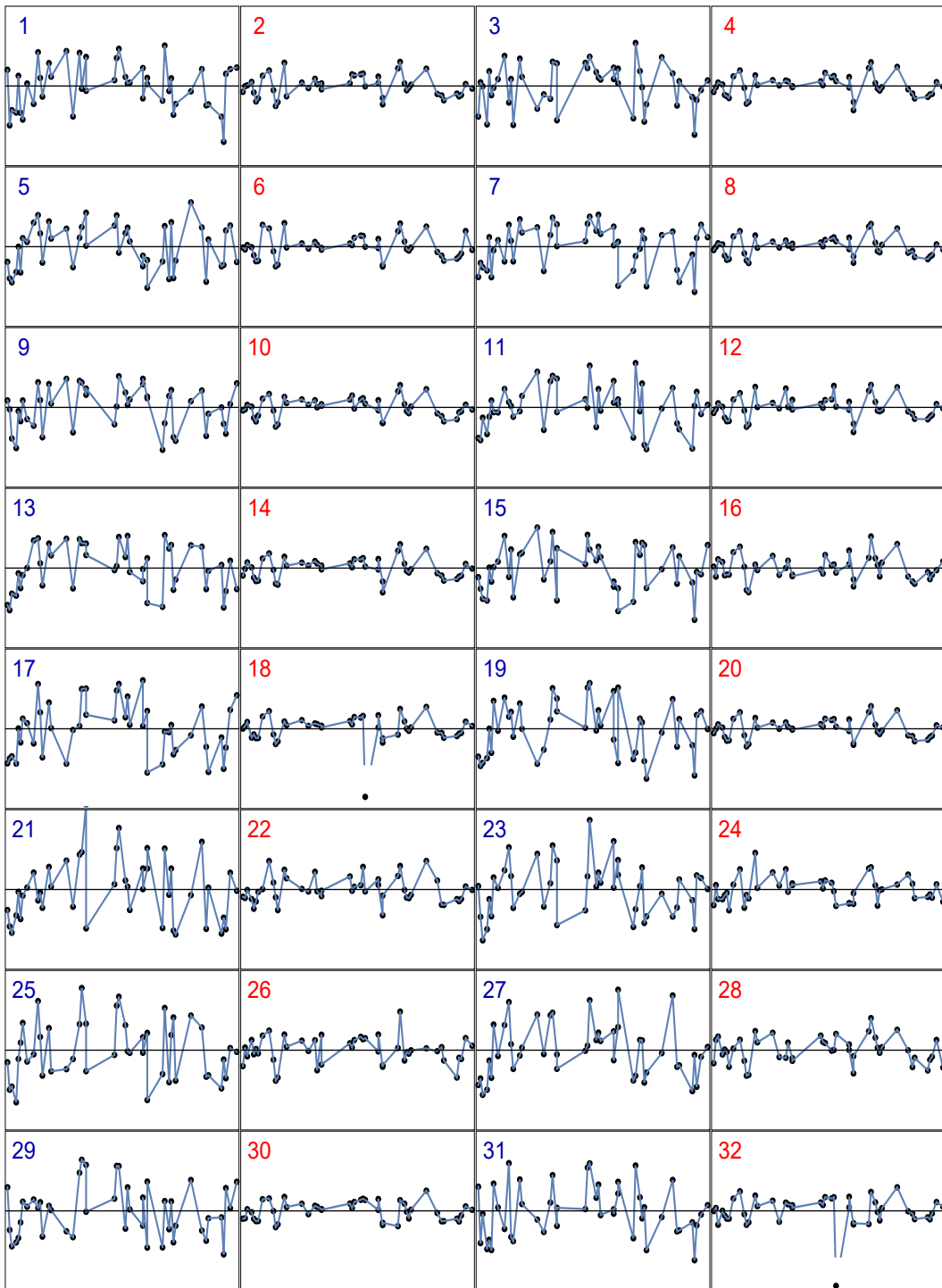


Figure 7.18: Droop residuals from the regressions in Figure 7.16. The variation in the default testbed monitoring data after accounting for its systematic droop appears random and homoscedastic over time, and heteroscedastic over configuration. The blue- and red-colored configuration numbers correspond to $A = -1$ and $A = +1$ attenuation levels, respectively.

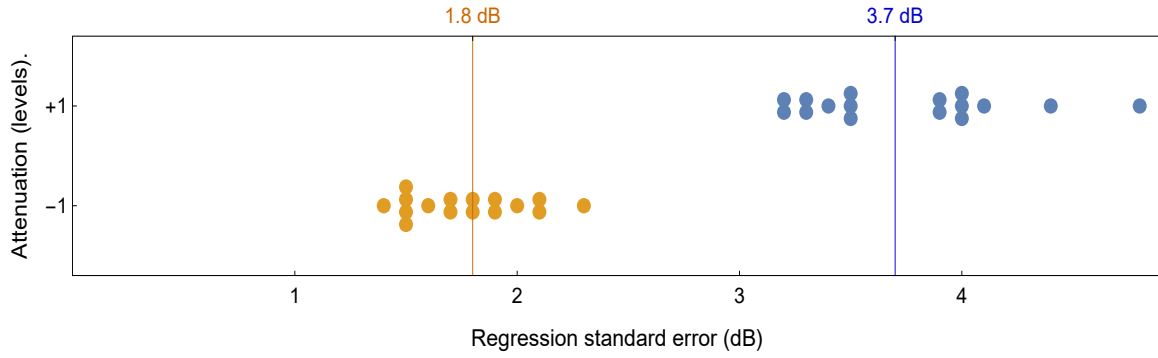


Figure 7.19: Random component of variation in measured C_{50} PUSCH power data for 32 default configurations, estimated by regression standard error. These errors are grouped by attenuation level, $A = -1$ and $A = +1$. The mean regression errors in the two groups are 1.8 dB and 3.7 dB, respectively.

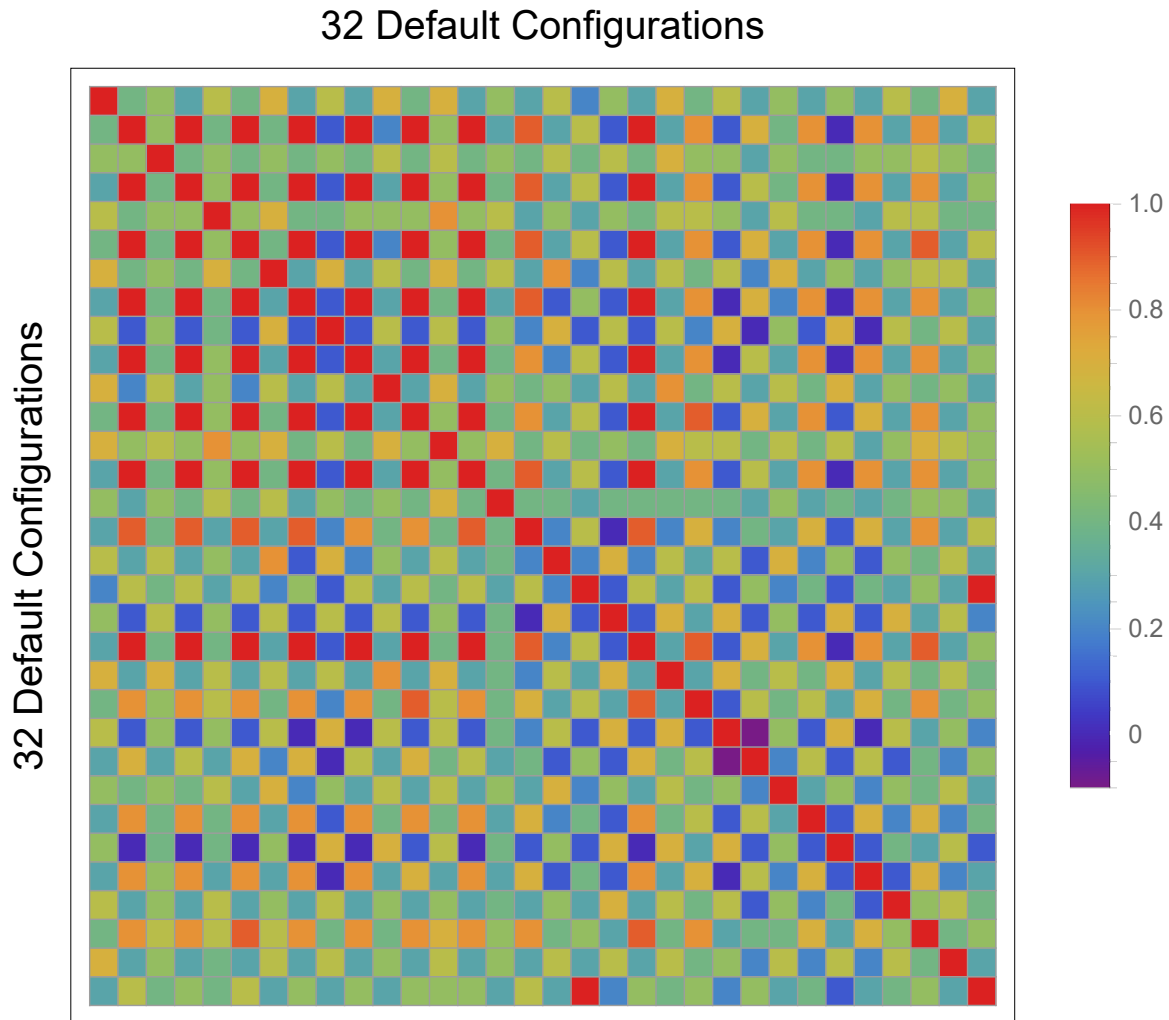


Figure 7.20: Cross-correlation in C_{50} measured PUSCH power over time in the testbed default data. The cross-correlations are those for droop residuals for the 32 default configurations.

7.2.7 Statistical Best Practices for Wireless RF Communications Experiments

This screening experiment involved a large challenging number of factors with levels that sometimes pushed the performance of the system under study outside its normal operating conditions. The unusual features of this experiment highlight some statistics lessons for future similar experiments.

Choice of factors: A screening experiment's purpose is to identify factors for further experimentation. Factors included in the experiment should be limited to those for which there is genuine uncertainty about their effect. For example, a factor may be known to have an important engineering effect and there may be interest in ascertaining in detail the degrees and types (main/interaction, linear/nonlinear/monotonic) of its effects. Such a variable, because it is already known to have an important effect, would not typically be appropriate as a factor within a screening experiment.

Choice of factor levels: A screening experiment's purpose is to identify factors for subsequent follow-up investigation. Usually, only two levels of each factor are needed for this purpose. These factor levels should be chosen at the endpoints of meaningful ranges to discover the presence of an interesting factor effect, if one exists. Factor levels extreme to the point of overstressing the system or creating data collection problems, or that are rare in system operation should be avoided in screening experiments. Extreme factor endpoints may, in particular, yield little data relative to the amount of data collected at other, more natural, endpoints. Large differences in sample sizes can result in widely varying random error (heteroscedasticity) among response statistics at different factor level combinations. MANOVA model (7.1) assumes responses are homoscedastic, and heteroscedasticity can undermine conclusions drawn from the model. An often-offered guideline is to avoid any differences in response statistic random error greater than a factor of two. Equivalently, in the screening experiment using centiles as responses, differences in sample sizes across all factor level combinations should not exceed a factor of four.

Pilot study: A pilot study is a small study done prior to and as part of planning for large, complex experiments. A pilot study allows the experimenter to:

- estimate the chance variation that can be expected and plan accordingly to collect sufficient data to achieve the experiment's goals for precision and types I and II error without unnecessary expenditure of experiment resources
- confirm the theoretical assumptions that underpin the planned statistical analysis
- assess the viability of planned levels (settings) for experiment factors
- assess the stability of the testbed, including the system under investigation

Pilot studies have many benefits, need not involve too much expenditure of experiment resources, and are sound practice.

Simpler designs: A screening experiment with a large number of factors should be subdivided into a series of smaller experiments based on subsets of factors. This may reduce the efficiency of the screening experiment—requiring more data to be collected for the same desired precision—but allowing more flexibility in choices of factor levels and experiment designs and localizing the impact of anomalous measurements and testbed failures.

Monitoring and validation plans: A plan should be in place to monitor data as it is collected in the experiment. This monitoring plan should include specified data checks, including checks for outliers, missing data, and other anomalies. Monitoring the data collection process allows the experimenter to halt the process in case a problem is detected. Data monitoring is complementary to data validation. Data validation involves subjecting the full data set, after collection and prior to analysis, to planned checks for inconsistencies, anomalies, and systematic biases. Effective validation will also usually include a few design points in the experiment for which data are collected throughout the experiment at a much higher rate than for other design points. The data from these validation design points allow the experimenter to ascertain post-experiment whether the data collection process (the testbed, in particular) was stable throughout the period of data collection.

Statistical analysis: The statistical analyses available for an experiment depend in many ways on the experiment's design. In the most extreme cases no statistical analysis may be possible. Ideally, an analysis plan should be chosen at the time of and in coordination with the design of the experiment.

Chapter 8

Discussion & Topics for Further Research

8.1 Discussion

The primary aim of the factor screening experiment was to determine which factors have a statistically significant impact on the distribution of PUSCH power per PRB. Specifically, the experiment screened the factors listed in Table 2.1. As explained in Chapter 2, these factors were selected after extensive discussions with LTE experts and feedback from stakeholders.

The data analysis results for the screening experiment are in Chapters 6 and 7, which present the exploratory and inferential analyses, respectively. The data underlying the results in those chapters is publicly-available at <https://doi.org/10.18434/M32130>.

The main results of the inferential data analysis for PUSCH are summarized in Figures 7.7-7.9. In particular, from Figure 7.7, which summarizes the ANOVA results for the median PUSCH power per PRB, the analysis found that several factors (K, Ω , O, P, S, W, Y, and b) had statistically significant effects greater than 3 dB. Among these factors, the effect sizes for W, Y, and b were a surprise, since they were not expected to have a large impact. Note that as discussed in Appendix C, the isolation between Cells A and B was not as high as expected. This impacted the ability to control the influence of each cell on the other. From the results shown in subsection 6.2.3, some influence between cells is evident. To better explore the influence of a neighboring cell, an additional research question is posed in the next Section.

Figures 7.8 and 7.9 show similar results for the analysis including spread and skew, respectively. These results show that including additional measures of distribution shape in the analysis led to a larger number of factors with statistically significant effects. Interpretation of the effect sizes for the quantile-based measures of spread, C_S , and skew, C_Q is more difficult than for the median. However, large changes in these measures of distribution shape are potentially important for modeling UE emissions. In particular, changes to the upper tail of the PUSCH power distribution could increase the impact of UE emissions on incumbent systems that must share the band with commercial LTE networks.

From the graphical exploratory data analysis results presented in Chapter 6, NASCTN can make three noteworthy observations that indicate potential directions for further investigation. First, as shown in Figure 6.31, which summarizes the empirical CDFs for measured PUSCH power per PRB across all tests, the range of power distributions was much tighter under closed-loop power control than for open-loop power control. Moreover, the median PUSCH power per PRB under closed-loop power control was generally much lower than under open-loop power control. This observation suggests that LTE deployments with closed-loop power control may be more predictable and result in lower aggregate emissions.

Secondly, from the comparison of UE-reported and measured PUSCH power per PRB in subsection 6.3.5, there were many test configurations where the measured and reported power differed substantially, by as much as 15 dB; see Figure 6.35. Importantly, the UE-reported power was consistently higher than the measured power, which implies that

field observations of UE-reported power provide an upper bound on emission levels.

Third, as shown in subsection 6.3.6, the analysis found that for most of the test configurations, the open-loop component of the PUSCH power control equation was a poor predictor of UE-reported power. This finding suggests that uplink emission models based primarily on the open-loop component of the LTE power control equation may require revision. Additional investigation is needed to clarify the conditions under which the open-loop component of the power control equation is a poor predictor of emitted PUSCH power.

Two appendices to this report (Appendix D and Appendix E) summarize supplemental investigations that were initially undertaken to support the laboratory experiments. These efforts proved to be fruitful, since they yielded findings that are potentially relevant to UE emission modeling. Namely, Appendix D summarizes measured radiation patterns for six different UEs. The variations in the radiation patterns for different phones indicate the extent that commonly-used isotropic radiation assumptions may break down. Appendix E presents path loss distributions estimated from a database of 14 000 macro-cell eNB locations and antenna heights in the United States. Path loss distributions were estimated for rural, suburban, and urban morphologies by combining the eNB data with a database of land cover categories and using the Extended Hata-Okumura path loss model. The estimated path loss distributions can be used for many purposes. First, they can inform the selection of relevant path loss values in future laboratory testing. Second, they can be used for modeling UE emissions when combined with a power control model, as illustrated in Appendix E. Third, estimated path loss distributions can be used for modeling average UE emissions over a typical cell, as described in the next paragraph.

It is beyond the scope of the present work to develop a model for aggregate UE emissions. However, the findings presented in this report could potentially be used to inform the development of such models. For example, the EEPAC model [22] currently used by DSO includes a component representing the EIRP of a spatially-averaged “model” UE in a cell [1]. Given an EIRP distribution for a single UE, the EIRP distribution for a single spatially-average UE could be estimated by evaluating the integral

$$f_E(x) = \int_A^B f_S(x | l) f_{PL}(l) dl, \quad (8.1)$$

where $f_E(x)$ is the probability density function (PDF) for the EIRP of a spatially-averaged UE, $f_S(x | l)$ is the PDF of EIRP for a single UE at a given path loss value, l , $f_{PL}(l)$ is the PDF for path loss, and $[A, B]$ is an interval of path loss values covering the support of $f_{PL}(l)$.

Because the power of UE PUSCH emissions is heavily dependent on resource allocations (see subsection 2.1.7), and because network loading conditions are artificially prescribed in the test set-up, the measurements focused on characterizing the power per PRB for specific LTE configurations. Therefore, the measurement method described here can be used to estimate one aspect of the PUSCH power distribution. However, a complicated issue deserving further research is a characterization of “typical” distributions for resource allocations to a single UE.

The results presented here have raised several interesting questions deserving further research. A list of potential topics for further investigation is presented in the following section.

8.2 Potential Topics for Further Investigation

During the course of this work, a number of additional questions/topics were identified. Due to budget, time constraints, and technical priorities, the test team was unable to explore and answer these questions. The list below outlines these additional questions from a conceptual perspective. The items are in no order.

Some of the topics listed could be addressed via additional factor-screening type experiments, while other are more

confirmatory in nature.

- **Impact of power control.** Results from this factor-screening experiment indicated that the use of power control (open-loop or closed-loop) has a significant impact on the uplink emissions of a UE. In addition to this primary impact, the use of power control may also have a secondary impact on other factors. For example, the use of open-loop power control *and* a given scheduling feature may have a larger combined impact than either factor alone. Similarly, the use of closed-loop power control may negate the impact of another factor, resulting in a significant reduction in UE emissions. Future work could investigate how power control interacts with primary factors. In cases where closed-loop power control is predominantly used, this experiment would provide more realistic results on what factors impact UE emissions
- **Variations amongst eNB and UE vendors.** The factor-screening measurements shown here were done with an eNB from a single vendor and a single model of UE from a single vendor (two UEs of the same model were used). Additional experiments could be done to examine how similar the results are for an eNB or UE from a different vendor. For eNB testing, additional consideration is necessary as there may be features unique to each eNB vendor. Such features may have an impact on UE emissions. Less variation is expected between UEs from different manufacturers as most UEs operate on the same 3GPP standard feature set. The AWS-3 band has an additional advantage in that it will not feature any legacy devices (i.e., devices based on older version of the 3GPP standard).
- **Impact of Handovers and “Hand-Downs”.** As discussed in section 1.4, measurement cases and acquisition sequences were specifically designed to exclude the possibility that a UE would be handed over from one cell to another. One possible path for future work would be to design an experiment that would identify factors that influence UE emissions during a hand-over. Note that a hand-over could be defined as the transition from one cell to another at the same frequency or the transition from one frequency to another within the same geographic cell (e.g., from an AWS-3 frequency channel to a channel in the 700 MHz LTE band).
- **Characterize UE emissions during attach.** One aspect that is not covered in this work is the emissions during the attach or detach process. It is possible that the emissions from a UE are markedly different from emissions observed in the PUSCH and PUCCH regions. In addition to different emissions during the attach process, there may be additional factors that impact such emissions that do not have an impact on PUSCH or PUCCH emissions. The LTE attach process has its own method of calculating the initial transmit power (aside from the PUSCH, PUCCH, and SRS methods described in subsection 2.1.7. Based on a search of prior literature, this question has not been addressed elsewhere, and may be of interest. However, attach sequences occur rarely and represent a very small portion of overall UE emissions (in terms of PRBs used).
- **Characterize UE emissions of SRS.** Similar to with emissions during the attach process, emissions of SRS transmissions could be characterized. SRS transmissions were captured in the measurements shown here (see subsection 6.3.4), but they were filtered out of the PUSCH emissions. The impact of the use of SRS on PUSCH emissions was examined through factors L and M. An additional set of factors could be devised and a screening experiment performed that addresses SRS emissions and the factors that impact them.
- **Characterize UE PUCCH emissions.** Factors O, a, and b had direct influences on the PUCCH emissions, but only their impact on PUSCH emissions were considered. If PUCCH emissions were of specific interest, a factor-screening experiment could be devised and executed. Given the measurements performed here, a limited number of additional measurements would be required. From the results shown in subsection 6.3.3, there is generally decent agreement between the distributions of PUSCH and PUCCH emissions. This may be an indication that future measurements may not produce distributions of emissions that are significantly different from those captured here. Future work could also examine the difference in the level of PUSCH and PUCCH emissions. That is, examine the level of PUCCH emissions compared to the PUSCH emissions at the same instant in time. A careful review of the data reveals that there can be cases where the PUCCH emissions are higher than emissions in the PUSCH for the same LTE frame.
- **UE behavior in negative PHR conditions.** One way to approach modeling UE behavior is to break it down into two

regimes: positive PHR and negative PHR. In negative PHR conditions, the UE does not have the ability to transmit as much power as is necessary to meet a target SNR. While in a negative PHR condition, the UE may not behave as expected. As discussed in subsection 6.2.2, the open-loop component of the LTE power control equation is not a useful predictor of UE emissions. An investigation specifically designed to probe factors impacting emissions while the UE is in negative PHR may be useful. From the combined CDF plots in subsection 6.3.2, there is some indication that the eNB may force the DUT UE into a negative PHR condition, even if just temporarily. The reason for this is not known.

- **Impact of eNB scheduler settings.** In these factor-screening measurements, several factors - I, J, L, M, and X - were combined into one factor. Their individual effects were difficult to estimate as a result of the dependencies between them. Of particular interest is the impact of specific scheduler settings. An additional factor-screening experiment could be conceived that focuses on scheduler specific factors. An eNB's scheduler is typically proprietary to its manufacturer. An experiment focused on scheduler settings may also need to be done with eNBs from multiple vendors to gauge the full impact of the scheduler on uplink emissions.
- **Repeat measurements with realistic settings.** The +1 and -1 values selected for factors was based on extreme settings. This was thought to make differences between factors settings easier to identify. The downside of this approach is that the values tested may not reflect actual network deployments. If desired, the factor-screenings measurements could be repeated - nearly verbatim - but with +1 and -1 values that are used in the real-world. Performing additional tests in this manner would not negate the results here, rather they would provide additional information about effect sizes.
- **Analyze Power per PRB and PRB occupancy distributions.** The data from this factor-screening experiment can be examined in many different ways. The existing measurement data could be re-analyzed to determine if there is a correlation between the emitted power per PRB and the size of the resource grant from the eNB. If a correlation is detected, a limited number of additional experiments could be done to confirm or refute the hypothesis. If a correlation between the distribution of emitted power per PRB and the grant size, it could enable new types of interference modeling. One such method would be sector-based modeling, where emissions could be modeled based on estimations of network loading. The measurements necessary to confirm this would require putting the DUT UE in a variety of conditions, which would provide some insight into the behavior of a UE in a negative PHR condition, as discussed above.
- **Develop a predictive model for UE uplink emissions.** One way to compliment current and future aggregate interference models is to develop a predictive model for the uplink emissions from a single UE. This empirically-based, predictive model would be based on a large number of measurements in a variety of configurations and aim to predict the UE's transmit power based on a given set of parameters (e.g., RSRP, path loss, number of PRBs, etc.). The model discussed here would likely not be a modification to an existing model - such as the LTE power control equation. Rather it would be an all-new, measurements-based model. The measurements performed in this effort would be a start towards this goal. It is not clear what additional measurements would be required to develop such an empirical model.
- **Testing with future waveforms.** The eNB used operates on release 9 of the 3GPP. As new LTE features and waveforms are released and put into service, the testing done here could be modified and/or repeated. Such future testing would examine the influence of new features and waveforms on UE uplink emissions.
- **Additional exploration of self-reported vs. measured power.** Section 6.3.5 shows the difference between the UE-reported power and the measured PUSCH power per PRB. Region three of this comparison indicates areas where there is poor agreement between the actual radiated power and the UE reported power. A preliminary analysis did not reveal the cause of the behavior in region three. Additional measurements could be devised to identify the scenarios when UE-reported power is unreliable. This may be of particular use to those conducting field measurements or analysis based on UE reported power.
- **Influence of neighboring sector(s).** Beginning with the conceptual design of the test circuit, the ability to investigate the impact of an adjacent cell was included. However, as discussed above, the adjacent cell impacts were not fully characterized as a result of a lack of hardware isolation between cells. The test circuit could be connected to

a different set of eNBs which feature physically separate pieces of hardware for each cell. Furthermore, additional test configurations could be developed to more thoroughly investigate how the behavior in an adjacent cell impacts the cell of interest. For example, the resource block allocations and scheduling methods of the adjacent cell could be altered and their impact examined.

Appendix A

Additional Factors Considered

In addition to the 28 factors that were included in the factor-screening measurements, several other factors were considered but not included. The factors shown below were considered up until the final phase of the experiment design when a few factors were eliminated because engineering judgment indicated that their impact on UE uplink emissions was likely low, there was no assertion in prior literature that they had an impact, and/or if their inclusion would have pushed the experimental design beyond what was feasible. If desired, the measurement method and test circuit described in this report could be reused to focus on the factors shown below.

There were factors considered that are not part of this list. Factors that made it to the final stage of consideration but not shown here are very specific to a particular eNB vendor and are only used in rare circumstances. Their description is omitted here out of a desire to remain neutral.

A.1 Maximum Number of UEs transmit per TTI

The maximum number of UEs per TTI is a configurable parameter within the eNB. Assuming the UEs are not in a negative power headroom situation and this parameter is set above 6, the impact of this factor on the uplink transmission power is expected to be negligible. Conceptually, if this parameter was configured to be 2, then the resources available in the high loading cases would be severely constricted. There is no indication that this parameter is configured to a low value in field deployments, so a higher value was used. During the factor screening experiment, the eNB was always configured to allow up to 14 UEs per TTI.

A.2 Downlink Scheduling Algorithm Type

The eNB's uplink and downlink scheduling algorithm and method can be configured separately. This capability gives wireless carriers the flexibility to control traffic flow and resource allocation in different ways for each link direction. As the focus of this work is the uplink emissions from a DUT UE, and downlink traffic is not considered, the scheduling method and algorithm are left in their default states.

A.3 TTI Bundling

TTI bundling is a feature which improve reliability of time sensitive traffics (e.g VoLTE) by re-transmission of small datagrams. The advantage of this feature is that the transmitter doesn't need to wait for 4 millisecond failure acknowledge which may cause a bad user experience. However, it is not implemented here as only QCIs 5 and 9 were used in the factor-screening measurements. Even when implemented, the expectation is that it would only impact a very small percentage of PRBs and not cause a meaningful change in total resource distributions.

A.4 Time Interval for Power Command Decisions

This eNB parameter can be configured to adjust how frequently the received signal strength indicator (RSSI) or SINR value is sent to determine power corrections in close loop power control. The time interval can range from 10ms to 2000 ms, and is set to 1050 ms in the factor screening measurements. This value is also the default value.

In the factor-screening measurements, no impact on the distribution of uplink emissions is expected as all measurements were done in static conditions and included a wait time between when the scenario was configured and when the emissions were captured. Once the scenario has been configured, UE power control from the eNB should be rare (when closed-loop power control is in use).

Appendix B

Parameters Collected

Table B.1 is a list of the parameters collected from the various sources (e.g., UTG, VSA, UE diagnostic monitor). Not all of these parameters were parsed and used in the analysis process. Some parameters were used in the initial stages of the measurement as cross-checks and verification variables to ensure validity of other parameters. Some parameters were recorded in 1 ms increments (i.e., every subframe) while others were only available as averages over 500 ms. Values recorded as averages over 500 ms are still considered useful because the test configurations are static.

This list of parameters may be helpful when attempting to replicate the measurements shown here. In addition to measuring the parameters required for the deliverables, capturing the parameters shown here would likely aid in troubleshooting and verification.

Table B.1: Summary of Data Sources.

Key Performance Indicator	Source	Frequency [ms]	Description
Number of Attached Loading UEs in Cell <i>A</i>	UTG	500	Number of UEs currently attached in Cell <i>A</i>
Number of Attached Loading UEs in Cell <i>B</i>	UTG	500	Number of UEs currently attached in Cell <i>B</i>
Buffer Status Register (bytes)	UE Diag Monitor	1	Status of the buffered data by a DUT
Mean UEs Signalled Per TTI	UTG	500	Mean Number of UEs signaled in each subframe
MCS Index	UE Diag Monitor	1	Modulation and Coding Scheme used by DUT
Mean PRBs Used in Cell <i>A</i>	UTG	500	Mean PRBs used by UEs in Cell <i>A</i>
Mean PRBs Used in Cell <i>B</i>	UTG	500	Mean PRBs used by UEs in Cell <i>B</i>
Mean UEs Signaled Per TTI	UTG	500	Mean UEs used per millisecond
Measured Power Per PRB at VSA	VSA	1	measured power per PRB by VSA
Measured Power Per TTI at VSA	VSA	1	measured per millisecond by VSA
Number of Active PRBs	UE Diag Monitor	1	Number of Active PRBs by DUT
Reported Power By UE	UE Diag Monitor	1	Reported Power By DUT
UE's PHR ind	UE Diag Monitor	1	Power Headroom Index of DUT
UE's Resource Block Start	UE Diag Monitor	1	The start of DUT's PRB
UE's SRS present flag	UE Diag Monitor	1	SRS On/Off flag by DUT
Mac Padding Overhead	UTG	500	The Percentage of MAC Padding by UEs
Number of RACH Initiated/Error/Complete	UTG	500	RACH Initiated/Error/Complete by UEs
service data unit (SDU) throughput	UTG	500	UEs SDU throughput
protocol data unit (PDU) Uplink throughput	UTG	500	UEs PDU throughput
Aggregate Uplink throughput	UTG	500	UEs Aggregate UL throughput
UE's PUCCH transmit power	UE Diag Monitor	1	DUT's PUCCH transmit power
Mac Padding Overhead	UE Diag Monitor	1	The Bytes of MAC Padding by DUTs
downlink control information (DCI)	UE Diag Monitor	1	UL grant, TPC, hybrid automatic repeat request (HARQ) ID
transport block size (TBS) and Freq Hopping Flag	UE Diag Monitor	1	Transport Block size and Freq Hopping Flag
RSRP, reference signal received quality (RSRQ) and RSSI	UE Diag Monitor	1	downlink band (DL) RSRP, RSRQ and RSSI
PUCCH format , DL Path loss	UE Diag Monitor	1	PUCCH format , DL Path loss
PUCCH actual Tx Power and gain	UE Diag Monitor	1	PUCCH actual Tx Power and gain

Appendix C

Calibration and Verification Measurements

The test team performed several measurements to ensure RF signal integrity and arrive at calibration values for path loss. This chapter separates the verification measurements into several sections, mainly those of the testbed sub-components and the aggregated testbed.

C.1 Radiated Environment

The radiated section of the testbed consists of a custom-sized shielded chamber with exterior dimensions of 94 cm in width, 94 cm in depth, and 182 cm in height. The chamber's RF absorber is a combination of tapered wedge, slimming from 30 cm to 20 cm on the side walls of the chamber, and 20 cm pyramidal absorber at the top and bottom section of the chamber. The chamber has five access locations: a shielded door, a removable bulk head panel on the top of the chamber that also accommodates antenna mounting, a removable section in the side wall, a bulk-head connector panel, and a feed for filtered alternating current (AC) power. Two of these small chambers, as well as the 3 m quiet zone fully anechoic chamber of NIST Broadband Interoperability Testbed (NBIT), were used for the calibration and verification measurements. The chambers are referred to as the test chamber (the primary chamber for the factor-screening measurements), small chamber (a secondary chamber of the same features as the test chamber), and NBIT.

C.1.1 Shielding Effectiveness

The small chamber was tested for its shielding effectiveness in order to ensure that the measurements were not affected by RF leakage into the test enclosure. The procedure evaluates the shielding effectiveness from path loss measurements between two horn antennas, separated by 90 cm in two scenarios. The horn antennas were linearly-polarized dual ridge horn antennas with a frequency range of 1 to 18 GHz: one where the chamber's shielded door was opened (see Figure C.1 left, measurements in Figure C.2 black line), and one where the chamber's shielded door was closed (see Figure C.1 right, measurements in Figure C.2 blue line). Prior to the measurements, the vector network analyzer (VNA) was calibrated to the ends of the cables with an electronic calibration kit. A third measurement with RF load terminated cables evaluated the VNA's noise floor (measurements in Figure C.2 orange dash).

The shielding effectiveness was given by ratio of the "open" door measurement to the "closed" door measurement (in linear units, or a subtraction in logarithmic units) and is shown in Figure C.3. The shielding effectiveness is better than 105 dB in the frequency region of interest and is sufficiently large to minimize RF leakage.

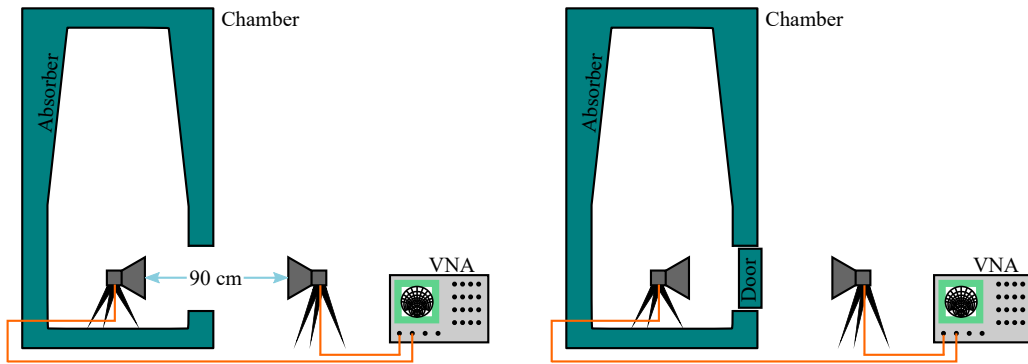


Figure C.1: Drawing of the measurement setup with the shielded chamber's door in the open position left, and closed position right.

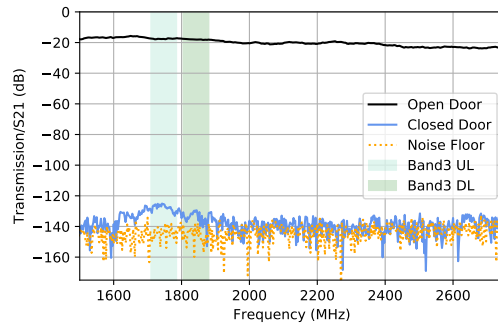


Figure C.2: Measurement results of the horn to horn transmission with the chamber shielded door open (black line), closed (blue line), and noise floor (orange dash) of the VNA. The figure also shows the frequency spans of interest for LTE Band 3 UL (light green), and LTE Band 3 DL (dark green).

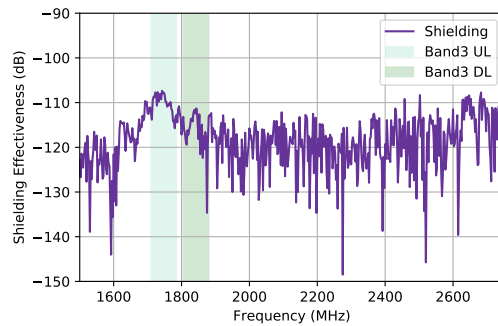


Figure C.3: Calculated shielding effectiveness (purple line) from measurement results in Figure C.2. The shielding effectiveness of the chamber is better than 105 dB in the frequency span of interest for LTE Band 3 UL (light green), and LTE Band 3 DL (dark green).

C.1.2 Horn Antenna - Gain

The radiated link of the testbed makes use of a linearly-polarized dual ridge horn antenna to communicate with the DUT UE. In order to effectively understand the path loss from the DUT UE to the eNB, the testbed's horn antenna needs to be characterized for its gain.

The gain is evaluated from measurements within the test chamber, secondary small chamber (Figure C.4 left), and from measurements within NBIT (Figure C.4 right).

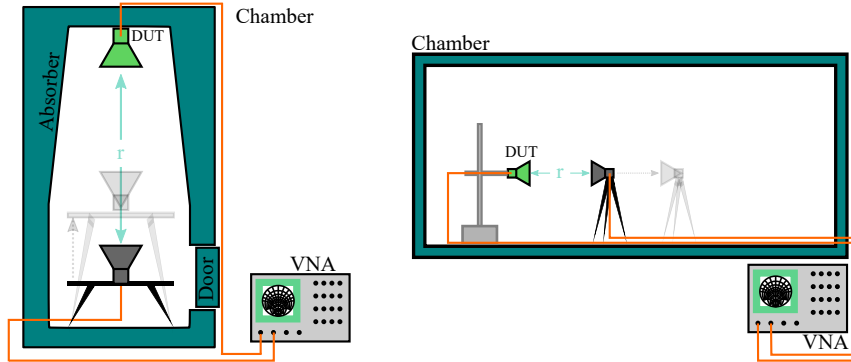


Figure C.4: Experiment setup for measuring the gain of the DUT antenna's and platform's effect on the antenna radiation pattern. Experiment setup in the test and small chamber (left). Experiment setup in NBIT (right). Both test setups incorporate measurements at several distances of r .

The test setup consists of identical make and model dual ridge horn antennas placed at various separation distances within the chambers. The gain of the testbed antenna can be derived from the Friis equation [23] (Equation C.1) under the assumption that the paired antennas of identical make and model have the same gain.

$$P_{rx} = P_{tx} G_{tx} G_{rx} * \left(\frac{\lambda}{4\pi r}\right)^2 \quad (C.1)$$

Where:

- P_{rx} = Power received;
- P_{tx} = Power transmitted;
- G_{rx} = Gain of the receiving antenna;
- G_{tx} = Gain of the transmitting antenna;
- λ = Wavelength; and
- r = Separation distance between the antennas.

Given the assumption that $G_{tx} \approx G_{rx}$ holds, the gain of the testbed antenna (G_{DUT}) can be derived from Equation C.1.

$$G_{DUT} = \frac{4\pi r}{\lambda} \sqrt{\frac{P_{rx}}{P_{tx}}} \quad (C.2)$$

In the experiment implementation, a VNA was used to measure the RF propagation path, including the antennas and the radiated link. The VNA calibration planes were set at the input to the horn antennas, and the horn-to-horn antenna separation distance was assessed as the aperture-to-aperture distance of the horns.

The nominal measurement separation distance for the measurement campaign was equivalent to a 78 cm separation

Table C.1: Horn aperture to horn aperture separation distances measured with in the small chamber and in NBIT.

Test chamber	Small chamber	NBIT
79 cm	80 cm	146 cm
78 cm	48 cm	61 cm
63 cm	32 cm	

between the horn apertures. The S-parameter S_{21} measurement of path loss and the calculated gain as a function of frequency are shown in Figure C.5. Furthermore, the calculated gain over the LTE Band 3 for all of the measurements in Table C.1 are shown in Figure C.6. This graphic also indicates the median calculated gain and 95th percentile confidence interval for the gain. The confidence region is estimated on the measurements that fall within two categories: first, data that is within the LTE Band 3 frequency range, and second, horn-to-horn aperture separation distances within 60 cm and 85 cm. These bound the estimate to reasonable frequency and separation distances. Moreover, calculating the gain over several different measurement environments, experimental configurations effectively incorporate uncertainties in spatial variations, frequency flatness, and chamber effects into the confidence estimate of the gain.

The median estimated gain for the frequencies of interest is 8.4 dBi (where dBi is the gain of an antenna relative to an isotropic antenna), and the 95th percentile confidence is encompassed by ± 0.8 dB.

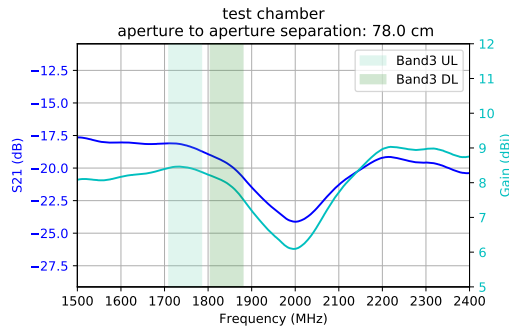


Figure C.5: Measured Transmission (S_{21}) in blue and calculated gain in cyan with the aperture to aperture distance at 78 cm. The frequency span of interest for LTE Band 3 UL (light green), and LTE Band 3 DL (dark green) is also indicated.

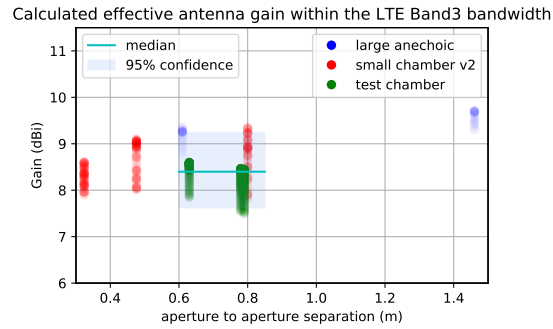


Figure C.6: Calculated gain from S-parameter measurements for the measurement setups in Table C.1. The scatter graph represents the Band 3 frequency band of interest from 1710 MHz to 1880 MHz. The median and 95 % confidence region represents the estimated gain, and respective confidence in the median gain over the frequency band and test campaign measurement separation distance of approximately 78 cm horn aperture to the top of the UE.

C.1.3 Horn Antenna - UE interaction

The separation distance between the test antenna and the UE is close to the boundary condition for the radiated far-field criteria of the dual ridge horn antenna, necessitating a check for the impact of the DUT UE on the radiating behavior of the horn antenna. Furthermore, it is preferential to maximize the dynamic range in the test setup by reducing the radiated path loss between the test antenna and the DUT UE.

In the verification measurement of the VNA's S_{11} S-parameter functionality, the calibration plane was at the input to the test antenna and established with the VNA's paired electronic calibration unit (see Figure C.7 for a drawing of the test setup). The calibration was checked with a $50\ \Omega$ reference load at the calibration plane. Figure C.8 shows a response at less than -45 dB, indicating a good match in the calibration.

Subsequently, the test antenna's S_{11} response in free space was measured by pointing the test antenna into an empty room (Figure C.9 green line) in the presence of the test chamber (Figure C.9 blue line). The comparison between the different environments shows some effect of the test chamber on the test antenna, likely due to the chamber's small volume slightly altering the antenna's radiating behavior. It is of note that the chamber's effect on the test antenna in this measurement campaign is systematic as the test horn antenna placement is non-dynamic.

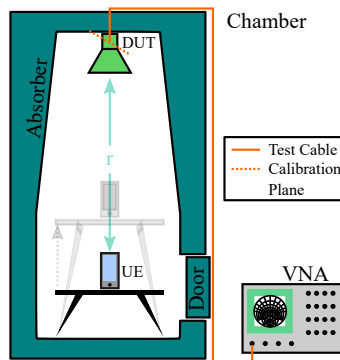


Figure C.7: Experiment setup for ascertaining the UE's and platform's effect on the antenna radiation pattern

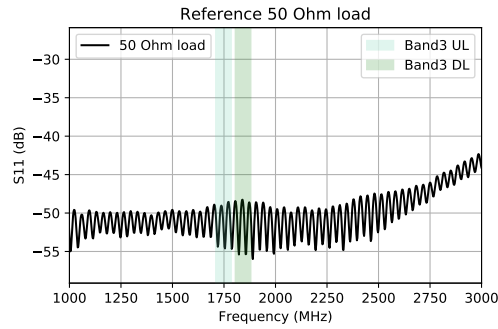


Figure C.8: S_{11} measurement of a 50 Ohm reference load. Over the LTE Band 3 of interest the load matches well, verifying the S-parameter calibration

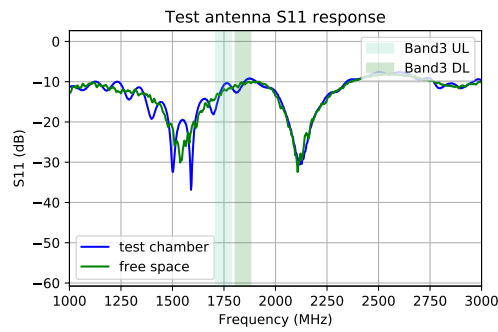


Figure C.9: S_{11} measurement of the measurement horn pointed into free space (green) as compared to the antenna response when placed into the small chamber (blue). The frequency span of interest for LTE Band 3 UL (light green), and LTE Band 3 DL (dark green) is also indicated.

To assess the UE's effects on the radiating behavior on the horn antenna, placing UE along the center axis of the test chamber and aligning the top edge of the UE with the polarization of the test antenna produced a measurement of the test antennas' S_{11} response in the presence of the UE.

For comparison the team also included a measurement of a large reflective target, an approximately 15 cm by 15 cm square plate of sheet metal, which was placed flat on to the test platform. The test antenna S_{11} response is documented in Figure C.10. As is expected the relatively small geometric signature (7.6 cm by 0.7 cm) of the edge-on UE poses little deviation from the baseline response in Figure C.9 (blue). The metal plate, however indicates a large response as is expected, given its large physical size and near ideal reflection coefficient.

Checking the UE's impact on test antenna response as a function of separation distance helps minimize the path loss between the test antenna and UE, enabling greater gain in dynamic range of the overall test system. As is indicated in the Figure C.7, the test platform and UE were placed closer to the test antenna, while minimizing the position deviation along the center line of the test chamber. Ultimately, it was decided to keep the separation distance within the test chamber at a maximum distance as the potential increase in dynamic range was minimal and better adherence to the far field condition, and minimizing potential impact of the UE onto the radiating behavior of the test antenna outweighed the potential benefits of increased the dynamic range within the test system.

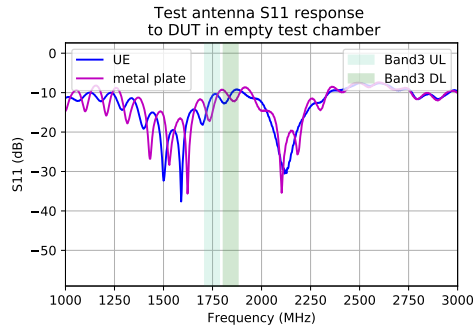


Figure C.10: The S_{11} response of the measurement antenna in the presence of a UE (blue), and a 15 cm by 15 cm large metal plate (magenta). The metal plate shows significant deviations from the reference measurement, whereas the UE doesn't.

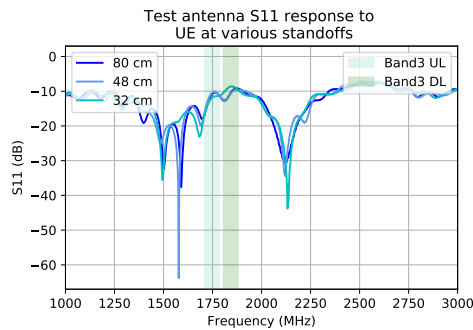


Figure C.11: The S_{11} response of the measurement antenna when the UE is placed progressively closer to the measurement antenna. At the shortest separation distance there is a significant effect on the measurement antenna response, whereas the initial and intermediate placements show very little change.

C.1.4 UE placement

In measuring the impacts of UE placement and orientation in the test chamber on the UE's overall transmit power to ascertain possible variability in measured UE power due to positioning error, a simplified test setup of the overall measurement system was developed with the use of the mobile anechoic chamber with the test antenna, a communications tester, and a signal analyzer (SA) on a directional coupling port (see Figure C.13). The communications tester takes the place of the RF circuitry and eNB, and the SA is used to double check the UL transmit spectrum.

Communications Tester The communications tester was setup to allocate all possible PRBs to the UE under test and report the transmit power of the UE. The frequency was set to mirror the Band 3 frequencies with a 10 MHz allocation. A screen shot of the communication's tester's setup is shown in Figure C.12, here the right hand graphic indicates the UE's transmit power.

For specific settings of the communications tester, please refer to National Institute of Standards and Technology (NIST) Technical Note [2].

UE positioning The UE was placed along a diagonal path on the platform within the test chamber for a total of seven measurement positions. The positioning can be referred to as from bottom left, through the center, to top

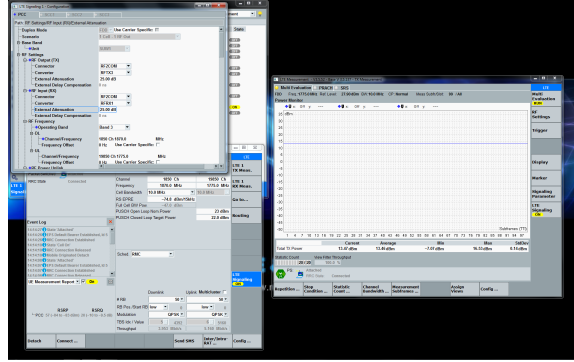


Figure C.12: Screen-shot of the communication tester's parameter space and measurements. The reported data is for the UE positioned along the center line of the test chamber, and its top edge is geometrically aligned with the polarization of the test antenna.

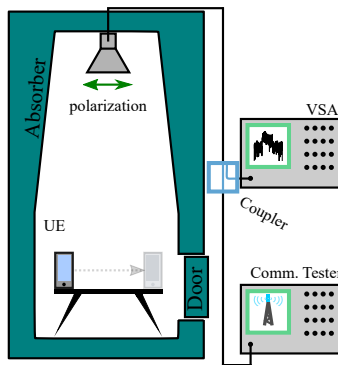


Figure C.13: Experiment setup for ascertaining the UE transmit power as a function of placement along the platform.

right, as viewed from the test chamber's access door, and is shown in Figure C.14. The top edge of the UE was geometrically aligned with the polarization of the test antenna, and at three measurement positions. The UE's transmit power was verified with the UE being rotated by 180 deg along the axis of the test chamber (i.e. the UE faced "east", including three positions with the UE facing "west"). The UE's transmit powers are tabulated in Table C.2. The measurements reveal a preferential orientation for maximizing the transmit power as a function of position, likely due to a combination of proximity to the absorber walls in the test enclosure, test antenna radiative profile, and UE's internal antenna position, leading to an asymmetry in coupling. To minimize variability, the test team performed the measurements at the center of the test platform, rather than trying to "peak" the transmit power, as any gains in dynamic range could be counter-weighted by increases in measurement uncertainty due to placement.

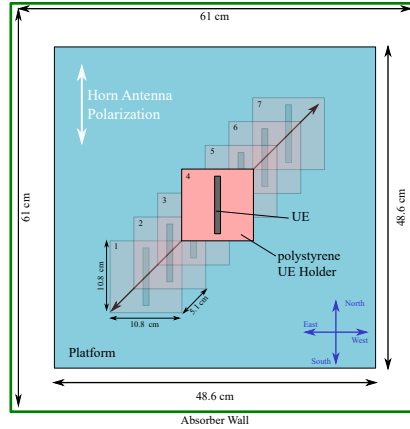


Figure C.14: Diagonal placement of the UE and reference orientations. Positions will be referred to as position 1 (bottom left) through 4 (center) to 7 (top right). The phone orientation was facing "east" for all positions and cross checked with facing "west" at positions 1, 4, and 7.

Table C.2: UE transmit power as a function of placement along the diagonal path of the platform. Graphical representation is in Figure C.14

Position	UE aligned "east" Transmit Power (dBm)	UE aligned "west" Transmit Power (dBm)
1	19.4	17.1
2	20.0	—
3	21	—
4	21.7	21.2
5	20.3	—
6	18.9	—
7	17.6	19.7

Polarization Mismatch Although several measurements were performed to evaluate the pattern characteristics of various UEs, a simple verification was performed with one of the measurement UEs mounted in the measurement chamber to a vertical sheet of a polystyrene foam board using hook and loop fasteners. In rotating the UE and foam board about the center line of the chamber, the polarization of the UE could be changed relative to the horn antenna in the chamber.

Figure C.15 shows a simplified measurement system using a commercial communications tester to connect a UE in the test chamber as a cross check on the performance of the spectrum analyzer and the full measurement system. A directional coupler was used to sample the uplink signal on a spectrum analyzer.

The UE was mounted to a polystyrene sheet using a hook-and-loop fastener to coarsely adjust (approximately 5 degree resolution) the alignment relative to the receiving antenna. By careful adjustment of the azimuth and elevation of the UE, the signal level (both transmitting and receiving) could be increased by approximately 1 dB over the default configuration. Based on the previous evaluation of UE pattern, the default configuration appears to be within 2 dB of the optimal configuration.

In addition to the orientation evaluation, readings were compared between the spectrum analyzer and the communications tester. In all cases, differences between the two instruments were within 1.5 dB, placing them within the bounds of instrumental uncertainty.

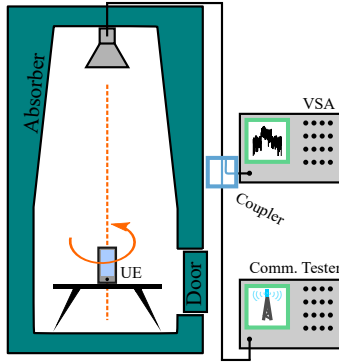


Figure C.15: Experiment setup for ascertaining the impact of UE rotational positioning.

C.2 Test System

The overall test architecture consists of four classes of components: a) the RF circuitry, b) the radiated environment, c) LTE hardware, and d) DUT UE.

The previous section focused on characterizing b) the radiated environment and the placement of d) the DUT UE within the environment. This section will investigate the major paths in the RF circuitry and discuss isolation within the LTE hardware.

C.2.1 RF Circuitry

In measuring the major RF paths within the RF circuitry, the circuit Figure C.16 can be considered as an 11-port unit with an additional 10 test-ports for diagnostic and verification. The major combinations of port-to-port paths and RF attenuator settings are tabulated in Table C.3. While there are many more possible combinations than outlined in this table, individual plots of all possible measurements are beyond the scope of this investigation as minor contributors to the primary paths (primary paths are shown in Figure C.17, Figure C.18, and Figure C.19).

A 4-port VNA was used to investigate signal paths and minimize required test combinations. The circuitry was evaluated for frequencies well beyond the primary interest in LTE Band 3. The noise floor of the measurement setup was better than -120 dB, sufficient to investigate potential leakage and cross-talk within the test circuit.

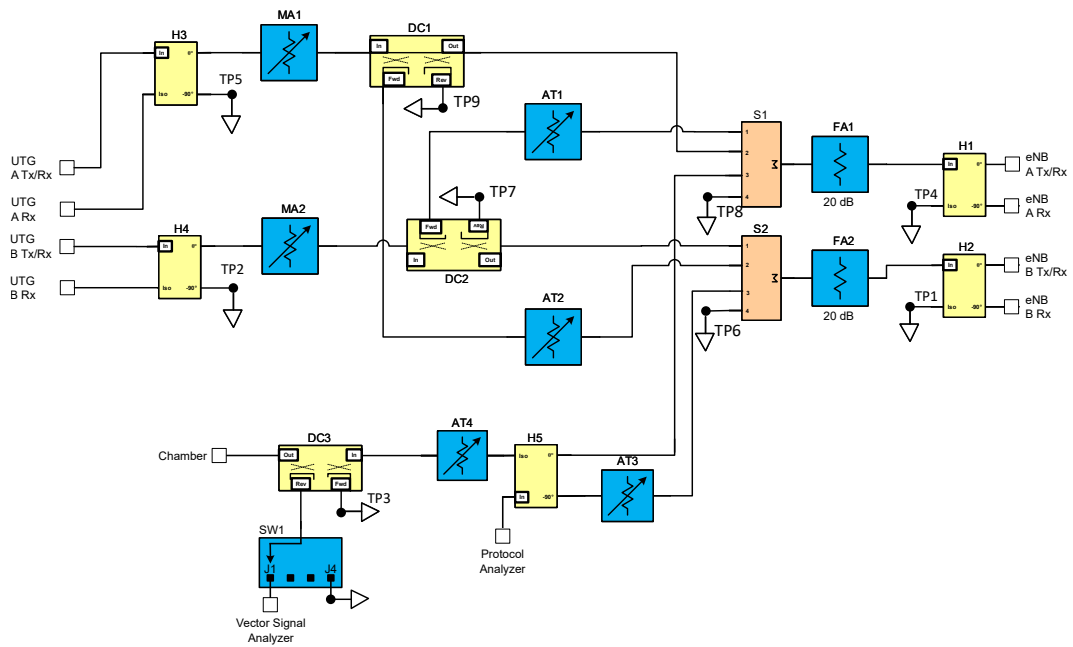


Figure C.16: The drawing outlines the block diagram of the RF leveling and combining circuitry used for the measurement campaign. The overall circuitry shows primary connection points (□□ connections) and denotes diagnostic test ports (● – ▷ TP#) that were built into the system. A series of 4-port measurements were performed on the RF leveling and combination circuitry to verify path loss and isolation.

Table C.3: VNA S-parameter measurement checks of the conducted portions of the RF test bed.

Test	Port 1	Port 2	Port 3	Port 4	MA1	MA2	AT1	AT2	AT3	AT4	Switch
Isolation	50 Ohm load	50 Ohm load	50 Ohm load	50 Ohm load	—	—	—	—	—	—	
1	eNB A TX/RX	UTG A TX/RX	eNB B TX/RX	UTG B TX/RX	0	0	110	110	110	110	J1
2	eNB A TX/RX	UTG A TX/RX	eNB B TX/RX	UTG B TX/RX	54	54	110	110	110	110	J1
3	eNB A TX/RX	UTG A TX/RX	eNB B TX/RX	UTG B TX/RX	54	54	0	0	110	110	J1
4	eNB A TX/RX	UTG A TX/RX	eNB B TX/RX	UTG B TX/RX	54	54	110	110	0	110	J1
5	eNB A TX/RX	UTG A TX/RX	eNB B TX/RX	UTG B TX/RX	54	54	0	0	0	110	J1
6	eNB A TX/RX	UTG A TX/RX	eNB A RX	UTG A RX	54	54	110	110	110	110	J1
7	eNB A TX/RX	UTG A TX/RX	TP9	TP5	54	54	110	110	110	110	J1
8	eNB B TX/RX	UTG B TX/RX	eNB B RX	UTG B RX	54	54	110	110	110	110	J1
9	eNB B TX/RX	UTG B TX/RX	TP7	TP2	54	54	110	110	110	110	J1
10	eNB A TX/RX	TP3	VSA	Chamber	54	54	110	110	110	110	J4
11	eNB A TX/RX	TP3	VSA	Chamber	54	54	110	110	110	0	J1
12	eNB A RX	TP3	VSA	Chamber	54	54	110	110	110	0	J1
13	UTG A TX/RX	TP3	VSA	Chamber	54	54	110	110	110	110	J4
14	UTG A TX/RX	TP3	VSA	Chamber	54	54	110	110	110	0	J1
15	UTG A RX	TP3	VSA	Chamber	54	54	110	110	110	0	J1
16	eNB B TX/RX	TP3	VSA	Chamber	54	54	110	110	110	110	J4
17	eNB B TX/RX	TP3	VSA	Chamber	54	54	110	110	0	0	J1
18	eNB B RX	TP3	VSA	Chamber	54	54	110	110	110	110	J1
19	UTG B TX/RX	TP3	VSA	Chamber	54	54	110	110	110	110	J4
20	UTG B TX/RX	TP3	VSA	Chamber	54	54	110	110	0	0	J1
21	UTG B RX	TP3	VSA	Chamber	54	54	110	110	110	110	J1
22	TP9	TP3	TP7	Chamber	54	54	110	110	0	0	J1
22	TP9	TP3	TP7	Chamber	54	54	0	0	0	0	J1

Of particular importance to an RF measurement setup using a live LTE network is the link budget for UL and DL. In this case there needs to be sufficient link strength to allow for the UL transmissions to meet the eNB's specified power control budget. Furthermore, the path loss between UL and DL ought to be balanced to allow for the LTE's power control mechanism to work in an optimal regime. Figure C.17 shows the path loss of the RF circuitry between the eNB and UTG for both cells. It is of note, that the path loss is well balanced for UL and DL and both cells show near identical path loss within the LTE Band 3.

The measurement campaign also made use of cross coupling between Cell *A* and Cell *B*. Figure C.18 shows the realizable intercell cross coupling on both UL and DL. In this case, the introduced coupling is very small (in the -115 dB range), and is ≈ 7 dB above the noise floor of the measurement setup. The potential for cross coupling was purposefully small, so as to meet power protection criteria on the UTG, as well preserve link budget between the direct link paths (eNB cell *A* to UTG cell *A*).

Of particular interest to this measurement campaign was the realizable link between the eNB and the DUT UE. Figure C.19 contains the line loss between the eNB and the RF circuitry's "Chamber" port as indicated in Figure C.16. Note that this path loss does not include the radiated portion of the test system.

C.2.2 Integrated system

This section describes the end-to-end path loss between the eNB and the DUT UE. Similar to the previous section, a 4-port VNA was used to measure the S-parameters. Unlike the previous section, as shown in Figure C.20, the measurement spans both the conducted and radiated portions of the test architecture.

The programmable variable attenuator AT4 was set to 0 dB, 10 dB, or 20 dB attenuation and the programmable switch to J1. The measurement of S-parameters is over three ports: the eNB cell *A* Tx/Rx port (including the test cable between the test circuit and the eNB), the VSA port (including the test cable between the VSA and the test circuit), and the reference antenna in the plane of the DUT UE. The results of the link path loss between the eNB and the reference horn antenna are graphed in Figure C.21.

The reference antenna is the same make and model as the test antenna, and the gain calculation of the reference antenna follows the discussion in the previous section on "Horn Antenna - Gain". In order to pursue the path loss in the test system, the reference horn's antenna is subtracted from the gain curve from the measured S-parameters to arrive at path loss between the DUT UE, Figure C.22, and the eNB and VSA ports, Figure C.23.

The presented curves are the basis for the calibrated path loss value for the DUT UE to the RF input to the eNB Cell *A* Tx/Rx port and the path loss value between the DUT UE and the RF input to the VSA. The median path loss within the LTE Band 3 is 73.2 dB from the plane of the DUT UE to the input to the eNB and 54.1 dB path loss between the DUT UE and the VSA.

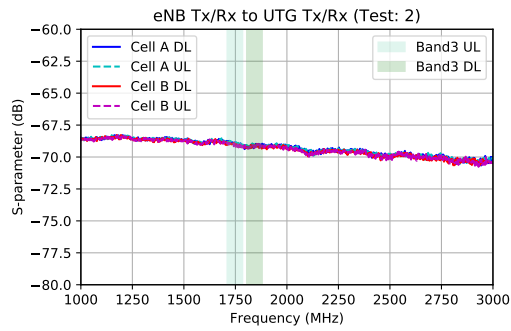


Figure C.17: The S-parameter measurements showing a very well balanced test circuit, where cell *A* and *B* uplink and downlink pathloss are equivalent. A well balanced UL and DL path are imperative to the stability of the LTE physical layer performance.

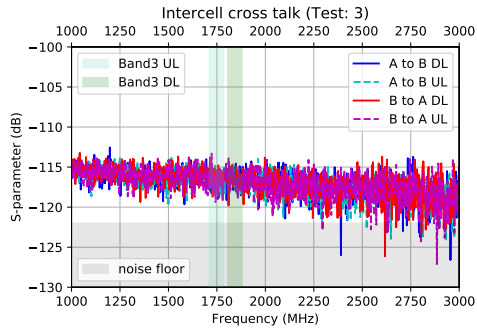


Figure C.18: The S-parameter measurement here highlights the realizable cross talk in the test architecture with attenuators AT1 and AT2 set to 0 dB attenuation.

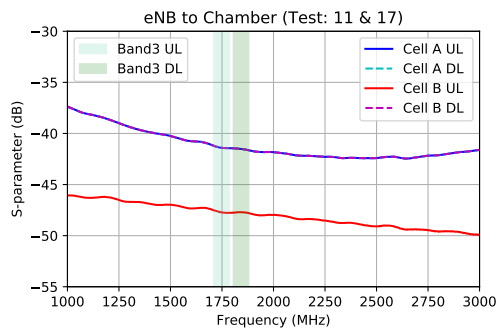


Figure C.19: The S-parameter measurements here show the conducted path loss between the eNB cell a, b ports and the chamber test port.

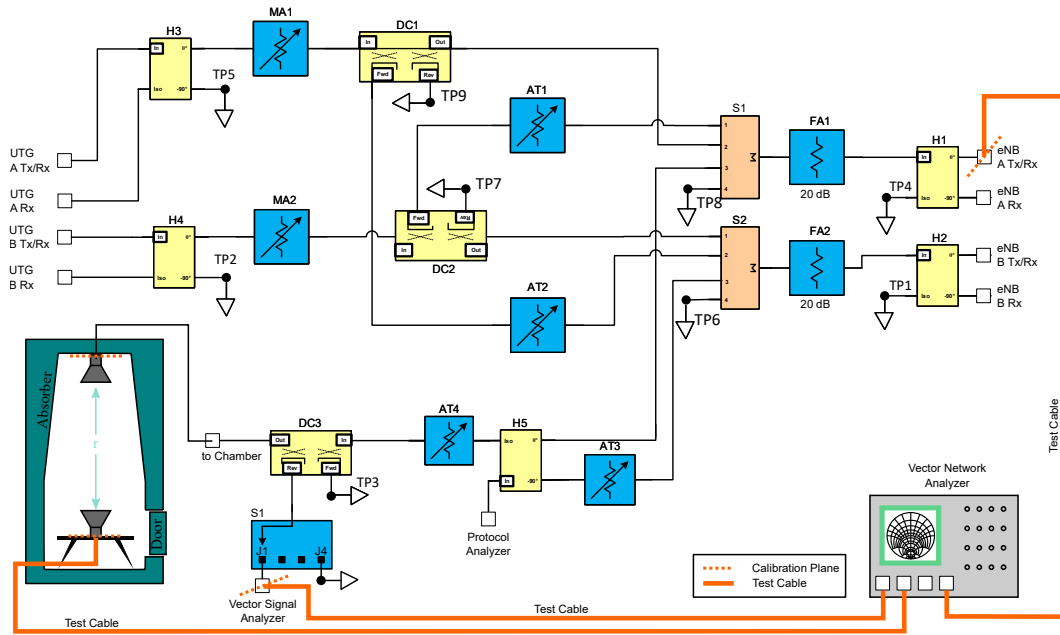


Figure C.20: The test case for the end-to-end measurements of path loss between the major components in the test bed. The calibration planes are shown in the graphic, as close as possible to the actual input of the radiated units. r is the test height, configured at 78 cm.

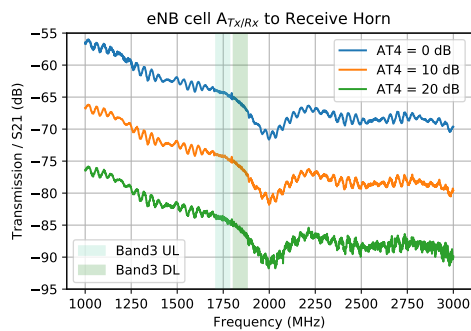


Figure C.21: S-parameter measurement of the transmission between the eNB cell $A_{Tx/Rx}$ port and the reference horn at the bottom of the test chamber, here AT_4 was varied. The test values for AT_4 were varied to evaluate whether the programmable attenuator tracks the specified attenuation.

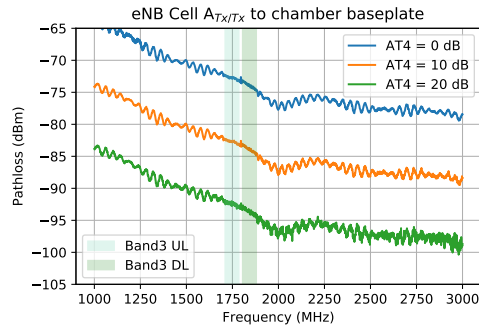


Figure C.22: S-parameter measurement with the gain of the reference horn at the bottom of the base plate subtracted out. The median within the band of interest (highlighted in green) for the AT4 = 0 curve represents the calibration value for the testbed for the path loss between the UE and the RF input to the eNB cell A_{Tx}/R_x .

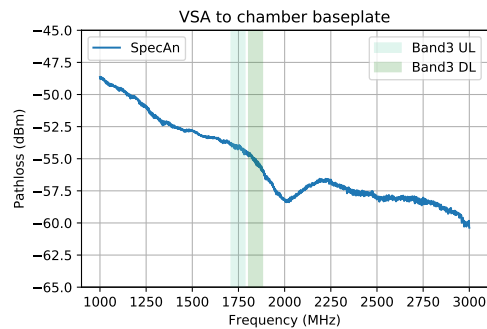


Figure C.23: The S-parameter measurement with the gain of the reference horn at the bottom of the base plate subtracted out. The median transmission value in the band of interest (highlighted in green) is the calibration value for the path loss between the DUT UE and the input to the VSA.

C.2.3 eNB isolation

To ensure that all cell-to-cell coupling is controlled by the test circuit and not by inadvertent coupling by some other mechanism, results of testing coupling through the eNB from Cell *A* to Cell *B*, and from Cell *B* to Cell *A* would be negligible. Ideally, this test would be performed with both Cell *A* and Cell *B* eNBs active. Unfortunately, this test requires sensitive measurements with minimal added attenuation between the ports, and direct connections between the outputs of the eNB and the measurement equipment could create signals large enough to damage sensitive receivers. Instead, the team measured coupling between the cells with the eNB powered on but the outputs of the eNB disabled. This should give an approximate estimate of the coupling, but more complicated measurements may be required to evaluate the potential coupling between fully operating cells.

Attenuation between Cell *A* and Cell *B* was less than 100 dB between 1.76 GHz and 1.80 GHz, less than 90 dB between 1.76 GHz and 1.78 GHz, with minimum attenuation of approximately 85 dB near 1.76 GHz and 1.78 GHz. Attenuation is somewhat greater when transmitting into Cell *B* and receiving on Cell *A*. Results are shown in Figure C.24.

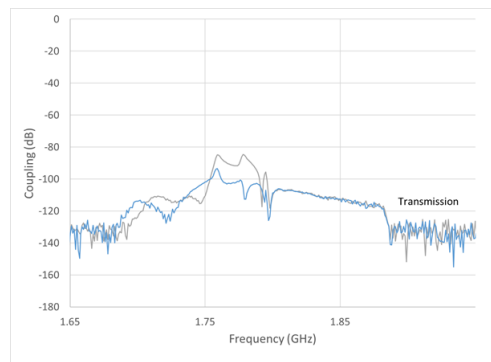


Figure C.24: Coupling between Cell *A* and Cell *B* on the eNB with both cells disabled.

C.2.4 Spectrogram power level

Calibrating the downsampled spectrogram power levels against a power sensor ensures that spectrograms are normalized to dBm per PRB. These additive offsets, in decibels, can originate from physical or calibration offsets in the instrument, or scaling factors in the re-binning and downsampling process described in subsection 4.2.3.

The calibration signal is an LTE test pattern synthesized with a commercial generator at 1.77 GHz. The test pattern, a sequence of 5 TTIs, is repeated in a loop. All PRBs are disabled in each TTI except for RB25. For RB25, the sequence of TTIs consists of 2 “off” TTIs, QPSK, 16QAM, then 64QAM. The data payload to the 3 active TTIs is pseudo-random. The use of different constellation types serves as a check for the response of the power sensor spectrogram.

First, the signal analyzer is connected to the signal generator, the signal analyzer acquires a 5 s spectrogram, and the re-binning procedure is performed according to subsection 4.2.3. Next, the power sensor is connected in place of the signal analyzer, and a trace of power over time is collected, spanning 4 TTIs. The average power (for only RB25, on the spectrogram) during active TTIs is taken as the power reading, in dBm/PRB.

These calibration measurement data are shown by Figure C.25. The uncalibrated spectrogram average power reading, -46.12 dBm, under reports relative to the calibrated power sensor reading, -36.40 dBm. Thus, the offset correction needed to calibrate the spectrograms to physical power (in dBm/PRB) is +7.72 dB. The uncertainties in this measurement are incorporated into the spectrum analyzer uncertainty in section C.3, including the ± 0.2 dB variability in spectrogram response to different types of modulation.

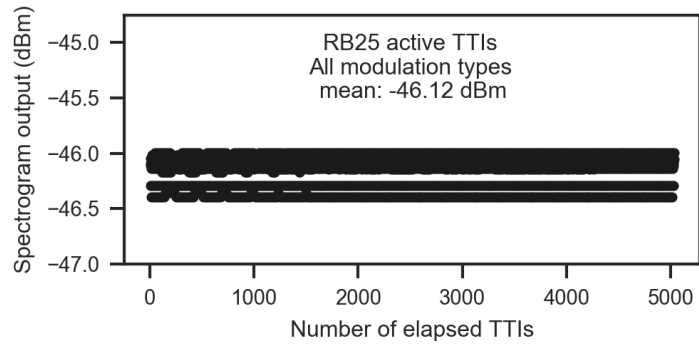
C.3 Uncertainty

The principal output of the testbed is the maximum EIRP per PRB from a UE. Grouping the measured and calculated terms into a single equation helps to identify the sources of uncertainty and the relationship between terms. A summary equation for the EIRP is:

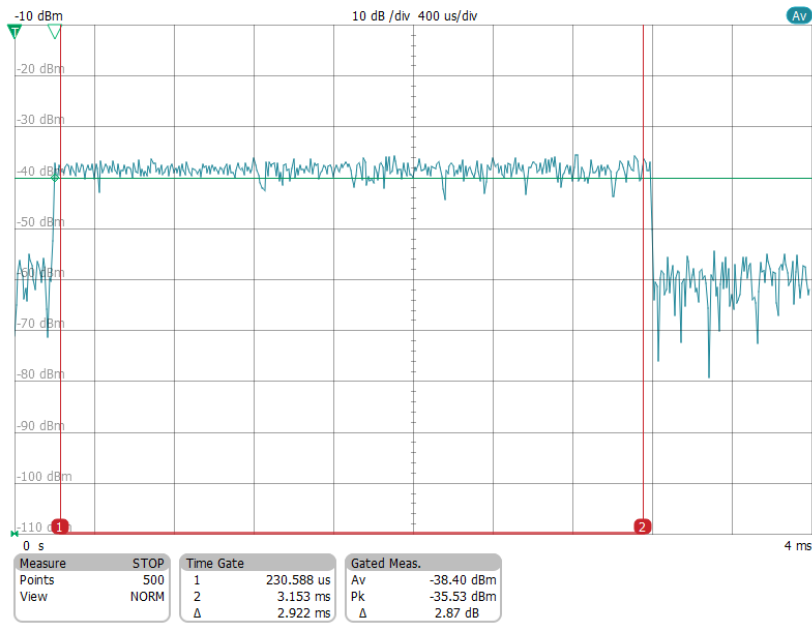
$$\text{EIRP [dBm]} = P_{\text{SA}} + C_{\text{Through}} + G_r + 20 \log_{10}(4\pi d_{\text{setup}} \lambda_0) + C_{\text{Align}} + C_{\text{position}}. \quad (\text{C.3})$$

where:

- P_{SA} = Power measured at the vector signal analyzer in dBm;
- C_{Through} = Coupling between the input of the spectrum analyzer and the output of the receiving antenna in dB;
- G_r = Gain of the receiving antenna in dBi;
- $\lambda_0 = c_0 f$ = the wavelength at the center frequency of the measurement band in free space, expressed in meters;
- C_{Align} = possible misalignment factor (both in terms of pattern and polarization) between the DUT UE and the receiving antenna in dB;
- C_{position} = possible position effects in the small shielded chamber in dB.



(a)



(b)

Figure C.25: Measurements taken to calibrate (a) spectrogram data from the signal analyzer against (b) the calibrated power sensor reference.

Table C.4: Sources of uncertainty and uncertainty budget for VSA captures of UE emissions.

Classification	Factor	Probability Distribution	Evaluation Type	Designator Designator	Uncertainty (dB)	Correction for Distribution	Standard Uncertainty
Antenna Calibration	Non-ideal Antennas	Normal	B	U1	0.5	1	0.5
	Spatial variations	Normal	A	U2	0.3	1	0.3
	Network analyzer calibration	Normal	B	U3	0.1	1	0.1
	Frequency flatness	Normal	A	U4	0.3	1	0.3
	Polarization mismatch	Normal	B	U5	0.1	1	0.1
	Separation distance	Normal	B	U6	0.5	1	0.5
Instrumentation	Spectrum analyzer	Normal	B	U7	0.5	1	0.5
Testbed	Calibration	Normal	B	U8	0.1	1	0.1
	Antenna mismatch	U-shaped	B	U9	0.1	0.5	0.05
	Antenna connection repeatability	Normal	A	U10	0.1	1	0.1
	Separation distance	Normal	A	U11	0.5	1	0.5
	Chamber uniformity	Normal	A	U12	0.3	1	0.3
Total	Combined standard uncertainty						1.1
	Expanded uncertainty (k=2)						2.3

C.3.1 Spectrum Analyzer Power Measurement Uncertainty Components

Based on specifications given by the manufacturer, the standard uncertainty of a power measurement is 0.3 dB. However, the manufacturer also recommends to increase the uncertainty by 0.2 dB if measurements are taken over a long time period without aligning the system (this was sometimes required for some of the measurements). Therefore, the standard uncertainty of 0.5 dB for measurements of power is given using the spectrum analyzer. Since the signal source was a commercial UE, there was additional variability in the received signal. However, this variability is accounted for separately.

C.3.2 Coupled Output Power Calibration Uncertainty Components

The RF path needed calibrations so any variations in the testbed before the directional coupler should be observable as changes in power detected by the spectrum analyzer (the directional coupler and the cables from the incident sidearm to the spectrum analyzer and to the transmitting antenna). Rather than measure the coupler and cables separately (which increases uncertainty), the coupler and cables are calibrated as a system. The uncertainty in these calibrations is given by a spreadsheet provided by the manufacturer of the network analyzer. (Note: the original spreadsheet downloaded from the the manufacturer's website was non-functional, so technical support provided an older version. The spreadsheet used was Revision 3.0.0, with dynamic link library (DLL) Revision 4, 9, 6, 31). The spreadsheet gave a standard uncertainty of the transmission coefficient for the test conditions of less than 0.1 dB.

C.3.3 Programmable Attenuators

The same models of programmable attenuators used in a previous effort [24] were used in this effort. A conservative standard uncertainty of 0.5 dB is assigned to these attenuators.

C.4 Offset Calibration to DUT EIRP

An offset calibration is required to convert the power reading in the VSA spectrogram to EIRP at the DUT UE. The offset correction from the re-binned VSA spectrogram to the VSA input connector is +7.7 dB (see subsection C.2.4), and the correction offset from the VSA input connector to the EIRP at the DUT is +54.1 dB (see Section C.2.2). Hence, the total offset correction applied to convert the re-binned VSA spectrogram reading to calibrated DUT UE EIRP is +61.8 dB. The expanded uncertainty of the calibrated measurement result is ± 2.3 dB (see section C.3).

Appendix D

User Equipment Antenna Pattern Measurements

In support of the NASCTN project, a separate effort was conducted to understand of the three dimensional emissions of typical LTE UEs. Six discrete UEs were measured. The approach, testbed, methodology, and results of this work are published as a separate NIST Technical Note [2]. In this appendix, only the results of the six evaluated UEs are presented.

The setup for the full 4π emission measurements is shown figure D.1 in both a schematic and a photograph. The UE is mounted on an acrylic block and attached to a rotation stage with an acrylic rod which provides the azimuth angle, ϕ , rotation. The elevation angle, θ , rotation is controlled by a turntable sitting below the photograph in figure D.1. The top of the UE is closest to the measurement antenna at $\theta = 0^\circ$ and furthest at $\theta = 180^\circ$. Additionally, $\phi = 0^\circ$ corresponds to the top of the phone being copolarized with the vertically polarized measurement antenna.

The three-dimensional measurements for the radiation pattern from the six UEs with a vertically polarized measurement antenna are shown in Figure D.2 and measurements for horizontally polarized measurement antenna are shown in Figure D.3. The equator of the plots correspond to $\theta = 90^\circ$ with rotation in ϕ . Likewise, the top of the plots correspond to $\theta = 0^\circ$. Finally, vertical cuts in the plots are given by rotation in elevation, θ . The first feature that stands out is the similarity in phones A, B, and C. These are different manufacturers with very different price points and dimensions, yet all three phones exhibit the same antenna behavior. Phones D and E are similar to each other, but not the first three. They have a very different design. It may be that the design allows higher EIRP for most orientations while sacrificing some isotropy compared to the other antenna design. Another feature to note is the presence in all UEs of a 30 dB to 40 dB null in the pattern.

171

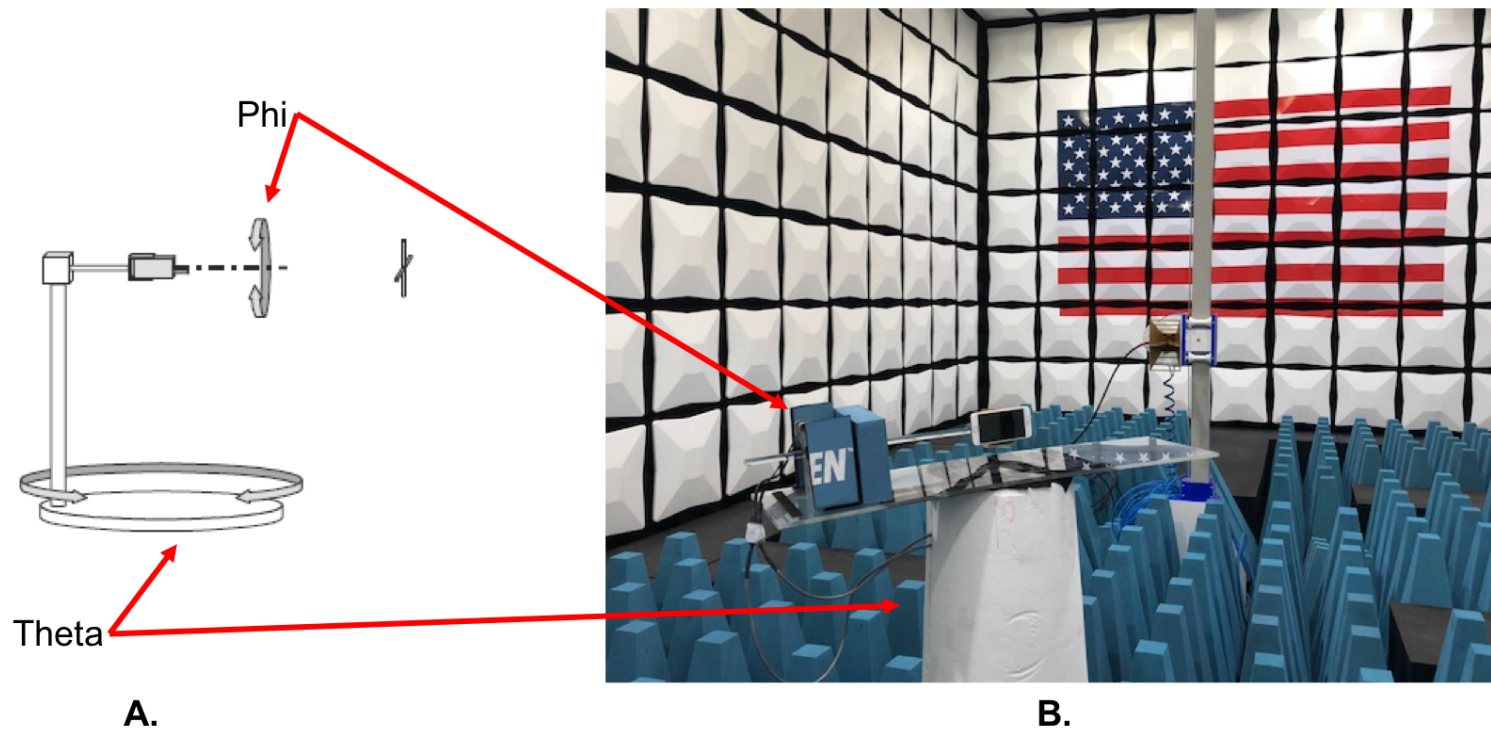


Figure D.1: (A.) Sketch of UE in a motorized fixture with θ and ϕ . (B.) The fixture built to correspond to the schematic in A. The corresponding rotating elements are shown with red arrows.

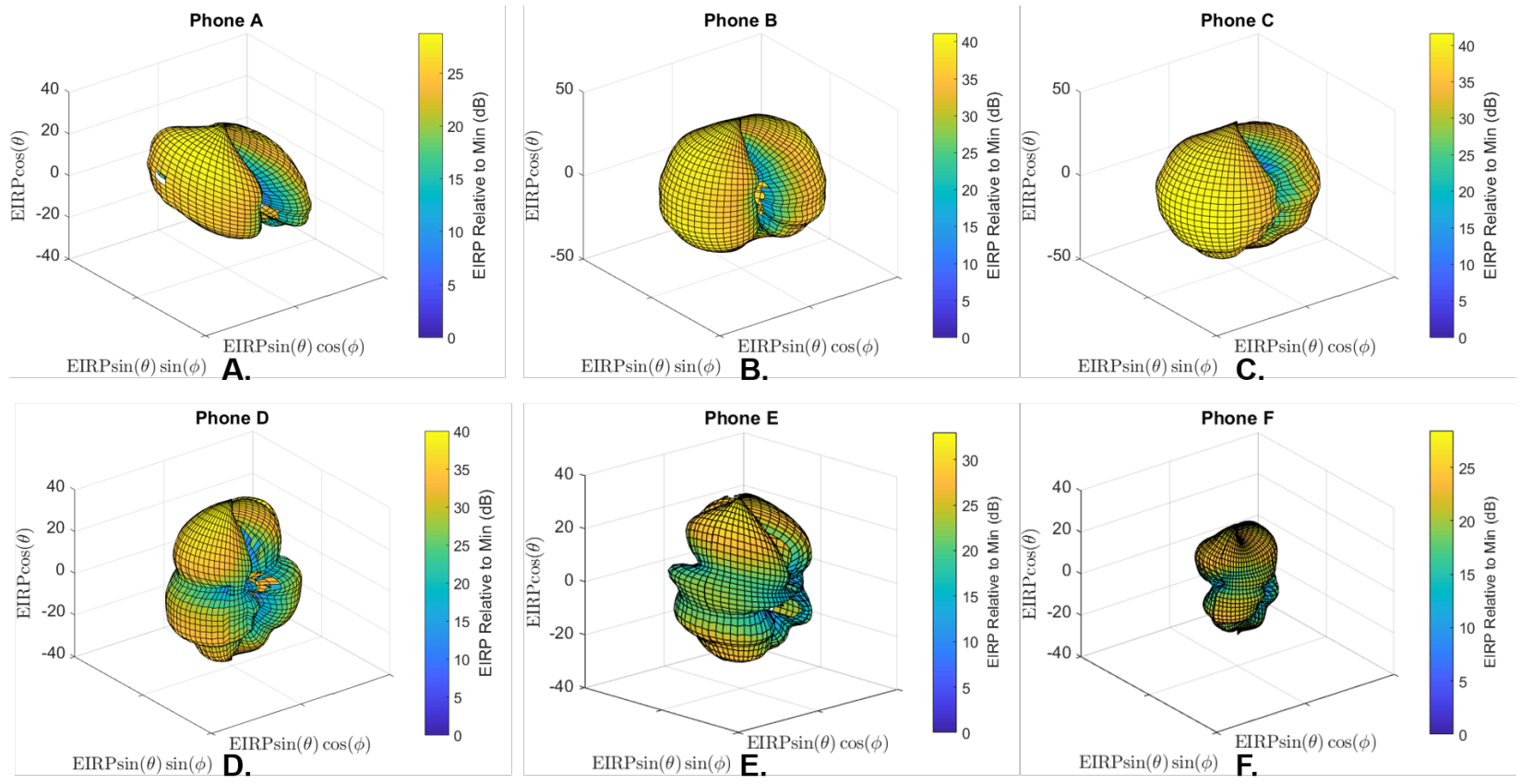


Figure D.2: Three-dimensional radiation pattern with vertically polarized measurement antenna of (A.) phone A, (B.) phone B, (C.) phone C, (D.) phone D, (E.) phone E, (F.) phone F.

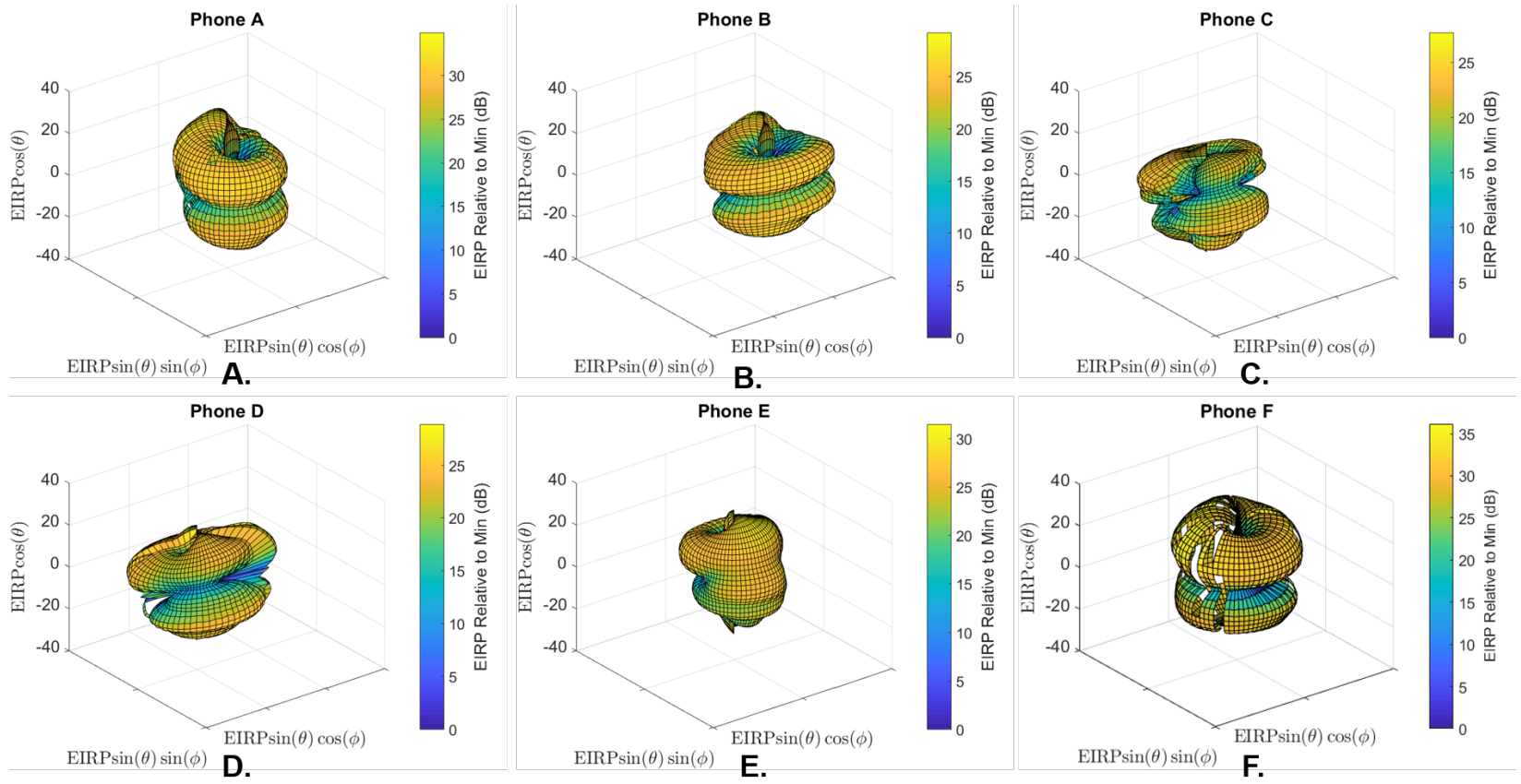


Figure D.3: Three-dimensional radiation pattern with horizontally polarized measurement antenna of (A.) phone A, (B.) phone B, (C.) phone C, (D.) phone D, (E.) phone E, (F.) phone F.

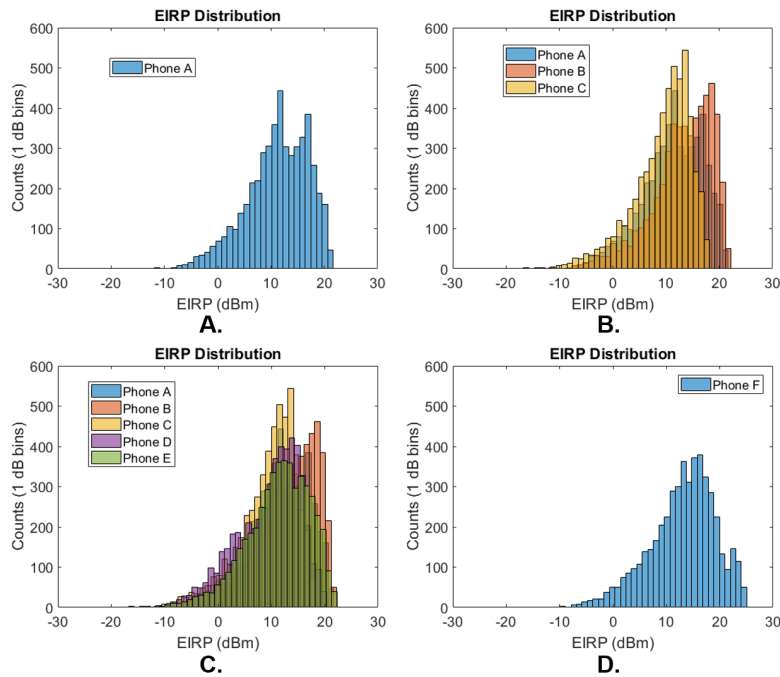


Figure D.4: Histograms of the EIRP measured at all the angles with both horizontal and vertical polarization of the measurement antenna. A.) The histogram of only phone A. B.) Histogram of Phones A-C. C) Histogram of Phones A-E for comparison D.) Histogram for phone F.

A useful metric when modeling the emissions (or aggregate emissions) of a UE is the distribution of power measured from the full UE patterns. These distributions could provide a better sense of the average interference power that will be seen by a victim device. Furthermore, the distributions provide an excellent source for a Monte Carlo sampling of expected power from the UE which could assist with understanding deviations from peak power. These distributions are shown in Figure D.4. To ease with interpretation, distributions from the different phones are included in the four plots. Phones A-C show a sharp cutoff at their highest EIRP values. Phones D-F have histogram peaks at lower power, but have fewer points in the lowest-power regime.

Appendix E

Estimation of Cell-Site Path Loss Distributions

This appendix summarizes two separate efforts supporting the NASCTN test. Cell site radii and path loss distribution calculation methods are documented in a MITRE Product (MP) titled "Investigations and Analyses of LTE Network Cell Tower Deployments and Impact on Path Loss Calculations [25]." Also summarized here is a method of predicting power outputs of UE (P_{UE}) using the open-loop component of the LTE power control equation.

The objective of the path loss prediction effort was to take a data set of real-world cell tower locations, calculate cell site spacing (in kilometer (km)), sort into multiple morphologies (e.g., urban, suburban, rural), then use a propagation model to calculate path loss at the edge of the cell radii. Results of the path loss is shown as a distribution of loss (in decibel (dB)) the the edge of the cell tower radius. The remainder of this appendix will demonstrate how the open-loop power control equation can be used to predict P_{UE} .

E.1 Data Set: LTE Network Service Provider

The eNB location data set provided to NASCTN from a national wireless network operator (WNO) encompasses a large set of eNB deployment information. For the purposes of developing the cell radii predictions and subsequent analyses, this appendix uses the coordinates (latitude and longitude) of current and future macro-cell eNB deployments and their anticipated or deployed antenna heights. Macro cell eNB were used in the cell radii and path loss calculations to mirror the NASCTN experiment. The eNB location data set covers approximately 14 000 cell tower points in the United States. The literature shows as of 2017 there are an estimated 215 000 eNB cell tower sites across the continental United States [26]. Although the AWS-3 eNB location data set is limited in quantity, the data set spans a large number of land cover types and gives data across major regions in the United States.

E.2 Morphology

The eNBs were grouped into three *clutter categories* (hereafter referred to as morphologies), a sorting used to apply clutter loss to the propagation distributions. The propagation channel between eNB and UE is *ground to ground* which is highly dependent upon the clutter, such as ground cover, buildings, foliage. The set of clutter categories, or morphologies, are urban, suburban, and rural. These morphologies were determined by the National Land Cover Database (national land coverage database (NLCD)) methodology described in [25, 27].

The NLCD land use categories are determined by using 30 m x 30 m squares across the entire United States land area. A generalized coverage area of a cell is used to cut an area out of the data.

Due to the greater resolution and granularity, the NLCD categorization techniques can go beyond just the three morphologies provided by the census data.

E.3 Cell Radius

The eNB location dataset was used to calculate the distances between eNBs, half the distances is the *cell radius*. Cell radius is used to describe the radius of an assumed circular signal coverage area of a cell tower, as a representation of its coverage area. This circular coverage region does not account for antenna patterns or variations due to terrain. The calculations assumed coverage from the same provider did not overlap (on average, there is equal likelihood a user would attach to either eNB in an overlapping coverage scenario). The cell radius of a tower is assumed to only reach as far as the nearest neighbor's cell radius. For example, if two towers are one kilometer apart, the cell radius of each tower is 500 m (no overlapping was considered in this paper). Finding cell radii across the eNB location dataset allows calculating the distributions of cell radii sorted by morphology. The distance calculation method used is known as a *nearest neighbor* calculation. Specific implementation details of this calculation are provided in [25].

Table E.1 shows the mean cell radii calculated. A UE located at this distance from the eNB is considered to be on the cell edge.

Type:	Cell Radii Mean(km)		
	Rural	Suburban	Urban
NLCD	3.16	1.73	1.03

Table E.1: Mean cell radii calculated using the ball tree algorithm after grouping eNBs into their respective morphologies.

E.4 Path Loss by Morphology

With an understanding of the cell radii distributions, eNB frequencies and antenna heights, the Extended Hata-Okumura model (hereafter referred to as E-Hata model) was used to determine path loss. The E-Hata propagation model is an appropriate path loss model as it applies to frequencies from $1500 \text{ MHz} < f \leq 2000 \text{ MHz}$ and includes clutter loss factors for urban, suburban, and rural morphologies.

The E-Hata model contains loss factors for each of the three morphologies investigated (rural, suburban, and urban). The inputs to the E-Hata Model are the frequency f (set to 1775 MHz), cell tower heights (provided in the carrier provided eNB location dataset) distance (d , each cell radius for edge case path loss). The outputs of the E-Hata are path loss distributions for each of the three morphologies.

The median E-Hata path loss values are shown in Table E.2. At the cell edge, the urban morphology has 20 dB path loss more than the rural, which is to be expected as there is more man-made clutter loss (such as buildings) in an urban setting.

Path Loss Function:	Median(dB)		
	Rural	Suburban	Urban
NLCD Hata	115	125	135

Table E.2: Median modified Hata path loss for each morphology by cell tower data set.

Figure E.1 shows the distributions of cell edge path loss across the set of eNB locations.

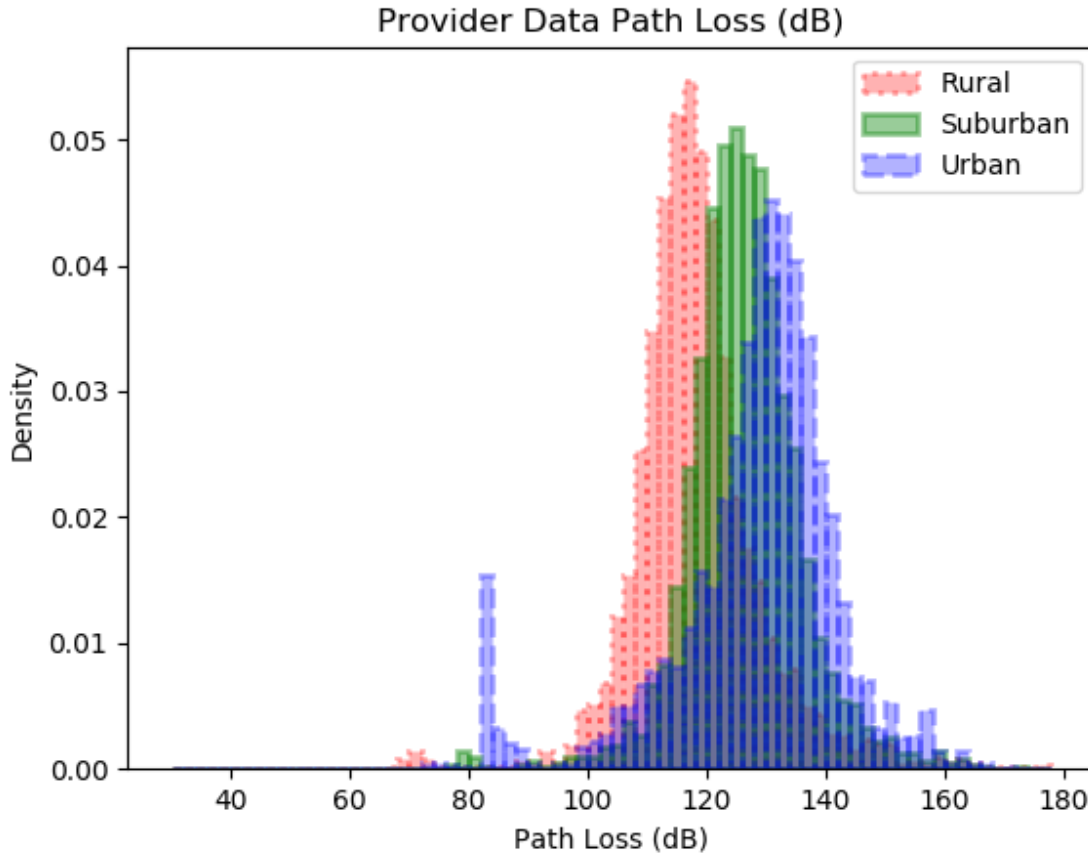


Figure E.1: NLCD based Hata-Okumura Model path loss distributions.

E.5 Producing P_{UE} Distributions Using Open-Loop Power Control Equation

Given the path loss to a cell edge and the radius of the cell, eNB open-loop power control equation can predict UE output powers (P_{UE}) required to close the UE to eNB link. The LTE open-loop power control equation is shown in Equation E.1 below.

$$P_{UE} = P_0 + \alpha \cdot PL \tag{E.1}$$

The P_{UE} and α are network settings of an eNB. Drive testing by the DSO show values for α commonly range from 0.8 to 0.9 and P_0 ranges from -80 dBm to -90 dBm. Using a Monte Carlo simulation with 1000 trials. Figures E.2, E.3, and E.4 show the cumulative density functions for rural, suburban, and urban P_{UE} across the ranges of α and P_0 .

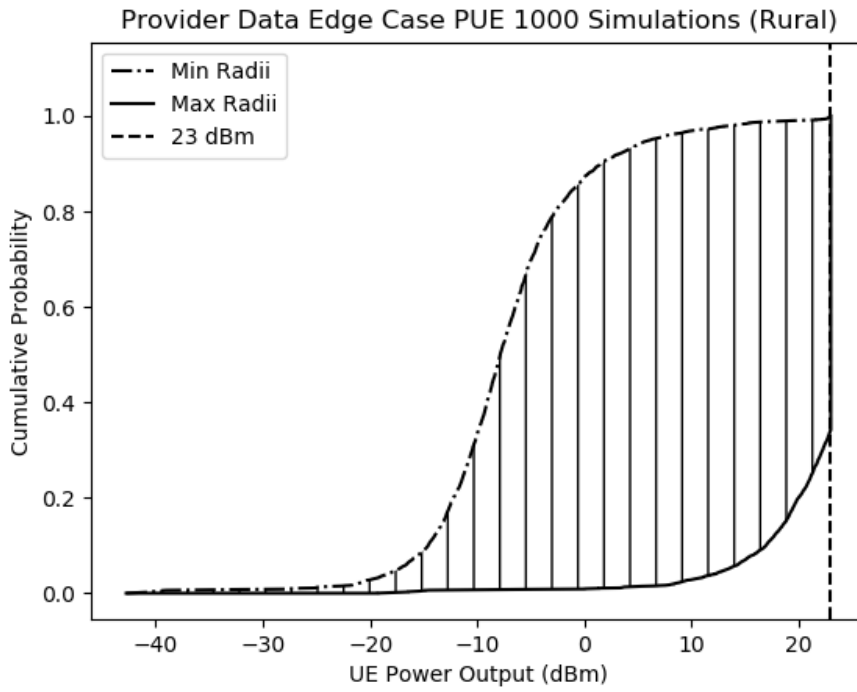


Figure E.2: Cumulative density function for rural.

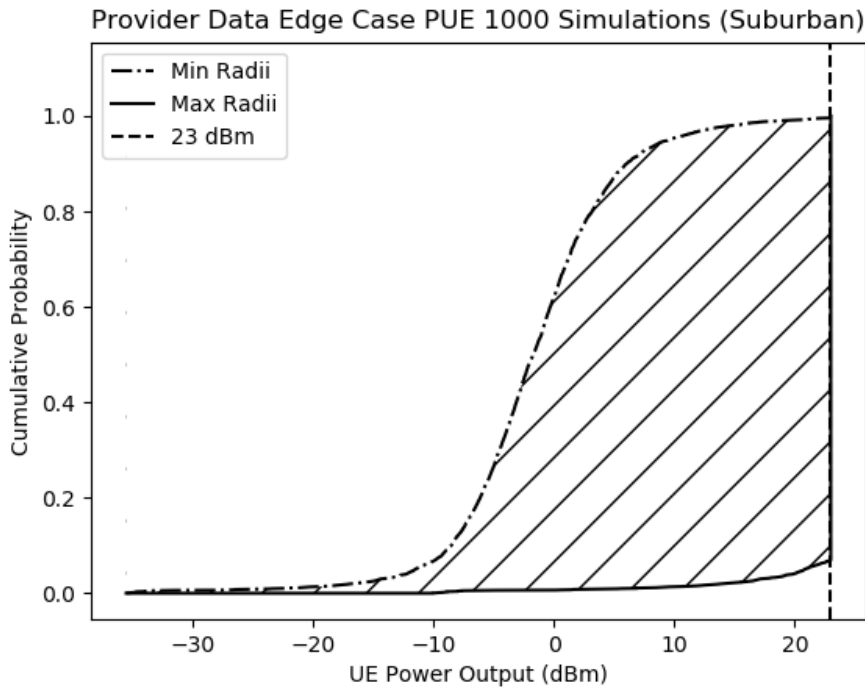


Figure E.3: Cumulative density function for suburban.

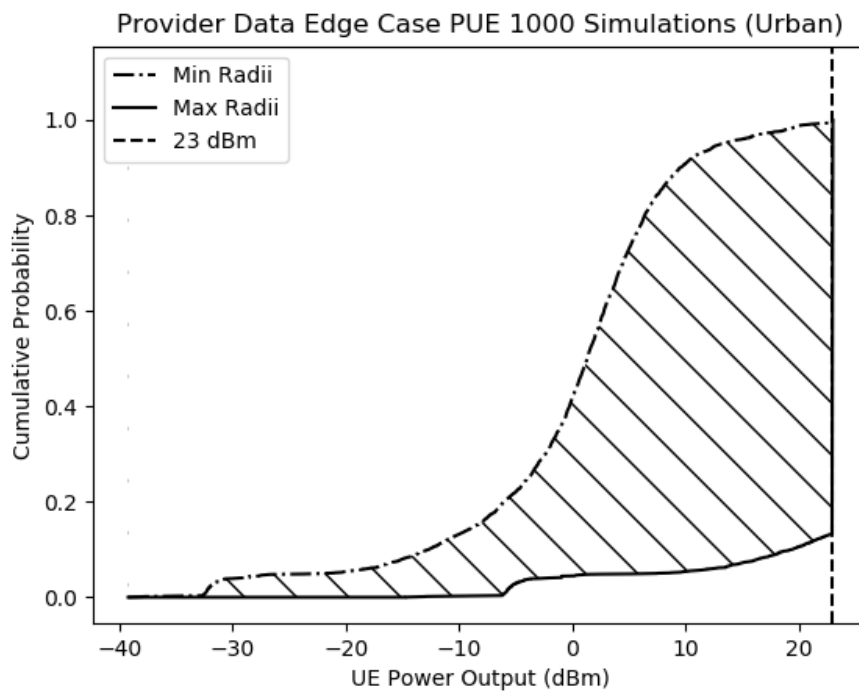


Figure E.4: Cumulative density function for urban.

Appendix F

MITRE Lab Results In Support of NASCTN Test

MITRE's role in the factor selection process was to independently repeat aspects of NASCTN experiments, including RF power measurement and comparison to chipset readings, and validation of variance and mean in power levels. These tests were complementary in nature to determine the similarity of observations from the test methodology using a different testbed setup. The following sections will describe the multi UE system emulator (MUSE) in terms of hardware, software, control, and the results obtained from the system to verify power measurement.

F.1 MITRE's Multi-UE System Description

The MUSE, shown in Figure F.1, was designed to emulate the behavior of many real UEs in an LTE band 66 network. The system is scriptable and automatically produces reports at the end of each set of tests. Network parameters and hardware settings are configurable through configuration files used by MITRE's automation software. Each UE in the system reports individual transmit power which is used to analyze the effects of various configurations and data flow profiles.

Every UE has its own connection to the RF network through an attenuator board with a range of 63 dB per path, with the capability to connect to up to two eNBs and one downlink interference source. An uplink interference source can be injected into the uplink path through a splitter closer to the eNB. The UEs are distributed in sets of eight in three RF screen boxes, each containing an attenuator board with a connection from each UE. Because the uplink is attenuated prior to reaching the channel emulator, designed for stronger signals, the block amplifies the uplink and passes the downlink. Since each set of UEs is connected to a unique channel on the channel emulator, up to three channel models can be emulated per test. A second port on the screen box is used to record absolute UE power prior to attenuation since measurements post attenuation would be the same from every UE in order to meet eNB p_0 power requirements. The port is connected to an IQ recorder. The downlink is passed out of a splitter connected to the eNB twice: one port is used for protocol analysis, and the other is connected to an IQ recorder. Lastly, the uplink is passed from a coupler connected to the eNB for protocol analysis. The IQ recoder and protocol analyzer record both uplink and downlink channels synchronously.

The system, shown in Figure F.2, is fully automated through USB and network connections to a central control server, and a commercially available chipset diagnostics tool. The controller computer hosts a platform for automation, developed by MITRE, which facilitates the initialization and per-test configuration of components, and the collection and analysis of data that comes out of the system. The chipset diagnostics software runs scripts generated by a script generator, developed by MITRE, that controls data flow from the test devices. The scripts can instruct the UEs to ping, file transfer protocol (FTP), and wait (no activity). From these inputs, the system emulates a real-world scenario where UEs are transmitting from different locations in the network, set by the attenuator board.

The outputs of the system come from the simultaneous uplink and downlink IQ recordings, protocol recordings,

and protocol and chipset recordings made by the chipset diagnostics software. The downlink IQ capture aligns the recordings to a frame and subframe, and the uplink capture is used to measure actual transmit power and compared to the reported transmit power from the chipset readings. The data analysis software uses the protocol captures to align chipset readings of transmit power from the chipset diagnostics software and merge them into a single file. The file is parsed to create statistics including CDFs of transmit power per resource block, histograms of resource block utilization, histograms of which resource blocks were scheduled, histograms of MCS per UE and total, and histograms of RSRP.

Figures F.1 and F.2 detail the hardware RF and software diagrams at the top-level.

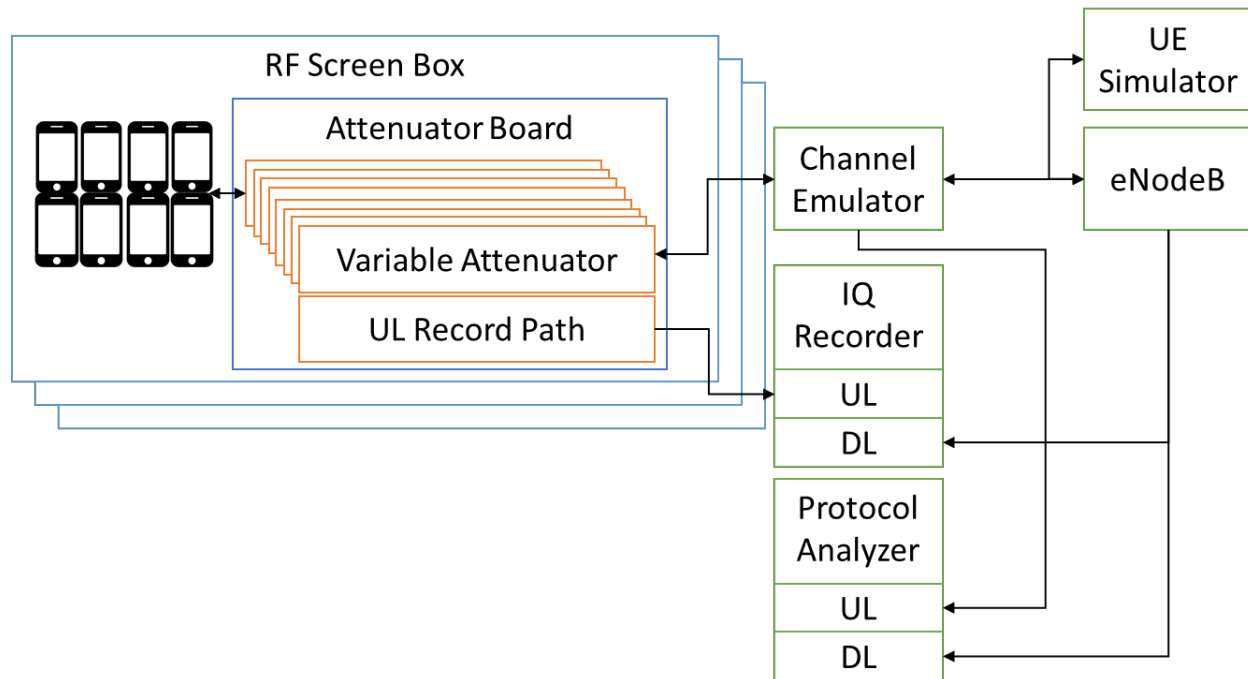


Figure F.1: RF Hardware Functional Concept of MITRE Multi-UE System.

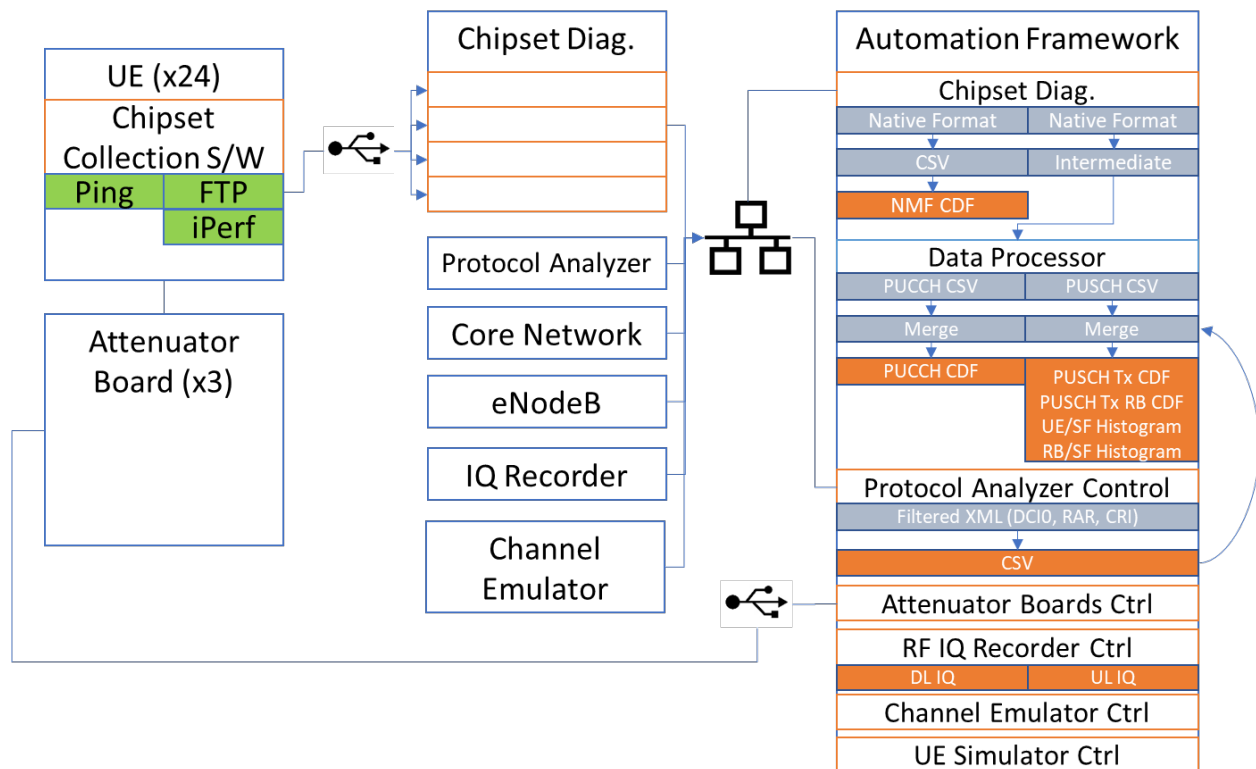


Figure F.2: Software Functional Concept of MITRE Multi-UE System.

F.1.1 Software Control

MUSE leverages a MITRE-developed test automation framework to execute tests autonomously in a controlled, repeatable manner. The test automation framework architecture is shown in Figure F.3.

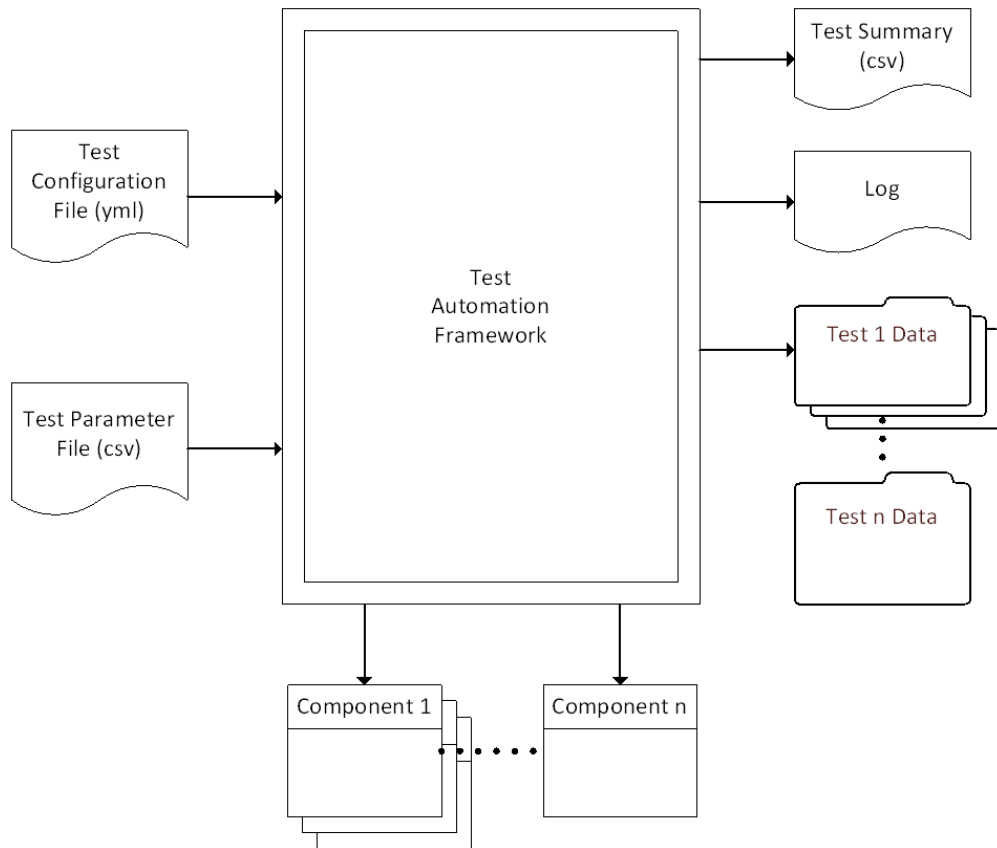


Figure F.3: Test Automation Framework Architecture.

The test automation framework executes a variable number of tests within a test run. Test runs are defined by two files: a test configuration file defines the various test components that will be used in the test run, along with their initial configurations.; and a test configuration file which defines the number of tests to execute and parameters of individual test components that may be modified during each test within the test run. The Test Automation Framework uses these files to create and manipulate the test components for each test in the test run. The test components provide feedback to the Test Automation Framework in the form of log messages, per-test data, and warning/error conditions.

For MUSE, five test components are used. The attenuator board sets the path loss between each UE and the eNB. The UE control and metrics component configures the number of UEs in the test, configure the traffic generation configuration of each UE, and record per-UE metrics, such as RSRP, reported Tx power, number and location of PRBs transmitted per subframe. The eNB component configures and queries the configuration of the eNB. The RF IQ recorder automates the recording of UL transmissions. The protocol analyzer monitors and logs UL and DL messaging.

The test automation framework generates several outputs for each test run. The test summary log file contains summarized data points from the test components in CSV format. The test log provides a timestamped log of the test run process and log messages that were generated from each of the test components. The test report contains per-test

iteration configurations, metrics, and charts. Finally, a directory is created per test which contains component data logs, which are any output files specifically generated by the components in the test. For MUSE, these include per-subframe data outlining all traffic from all UEs for the duration of the test (e.g., number and location of PRBs, reported Tx Power, MCS), DL and UL IQ recording, and charts outlining various LTE key performance indicators (KPIs), such as those shown in Figure F.4 and Figure F.5.

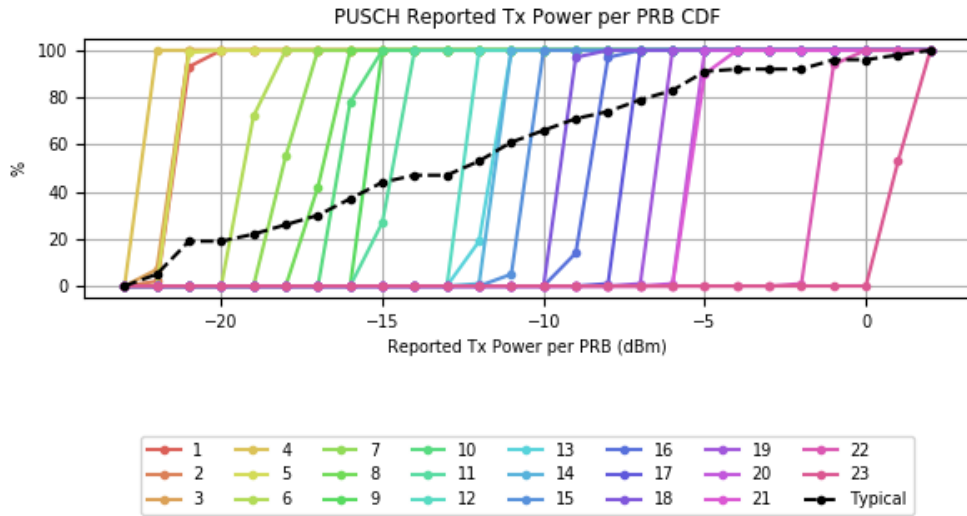


Figure F.4: Reported Tx Power per PRB CDF.

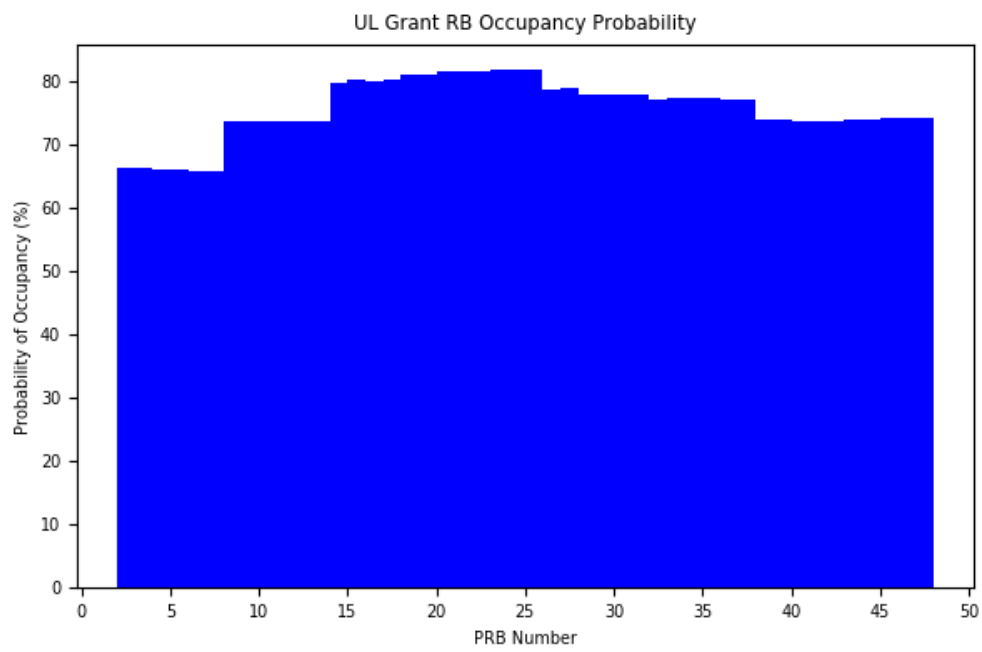


Figure F.5: PRB Occupancy.

F.1.2 Test Design

Each test is designed to replicate a real-world or experimental scenario involving UEs, their traffic, and a cellular network. As explained in prior sections, up to 24 UEs can be configured per test, and they connect to the same eNB. The UEs can be configured to be in airplane mode or to transmit data. The network replicated by the tests usually represents a probability of UE activity in terms of number of resource blocks active, number of occupied subframes, and number of UEs transmitting simultaneously.

F.1.2.1 Traffic Generation

MITRE's script generation tool generates traffic profiles based on three input distributions: burst rate, payload size, and off time. If the burst rate is sufficiently high, FTP transfer is used instead to represent a large file upload. In the case of NASCTN tests, a simpler approach was used: a throughput of 194 kbit/s or 388 kbit/s was chosen and applied to every UE in the test.

F.1.2.2 eNB Configuration

Various parameters in the eNB configuration were manipulated to elicit different power transmission characteristics from the UE. Namely, P_0 -nominal PUSCH, P_0 -nominal PUCCH, and α were changed for different tests. α is a path loss coefficient that is designed to lower the transmission level of UEs further from the eNB to reduce intercell interferences.

P_0 -nominal PUSCH is the target power at the eNB for uplink shared channel transmissions. Power control uses the value as a base, but the actual transmission power is affected by α , power control commands, and limitations to the UE transmit power.

F.2 Data Acquisition

Each run of the MUSE produces three types of data: downlink control information, chipset and protocol recordings, and baseband IQ recordings.

Downlink control information (DCI) Format 0 (DCI0) messages are recorded from the physical downlink control channel (PDCCH) by the RF protocol analyzer. DCI0 specifies the uplink allocation in terms of starting resource block, number of resource blocks, and the MCS. They are not guaranteed to match the grants as decoded by the UE due to a low probability of decoding error. However, the RF protocol analyzer recordings offer a consolidated view of all the UL allocations granted by the eNB and are used to line up, subframe by subframe, the outputs from each UE, which are described in the next section. The RF protocol analyzer's log is saved as an XML file, which is converted to a CSV file with fields matching those of the chipset log.

Chipset and protocol recordings are made by the chipset diagnostics tool. These recordings are pulled from individual UEs, and they contain reported transmit power at the antenna port of each UE and the resource blocks at which the transmission occurred. Each UEs log is converted to a CSV file.

A baseband IQ recording of the UL and DL is captured by the IQ recorder. These are stored as binary files, where each IQ sample is represented by two 16-bit signed integers. A peak voltage value, logged by the device, is used to convert each pair of binary integers into the actual voltage measured by the instrument. After each experiment, the DCI0 grants from the RF protocol analyzer and the chipset recordings are merged to produce a CSV file which contains the uplink allocation information and reported transmit power for every UE per subframe (1ms) of the experiment. This is referred to as the merged UE grant file. The system frame and subframe information is also recorded in the merged UE grant file, which enables the identification of each UL transmission in the raw IQ data.

F.2.1 System Calibration

The RF power loss between the UE and the IQ recorder must be measured to directly compare the UL transmit power recorded by the IQ recorder to that reported by the UE chipset. The path loss was measured using a commercially available network analyzer. The device was set up to perform a frequency sweep across the range of the UL band, and an electric calibration module was used to calibrate the equipment and the attached cables to the desired settings. Port 1 was connected to the UE antenna port, and Port 2 was connected to the signal analyzer input port. The S-parameter information for the measured loss was saved at the center frequency, against multiple attenuation values. The insertion loss was determined from the S21 measurements.

F.3 Data Processing

The processing of the IQ recordings was performed in MATLAB. The process can be broken down into three steps: downlink synchronization and system information extraction, epoch subframe alignment with the merged allocation information file, and uplink power computation and spectrogram analysis.

F.3.1 Downlink Synchronization and Master Information Block Extraction

Processing the IQ recordings requires synchronization to a frame boundary, which is where the master information block (MIB), and the primary synchronization signal (PSS) and secondary synchronization signal (SSS) reside. Once synchronization is achieved, the MIB can be decoded, specifying the bandwidth and frame number. The control format indicator (CFI) is read to determine the size of the control channel, including the DCI0 UL resource grants.

F.3.2 Epoch Subframe Alignment

LTE frame numbers are cyclic over a period of 1024, which means the frame and subframe numbers are only unique over a 10.24 second interval, referred to as the LTE “epoch”. For experiments lasting more than one epoch, there will be multiple offsets, spaced at intervals of 10.24 seconds, in the IQ file which could correspond to any subframe in the merged UE grant file. To resolve this issue, each candidate offset is checked by decoding 200 UL grants chosen randomly from the merged UE grant file. A correct alignment will produce decoded grants which largely agree with those from the file, while an incorrect alignment will yield many mismatches. Mismatches are expected even with correct alignment due to a non-zero probability of the processing software incorrectly decoding the DCI message. An offset is recorded as the correct epoch offset if there are no more than 5 % mismatches. The 5 % threshold was chosen with the expectation that the match percentage will either be close to 100 % for correct alignment or close to 0 % for incorrect alignments. Since the UL and DL are synchronized, the correct epoch offset is used to identify the offset of each UL transmission in the IQ UL waveform.

F.3.3 Uplink Power Computation and Spectrogram Analysis

Once synchronization and alignment was achieved, the UL LTE resource grid corresponding to each grant can be demodulated. Using the epoch offset, system frame number, subframe number, starting resource block number, and grant size, each grant given in the merged UE grant file can be located exactly in the uplink spectrogram. The power in that portion of the spectrum can then be easily computed.

Figure F.6 shows an example of a demodulated grid from the IQ UL data. The merged UE grant file contained a grant in subframe 1, starting at resource block 1, of size 1. This hypothetical location of the UL transmission has been outlined by a red box. There is energy in the indicated region, which means that the grant was decoded correctly, and a transmission did occur.

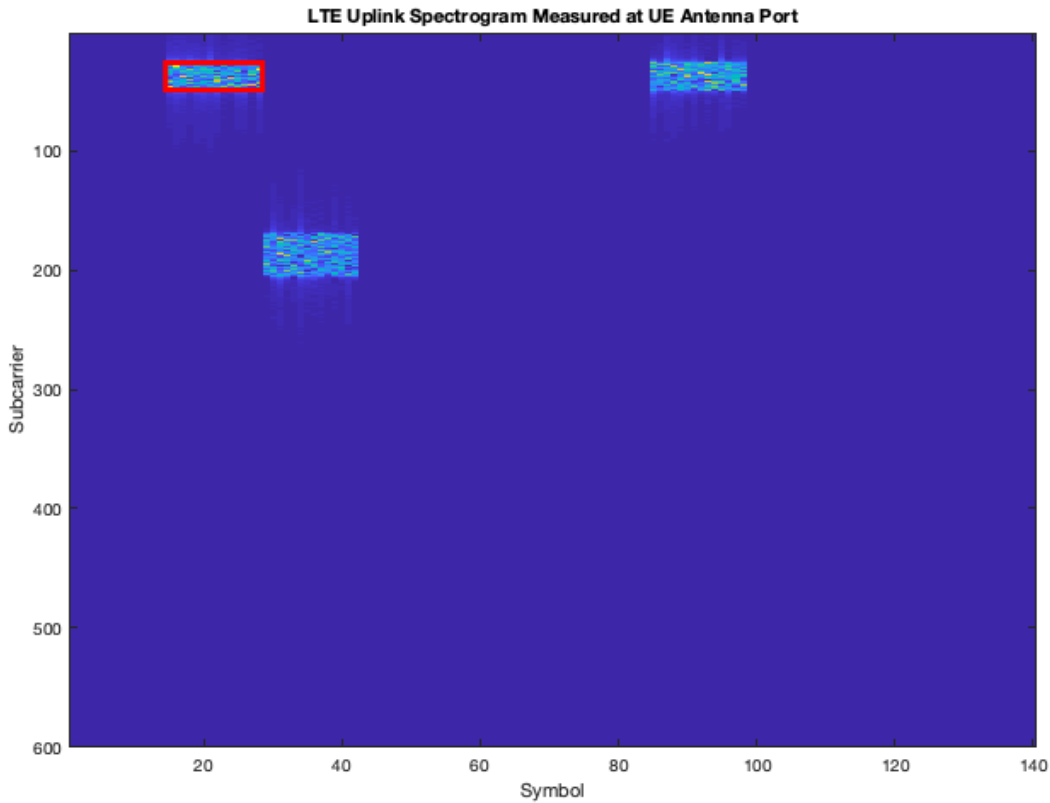


Figure F.6: Resource Grant from Merged Data Highlighted in Spectrogram.

To compute the power for each grant, the resource blocks corresponding to that grant are filtered out of the signal in the frequency domain via masking. The subframe containing the grant is then demodulated to a time domain signal. The root mean square (RMS) power is computed as $P_{rms} = \langle \frac{|V|^2}{2R} \rangle$, where $\langle \cdot \rangle$ is the time average, V is the complex voltage (i.e. value of each IQ sample) and R is 50, corresponding to the standard 50 ohm impedance in the RF feed of the IQ recorder. The RF loss between the chipsets and the IQ recorder input is added to the computed RMS power to correct them for direct comparison with the transmit power reported by the chipset.

The RMS power was not computed directly in the frequency domain to avoid complications with scaling factors that may be introduced by the fast fourier transform (FFT) and cyclic prefix. Since subcarriers are orthogonal in OFDM, the masked grid should be identical to the grid the UE modulated for transmission.

F.3.4 Results

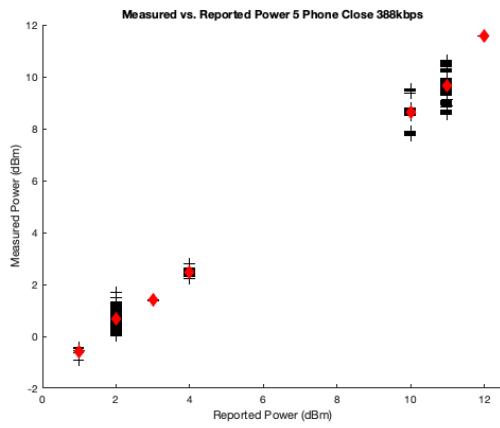
A series of tests were conducted to compare the measured and reported power of a single UE under the conditions shown in Table F.1.

A set of measured power values were calculated from the IQ data for each reported power recorded by the UE chipset during the test. Figure F.7 shows scatter plots from each test, comparing the reported power (horizontal axis) with the measured power (vertical axis). The mean measured power for each reported power is denoted by a red diamond.

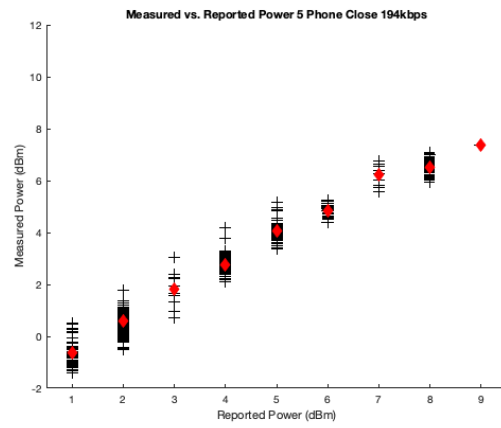
Table F.1: Test Description.

Test Number	Nominal UL Throughput	RSRP	# of UEs
1	388 kbit/s	-68 dBm (close)	5
2	194 kbit/s	-68 dBm (close)	5
3	388 kbit/s	-88 dBm (far)	5
4	194 kbit/s	-88 dBm (far)	5

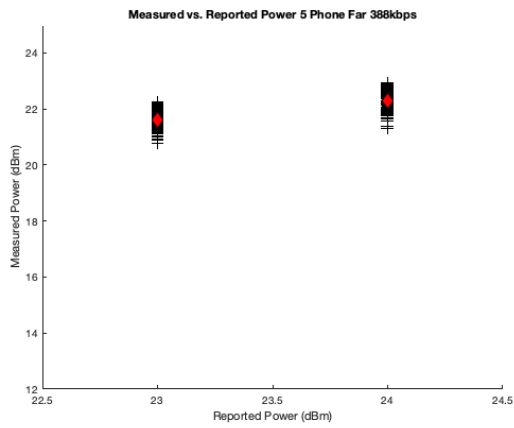
The mean measured powers were generally 1 dB lower than the corresponding reported powers. The offset seems consistent over all reported power, which suggest there is a source of power loss that is not being accounted for. Note that the spread of the measured power increases significantly near the 23 dBm limit. More data points collected at reported power levels between 12 dBm and 23 dBm may reveal when the degradation of precision occurs. Also, it is worth mentioning the measured power never exceeds 23 dBm even when the chipset is reporting a transmit power of 24 dBm. This is consistent with the hardware specifications outlined in the LTE standard.



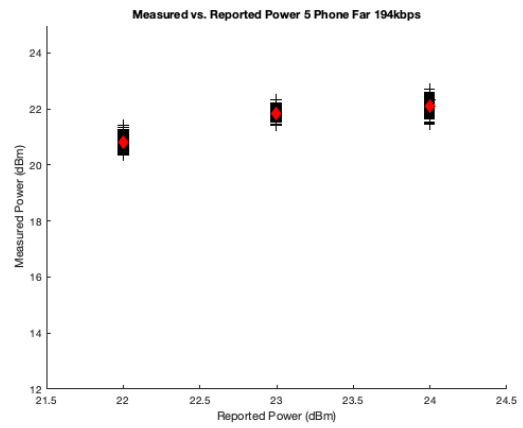
(a) Test 1



(b) Test 2



(c) Test 3



(d) Test 4

Figure F.7: Measured vs Reported Power Comparison

Bibliography

- [1] P. Hale, S. Genco, J. Coder, M. Lofquist, A. Wunderlich, J. Ladbury, A. Kord, J. Cook, T. Hall, and K. Hartley, "Aggregate LTE: Characterizing User Equipment Emissions Metrology Plan," 2017. [Online]. Available: https://www.nist.gov/sites/default/files/documents/2017/11/30/aggregate_lte_test_plan_update_2017.11.28.pdf
- [2] R. Horansky, J. Coder, and J. Ladbury, "LTE Handset Emissions: Radiation Pattern Measurements Final Test Report," NASCTN, Tech. Rep. 2056, Aug 2019. [Online]. Available: <https://doi.org/10.6028/NIST.TN.2056.pdf>
- [3] U.S. Government Publishing Office. (2010) Presidential memorandum: Unleashing the wireless broadband revolution. [Online]. Available: <https://www.gpo.gov/fdsys/pkg/CFR-2011-title3-vol1/pdf/CFR-2011-title3-vol1-other-id236.pdf>
- [4] National Telecommunications and Information Administration. An assessment of the near-term viability of accommodating wireless broadband systems in the 1675-1710 MHz, 1755-1780 MHz, 3500-3650 MHz, and 4200-4220 MHz, 4380-4400 MHz bands. [Online]. Available: https://www.ntia.doc.gov/files/ntia/publications/fasttrackevaluation_11152010.pdf
- [5] Federal Communications Commission. Auction 97, Advanced wireless services (AWS-3). [Online]. Available: http://wireless.fcc.gov/auctions/default.htm?job=auction_summary&id=97
- [6] D. C. Montgomery, *Design and Analysis of Experiments*, 9th ed. Hoboken, NJ: John Wiley & Sons, 2017.
- [7] C. F. Wu and M. S. Hamada, *Experiments: Planning, Analysis, and Optimization*, 2nd ed. Hoboken, NJ: John Wiley & Sons, 2009.
- [8] 3rd Generation Partnership Project, "Policy and charging control architecture (3GPP TS 23.203 Release 8)," 3GPP, Tech. Rep., 2010. [Online]. Available: https://www.etsi.org/deliver/etsi_ts/123200_123299/123203/08.09.00_60/ts_123203v080900p.pdf
- [9] 3rd Generation Partnership Project, "Physical layer procedures (3GPP TS 36.213 Release 10)," 3GPP, Tech. Rep., 2011. [Online]. Available: https://www.etsi.org/deliver/etsi_ts/136200_136299/136213/10.03.00_60/ts_136213v100300p.pdf
- [10] 3rd Generation Partnership Project, "LTE: E-UTRA Radio Resource Control (RCC) (3GPP TS 36.331 version 13.0.0 Release 13)," 3GPP, Tech. Rep., 2016. [Online]. Available: https://www.etsi.org/deliver/etsi_ts/136300_136399/136331/13.00.00_60/ts_136331v130000p.pdf
- [11] 3rd Generation Partnership Project, "LTE: E-UTRA User Equipment (UE) radio transmission and reception (3GPP TS 36.101 version 14.3.0 Release 14)," 3GPP, Tech. Rep., 2017. [Online]. Available: https://www.etsi.org/deliver/etsi_ts/136100_136199/136101/14.03.00_60/ts_136101v140300p.pdf
- [12] B. Benammar, N. Thomas, M.-L. Boucheret, C. Poulliat, and M. Dervin, "Analytical Expressions of Power Spectral Density for General Spectrally Shaped SC-FDMA Systems," Tech. Rep., 2013. [Online]. Available: <http://www.eurasip.org/Proceedings/Eusipco/Eusipco2013/>
- [13] U. Groemping, "FrF2: Fractional Factorial Designs with 2-Level Factors," 2016, version 1.7-2. [Online].

Available: <https://cran.r-project.org/package=FrF2>

- [14] A. S. Hedayat, N. J. A. Sloane, and J. Stufken, Orthogonal Arrays: Theory and Applications. New York: Springer, 1999.
- [15] W. F. Kuhfeld, “Orthogonal Arrays,” SAS Institute, Inc., Tech. Rep. TS-723, 2006. [Online]. Available: <https://support.sas.com/techsup/technote/ts723b.pdf>
- [16] T. Naes, A. Aastveit, and N. Sanhi, “Analysis of split-plot designs: An overview and comparison of methods,” Quality and Reliability Engineering International, vol. 23, pp. 801–820, 2007.
- [17] G. Milliken and D. Johnson, Analysis of Messy Data: Volume 1 Designed Experiments. Belmont, CA: Lifelong Learning Press, 1984.
- [18] R. A. Johnson and D. W. Wichern, Applied Multivariate Statistical Analysis, 6th ed. Upper Saddle River, NJ: Pearson Prentice Hall, 2007.
- [19] I. Jolliffe, Principal Components Analysis, 9th ed. New York, NY: Springer-Verlag, 2002.
- [20] T. Seo and M. Siotani, “The multivariate studentized range and its upper percentiles,” Journal of the Japanese Statistical Society, vol. 22, no. 2, pp. 123–137, 1992.
- [21] D. S. Moore, W. I. Notz, and M. Fligner, Basic Practice of Statistics, 7th ed. New York, NJ: Freeman and Company, 2015.
- [22] Defense Spectrum Organization, “Advanced wireless services-3 early entry portal analysis capability algorithm definition document,” March 2016, SO-HDBK-16-097.
- [23] H. Friis, “A Note on a Simple Transmission Formula,” Proc. IRE, vol. 34, no. 5, pp. 254–256, 1946.
- [24] W. Young, A. Feldman, S. Genco, A. Kord, D. Kuester, J. Ladbury, D. McGillivray, A. Puls, A. Rosete, A. Wunderlich, and W.-B. Yang, “LTE Impacts on GPS: Final Report,” National Institute of Standards and Technology, Tech. Rep. 1952, Feb 2017.
- [25] J. Carpenter, J. Johnson, M. Lofquist, and K. Hartley, “Investigations and analyses of LTE network cell tower deployments and impact on path loss calculations,” The MITRE Corporation, Tech. Rep. MP190327, 2019. [Online]. Available: <https://www.dtic.mil>
- [26] Statistic Brain Research Institute, “Cell phone tower statistics,” crowd-sourced data. [Online]. Available: <https://www.statisticbrain.com/cell-phone-tower-statistics/>
- [27] Multi-Resolution Land Characteristics Consortium, “National Land Cover Database.” [Online]. Available: <https://www.mrlc.gov/data>